Solid-State Dynamics of Porous Materials

by

Ilne Grobler

Promoter: Prof. L. J. Barbour

Co-Promoter: Prof. C. Esterhuysen

Submitted in partial fulfilment of the requirements for the degree

Doctor of Philosophy

Department of Chemistry and Polymer Science

Faculty of Science

Stellenbosch University

December 2013

DECLARATION

By submitting this dissertation electronically, I Ilne Grobler hereby declare that the entirety of the work contained herein is my own, original work, that I am the owner of the copyright thereof (unless to the extent explicitly stated otherwise) and that I have not previously in its entirety or in part submitted it for obtaining any qualification.

Date: 19 November 2013

ABSTRACT

A number of porous metal-organic and organic crystalline materials were prepared with a view to study the solid-state dynamics involved in sorption and guest-exchange processes. The main goal was to gain an understanding of the mechanisms involved in structural changes induced by external stimuli. To this end, single-crystal X-ray diffraction (SCD) experiments were carried out under variable temperature and pressure conditions, supplemented by thermal analysis and sorption experiments.

In the first section, the synthesis of metal-organic frameworks from the combination of rigid and unsymmetrical ligands with transition metal salts was studied. Only three of the twelve novel MOFs could undergo single-crystal to single-crystal transformations. The two-dimensional (2D) MOFs (**IMOFF-1** and **IMMOF-2**) formed with 4-(1*H*-benzo[*d*]imidazol-1-yl)benzoic acid (**L6**) drastically transform their structures during guest-exchange processes owing to mutual displacement of the 2D layers. These MOFs can be classified as third-generation soft porous materials. Specifically the MOF formed with **L6** and $Zn(NO_3)_2$ has transformable void space and converts to a lower density phase with double the carbon dioxide (CO_2) capacity upon exposure to high CO_2 pressure. MOFs with gate-opening sorption behaviour are rare and this study is distinctive, as it combines high pressure differential scanning calorimetry with SCD under gas pressure. The MOF includes the CO_2 within discrete pockets of space where it is stabilised by many host-guest interactions. Consequently, there is extreme hysteresis in the desorption of CO_2.

The second section outlines the sorption and guest-exchange properties of a three-dimensional and permanently porous MOF (**IMMOF-3**). The single crystals of **IMMOF-3**, incorporating 4-(1*H*-naphtho[2,3-*d*]imidazol-1-yl)benzoic acid (**L7**), are extremely robust and chemically stable, owing to favourable intra-framework interactions between the ligands. Gas and vapour sorption affirmed its versatility in including a wide range of guest molecules within the one-dimensional channels. Moreover, the MOF exhibits anisotropic thermal expansion with coefficients of thermal expansion that can be fine-tuned by the inclusion of a series of related guest molecules within the channels.

In the third section, the transient porosity of a metallocyclic material (**MC1**) with discrete voids was explored. Small molecules can be transported through the crystal structure despite the absence of permanent channels, as demonstrated by the sorption of CO_2, nitrogen (N_2) and ethylene (C_2H_4). During the course of the studies, it was discovered that the material is the

kinetic product of the crystallisation and is not a stable porous material due to its spontaneous conversion to an unknown phase over time.

In the final section, the entrapment of CO_2 within the interstitial voids of calix[4]arene was studied. The first experimental evidence of an inclusion complex for this well-known organic host with CO_2 is presented here. Calix[4]arene was crystallised from supercritical CO_2 and an SCD structure of the inclusion complex was determined. The SCD structure was inconclusive about the true position of the CO_2 molecule within the void. A computational study of the various possible positions of the molecule was carried out with the conclusion that only one CO_2 molecule can occupy the interstitial void and that the CO_2 molecule is disordered over four positions. The occupancy for each of the positions was derived from the Boltzmann distribution calculated from host-guest interaction energies.

OPSOMMING

'n Aantal poreuse metaal-organiese en organiese kristallyne materiale is berei met die doel om die vaste-toestand dinamika wat betrokke is in sorpsie en gas-uitruil (E. *guest-exchange*) prosesse te ondersoek. Die hoofdoel is om 'n begrip van die meganismes wat betrokke is in die strukturele veranderinge veroorsaak deur eksterne stimuli, te verkry. Dus is enkel-kristal X-straal-diffraksie eksperimente uitgevoer onder verskeie temperatuur- en drukkondisies. Die X-straal diffraksie eksperimente is aangevul deur termo-analise (E. *thermal analysis*) en sorpsie eksperimente.

Die eerste afdeling bevat 'n studie van die sintese van metaal-organiese raamwerke deur die kombinasie van starre en onsimmetriese ligande met oorgangmetaalsoute. Slegs drie van die twaalf nuwe metaal-organiese raamwerke kon enkel-kristal na enkel-kristal omsettings ondergaan. Die tweedimensionele (2D) metaal-organiese raamwerke (**IMOFF-1** en **IMMOF-2**) gevorm met 4-(1*H*-benso[*d*]imidazool-1-yl)bensoësuur (**L6**) verander drasties hul strukture tydens gas-uitruil prosesse weens wedersydse verplasing van die 2D lae. Hierdie metaal-organiese raamwerke kan geklassifiseer word as derde-generasie sagte poreuse materiale. Spesifiek die metaal-organiese raamwerk wat bestaan uit **L6** en $Zn(NO_3)_2$ bevat vervormbare leemte ruimtes en verander na 'n laer digtheid fase met dubbel die CO_2 kapasiteit ter blootstelling aan hoë CO_2 druk. Metaal-organiese raamwerke met “hek-oopmaak” (E. *gate-opening*) sorpsie gedrag is skaars en hierdie studie is tot 'n mate uniek aangesien dit hoë druk differensiële kalorimetrie (E. *differential scanning calorimetry*) met X-straal diffraksie onder gas druk

kombineer. Die metaal-organiese raamwerk berg die CO_2 in afsonderlike holtes in die struktuur waar dit deur talle gasheer-gas (E. *host-guest*) interaksies gestabiliseer word. Gevolglik is daar uiterse histerese gedurende die desorpsie van CO_2.

Die tweede afdeling omskryf die sorpsie en gas-uitruil eienskappe van 'n driedimensionele en permanent poreuse metaal-organiese raamwerk (**IMMOF-3**). Die enkelkristalle van **IMMOF-3**, wat 4-(1*H*-nafta[2,3-*d*]imidasool-1-yl)bensoësuur (**L7**) bevat, is baie sterk en chemies stabiel, weens die gunstige intra-raamwerk interaksies tussen die ligande. Gas- en dampsorpsie eksperimente getuig van die raamwerk se veelsydigheid aangesien dit 'n wye verskeidenheid gas molekules in die eendimensionele kanale kan opneem. Verder vertoon die metaal-organiese raamwerk anisotrope termiese uitsetting, met koëffisiënte van termiese uitsetting wat sistematies verander kan word, deur 'n reeks verwante gas (E. *guest*) molekules in die kanale te inkorporeer.

In die derde afdeling, word die “tydelike porositeit” (E. *transient porosity*) van 'n metallosiklieseverbinding (**MC1**) met afsonderlike porieë verken. Klein molekules kan deur die kristal vervoer word ten spyte van die afwesigheid van kanale in die struktuur, soos gedemonstreer deur die sorpsie van CO_2, stikstof (N_2) en etileen (C_2H_4). Tydens die studie is gevind dat die materiaal die kinetiese produk van die kristallisasie is en dus nie 'n stabiele poreuse materiaal is nie. Die material ondergaan 'n spontane omsetting na 'n onbekende fase met die verloop van tyd.

Die laaste afdeling beskryf 'n studie wat handel oor die omsluiting van CO_2 in die interstisiële ruimtes van kaliks[4]areen (E. *calix[4]arene*). Die eerste eksperimentele bewyse vir 'n kompleks van hierdie bekende organiese gasheer met CO_2, word hier beskryf. Op grond van die X-straal diffraksie struktuur, is daar steeds onsekerheid oor die presiese posisie van die CO_2 molekule binne die interstisiële ruimte. Verskeie berekeninge van die verskillende moontlike posisies van die molekule binne die leemte is uitgevoer met die gevolgtrekking dat slegs een CO_2 molekule die interstisiële leemte kan beset en dat wanorde van die CO_2 molekule oor vier verskillende posisies voorkom. Die persentasie besetting van elk van die posisies is afgelei uit die Boltzmann verspreiding wat bereken word vanaf die gasheer-gas interaksie energieë.

ACKNOWLEDGEMENTS

I would like to acknowledge the following people for their contribution to the research presented in this dissertation and my learning experience as a postgraduate student as a whole:

Firstly, I would like to thank my supervisor, Len Barbour, for creating an exceptional research environment. All of us in the research group are very fortunate to have a wide range of equipment and instrumentation of great quality and worth available to us, as well as a lot of expertise on the subjects of crystallography, porosity and supramolecular chemistry. Thank you for the opportunities that you created for attending international and national conferences and especially for the opportunity to visit the European Synchrotron Radiation Facility in France. Thank you for the tedious editing of documents and for your guidance and support. You taught me that the only limitation/obstacle towards achieving your research goals is your imagination.

I would also like to express my gratitude to my co-supervisor, Catharine Esterhuysen, for the support and guidance. Thank you for your contribution to the computational work, providing great research ideas and for the opportunities to attend symposia and workshops. Thank you for your approachable and caring nature and the help in planning and editing my dissertation.

I would like to thank all the people who have been a part of the Supramolecular Materials Research Group in the last four years: Himanshu Aggarwal, Eustina Batisai, Charl Bezuidenhout, Prashant Bhatt, Raj Das, Dawie de Villiers, Marike du Plessis, Emile Engel, Jan Gertenbach, Guillaume Greyling, Simon Herbert, Anneli Heyns, Tia Jacobs, Agnieszka Janiak, Prem Lama, Leigh Loots, Matteo Lusi, Subhadip Neogi, Varia Nikolayenko, Storm Potts, Sean Robinson, Phumile Sikiti, Vincent Smith, Dewald van Heerden, Laura Jane van Laeren and Helene Wahl. It has been a great experience to share an office and lab with you. A special thanks to Charl for the help with the computational work, Simon for the help with the synthesis, Tia for the sorption experiments on the IGA, Himanshu for the pressure DSC measurements, Vincent for the general guidance and Marike for helping me submit all of the examination documents. I would also like to thank the Wilhelm Frank bursary scheme for financial support. Finally, I am very grateful for the support of my parents, Johan and Margot Grobler, who provided me with the opportunity to attend Stellenbosch University.

PUBLICATION

1. I. Grobler, V. J. Smith, P. M. Bhatt, S. A. Herbert, L. J. Barbour, Tunable Anisotropic Thermal Expansion of a Porous Zinc(II) Metal–Organic Framework, *J. Am. Chem. Soc.* **2013**, *135*, 6411-6414.

CONFERENCES

1. The European Powder Diffraction Conference (EPDIC), Grenoble, France, 28-31 October **2012**. Poster contribution: *The Anisotropic Thermal Expansion of a Porous Zinc(II) Metal-Organic Framework.*
2. South African PhD Project Conference, CTICC, Cape Town, 27 September **2012**.
3. Indaba 7: Insights from Structure, presented by the South African Crystallographic Society, Skukuza, Kruger National Park, South Africa, 2-7 September **2012**, Poster contribution: *The Anisotropic Thermal Expansion of a Porous Zinc(II) Metal-Organic Framework.*
4. XXII Congress and General Assembly of the International Union of Crystallography , Madrid, Spain, 22-30 August **2011**, Poster contribution: *Single-crystal to single-crystal guest exchange in a dynamic porous crystal*.
5. Centre for High Performance Computing (CHPC) National meeting 7-9 December **2010**.

LIST OF ABBREVIATIONS

1D, 2D, 3D	one-, two- or three-dimensional
ADP	atomic displacement parameter
ASU	asymmetric unit
CIF	crystallographic information file
CSD	Cambridge structural database
DSC	differential scanning calorimetry
DCM	dichloromethane
H:G	host to guest ratio
HPDSC	high-pressure differential scanning calorimetry
IR	infrared spectroscopy
MOF	metal-organic framework
NMR	nuclear magnetic resonance
NTE	negative thermal expansion
PTE	positive thermal expansion
PXRD	powder X-ray diffraction
SBU	structural building unit
SCD	single crystal X-ray diffraction
sCO_2	supercritical carbon dioxide
SHG	second harmonic generation
SOF	site occupancy factor
STP	standard temperature and pressure
TGA	thermogravimetric analysis
ZTE	zero thermal expansion

ATOMIC COLOUR KEY

Hydrogen

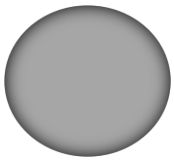

Carbon

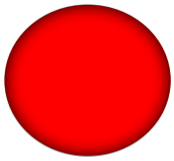

Oxygen

Nitrogen

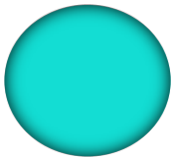

Metal

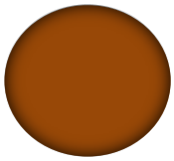

Iodine

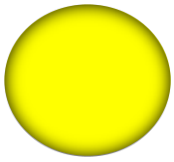

Bromine, Chlorine

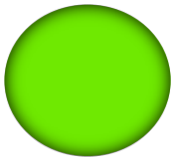

Fluorine

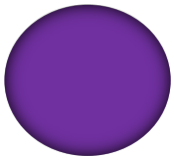

Sulphur

TABLE OF CONTENTS

CHAPTER 1

AN INTRODUCTION TO SUPRAMOLECULAR CHEMISTRY

Supramolecular chemistry is the investigation of how individual molecules interact and assemble. If the assembly of the molecules is periodic in all three dimensions, the material is crystalline and can be studied by single-crystal X-ray diffraction (SCD) methods. The knowledge gained from a molecular level three-dimensional "photograph" of a solid material by SCD methods allows us to relate the structure of the material to its properties. Some of the main concepts that are relevant to supramolecular chemistry are presented here.

1.1 SUPRAMOLECULAR CHEMISTRY AND MATERIALS SCIENCE

Supramolecular chemistry has been defined as "*The study of systems involving aggregates of molecules or ions held together by non-covalent interactions, such as electrostatic interactions, hydrogen bonding, dispersion interactions and solvophobic effects*."[1] In other words, it involves the investigation of the chemical and physical properties of materials assembled by non-covalent interactions between the constituent molecules. Supramolecular chemistry[1] was first defined by Jean-Marie Lehn as *"…the chemistry of molecular assemblies and of the intermolecular bond*"[2] and was later referred to as "*the chemistry beyond the molecule*". In this context, a supermolecule is a higher order entity consisting of molecules assembled by attractive intermolecular interactions.

The molecular assembly of a solid-state material has specific properties that are related to the types of molecules (or atoms) that it is comprised of, as well as the manner in which these molecules pack. The three-dimensional arrangement of the molecules or atoms in space, more conveniently referred to as the crystal structure, can be elucidated using SCD methods. SCD data provide an extremely accurate three-dimensional model of the positions of atoms in space based on an electron density map derived from X-ray diffraction patterns. The structure aids in the understanding of the properties of the material. Moreover, understanding structure-property relationships is central to defining Supramolecular Chemistry as a materials science. Materials science involves the synthesis and study of materials with desired properties such as porosity, anomalous thermal expansion, non-linear optical and mechanical properties. Porous materials

have potential applications in gas storage and separation. Materials with anomalous thermal expansion can be used as actuators or sensors. Polar materials with non-linear optical properties such as second harmonic generation (SHG) capabilities have applications in various electronic devices as well as in laser technology.

1.2 CRYSTAL ENGINEERING

Crystal engineering is "*the bottom-up construction of functional materials, starting from molecular or ionic building blocks assembled by means of noncovalent interactions*".[3] Desiraju defined crystal engineering as "…*the understanding of intermolecular interactions in the context of crystal packing and the utilisation of such understanding in the design of new solids with desired physical and chemical properties*."[4] The word "engineering" refers to the use of specific strategies and design principles when combining different molecules together to form a supermolecule. In principal, the crystal engineer makes use of the different synthons or structure directing interactions in order to synthesise a "predesigned" crystal lattice.[5] Supramolecular synthons are "*recurring motifs between functional groups that can be applied towards the design of novel systems*". The recognition of synthons in a structure is achieved by reducing the structure to its simplest components in a manner similar to which organic chemists use retrosynthetic analysis to find a method to make a more complex molecule.

The concept of crystal engineering was first defined approximately 30 years ago by Schmidt[6] and the crystal engineering community is still in the process of gathering enough structural information for identifying and understanding trends and relationships. These trends can be used to predict and explain the probability of the formation of a specific type of molecular assembly and to predict its properties. The Cambridge Structural Database[7] (CSD) is an excellent and vital tool for the extraction of structural information that can be used for crystal engineering because of the wealth of structural data that it contains.

Intermolecular interactions

The crystal engineering research area has grown immensely in terms of understanding the energetic nature and geometrical properties of intermolecular interactions. Intermolecular interactions are non-covalent "bonds" that range from 2 kJ mol^{-1} for dispersion interactions to 300 kJ mol^{-1} for ion-ion interactions.[3]

The two main types of interactions that direct structure formation in organic materials are, firstly, the medium-range isotropic forces that include C···H, C···C and H···H interactions and, secondly, the long-range electrostatic forces between heteroatoms such as oxygen, nitrogen, sulphur and halogen atoms such as chlorine, bromine, iodine and fluorine. Electrostatic interactions between heteroatoms and carbon and hydrogen are also categorised as long-range interactions.[3] More specifically, the long-range electrostatic interactions are considered important synthons in the design of supramolecular architectures, such as the hydrogen bond (including CH-π hydrogen bonds) and halogen bonds. The hydrogen bond is a dipole-dipole interaction between a proton donor and a proton acceptor (Figure 1).

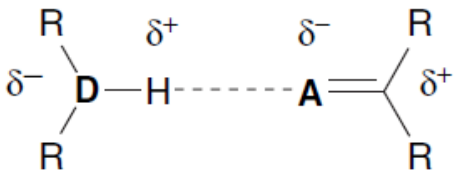

Figure 1. The hydrogen bond as a dipole-dipole interaction.[8]

Hydrogen bonds are directional and vary in strength between 4-120 kJ mol^{-1}.[3] Halogen bonds are attractive donor-acceptor interactions that involve halogen atoms functioning as Lewis acids by accepting an electron lone-pair.[3] These interactions have energies that range between 10 and 200 kJ mol^{-1} and are, like hydrogen bonds, highly directional based on the orientation of the lone pair orbital-axis.[3]

The weaker non-directional interactions such as π-π stacking that are based on isotropic C···C and C···H interactions form more flexible or transformable molecular assemblies. There are two main types of π-π interactions: face-to-face interactions, Figure 2a and edge-to-face interactions, Figure 2b. Face-to-face interactions are offset interactions between the centre and corner of two parallel ring-systems separated by approximately 3.5 Å.[3] An edge-to-face π-π interaction occurs when the hydrogen atom from one ring points towards the centre of the other ring. These interactions arise from the attraction between the negatively charged π-electron cloud of one conjugated system and the positively charged σ-framework of a neighbouring molecule.[3]

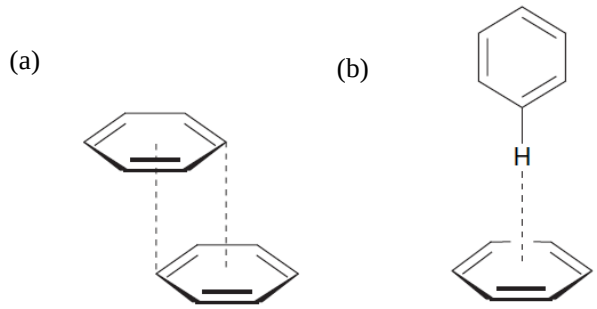

Figure 2. (a) Face-to-face and (b) edge-to-face π-π interactions.

In hybrid materials that consist of inorganic and organic components, the coordination bond is the most dominant and directional synthon. A coordination bond is an ion-dipole interaction that is formed between an acceptor metal cation and a ligand moiety that donates lone pair electrons. Coordination bonds with a bond enthalpy of between 80-200 kJ mol^{-1} are very directional and are stronger than electrostatic interactions such as hydrogen bonds (4-120 kJ mol^{-1}). Hybrid materials such as metal-organic frameworks (MOFs) are assembled by association of metal cations with organic ligands via coordination bonds. The transition metals are predisposed to take on a specific coordination geometry based on the electronic configuration and geometric arrangement of the d-orbitals. Consequently, the choice of metal cation is a vital part of crystal engineering desired molecular architectures in MOF materials. An important benefit of the coordination bond in terms of single-crystal transformations is that they are more chemically labile or maleable than covalent bonds. In many MOF materials the angular deformations or rotations around the metal centre provide flexibility for dynamic transformations in the solid state.

Crystal engineering with a given set of structural units (molecules) leads to a vast array of possible supramolecular assemblies that can collectively be defined as the "structural landscape".[8] The structural landscape comprises all the supramolecular isomers, solvates, co-crystals and other chemical variations that a chemical species may crystallise as. One structure can be considered as one data point within the structural landscape and the extended structural landscape provides insight into the crystallisation mechanism. This is especially relevant with regard to the self-assembly of MOFs. The prevailing conditions of different crystallisation techniques may lead to structures from different local minima in the structural landscape. It is therefore pertinent to mention that the novel MOFs to be discussed as part of this work represent a small fraction of the structural landscape of the components.

1.3 INCLUSION COMPOUNDS

Inclusion compounds are comprised of a host assembly or lattice that includes a guest molecule within discrete cavities (cavitands) or channels (clathrates). It can be said that Nature inspired the synthesis of inclusion compounds upon the discovery of host-guest systems such as enzyme-substrate complexes. Emil Fischer's lock-and-key model[9] (1894) for molecular recognition of a substrate in an enzyme's active site was an important conceptual development in biochemistry that inspired the synthesis of macromolecules for molecular recognition in the laboratory. The complementarity between the size and shape of the guest (substrate) and its binding site (active site) is a key concept in host-guest chemistry. Research in the area of host-guest chemistry intensified after the discovery of clathrates such as hydroquinone inclusion complexes, $Ni(CN)_2 \cdot NH_3 \cdot C_6H_6$ or Hofmann's benzene compound, Dianin's compound and clathrate hydrates (i.e. of SO_2, Br_2, CH_4) in the 1800s.[10] The most widely accepted definition of a host-guest complex was published by Cram *et al.* (1977):[11] *"The host component is defined as an organic molecule or ion whose binding sites converge in the complex. The guest component is defined as any molecule or ion whose binding sites diverge in the complex.*"

Host-guest inclusion can be described by the following equation:[12]

$$H_{(s)} + nG_{(s,l \text{ or } g)} \rightarrow H \cdot G_{n\,(s)}$$

where *n is* the stoichiometric guest:host ratio.

In terms of the application of inclusion complexes for the crystal engineering of porosity, the aim is to produce robust frameworks or scaffolds from which the guest can be expelled without rearrangement of the host lattice to form a close-packed phase. Another objective is to synthesise host frameworks that can accommodate a range of guest molecules or host frameworks that are selective for a specific size, shape or electrostatic topology of the guest. Guest selectivity can have wide-ranging applications in molecular separation, target-specific drug delivery or even slow-release of the guest molecules.

1.4 HOST-GUEST INTERACTIONS IN INCLUSION COMPOUNDS

Relatively weak non-covalent interactions such as the previously mentioned long-range electrostatic interactions, as well as dispersive van der Waals interactions, bind host and guest components together. SCD methods provide valuable structural information with regard to the host-guest interaction distances in inclusion compounds. The guest may have originally been a

solvent (liquid), a volatile solid or a gas. In the case of the guest being a gas, the determination of the atomic coordinates of the gas in the host framework may aid in the identification of interaction sites and provide valuable insight into the gas sorption process.

The role of host-guest interactions in gas sorption processes

With regard to gas sorption by MOF materials, most research has been devoted to creating frameworks with pores of ever-increasing size or internal surface areas in order to increase the material's capacity for gas storage.[13] Moreover, the literature in this area describes MOF sorption capacity by BET/Langmuir surface[14] areas measured with unreactive nitrogen gas as the standard sorbent. It is arguable whether the surface area alone can be considered indicative of the sorption capacity of a microporous material, since the material's affinity for a particular guest is not taken into account. Understanding the role of host-guest interactions during guest uptake processes is of considerable value for the engineering of porous materials. Such knowledge, would allow for the incorporation of specific sites for host-guest interactions by design with a view to increasing the affinity and selectivity for a guest rather than merely increasing void space.

There seems to be a general feeling that MOFs have in fact failed as sorbents at ambient conditions for use as storage materials of alternative fuels (hydrogen and methane), or for their application in post-combustion absorption of greenhouse gases (carbon dioxide). Holst *et al.* have expressly voiced this sentiment by saying, *"Many MOF networks and sorbents described, adsorb practically useful quantities of CO_2 at saturation under elevated pressures or at lowered temperatures. However, these materials are quite far from saturation under practically relevant conditions for post-combustion gas capture. In essence, there is plenty of surface but the affinity of the sorbent for the gas is too low. Molecular engineering of sorbate-sorbent interactions may therefore be a key to future success."*[15] The US Department of Energy, in collaboration with the automotive industry, has set the 2010 gravimetric capacity target at 6 wt% for H_2 storage, which has been exceeded (7.2 wt%[16]) but only at very low temperatures (77 K) or very high pressures.[17] Consequently the target was reduced and the most recent 2015 target has recently been quoted as 5.5 wt%.[17b] The target for methane is 35 wt% (180 v/v) under 35 bar, which has been achieved by activated charcoal. However, this is not a commercially feasible option owing to refuelling issues.[18] The abovementioned target for the storage of methane has not yet been met by MOF materials and requires further investigation. Instead, compressed natural gas is currently being used. This can be seen as a challenge, and the engineering of favourable host-guest interactions as a possible solution.

In addition, it is important to recognise and understand the role that host-guest interactions play in adding functionality such as selective uptake and storage for separation purposes. In contrast, a different type of functionality based on versatility of the host can also be achieved in the case of guest-responsive adaptation of the host framework to different guest molecules. Guest exchange experiments, during which the original guest is exchanged for another during a single-crystal to single-crystal transformation, provide structural information about the types of host-guest interactions that contribute to host-guest stabilisation. Even the structural adjustments and deformation of the host framework imposed by the inclusion of guest molecules provide additional information about the extent of the stabilisation offered by host-guest interactions.

1.5 SINGLE-CRYSTAL TO SINGLE-CRYSTAL TRANSFORMATIONS

Structural rearrangement can occur in the solid state in response to a variety of physical or chemical factors.[19] If the changes are small enough or the response concerted enough, a limited amount of mechanical stress is induced in the single crystal. Consequently, the crystal might retain its mosaicity with this process being termed a single-crystal to single-crystal transformation. These transformations are still relatively rare because the rigidity of the host lattice or framework is seldom sufficient to prevent disintegration of the single crystal during or after the transformation.

In the case of host-guest complexes, the removal of the guest molecules may result in the reassembly of the host into a more stable, efficiently packed phase that maximises close contacts between the host molecules, and is thus non-porous. If the host framework is invariant (except for small atomic displacements or adjustments) upon guest-loss, empty space or voids in the form of discrete pockets or channels may result. Guest-exchange transformations are processes where the original guest molecule is exchanged for another molecule following the immersion of a crystal in a different solvent or exposure to gas pressure. The transformation may involve slight geometrical changes to the framework while crystal intergrity is preserved. The direct study of these single-crystal to single-crystal transformations by SCD analyses provides an opportunity to study solid-state dynamics.[10c] These studies have changed the view that crystals are static and rigid structures with little interesting chemistry. The flexibility that some host compounds exhibit whilst retaining crystal mosaicity is evidence of the phenomenon of molecular cooperativity in the solid state.[19]

Specifically, MOFs have rigidity that arises from the incorporation of metal centres and strong coordination bonds into an infinite coordination network. These materials have been studied extensively with regard to their permanently porous nature and ability to undergo guest-exchange processes.[20]

1.6 CRYSTAL POROSITY

Porosity is not a common occurrence in Nature. Materials are stabilised by the attractive forces between molecules and thus tend to close-pack in the solid state. It is unusual for crystals to have open channels or discrete lattice voids larger than ~25 $Å^3$.[21] Instead, certain crystal engineering strategies need to be employed to produce porous systems. The crystallisation of irregularly-shaped molecules, such as calix[n]arenes,[22] or doughnut-shaped metallocycles[23] prevents close-packing and creates inherent porosity. Another strategy is the synthesis of infinite 3D metal-organic framework materials (MOFs) or coordination polymers that include solvent molecules in the framework apertures such that removal of the solvent yields porosity.

There is a need for the development of nanoscale porosity owing to its many industrial applications:[24] storage of sufficient amounts of methane and hydrogen gas, the separation of gaseous industrial by-products and post-combustion gas uptake. In terms of porosity aimed at solvent inclusion, the separation and purification of liquids as well as small-molecule storage, slow release and delivery (drug-delivery) are potential uses.

Porosity can be defined by the following two key features:

(i) that permeability is proven, and

(ii) that the host lattice must be largely unaffected by the passage of guest molecules (i.e. it may not become amorphous during the process or simply be an unknown phase or ensemble of the structural units of the host framework).[25]

Conventional porous crystalline materials have infinite channels with a minimum diameter of 3 Å in the host framework.[25] In a few cases porosity may be demonstrated without the presence of channels. The permeability of *p-tert*-butylcalix[4]arene to vinyl chloride, even though the host lattice only has discrete voids, is an example of this phenomenon that was termed porosity "without pores" or transient porosity.[25-26]

Another type of porosity, called "virtual porosity",[25] is fabricated porosity in which permeability has not been proven and small molecules such as solvent molecules or counterions are deleted from the structure such that the packing diagram then shows open channels or voids.

1.7 GAS SORPTION

For the aims of this dissertation, the term "gas sorption" refers to the association of gas molecules with the surfaces (internal or external) of a solid material by intermolecular interactions. The term "sorption" is used to describe the combined effects of adsorption and absorption. Adsorption (exothermic only) occurs when molecules adhere to the surface of another phase. Adsorption is also referred to as physisorption in the case of weak intermolecular interactions occurring between the adsorbent and adsorptive, or chemisorption when bond formation occurs.[27] Absorption is defined as the incorporation of a substance of one state into a material of a different state.[28] One can distinguish between the two types of sorption experimentally since adsorption is exothermic only, whilst absorption can be either endo- or exothermic. The sorbed substance (sorptive/guest) is removed from the sorbent by a process termed desorption. When desorption does not occur as readily as sorption, the material is said to display hysteresis.[29] Hysteresis indicates that there is an affinity of the sorbent (host) for the sorptive (guest).

There are three factors that influence the sorption properties of a material:

(i) size/shape exclusion,

(ii) thermodynamic effects such as host-guest interactions, and

(iii) kinetic effects such as the rate of diffusion, which may be dependent on the kinetic diameter and/or energy of the gas molecules.

In order to study the sorption properties of a porous material, sorption isotherms are measured. A sorption isotherm is the relationship between the amount of guest sorbed and the equilibrium pressure of the gas or vapour at a constant temperature. One can measure the sorption isotherm of a material using commercial sorption instruments that can measure the amount of gas sorbed in one of two ways. The first type of instrument measures the increase in weight upon gas exposure (gravimetric analyser). The second type of instrument determines the amount of gas sorbed by measuring changes in pressure in a fixed volume (volumetric analyser). According to the International Union of Pure and Applied Chemistry (IUPAC), the experimental

sorption isotherms can be classified into one of six different categories based on the shape and other characteristics of the isotherms (Figure 3). The IUPAC classification, published in 1985, is based on an extensive literature survey performed by Brunauer, Demming, Demming and Teller (BDDT).[30]

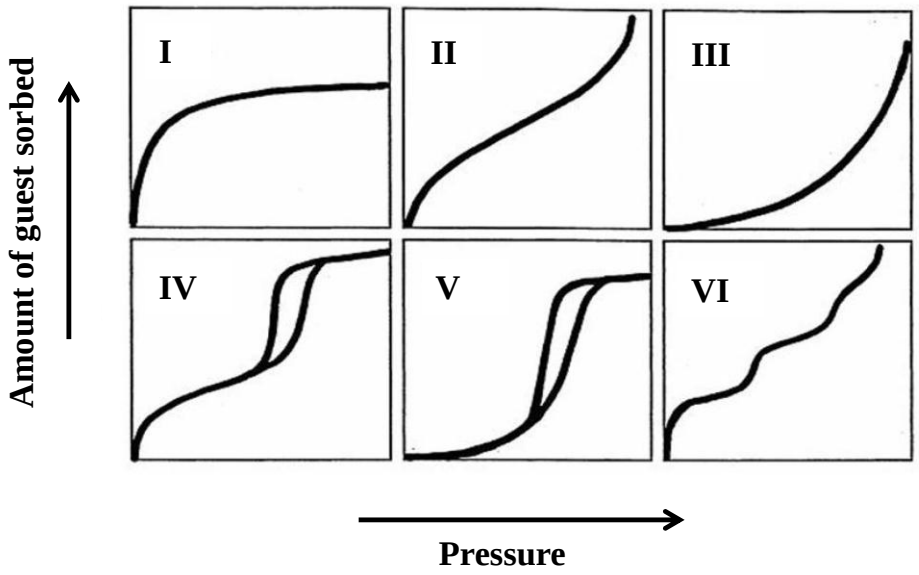

Figure 3. The different types of sorption isotherms based on the IUPAC classification.[29,31]

The six isotherms and the conditions of physisorption that lead to their occurrence are discussed further here. It must be noted that these classifications were derived from sorption data measured with porous zeolites and are not always applicable to all the materials discussed in this dissertation. Type I isotherms have a concave shape, are reversible, and plateau as saturation is reached. Saturation is limited by the amount of accessible pore space that is available. Most sorption occurs at low relative pressures. This is indicative of a small pore surface area since there is high affinity for the guest owing to the small micropore dimensions that afford many host-guest interactions.

Type II isotherms are reversible and are obtained for non-porous or macroporous materials, where unrestricted sorption occurs. The inflection in the curve specifies the point at which multilayer sorption starts.[30] The convex shape of a Type III isotherm results from very weak interactions between the sorbate and sorbent. Type IV isotherms are similar to the type II isotherm that typically occur for mesoporous materials with monolayer-multilayer sorption.[30] Mesoporosity (intermediate pore size) is evident from the plateau that signifies a limited amount of uptake. However, the non-reversible sorption or hysteresis loop shows that pore condensation occurs. Type V isotherms are rare. These isotherms are related to the initial curvature of a type

III (due to weak host-guest interactions) but with hysteresis that occur due to pore condensation. Finally, type VI isotherms show stepwise sorption that represents multilayer sorption on a uniform, non-porous surface.

Type I isotherms are obtained for most conventional permanently porous materials with micropores, whilst seemingly non-porous materials (transient porosity) or soft porous materials may have unique sorption isotherms or isotherms that are a combination of the abovementioned IUPAC classifications.

1.8 AIMS AND OBJECTIVES

The aim of the research conducted as part of this dissertation is to study the properties of different classes of porous materials, i.e. conventionally porous materials (with channels) and transiently porous materials (with discrete voids). The properties of the different types of materials, i.e. metal-organic frameworks, a metallocycle and an organic compound, were explored by applying the same analytical techniques and carrying out the same measurements on each of the different materials. The solid-state dynamics of the different types of host-guest materials were studied during desolvation, guest-exchange processes, temperature changes and exposure to gas pressures. The structural changes that are induced by these various chemical and physical stimuli were elucidated using single-crystal X-ray diffraction.

The main objectives are:

(i) To synthesise robust porous systems that maintain their single-crystal quality after the solvent is removed from the pores. Ideally, the material should be able to undergo single-crystal to single-crystal transformations with noticeable structural adjustments and changes in response to different guests. SCD methods will be used to study and characterise the flexible and dynamic nature of the material. This would require the acquisition of SCD data under different conditions;

(ii) To study the inclusion of guests into materials, i.e. their exchange for other guests and the process of diffusion of gases and liquids into the pores in order to gain an understanding of the role of host-guest interactions in exchange and sorption processes;

(iii) To study the effects of external stimuli such as temperature or very high gas pressures on a material (i.e. the structural response to temperature/gas pressure will be studied).

1.9 OUTLINE OF DISSERTATION

The primary aim of the dissertation is to apply a common set of experimental techniques towards elucidating the extent and type of porosity in a range of different materials. Chapter 2 contains descriptions of the experimental techniques that were applied to each of the different types of materials. Chapter 3 and chapter 4 describe the studies of the structure-property relationship of metal-organic framework (MOF) materials. In order to produce porous MOF materials, a set of organic ligands was originally synthesised by Dr. Subhadip Neogi, a post-doctoral fellow at Stellenbosch University. Previous studies were aimed at combining these ligands with metal salts to create MOFs from which the guest molecules can be removed to afford robust and porous scaffolds capable of absorbing gases. As the project evolved, an additional two ligands were synthesised with the aim of improving the rigidity of the frameworks such that single-crystal to single-crystal transformations can also be studied. During the course of the studies, it was found that, depending on the dimensionality of the framework, i.e. whether it is two- or three-dimensional, different classes of porosity and different types of sorption properties can be obtained. Two-dimensional (2D) MOFs (described in chapter 3) tend to be flexible or soft porous with unique sorption properties such as gate-opening gas sorption, whilst three-dimensional (3D) MOFs (described in chapter 4) tend to be permanently porous with guest-accessible channels that show type I sorption isotherms. A further goal, outlined in chapter 4, is to show that even conventionally porous MOF materials may reversibly respond to the presence of a guest or a physical factor such as temperature.

Chapter 5 explores the transient porosity of a metallocyclic material. The pores are isolated but, interestingly, guest transport through the crystal can still occur, despite the absence of channels in the host packing arrangement. The material shows type I sorption with CO_2, C_2H_4 and N_2 with a considerable amount of hysteresis. It was found that the porous structure is not the thermodynamic product of the self-assembly process and is, therefore, not stable. It converts to a different phase upon exposure to certain stimuli or as a function of time. Chapter 6 outlines the fact that even non-porous materials can be used to encapsulate volatile guests if they are soluble in the guest substance. The capture of a gas in a non-porous material, i.e. calix[4]arene, was studied. In this case permeability to carbon dioxide could not be proven, however the recrystallisation of calix[4]arene from supercritical CO_2 resulted in CO_2 capture. Chapter 6 summarises the outcomes of the work and some suggestions for possible future work are discussed.

CHAPTER 2

EXPERIMENTAL TECHNIQUES

2.1 SINGLE-CRYSTAL X-RAY DIFFRACTION (SCD)

Intensity data were collected on two different instruments:

i) A Bruker SMART Apex-2 CCD diffractometer with monochromated Mo-K_α radiation (λ= 0.71073 Å);

ii) A Bruker Apex-2 DUO CCD diffractometer with a multilayer monochromator. Mo-K_α radiation (λ= 0.71073 Å) was selected for the experiments.

Both instruments are equipped with an Oxford Cryosystems 700+ cryostat. Data reduction was carried out by means of standard procedures using the Bruker software package SAINT and correction of absorption and other systematic errors was performed using SADABS.[32] The structures were solved by direct methods using SHELXS-97 and refined using SHELXL-97.[33] X-Seed[34] was used as the graphical interface for the SHELX program suite. Hydrogen atoms were placed in calculated positions using riding models and assigned isotropic thermal parameters 1.2 or 1.5 times the U_{eq} of their parent atoms.

2.2 POWDER X-RAY DIFFRACTION (PXRD)

All samples were first ground into a powder (with a mortar and pestle) and diffraction patterns were measured on a PANalytical X'Pert PRO instrument with Bragg-Brentano geometry, using Cu-Kα radiation (λ = 1.5418 Å). Intensity data were recorded using an X'Celerator detector and 2Θ scans in the range of 5-40° were carried out.

Two different sample stage configurations of the instrument were used:

i) The reflection-transmission spinner PW3064/60 sample stage configuration; the sample was spun at 15 rotations per minute to minimise preferred orientation contributions to intensity data. A step size of 0.02° and a scan-speed of 2 seconds per step were used during data collection;

ii) The sample was sealed within a glass capillary (inside diameter of 0.3 or 0.5 mm) and the capillary spinner configuration (with the focusing mirror) of the instrument was

used to record powder patterns at variable temperatures. The capillary spinner configuration allows for more accurate temperature control using a short-nozzle Oxford Cryostream 700+ cryostat. An environmental gas cell can also be mounted onto the capillary spinner such that PXRD patterns can be measured whilst the sample is under gas pressure.

2.3 THERMOGRAVIMETRIC ANALYSIS (TGA)

A TGA trace was generated by measuring the percentage mass as the sample was heated at a constant rate. A TA Instruments Q500 thermogravimetric analyser was used and sample sizes typically ranged from 2-15 mg. N_2 gas flowing at a rate of 50 ml min^{-1} was used to purge the furnace. The temperature was ramped from room temperature to ~600 °C at a constant heating rate of 10 °C min^{-1}. The resulting thermograms were analysed using the TA Instruments Universal Analysis program.

2.4 DIFFERENTIAL SCANNING CALORIMETRY (DSC)

Differential Scanning Calorimetry is based on measuring the heat flow into or out of a sample, relative to a reference (empty pan), as a function of time or temperature in a controlled atmosphere.[35] A difference in temperature between the sample and the reference pan signifies that a thermal event (endo- or exothermic) has occurred. Thermal events are associated with physical or chemical changes in the material. DSC measurements were carried out using a TA Instruments Q100 differential scanning calorimeter with sample sizes of typically 3-10 mg. Samples were enclosed in a pan and lid that has been crimped together and two pin holes were made in the lid. Both the reference and the sample pans were prepared using the same method. N_2 gas, flowing at a rate of 50 ml min^{-1} was used to purge the furnace. A heating rate of 2 °C min^{-1} was used. Decomposition of the sample in the pan should be avoided and therefore the maximum temperature is dependent on the sample. The resulting thermograms were analysed using the TA Instruments Universal Analysis program.

2.5 GAS CELL FOR THE COLLECTION OF SINGLE-CRYSTAL DATA UNDER CONTROLLED ATMOSPHERES

Single crystal X-ray diffraction (SCD) data with the crystal under gas pressure were collected using a miniature pressure cell developed in-house (Figure 4).

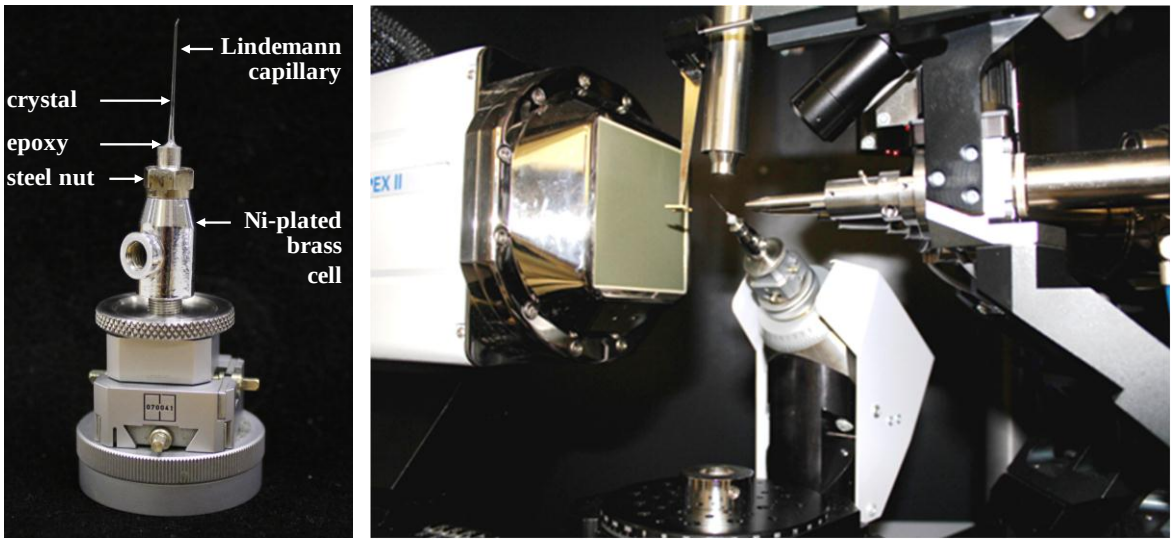

Figure 4. The in-house built gas cell for measuring SCD data with a crystal under controlled atmospheres.

The miniature gas cell consists of:

i) A stainless steel fitting to which a glass capillary containing the crystal is attached with epoxy resin;

ii) A nickel-coated brass cell with a port for the steel fitting, a valve stem and a gas inlet port on the side;

iii) A detachable gas inlet arm, which can be attached to the brass cell during gas loading.

Preparation of a gas cell proceeded as follows. A crystal was selected and glued to the end of a glass microfiber, which was then inserted and glued into a 0.3 mm glass capillary flame-sealed at the narrow end. The open end of the capillary was attached to the steel fitting with epoxy resin, which was left to cure for one hour. The steel fitting was screwed onto the gas cell, and an embedded rubber O-ring ensures a gas-tight seal. During gas loading the detachable gas inlet arm was attached to the gas cell, as well as a gas cylinder fitted with a regulator adjusted to the required pressure. The valve stem opens/closes the gas cell during/after gas loading. The detachable inlet arm can also be attached to a vacuum pump in order to evacuate the gas cell prior to gas loading. After removal of the inlet arm, the pressurised cell can be mounted on the X-ray diffractometer using a standard goniometer head (Figure 4).

2.6 ELECTRON DENSITY STUDIES (SQUEEZE)

Platon/SQUEEZE[36,37] uses the SHELXL .RES file and hkl data obtained from SCD structure analysis to calculate the void volume (geometrically) and the number of electrons within each void. The electron count is determined by summing the residual electron density within the void space. The software was used in an unconventional manner to estimate the number of guest molecules that occupy the voids of SCD structures.

The SQUEEZE manual states that the procedure takes into account the contribution of a disordered solvent to the calculated structure factors by back-Fourier transformation of the continuous density found in a masked region of the difference map. The masked region is defined as the solvent-accessible region left by the ordered part of the structure.[10c] The calculation relies on the quality of the low-order reflections. If the dataset is incomplete or contains many systematic errors, there may be a degree of uncertainty with regard to the accuracy of the SQUEEZE results.

2.7 GRAPHICAL REPRESENTATION AND CALCULATIONS OF VOLUMES AND GUEST-ACCESSIBLE SURFACES

POV-Ray[38] is a ray-tracing program that can be used to produce high quality molecular graphics. MSROLL,[39] a program that was incorporated into the X-Seed interface, was used to calculate the contact volumes of void spaces in a structure. MSROLL was originally designed by Connolly to map the accessible volumes of proteins and nucleic acids. In this context, the accessible volume, as defined by Lee and Richards,[40] is estimated from the surface area created by tracing the centre of a sphere with a known radius as it is rolled around a molecular assembly. The slightly modified version of MSROLL that was incorporated into X-Seed allows one to specify the probe radius.

In this study, MSROLL has been used to visualise cavities and channels in crystal structures. The guest molecules are first removed from the atom list (by “hiding” or deleting them). When cavities are mapped in a structure, a file (.cav) is created, which is then parsed into the POV-Ray program by means of the X-Seed interface. Images are rendered with the guest molecules reinstated to their original positions in order to show their locations within the solvent-accessible spaces.

2.8 SORPTION ISOTHERMS

Gas sorption isotherms were measured with an Intelligent Gravimetric Analyser (IGA-002) from Hiden Isochema, Warrington, UK [41] (Figure 5).

Figure 5. Photographs of the Intelligent Gravimetric Analyser (IGA-002).

The instrument measures the change in mass of a sample under controlled pressure and temperature conditions. It is equipped with an advanced pressure rating such that isotherm measurements can be carried out up to 20 bar of gas pressure. Gas buoyancy effects are corrected for automatically. The temperature of the sample chamber is kept constant (± 0.05 °C) by a Grant refrigerated recirculation bath. Ultra-high purity gases were used for the measurements and the entire system was outgassed after a new sample was loaded and after gas cylinder exchange. The sorption data are monitored by real-time software that analyses the pressure and weight equilibrium using least-squares regression to extrapolate a value for the asymptote.[42] A Linear Driving Force (LDF) relaxation model, during which each point is recorded once a 99% fit with the model was achieved, or the time-out was reached (set at 120 minutes), was used. The data are exported as values of mmol gas per gram of host, which can easily be converted to a host:guest (H:G) ratio or occupancy by using the molar mass of the guest and host and comparing it to the expected H:G ratio that is derived from the SCD structures.

Vapour sorption experiments can also be carried out on the IGA. However, during the measurement of vapour sorption isotherms, the weight of a sample is monitored as a function of a chosen set of partial pressures of the solvent. To avoid condensation, the maximum vapour pressure that can be measured is 95% of the vapour pressure of the solvent. Solvents were dried with molecular sieves, 3 Å, 3.2 mm pellets (Sigma-Aldrich) that were activated at 330 °C for 12 hours.

2.9 VAPOUR SORPTION KINETICS IN CONTROLLED ATMOSPHERES

An improved version of the microbalance[43] designed by Barbour, Achleitner and Greene was used to measure vapour sorption kinetics in controlled atmospheres. The sample is loaded into an aluminium sample pan, which hangs from a thin steel wire that is connected to a CI Microelectronic balance (Figure 6). Owing to the sensitivity of the balance, it is easily affected by vibrations and consequently the instrument is placed on a solid granite block. The sample is enclosed within a reaction vessel fitted with a glass jacket through which a thermostated liquid is passed.

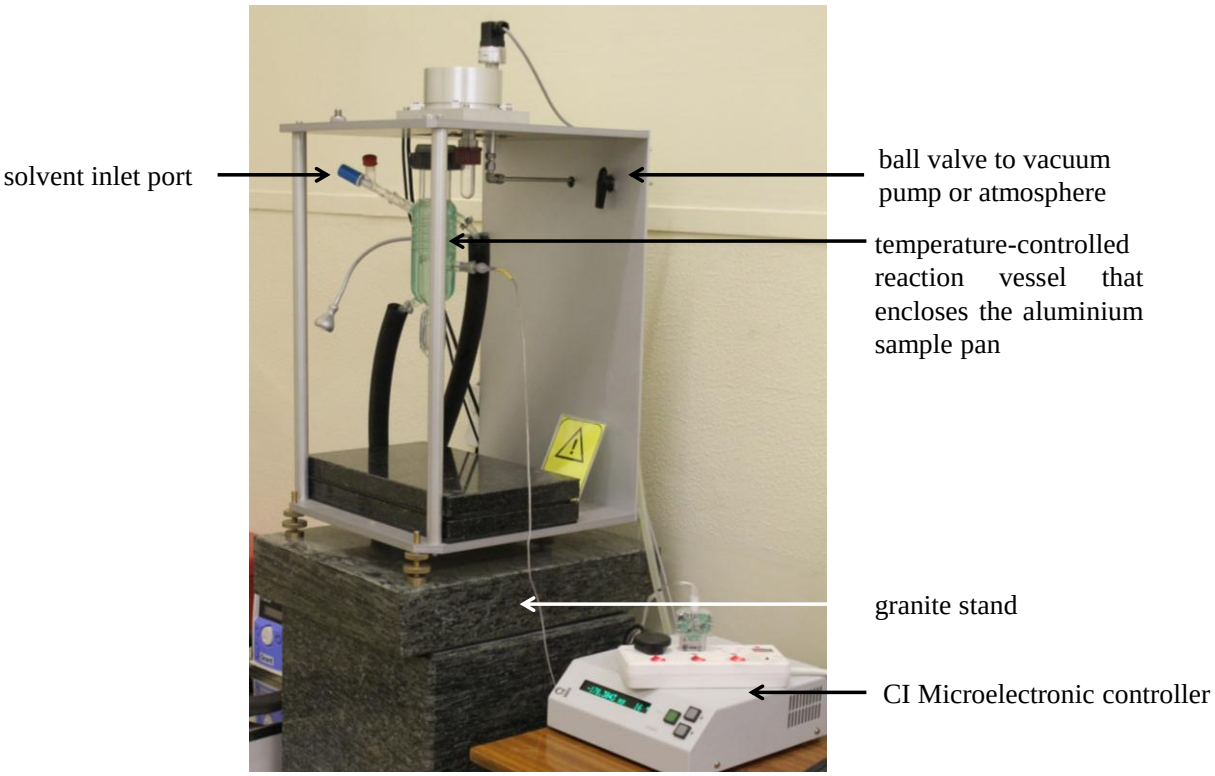

Figure 6. A photograph of the microbalance system for the measurement of vapour sorption kinetics in controlled atmospheres.

The pressure in the reaction vessel is monitored by an electronic pressure transmitter. The reaction vessel has a solvent inlet port through which the vapour is introduced. The entire system is also connected to a vacuum pump for outgassing purposes. Before an experiment, air in the reaction vessel is evacuated after sample loading until a constant sample weight is achieved. A sample of between 8 and 15 mg was used. The solvent is injected and allowed to equilibrate to its vapour pressure. The increase in weight of the sample is monitored as a function of time until it reaches an equilibrium weight or plateau. The data points are graphically represented in real time on the computer.[44]

2.10 HIGH PRESSURE DIFFERENTIAL SCANNING CALORIMETRY (HPDSC)

HPDSC measurements were carried out using a Setaram μDSC7 Evo module equipped with a high pressure sample holder. The instrument measures heat flow (like a conventional DSC) as a function of pressure. For a constant-gradient pressure measurement with a default rate of 0.1 bar min^{-1}, the DSC was coupled to a Teledyne ISCO 260D syringe pump, which was controlled with software developed by L. J. Barbour. For stepwise pressure increase, the DSC was connected to a PCTPro-2000 gas sorption analyser to supply the required pressure doses. Data were collected and analysed using Calisto software from Setaram.

CHAPTER 3

METAL-ORGANIC FRAMEWORKS: SOFT POROSITY

Metal-organic framework (MOF) materials are infinite frameworks of interconnected structural units.[45] The frameworks are usually constructed by the association of organic ligands with metal units or nodes to form 2D or 3D coordination polymers. The coordination bonds (dative bonding between a metal ion and a ligand) have strong directionality and this can be exploited by crystal engineers to provide a significant level of framework design.[19]

MOF materials are well-studied with regard to their chemical and thermal stability, permanent porosity and high surface area. The first porous MOF was a diamondoid framework synthesised by Hoskins and Robson[46] by the reaction of $Cu(I)(CH_3CN)_4^+$ with 4,4′,4″,4‴-tetracyanotetraphenylmethane. The framework has very large cavities such that two thirds of the crystal volume consists of void space.[10c] Since then Yaghi, Kitagawa and numerous others have prepared many networks based on this type of topology. Yaghi *et al*. use reticular synthesis to create rigid 3D frameworks with large cavities. Reticular synthesis involves combining inorganic or organic secondary building units (SBUs) of octahedra or tetrahedra by means of relatively strong interactions. The well-known and commercially available MOF-5, shown in Figure 7, is a prime example of a MOF that was synthesised by Yaghi *et al*. using this approach.[47]

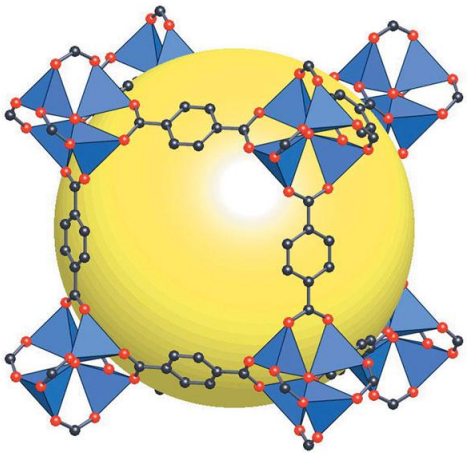

Figure 7. Graphical representation of MOF-5 synthesised by a combination of a dicarboxylate organic ligand (1,4-benzenedicarboxylic acid) with tetrahedral copper clusters.[48]

The combination of metals with different coordination geometries and an unlimited number of organic bridging ligands results in great structural diversity. The variable topology, pore size and geometry of MOFs yield a vast array of functional materials. In addition to porosity, these hybrid materials may have variable magnetic, electrochemical, optical and other physical or chemical properties.

In a recent review of soft porous crystals,[49] MOFs were categorised into three classes, according to their softness or rigidity, as shown in Figure 8.

(i) First generation materials collapse on guest removal;

(ii) Second generation materials have rigid frameworks that retain their crystallinity when the guest is no longer included within the pores;

(iii) Third generation materials are soft porous crystals that are transformable due to structural changes that result in freedom in structural and physical properties, i.e. a solvate that reversibly transforms to another phase and back upon guest removal and re-exposure.[49]

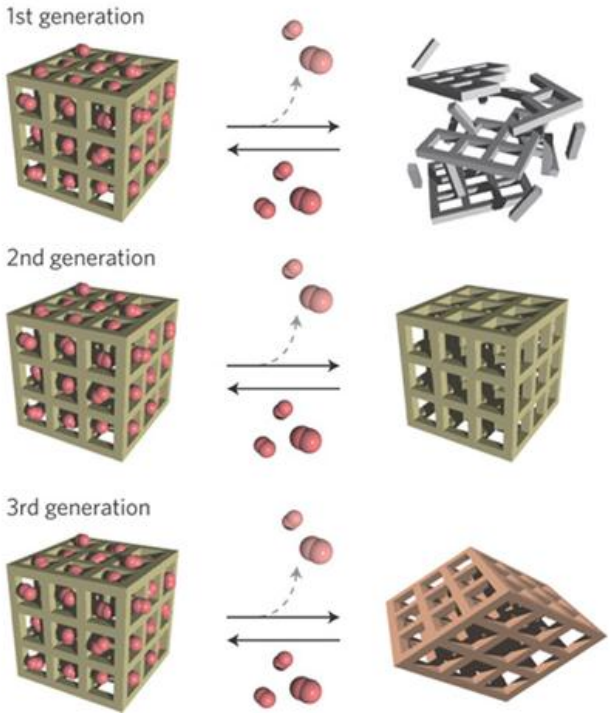

Figure 8. The categorisation of porous MOFs into three generations.[49]

Soft porous crystals are defined as porous solids that have highly ordered networks and structural transformability.[49] Permanent porosity must be present in one of the transformed

states. The transformation can be from single-crystal to single-crystal or to "imperfect crystallinity" (i.e. when the crystal loses its macroscopic integrity and becomes a powder). Softness is not only associated with a structural transformation but also accompanies other properties such as electron transfer and spin transition. The conditions for soft porosity include a structural degree of freedom, e.g. the mutual displacement of layers or cubic grids, and/or an electronic degree of freedom, such as when structural changes lead to spin crossover, magnetic ordering, electron/charge transport or dielectric properties.

Some of the crystal engineering strategies that can be employed to create soft porosity include:

(i) Interdigitation or interpenetration (i.e. when independent but identical networks are entangled). Interdigitation refers to extricable entanglement while interpenetrated networks are inextricable. These networks undergo dislocation of their mutual positions, resulting in an increased pore size and guest inclusion;[50]

(ii) The incorporation of a flexible component that can reversibly rotate, bend or break;[51]

(iii) Reversible bond cleavage and regeneration;[52]

(iv) Metal-metal interactions (e.g. Au-Au).[53]

The potential uses of soft porous frameworks for controlled release or delivery processes, on-demand guest-transport, enhanced molecular separation, molecular recognition, catalysis and physical stimulus-responsive systems (e.g. external stimulus-responsive memory devices), are all based on the unique properties of these unusual materials. Consequently, the investigation of flexible and dynamic MOFs assembled by weak intermolecular interactions has intensified in recent years.

This chapter describes the preparation of MOFs from the combination of rigid ligands with transition metal salts. Numerous MOFs were prepared, but not all of them could be studied structurally as the apohost could not be generated as a single crystal. The properties of two MOFs with different classes of porosity were studied in detail. In this chapter 2D layered MOFs that can be classified as third generation MOFs with soft porous or transformable properties are described. In the following chapter (Chapter 4), a 3D MOF that can be classified as a second generation MOF that is incredibly stable, possesses permanent porosity and unique thermal expansion properties is described.

3.1 SYNTHESIS AND STRUCTURAL ANALYSIS OF METAL-ORGANIC FRAMEWORKS

A number of MOFs were synthesised by the reaction of organic ligands with metal salts. Initially, a range of different crystallisation methods, including slow evaporation and layering techniques, were tested. However, crystallisation under solvothermal conditions with the reactants dissolved in high-boiling solvents was the best method of producing single crystals suitable for SCD methods.

3.2 ORGANIC LIGANDS

Several unsymmetrical ligands, each with a coordinating moiety on either side of a phenylene ring spacer, were synthesised. The ligands have an imidazolyl or triazolyl coordinating group on one end and a carboxylic acid moiety on the other end (Scheme 1). The ligands, 4-(1*H*-imidazol-1-yl)benzoic acid (**L1**), 4-(1*H*-1,2,4-triazol-1-yl)benzoic acid (**L2**), 4-(1*H*-benzo[d]imidazol-1-yl)benzoic acid (**L3**), 3-(1*H*-1,2,4-triazol-1-yl)benzoic acid (**L4**) and 4-(1*H*-imidazol-1-yl)-1-naphthoic acid (**L5**) were synthesised by Dr. Subhadip Neogi (a former member of our research group). The ligands, 4-(1*H*-benzo[*d*]imidazol-1-yl)benzoic acid (**L6**) and 4-(1*H*-naphtho[2,3-*d*]imidazol-1-yl)benzoic acid (**L7**) were synthesised as part of the present project, with a view to producing more robust porous two- and three-dimensional (2D and 3D) MOFs.

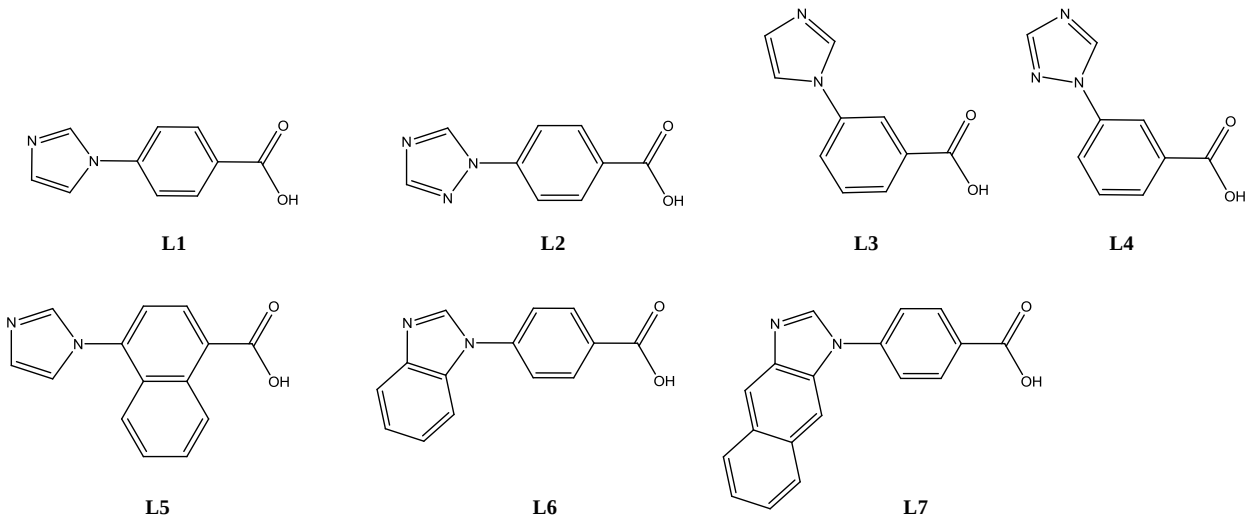

Scheme 1. The organic ligands **L1** to **L7** used to produce hybrid frameworks with metal salts.

These ligands have a number of unique features that make them ideal for preparing MOFs by reaction with a variety of metal salts:[54]

i) Rotatable C-N bonds for topological variety;

ii) Linear rigidity;

iii) Carboxylate groups for creating neutral frameworks devoid of "free" anions that may block the pores.

A novel method for synthesising of **L6** and **L7** was devised and carried out using a microwave reactor. Details about the synthetic procedures and the characterisation of the products are outlined in the experimental section at the end of the chapter (Section 3.8).

3.3 CRYSTALLISATION USING SOLVOTHERMAL METHODS

The ligands and $M(NO_3)_2$ (M = Cd, Zn, Cu, Mn, Ni and Co) salts were reacted together under solvothermal conditions, a synthetic technique commonly used for the production of zeolites. This involves the total or partial dissolution of the ligand and metal salt in a single or binary solvent mixture, which is then heated in an oven while sealed inside a Teflon-lined autoclave (or steel pressure vessel). The molar ratios of the components, their concentration, the nature of the solvent, the pH, reaction temperature and reaction time can be varied to generally yield different products.

Systematic variation of these conditions led to the determination of optimal conditions for MOF formation with **L1** to **L7**. During most reactions, 3 ml of dimethylformamide (DMF) or DMF/methanol was used as the solvent system in 10 ml Teflon containers. The ligand (0.1 mmol) was dissolved in 3 ml solvent and a stoichiometric ligand:metal ratio of either 1:1 or 1:2 was used. Two different temperature programs were used with a total reaction time of 48 hours in both cases:

i) The oven was preheated to 100 °C prior to adding the autoclaves, which were then removed after 48 hours and allowed to cool to room temperature;

ii) After introducing the autoclave, the temperature was ramped from room temperature to 100 °C (or 120 °C, 150 °C) over 30 minutes, kept isothermal for 12 hours and slowly returned to room temperature over 36 hours.

A disadvantage of crystallisations carried out under solvothermal conditions is that one cannot observe crystal growth. As a result, it remains unclear whether crystallisation of the MOF occurs during the high pressure conditions generated at elevated temperatures or whether it takes place during slow cooling of the reaction mixture. Moreover, it is well-known that this technique commonly yields concomitant polymorphs, as was the case when **L5** was crystallised with $Cd(NO_3)_2$. The variation of the conditions (reaction temperature, concentration and time) during a single experiment results in the production of mixed phases. In addition, reproducibility was found to be a major challenge owing to the inability to accurately control certain variables with regard to the experimental conditions.

3.4 MOFS PREPARED WITH LIGANDS L1-L5

During this study, nine novel imidazole-containing MOFs or IMMOFs (IM = imidazolyl) were synthesised using ligands **L1** to **L5**. The MOFs, summarised and described in Table 1, are mostly 2D with the exception of $\{[Cd(\mathbf{L2})_6]\cdot DMF\}_n$, which is 3D. Generally, the frameworks have either narrow solvent-filled channels or are close-packed. Unfortunately, most of the MOFs incorporating ligands **L1** to **L5** are not rigid enough to maintain single-crystal quality and/or their porous phase after guest removal. Only $Cu(\mathbf{L1})_4$ maintained its single-crystal quality upon heating; however the guest within the channels could not be removed (or exchanged) to afford the apohost material. It is believed that the entrapped guests may be disordered molecules of the ligand (**L1**) itself.

Table 1. A summary of the MOFs obtained with **L1** to **L5.**

Ligand	Metal salt, M:L ratio and solvent system of synthesis	Crystallographic data	Systematic name and framework description	Packing diagram (solvent omitted)	Additional studies
L1	$Cu(NO_3)_2$, 1:1, acetonitrile, methanol	*P*2/*n* *a* = 11.776(1) Å *b* = 15.457(1) Å *c* = 13.179(1) Å β= 111.287(1)° *V* = 2235.2(3) Å^3	$\{[Cu(\mathbf{L1})_2(NO_3)_2]\cdot 2CH_3OH\}_n$ 2D nets superimposed on one another and slightly displaced. Channels along [100] that contain disordered methanol	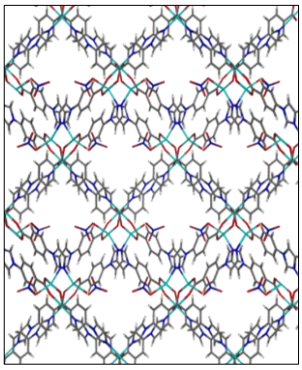 [100]	TGA shows that the methanol is removed at 200 °C and decomposition occurs at 280 °C. Hot-stage microscopy revealed that single-crystal quality is not maintained up to 200 °C.

L1	$Cu(NO_3)_2$, 1:1, methanol, water	$R\bar{3}$ a, b = 26.501(3) Å c = 9.989(1) Å V = 4778(1) Å^3	$\{Cu(\mathbf{L1})_4\}_n$ 2D interpenetrated hexagonal nets that form hexagonal-shaped channels along [001] with 60 electrons per 323 Å^3 channel section	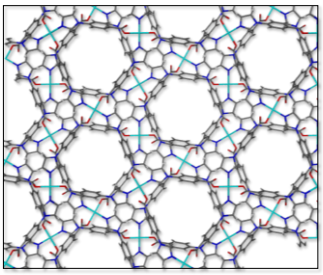 [001]	TGA shows that no weight loss occurs before decomposition at 320 °C. The same phase is maintained until decomposition. Channels must contain a non-volatile guest or strongly held water.
L2	$Cd(NO_3)_2$, 1:1, DMF	$C2/c$ a = 15.446(5) Å b = 15.902(5) Å c = 9.210(3) Å β = 104.656(3)° V = 2189(1) Å^3	$\{[Cd(\mathbf{L2})_6]\cdot DMF\}_n$ 3D Framework containing square-shaped channels along [001] that contain DMF.	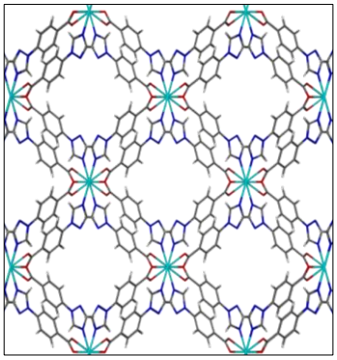 [001]	TGA shows that desolvation of the DMF guest is complete at 150 °C, and decomposition starts at 300 °C. The crystals become polycrystalline before 150 °C.
L3	$Cd(NO_3)_2$, 1:1, DMF, methanol	$P2_1/n$ a = 10.452(4) Å b = 10.731(4) Å c = 19.634(7) Å β = 92.084(6)° V = 2201(1) Å^3	$\{[Cd(\mathbf{L3})_5]\cdot DMF\}_n$ Interdigitated 2D layers with very narrow 1D channels that include DMF.	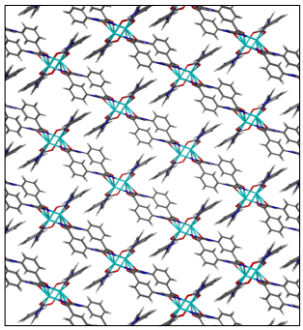 [010]	TGA and hot-stage microscopy revealed that guest-loss occurs between 150 and 220 °C and decomposition occurs at 300 °C. Single-crystal quality is not maintained after the guest is expelled.
L4	$Mn(NO_3)_2$, 1:1, DMF, methanol	$P\bar{1}$ a = 4.588(2) Å b = 8.348(2) Å c = 11.820(4) Å α = 71.780(5) Å β = 83.075(5)° γ = 75.192(5)° V = 415.3(2) Å^3	$\{Mn(\mathbf{L4})_6\}_n$ Close-packed assembly of 2D sheets. No solvent was included	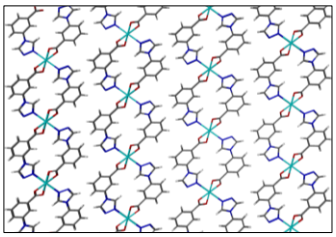 [100]	Non-porous, thus no further studies were carried out.
L5	$Cd(NO_3)_2$, 1:2, DMF, methanol	$P2_1$ a = 11.759(1) Å b = 13.657(1) Å c = 17.109(1) Å β = 94.429(1)° V = 2739.3(2) Å^3	$\{[Cd(\mathbf{L5})_4(DMF)]\cdot DMF\}_n$ 2D Sheets stacked in an offset manner. DMF is included in discrete pockets of 113.4 Å^3	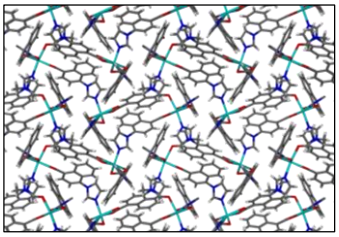 [100]	A concomitant supramolecular isomer. No further studies were carried out on this isomer because phase purity could not be obtained.

L5	$Cd(NO_3)_2$, 1:2, DMF, methanol	$P\bar{1}$ a = 15.477(1) Å b = 18.663(1) Å c = 18.945(2) Å α = 110.922(1)° β = 102.625(1)° γ = 107.728(1)° V = 4527.5(6) Å^3	$\{[Cd(\mathbf{L5})_4]\cdot 4(DMF)\}_n$ Twofold-interpenetrated 3D grid with narrow 1D channels along [100] that contain DMF	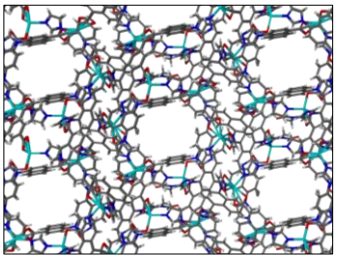 [100]	A concomitant supramolecular isomer with only a few crystals produced. Hot-stage microscopy showed that desolvation occurs from 50-90 °C and the crystal remained intact up to 300 °C. No further studies, since phase could not be re-synthesised.
	$Cu(NO3)_2$, 1:2, DMF, methanol in presence of bpy*	$P4/n$ a = 15.976(4) Å b = 15.976(4) Å c = 11.624(3) Å α, β, γ = 90° V = 2967(1) Å^3	$\{[Cu(II)(\mathbf{L5})_4\cdot Cu(I)(\mathbf{L5})_2]\cdot 3H_2O\cdot DMF\}_n$ 2D nets that are two-fold interpenetrated. Metal centres of mixed valence formed. Water and DMF are included in 1D channels	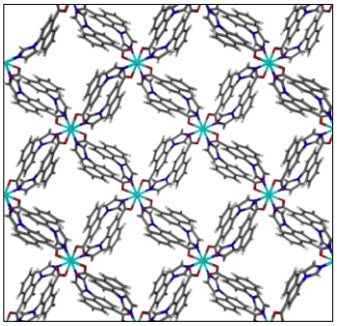 [100]	Hot-stage microscopy showed no sign of solvent loss before 230 °C, the temperature at which decomposition starts.
	$Cu(NO3)_2$, 1:1, DMF, methanol	$P2_1/c$ a = 7.529(1) Å b = 9.991(2) Å c = 14.770(2) Å β = 93.304(2)° V = 1109.3(3) Å^3	$\{Cu(\mathbf{L5})_4\}_n$ Close-packed 2D layered structure.	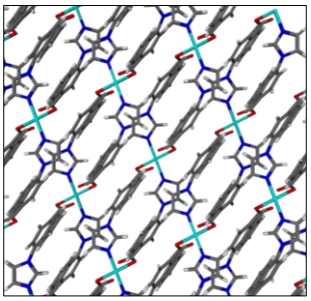 [010]	Non-porous, thus no further studies were carried out.

*bpy = 4,4′-bipyridine

Porosity studies were not carried out on the MOFs in Table 1 owing to the fact that, in each case, the empty phase could not be generated as a single-crystal transformation, or because of it being non-porous. As a result, an in-depth description and characterisation of these frameworks is not merited for the purposes of this dissertation since the aim of the project was to synthesise crystals that remain of diffraction quality following guest removal. This will permit single-crystal transformations involving the exchange of a guest substituent or its diffusion into the empty framework to be studied directly using SCD methods. Since the use of ligands **L1**–**L5** was unsuccessful, **L6** and **L7** were designed with a view to synthesising more robust 2D and 3D frameworks. It was anticipated that increasing the size of the π-electron system of the coordinating imidazole group might result in more robust structures that are stabilised by collective π-π interactions between the ligands.

3.5 2D MOFS PREPARED WITH L6

Organic ligand, **L6,** with a benzimidazolyl moiety instead of an imidazolyl group as in **L5**, contains an increased number of π-electrons available to produce frameworks that assemble in a manner that enhances the π-π interactions between the ligands. Owing to the rotational flexibility of the C-N bond, the benzimidazolyl moiety can rotate in order to form π-π interactions with neighbouring benzimidazolyl moieties. The resultant frameworks contain solvent-filled spaces or channels.

The advantage of having the additional phenylene ring on the coordinating moiety instead of the phenylene ring spacer becomes clear when one compares a framework that incorporates **L5** (from the previous section) with one that incorporates **L6 (**Figure 9**)**.

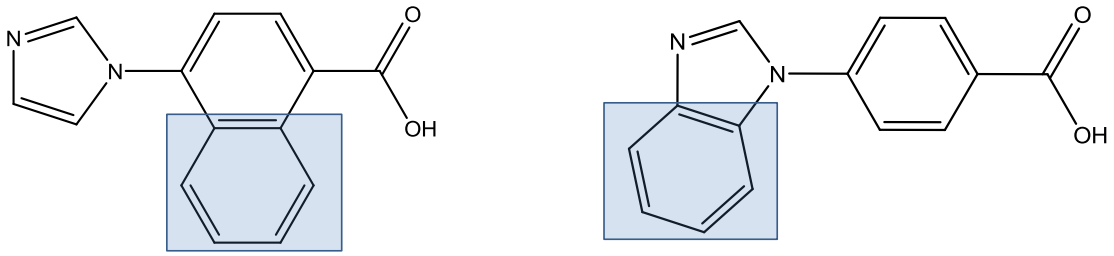

L5 **L6**

Figure 9. The additional phenylene rings on ligands **L5** and **L6**.

The difference in the topology of a framework synthesised with **L6** as opposed to **L5** is shown in Figure 10. The frameworks were assembled following the reaction of **L5** (Figure 10a), and **L6** (Figure 10b) with $Cu(NO_3)_2$. Both frameworks form a (4,4) net (2D grid), and possess square-planar coordination geometry around the Cu(II) centre. The different porosity of the structures arises from the fact that **L5** contains a naphthalene spacer moiety instead of the phenylene spacer, which forms part of **L6.**

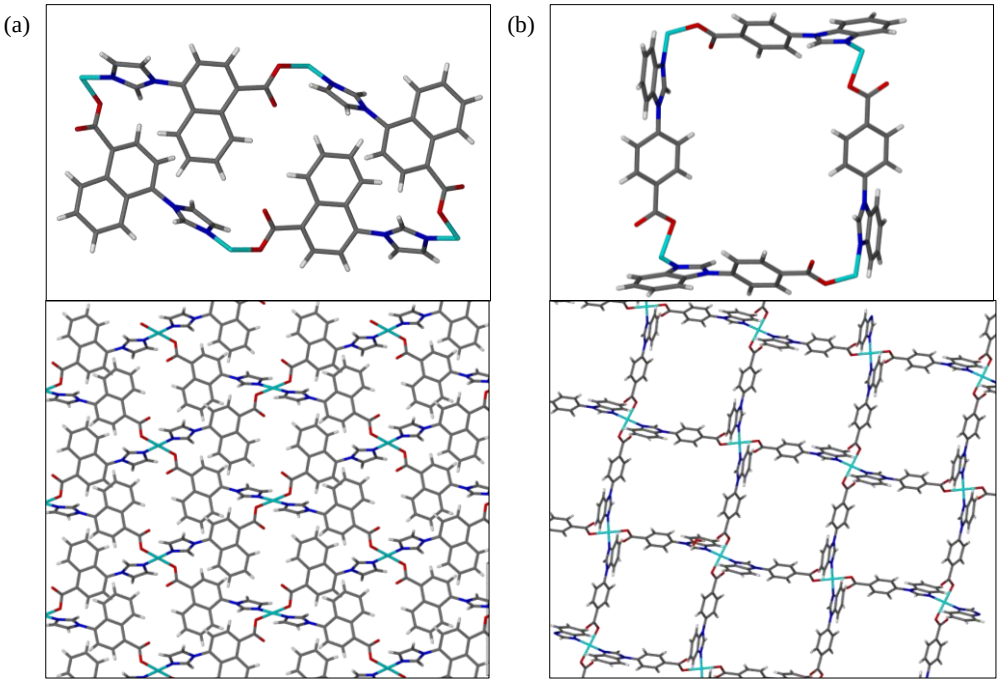

Figure 10. (a) One grid section and the entire flat 2D sheet of the $\{[Cu(\mathbf{L5})_4]\}_n$ MOF and (b) a square section and the 2D grid formed by $\{[Cu(\mathbf{L6})_4]\}_n$, with the guest molecules omitted for clarity.

The MOF incorporating **L5** packs in 2D layers of flat sheets without any appreciable solvent-accessible space, owing to the π-π interactions between the naphthalene spacer groups of stacked layers that allow for close-packing. However, in the MOF incorporating **L6,** structure-directing π-π interactions occur between the benzimidazole groups, which are rotated relative to the plane of the phenylene ring spacer. Consequently, each layer contains windows of solvent-accessible space. To summarise; the additional benzene ring on the spacer in **L5** plays a space-filling role, while the additional benzene ring on the coordinating imidazole group of **L6** stabilises a 2D layer structure and creates an "open" net with solvent-accessible space.

Generally, the frameworks incorporating **L6** consist of 2D motifs in which the π-π interactions between the organic ligands provide moderate stabilisation. These frameworks are able to undergo reversible sliding motions in a direction perpendicular to the π-π stacking to yield open or closed forms.

Preliminary results show that the 2D MOFs formed with **L6** can undergo reversible phase changes and/or shape-responsive fitting. This property will be described in more detail in the following sections (a) and (b). Both of the MOFs, formed with Cu and Zn ions, are capable of single-crystal to single-crystal transformation upon guest exchange, or desolvation. These frameworks form part of a new generation of porous materials, namely "soft porous materials".

(a) $\{[Cu(L6)_4]\cdot DMF\cdot 2H_2O\}_n$ or IMMOF-1

IMMOF-1 is formed by the reaction of **L6** with $Cu(NO_3)_2.6H_2O$ under solvothermal conditions (Scheme 2). The framework crystallises in the monoclinic space group, $P2_1/n$. The asymmetric unit consists of a ligand coordinated to Cu(II), one DMF guest molecule and two guest water molecules.

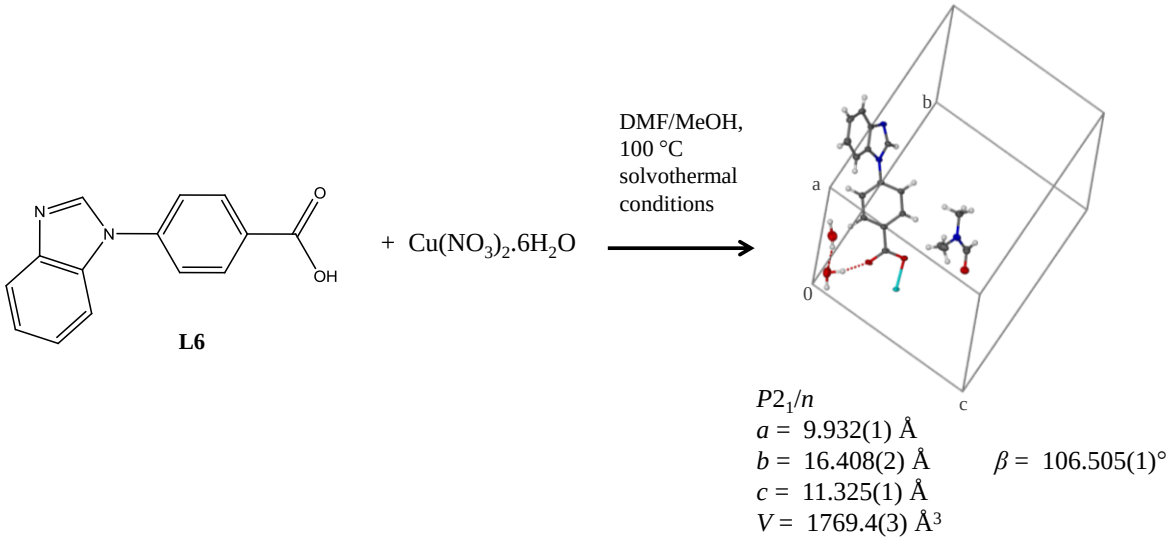

Scheme 2. The synthesis of **IMMOF-1** under solvothermal reaction conditions, with selected crystallographic information.

Four ligands coordinate to the metal centre in a square-planar coordination environment (Figure 11). Two ligands coordinate via the benzimidazole moiety (1.978(2) Å) and the other two ligands each via one of their carboxylate oxygen atoms (2.004(2) Å).

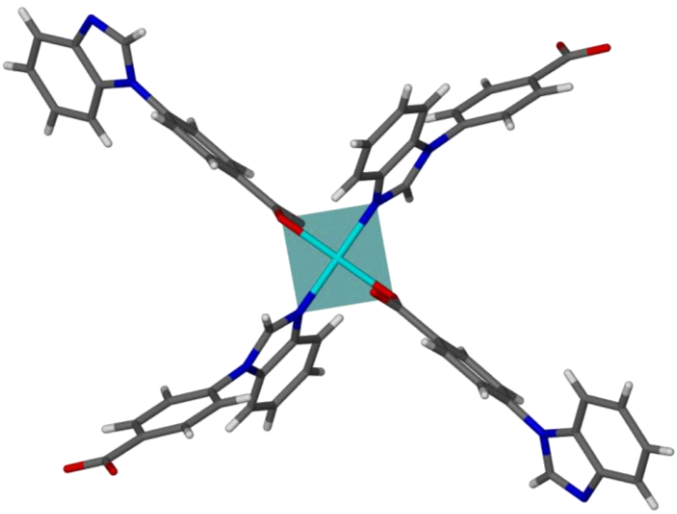

Figure 11. The square-planar coordination geometry around the Cu(II) centre of **IMMOF-1**.

The ligands and Cu(II) assemble to form a 2D square grid (Figure 12).

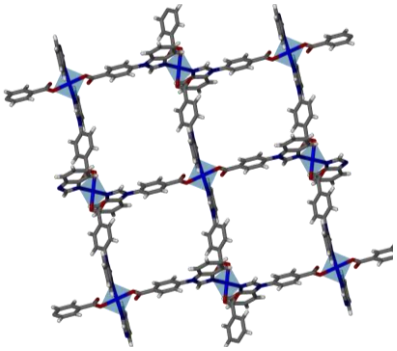

Figure 12. The 2D square grid of **IMMOF-1** viewed along [101]

The 2D grids stack on top of one another in a offset manner, with face-to-face π-π interactions (3.576 Å) between the benzimidazole moieties (Figure 13).

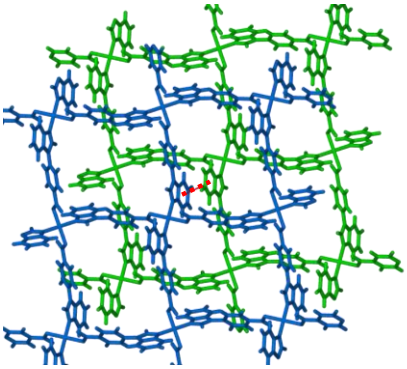

Figure 13. (a) The π-π interaction between two benzimidazole moieties of two stacked layers in the **IMMOF-1** structure (dashed red line).

The 2D layers (of windows) do not form 1D channels, but a 2D network of space for solvent molecules is evident (Figure 14).

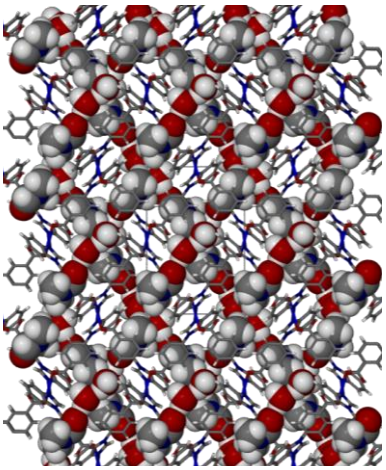

Figure 14. The network of solvent molecules present in **IMMOF-1** (in space-filled representation) viewed along [100] with the framework shown in capped-stick representation.

Thermal Analysis

The thermogram shown in Figure 15 reveals that solvent loss starts at room temperature and is complete by approximately 120 °C. The percentage mass loss occurring in this temperature range is 32.5%, which is slightly more than the calculated or expected mass loss of 26.6%, possibly owing to the presence of solvent on the surface of the crystals. The differential scanning calorimetry (DSC) trace correlates well with the TGA and indicates that "staggered" guest release occurs (i.e. the guest molecules are released in a stepwise process) as a result of the different host-guest interactions of the DMF and water molecules with the framework. The framework decomposes at approximately 290 °C.

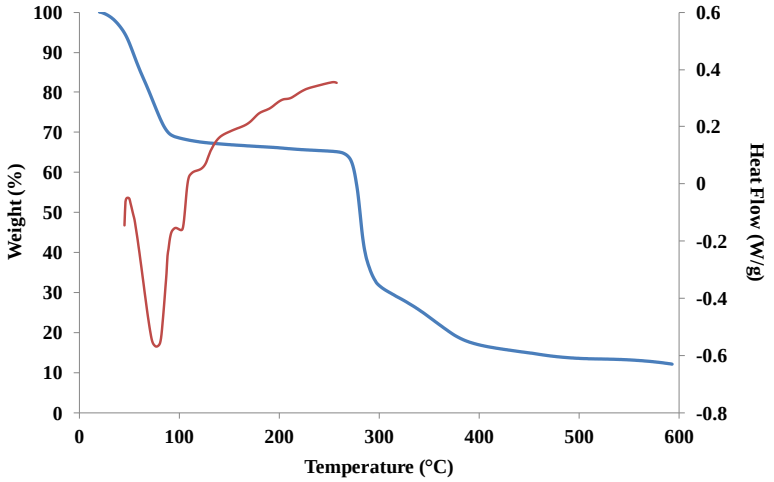

Figure 15. TGA (blue) and DSC (red) of **IMMOF-1**.

The DMF molecules included in **IMMOF-1** can be exchanged for methanol molecules as a single-crystal to single-crystal transformation (Table 2).

Table 2. The changes in the unit cell parameters, and structural features of **IMMOF-1** following guest exchange.

	As synthesised **IMMOF-1$_{DMF,water}$**	**Methanol exchange product** **IMMOF-1$_{MeOH,water}$**
Space group	$P2_1/n$	$P2_1/n$
Unit cell parameters	a = 9.932(1) Å, b = 16.408(2) Å, c = 11.325(1) Å β = 106.505(1)° V = 1769.4(3) Å^3	a = 9.68(2) Å, b = 16.18(3) Å, c = 10.94(2) Å β = 112.57(2)° V = 1582(5) Å^3
Guest molecules	One DMF and two water molecules per asymmetric unit	One and a half methanol molecules and one and a half water molecules per asymmetric unit

A single crystal of **IMMOF-1** was immersed in methanol for three days and thereafter a structure was determined from SCD data. Significant structural changes occur as a result of the single-crystal to single-crystal transformation: each of the unit cell axis lengths is reduced by ~0.3 Å, while the β-angle is increased from 106.505(1) ° to 112.57(2)°. The volume of the unit cell is reduced by ~190 Å^3 (10.6%). The changes in the unit cell parameters are indicative of a substantial structural rearrangement following the exchange of the original bulky DMF guest molecules for smaller methanol molecules. The coordination environment around the Cu(II) centre changes from square-planar to octahedral (Figure 16).

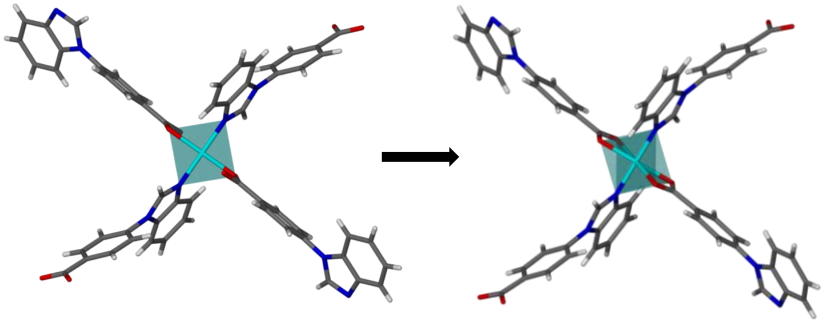

Figure 16. The coordination geometry converts from square planar (as-synthesised framework, **IMMOF-1$_{DMF,water}$**) to octahedral (methanol and water inclusion complex, **IMMOF-1$_{MeOH,water}$**).

The changes in the coordination environment around the Cu(II) metal centre are indicated in Table 3.

Table 3. Structural data concerning the metal-coordination environment after guest exchange.

	IMMOF-1$_{DMF,water}$	**IMMOF-1$_{MeOH,water}$**
Cu-N1 (Å)	1.978(2)	1.961(5)
Cu-N2 (Å)	1.978(2)	1.961(5)
Cu-O1 (Å)	2.004(2)	2.052(5)
Cu-O2 (Å)	2.004(2)	2.052(5)
Cu-O3 (Å)	2.465(2)	2.408(6)
Cu-O4 (Å)	2.465(2)	2.408(6)
N1-Cu-N2 (°)	180.00	180.00
O1-Cu-O2 (°)	180.00	180.00
N1-Cu-O1 (°)	89.13(7)	89.9(2)
N1-Cu-O2 (°)	90.87(7)	90.1(2)
N2-Cu-O1 (°)	90.87(7)	90.1(2)
N2-Cu-O2 (°)	89.13(7)	89.9(2)
N1-Cu-O3 (°)	89.37(7)	89.6(2)
N1-Cu-O4 (°)	90.63(7)	90.4(2)
N2-Cu-O3 (°)	90.63(7)	90.4(2)
N2-Cu-O4 (°)	89.37(7)	89.6(2)

The displacement of each 2D layer with respect to its adjacent layer is the largest contribution to the reduction in the unit cell volume. The offset π-π stacking interaction between adjacent layers is increased from 3.576 Å in the as-synthesised material, **IMMOF-1$_{DMF,water}$** to 3.948 Å in the methanol-exchanged product, **IMMOF-1$_{MeOH,water}$** (Figure 17). The sliding of the layers occurs in order to allow for close-packing (i.e. to fill the space that is no longer occupied by solvent).

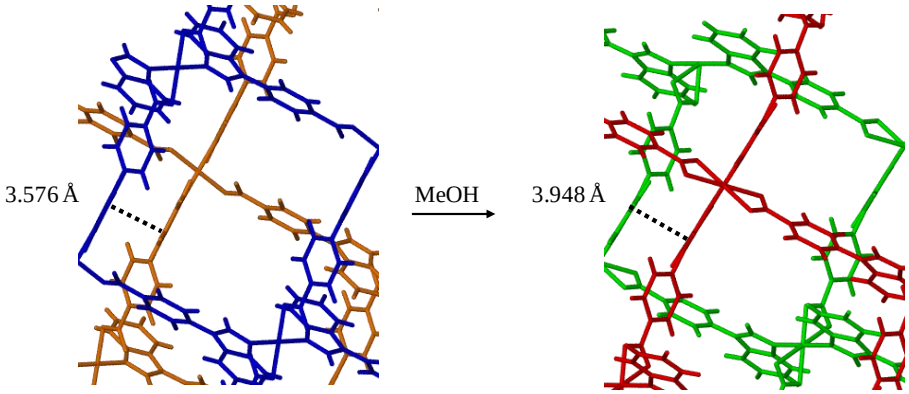

Figure 17. The change in the face-to-face π-π interaction distance after the DMF guest molecules in **IMMOF-1$_{DMF,water}$** were exchanged for methanol molecules (**IMMOF-1$_{MeOH,water}$**).

IMMOF-1$_{MeOH,water}$ loses 9.1% of its weight after being heated to 120 °C. The weight percentage is significantly less than the calculated value for loss of the methanol and water molecules (19.9%), owing to the fact that some of the methanol and water is lost at room temperature and thus during sample preparation (Figure 18).

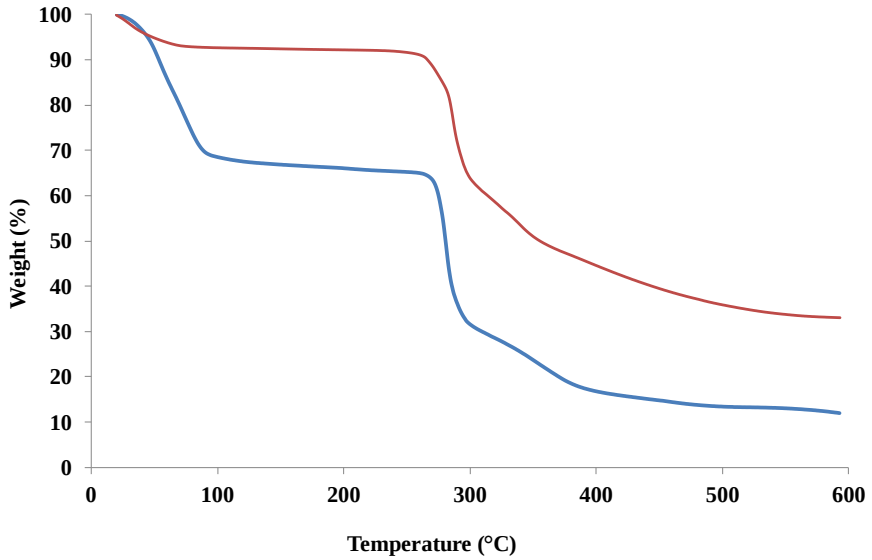

Figure 18. The thermograms of the as-synthesised material, **IMMOF-1$_{DMF,water}$** (blue), and the methanol and water inclusion complex, **IMMOF-1$_{MeOH,water}$** (red).

Crystals of both **IMMOF-1$_{DMF,water}$** and **IMMOF-1$_{MeOH,water}$** were heated to a temperature of 100 °C under reduced pressure. The solvent-free phase could not be generated without a loss of single crystallinity. PXRD measurements revealed that the solvent-free phase is different to the as-synthesised phase, although the methanol solvate can be reversibly generated (i.e. the "closed" apohost material absorbs methanol again and reverts to its "open" form, Figure 19).

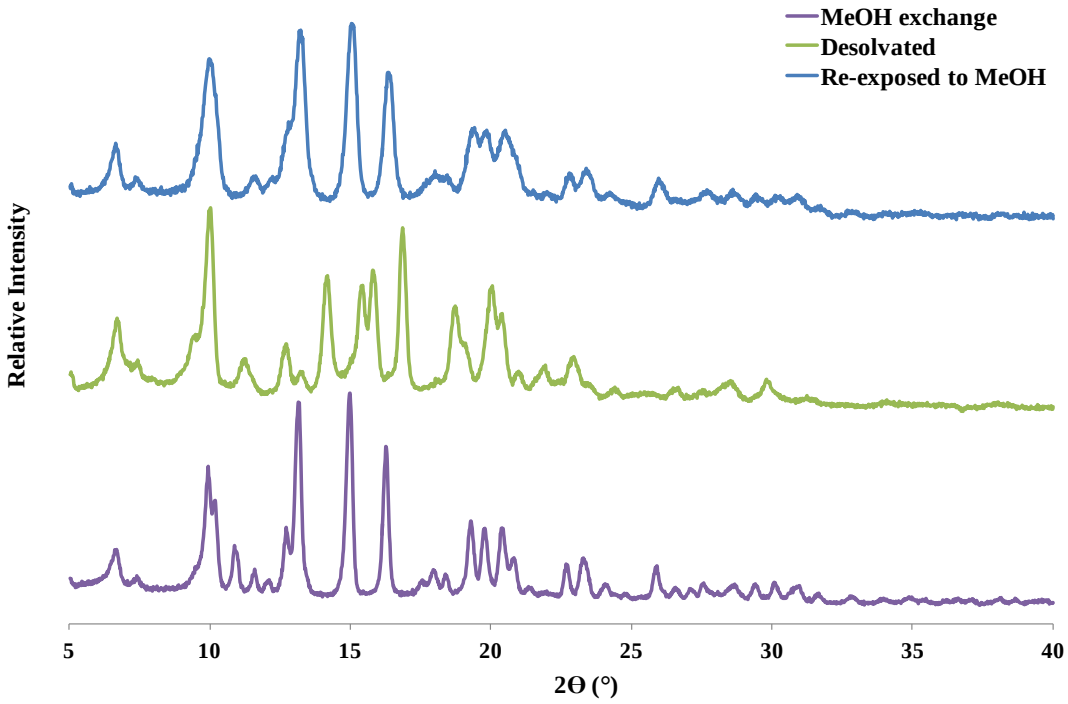

Figure 19. PXRD patterns of the **IMMOF-1$_{MeOH,water}$** after desolvation and re-exposure to methanol.

Since **IMMOF-1** becomes polycrystalline following structural changes, the material could not be studied by SCD methods, which was not the case for the MOF to be discussed next.

(b) {[Zn(L6)$_4$]·DMF·H$_2$O}$_n$ or IMMOF-2

IMMOF-2 was synthesised by the reaction of **L6** with $Zn(NO_3)_2.4H_2O$ under solvothermal conditions (Scheme 3). The asymmetric unit consists of two ligands coordinated to the Zn(II) centre, one water guest molecule and one DMF guest molecule. The water molecule hydrogen bonds to the carboxyl oxygen atom of a ligand, while the DMF, in turn, is hydrogen bonded to the water molecule.

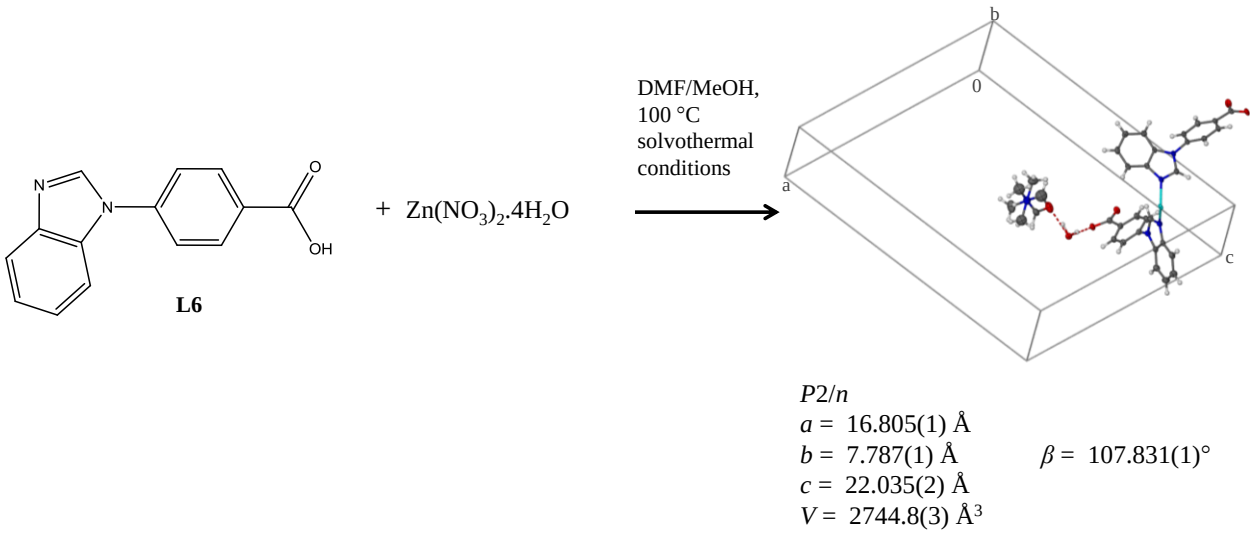

Scheme 3. The synthesis of **IMMOF-2** under solvothermal reaction conditions, with selected crystallographic information.

Four ligands coordinate to the Zn(II) centre in a tetrahedral coordination geometry. Two ligands coordinate via the benzimidazole moiety [2.011(2) Å, 2.014(2) Å] and the other two ligands each via one of the carboxylate oxygen atoms [1.931(1) Å, 1.969(1) Å], Figure 20.

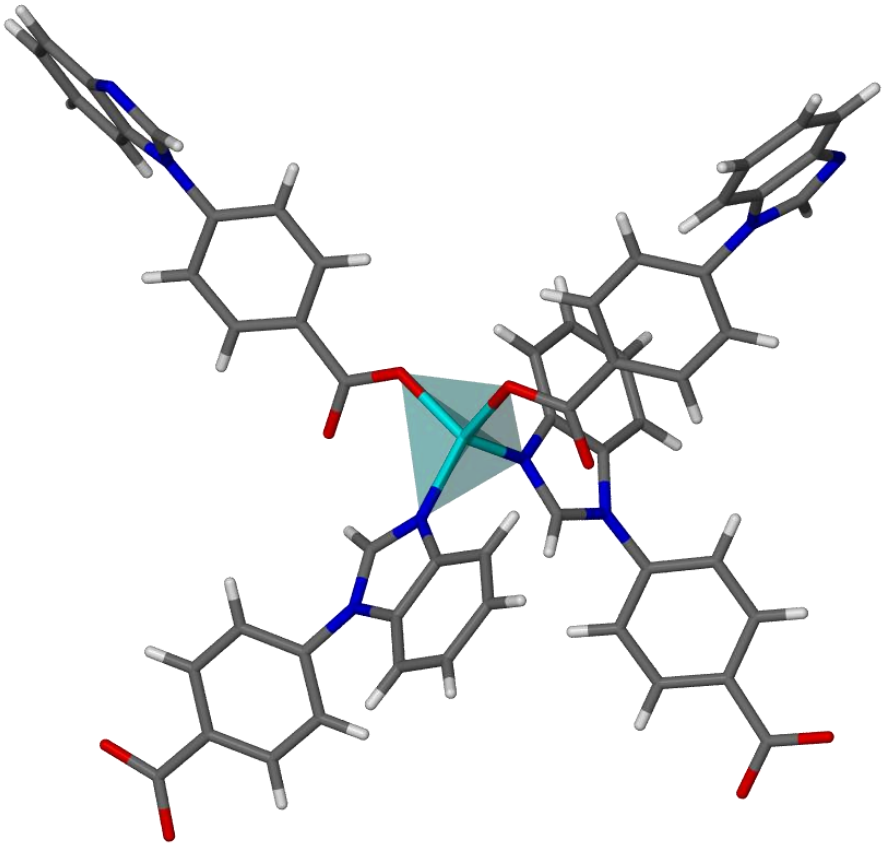

Figure 20. Tetrahedral coordination of four ligands to the Zn(II) metal centre in **IMMOF-2**.

The framework consists of layers of interpenetrated square grids (Figure 21).

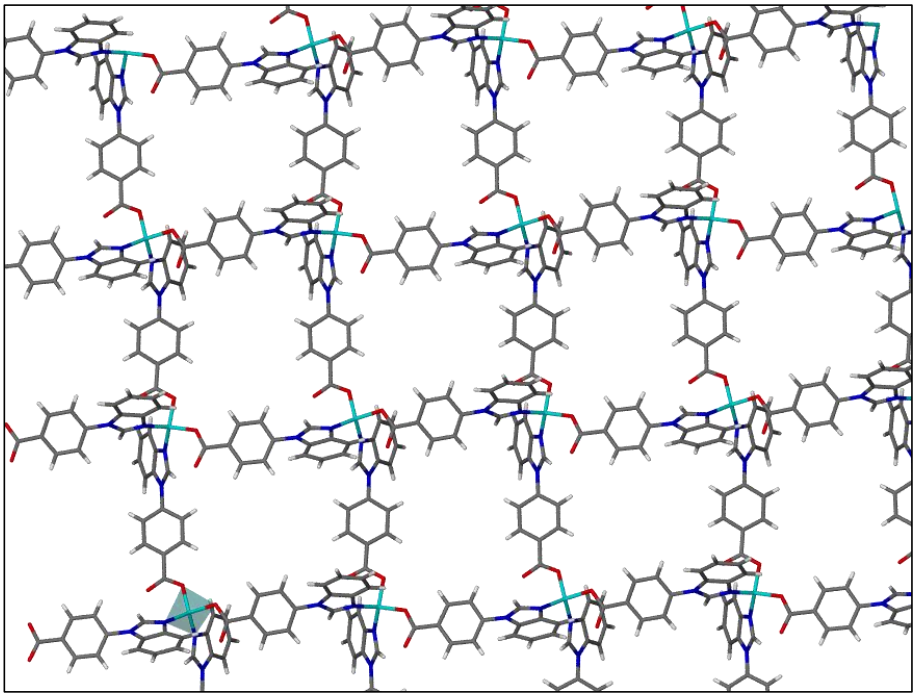

Figure 21. The (4,4) net of **IMMOF-2** without interpentration.

The interpenetrated layers are held together by edge-to-face π-π and CH-π interactions between benzimidazole rings (Figure 22).

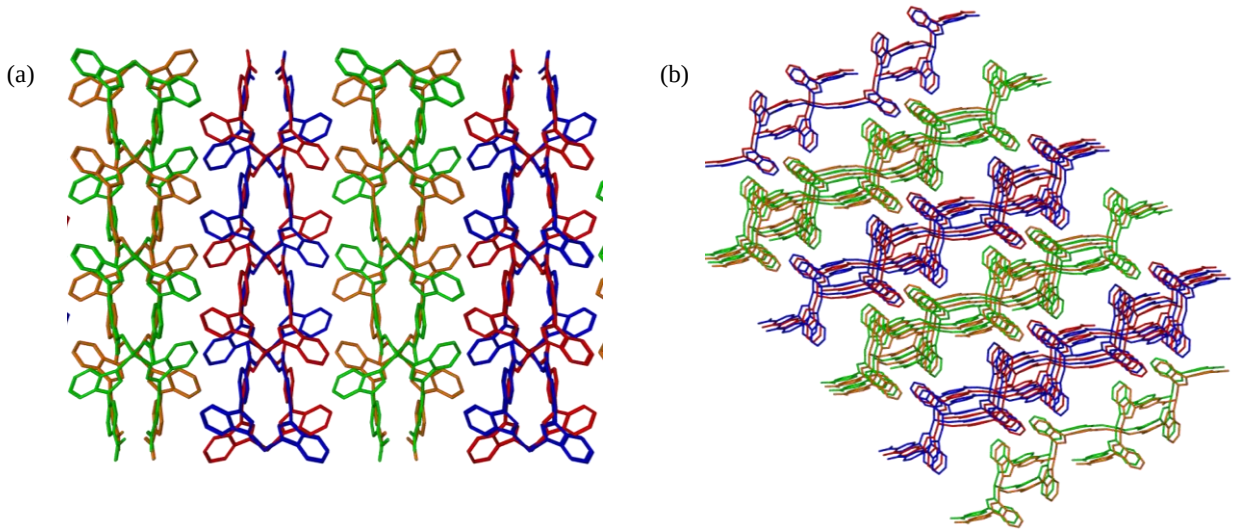

Figure 22. The interpenetrated (4,4) nets of **IMMOF-2** viewed along (a) [100] and (b) [010]. The blue and red nets are interpenetrated to form one layer, and in the neighbouring layer the interpenetrated nets are shown in green and orange. Hydrogen atoms have been omitted for clarity.

There are one-dimensional solvent-filled channels (DMF and water) that propagate along the *b* axis. The channels are situated between adjacent interpenetrated layers (Figure 23).

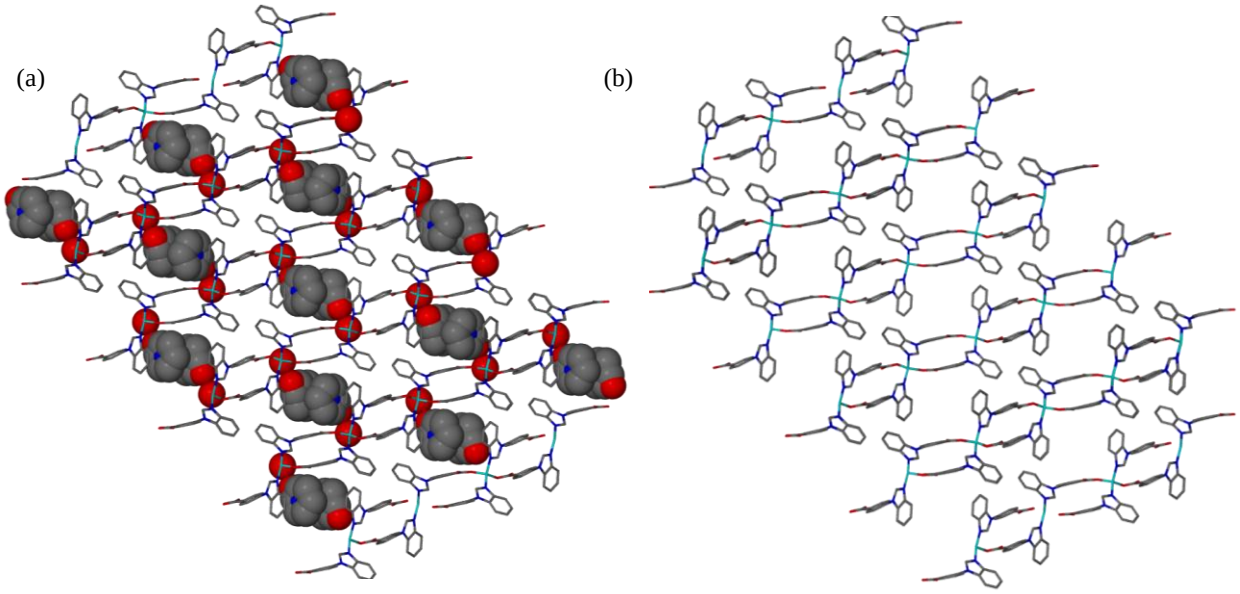

Figure 23. (a) a space-filled representation of the disordered DMF and water molecules that are included in the channels of **IMMOF-2** that propagate along [010] and (b) the host framework if the solvent molecules are hidden from view. Hydrogen atoms have been omitted for clarity.

Thermal analysis

TGA analysis showed that solvent loss starts at room temperature and is complete at ~200 °C (Figure 24). The measured mass loss of 15.1% corresponds reasonably well with the calculated value of 14.2% based on the stoichiometry of the SCD structure.

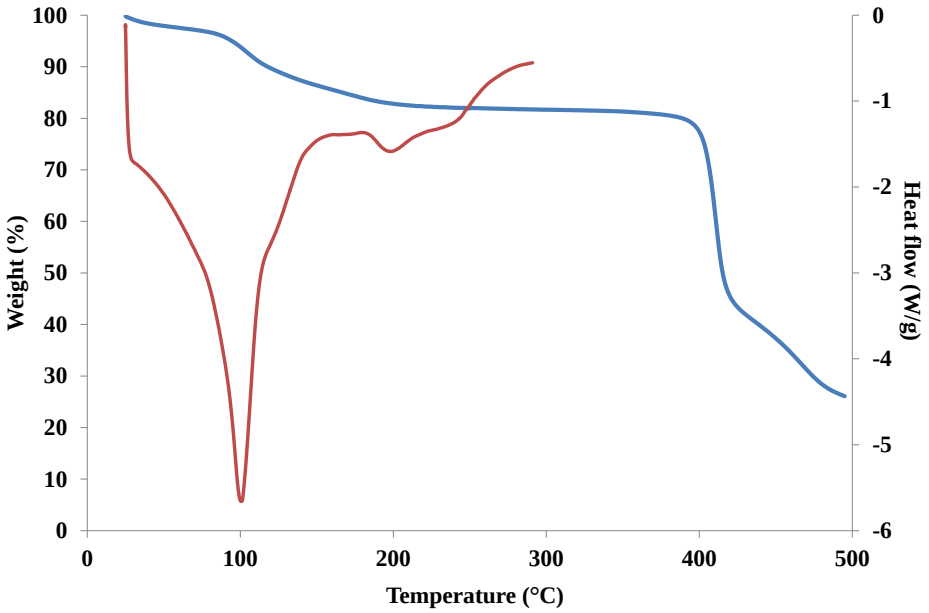

Figure 24. TGA (blue) of **IMMOF-2** with the DSC thermogram (red) overlaid.

Single-crystal to single-crystal transformations

Single crystals were immersed in methanol for two weeks prior to structure determination. A single-crystal to single-crystal transformation occurred, during which the original DMF molecules were removed from the host framework and only the water molecules that were hydrogen bonded to the framework-carboxyl group remained. Interestingly, methanol did not diffuse into the host material. The space group and unit cell parameters before and after the transformation are listed in Table 4.

Table 4. Selected information about the phase change upon partial desolvation of **IMMOF-2**.

	As synthesised framework IMMOF-2	**Partially desolvated framework IMMOF-2$_{water}$**
Space group	*P*2/*n*	*P*2$_1$/*n*
Unit cell parameters	*a* = 16.805(1) Å, *b* = 7.787(1) Å, *c* = 22.035(2) Å β = 107.831(1)° *V* = 2744.8(3) Å^3	*a* = 8.257(2) Å, *b* = 15.751(3) Å, *c* = 19.109(4) Å β = 102.336(4)° *V* = 2427.9(8) Å^3
Guest molecules	One DMF and one water molecule per asymmetric unit	One water molecule per asymmetric unit

A major concerted shift in the atomic positions of the framework occurred, which resulted in the shape-responsive fitting of the framework to the guest molecules (Figure 25).

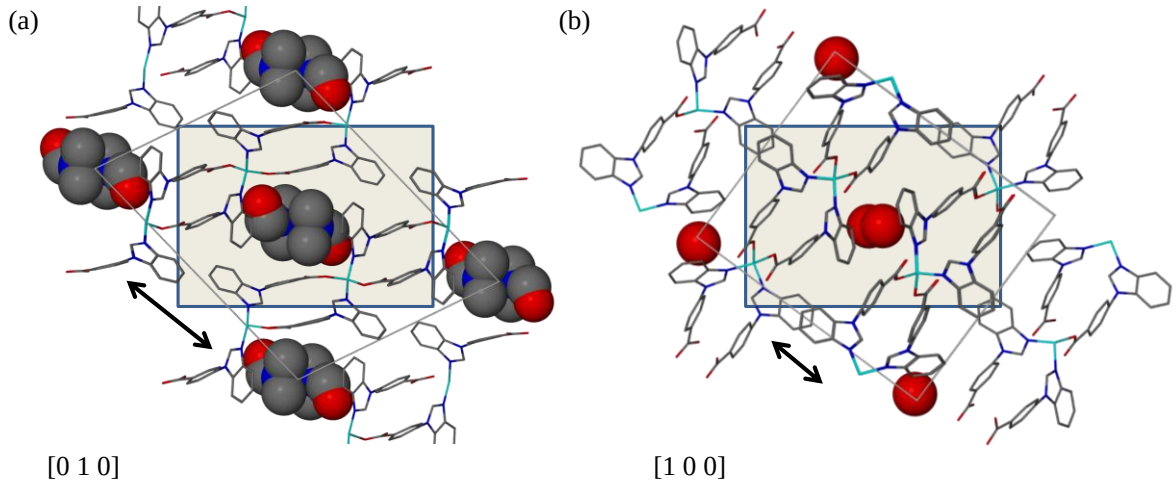

Figure 25. (a) The DMF solvate (**IMMOF-2)** with the molecules situated in the spaces between successive layers. (b) When the DMF molecules are removed, only water remains and the channels narrow (**IMMOF-2$_{water}$**). The deformation of the channels is based on a sliding motion that allows for a stronger interaction between the benzimidazole groups of neighbouring layers.

The 1D channels in the structure disappear and give way to discrete pockets as the 2D sheets shift closer to one another. The discrete pockets of solvent-accessible space contain only water after partial desolvation of the host framework (Figure 26).

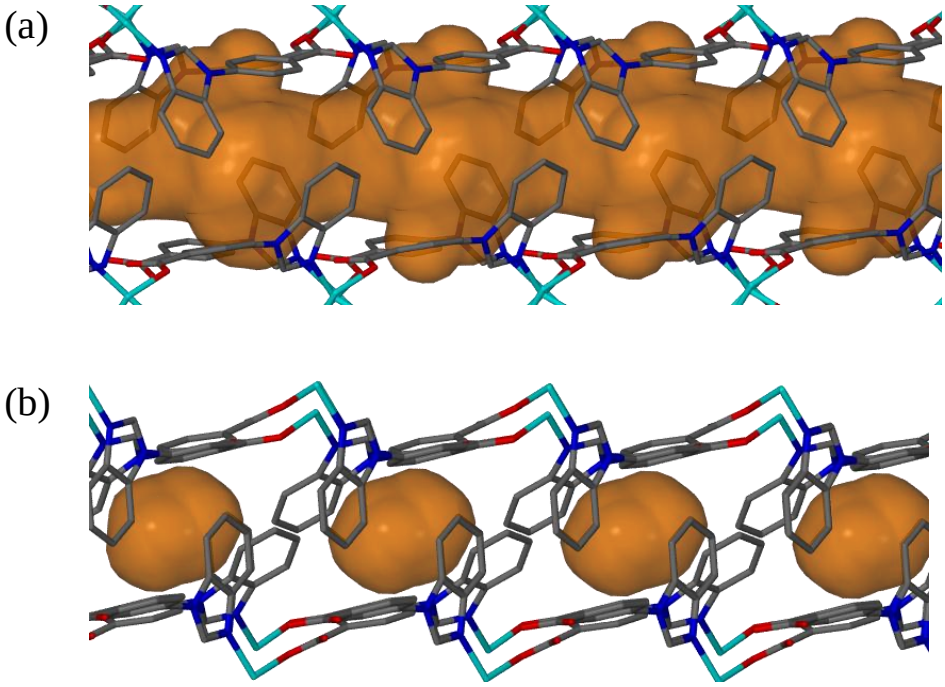

Figure 26. (a) The Connolly surface/solvent-accessible space (orange) calculated with MSROLL[39] of (a) the as-synthesised **IMMOF-2** host and (b) **IMMOF-2**$_{water}$ with discrete pockets that house the remaining water molecules. Hydrogen atoms have been omitted for clarity.

Structural analysis before and after partial desolvation shows that the coordination angles around the Zn(II) metal centre change significantly (Figure 27 and Table 5).

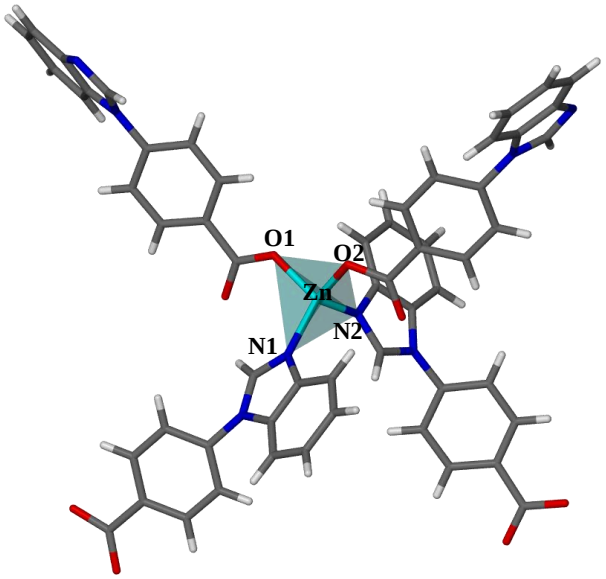

Figure 27. The tetrahedral coordination environment of **IMMOF-2** with the atom names referred to in Table 5.

Table 5. Selected bond lengths (Å) and angles (°) of the Zn(II) coordination environment.

	IMMOF-2	**IMMOF-2$_{water}$**
Zn-N1	2.014(2)	2.038(7)
Zn-N2	2.011(2)	2.031(6)
Zn-O1	1.931(1)	1.956(4)
Zn-O2	1.969(1)	1.936(4)
N1-Zn-N2	111.65(7)	105.4(3)
O1-Zn-O2	100.59(6)	99.7(2)
N1-Zn-O1	112.60(7)	107.4(2)
N1-Zn-O2	111.37(7)	109.8(2)
N2-Zn-O1	107.61(7)	120.1(2)
N2-Zn-O2	112.50(7)	114.0(2)

The coordination environment becomes distorted tetrahedral following partial desolvation. The coordination angles of **IMMOF-2** before the transformation do not deviate by more than ~3° from the ideal value for a tetrahedron (109.5°), except for the small O1-Zn-O2 angle. After the transformation, one of the coordination angles in **IMMOF-2$_{water}$** deviates by more than 10° (N2-Zn-O1 = 120.1(2)°) from 109.5°. The coordination environment around the Zn(II) node changes substantially; for instance, the N2-Zn-O1 angle increases by a massive 12.5(2)°.

Changes in the conformation of the ligand itself are also apparent. Specifically, the torsion angles around the labile C-N bond that connects the benzimidazole moiety to the phenylene ring spacer are subject to substantial deformation (Figure 28 and Table 6).

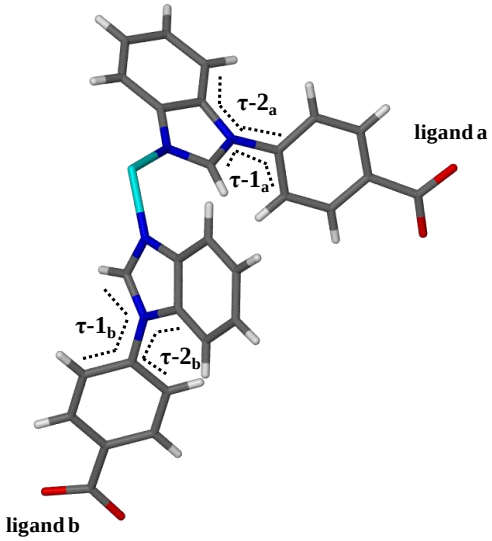

Figure 28. The torsion angles that are subject to most change following desolvation of **IMMOF-2**.

Table 6. Selected torsion angles of the two ligands in the asymmetric unit of the as-synthesised and the partially desolvated **IMMOF-2**.

Torsion angles (°)	IMMOF-2	IMMOF-2_{water}
τ-1_a	-53.9(3)	-47.8(11)
τ-2_a	-53.1(3)	-44.8(11)
τ-1_b	55.0(3)	102.7(9)
τ-2_b	59.8(3)	105.8(8)

The significant conformational changes of the torsion angles, τ-1_b and τ-2_b, are shown in Figure 29.

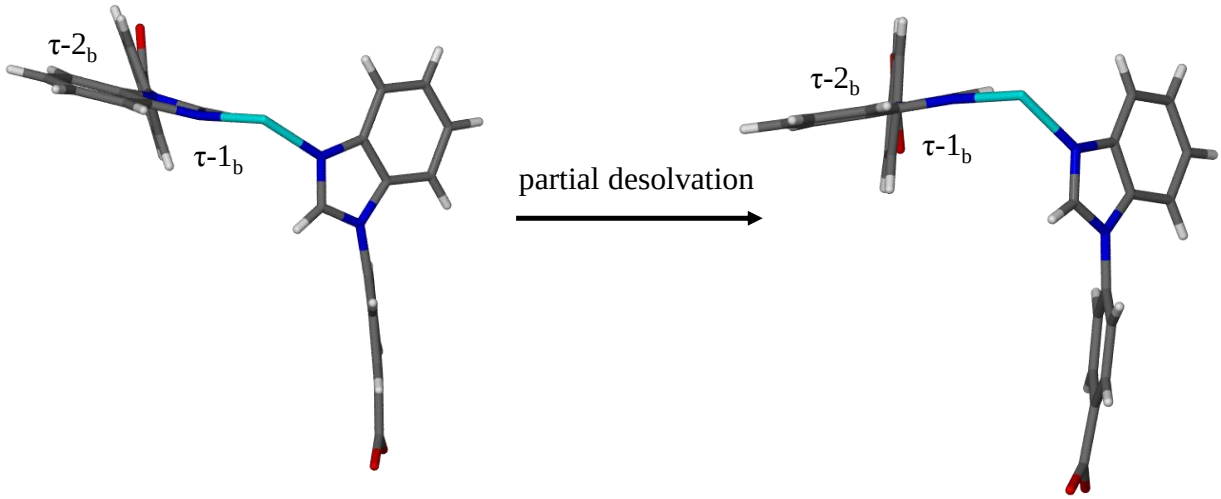

Figure 29. The asymmetric unit of **IMMOF-2** (solvent omitted) with the torsion angles τ-1_b and τ-2_b shown (viewed along the C-N bond that connects the benzimidazolyl and phenylene ring moieties of the ligand).

The adjustment of the torsion angles in the ligands is necessary for the 2D layers to close-pack more efficiently after the DMF guest molecules are removed. In the as-synthesised 2D framework there are edge-to-face π-π interactions (3.6(1) Å centroid···carbon distance) that are disrupted in order to allow the displacement of the layers to occur (Figure 30). The resultant phase is stabilised by face-to-face π-π contacts between the benzimidazole moieties (4.6(1) Å centroid···centroid distance).

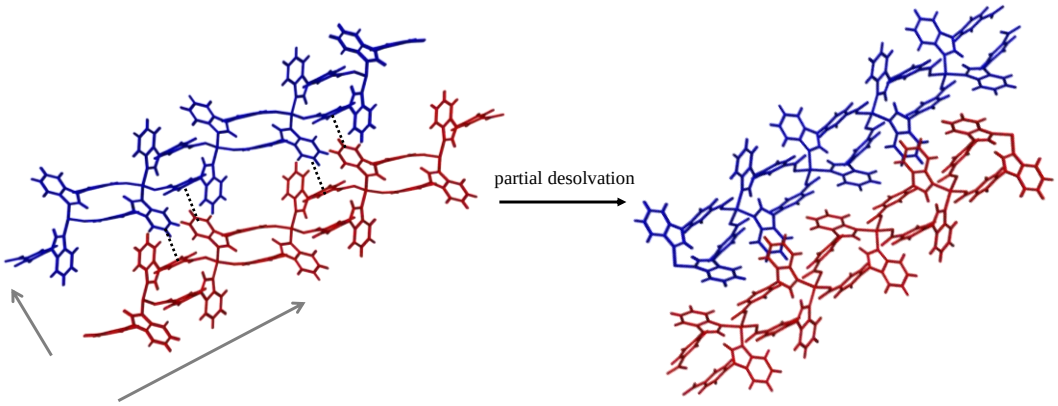

Figure 30. The 2D layers are displaced horizontally and vertically (grey arrows) in order to maximise close-contacts after partial desolvation of **IMMOF-2**. Dotted black lines represent the edge-to-face π-π interaction distances.

The thermogram of the partially desolvated framework, Figure 31, shows a weight loss of 3.4%, which is consistent with the expected loss of 3.2%, which represents the water included in the framework.

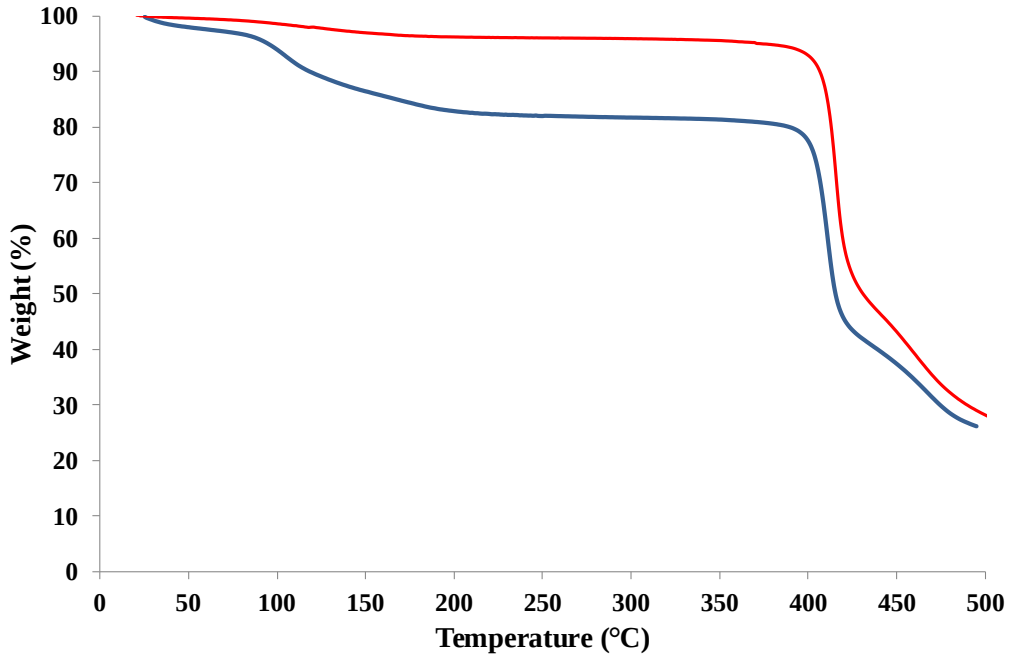

Figure 31. The TGA of the as-synthesised framework (**IMMOF-2$_{DMF,water}$**) is shown in blue, and that of the framework after partial desolvation (loss of DMF only, **IMMOF-2$_{water}$**) is shown in red.

The water that remained can be removed by heating, resulting in a new apohost phase. The hydrate phase can be regenerated by exposure of the apohost to water vapour, as is shown by the PXRD traces in Figure 32. The PXRD pattern measured for **IMMOF-2$_{water}$** does not exactly match the pattern calculated from the single-crystal structure, as some peaks are missing. Nevertheless, the traces show that the **IMMOF-2$_{water}$** phase can be regenerated by re-exposure of

the desolvated phase to water, thus implying that the framework has a structural degree of freedom and a "soft porous" nature.

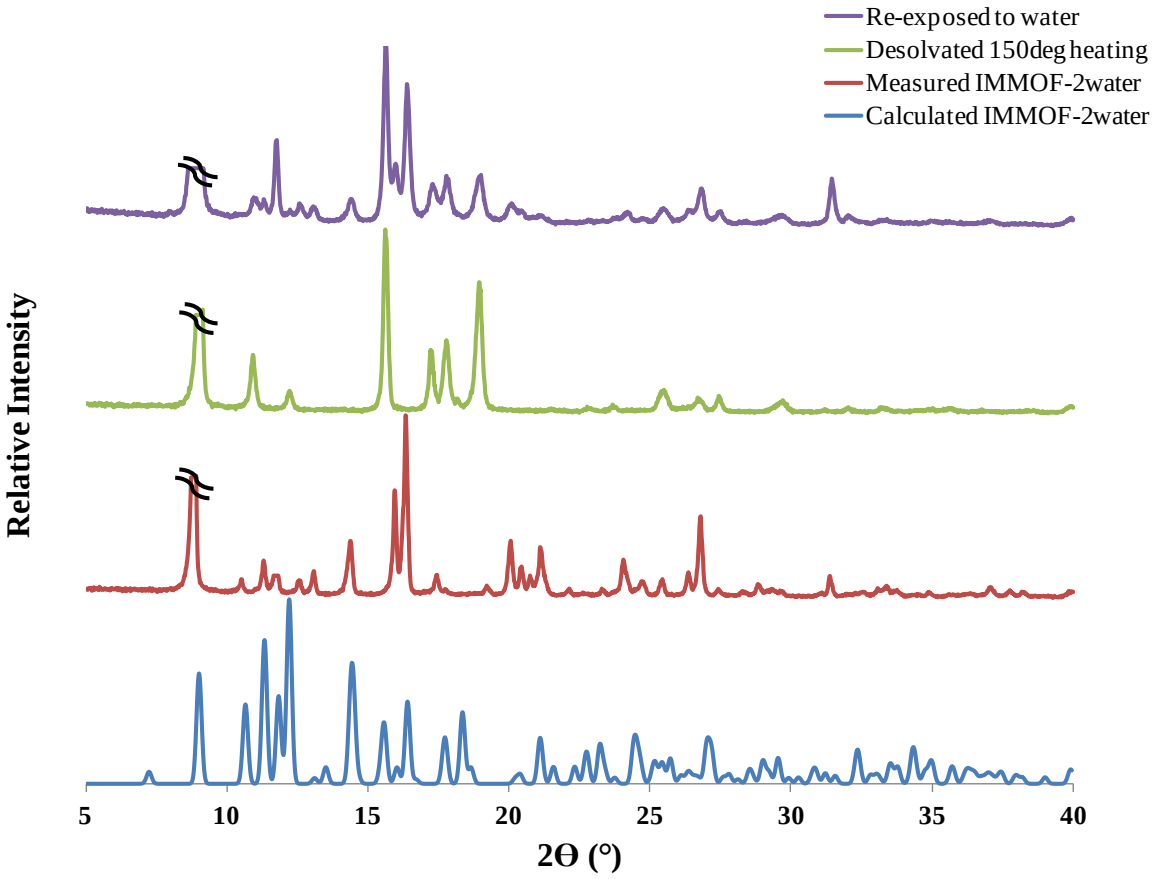

Figure 32. The calculated PXRD pattern of the hydrate (**IMMOF-2$_{water}$**) is shown in blue. The measured PXRD patterns of the hydrate (**IMMOF-2$_{water}$**), before (red) and after desolvation (green) are shown. When the material is re-exposed to water vapour (purple), it partially reverts back to the hydrate phase.

The desolvation of both **IMMOF-1** and **IMMOF-2** resulted in phase changes to structures that presumably are close-packed. Unfortunately desolvation by thermal methods results in single crystals disintegrating into a fine powder. Consequently, another method for the evacuation of **IMMOF-2** was attempted, namely supercritical carbon dioxide (sCO_2) processing. The evacuated phase of **IMMOF-2** can be generated via an exchange of the original guest molecules for CO_2 molecules, which eventually diffuse out of the host framework. This non-invasive process results in maintenance of single-crystal integrity and a structural study of the apohost **IMMOF-2** framework and its CO_2 sorption behaviour was undertaken. It was discovered that **IMMOF-2** displays reversible dynamic behaviour and extremely interesting CO_2 sorption properties.

3.6 THE STRUCTURAL TRANSFORMATIONS OF IMMOF-2 UNDER CO_2 GAS PRESSURE

The 2D layered structure of **IMMOF-2** is capable of dynamic behaviour involving the displacement of adjacent interpenetrated layers. In the previous section it was demonstrated that the layers can close-pack such that there are only small solvent-accessible voids between them, or they can move further apart, resulting in the formation of continuous 1D channels. After the apohost framework of **IMMOF-2** was prepared, the structural transformations of the framework when it absorbs CO_2 were studied by SCD methods.

3.6.1 Generating the apohost by means of supercritical CO_2 processing

A method for the generation of the apohost framework was investigated as an alternative to the use of heat and vacuum. Previous studies by Hupp *et al.* have shown that high internal surface areas in microporous MOFs can be achieved with sCO_2 processing.[55] More importantly, using a sCO_2 exchange process as a means of generating the apohost material is a less invasive and destructive technique than heating the crystals under vacuum. The sCO_2 conditions reduce the surface tension during the structural transformation. This may ensure that the crystal remains intact and of single-crystal X-ray diffraction quality such that structural analysis on the empty host is possible.

A single crystal of **IMMOF-2** was subjected to supercritical CO_2 conditions using a *SAMDRI-PVT-3D* critical point dryer from *Tousimis*, a commercial instrument normally used to freeze-dry biological samples. Within the sample chamber, the solvated single crystal (containing DMF and water) was immersed in liquid CO_2 under pressure. The liquid CO_2 was converted to its fluid supercritical phase at the critical point in the high-pressure chamber and the conditions were maintained for 12 hours. Thereafter, the gas was slowly exhausted at a temperature higher than 31.1 °C. This procedure resulted in the removal of the original guest molecules from the channels between the 2D layers. Subsequent SCD experiments revealed that CO_2 became entrapped within the solvent-accessible space of the **IMMOF-2** and could be stored for more than three days in a single crystal. It can be concluded that the DMF and water were exchanged for CO_2 under high pressure conditions reaching 73 bar at the supercritical point, and when the CO_2 pressure was reduced and eventually removed, the gas remained within the structure. The results demonstrate that **IMMOF-2** has a high affinity for CO_2.

The SCD data of to the CO_2 included complex (**IMMOF-2$_{sCO2}$**) yielded a model in which the CO_2 position could be modelled very accurately. The CO_2 bond lengths were refined without any restraints (1.147(5) Å). The CO_2 atoms have small thermal parameters (carbon U_{equiv} = 0.0485, oxygen U_{equiv} = 0.0947) and could be refined anisotropically. This is unusual for a gas inclusion complex and it is, therefore, evident that the CO_2 molecules are held in position by strong host-guest interactions.

The phase change to **IMMOF-2$_{sCO2}$** involves a substantial reduction in the unit cell volume from 2744.8(3) Å^3 to 2446.6(9) Å^3. Remarkably, the 10.8% reduction in the crystal volume occurs as a single-crystal to single-crystal transformation. The contraction of the unit cell is caused by the displacement of the 2D layers closer together to create an induced fit around the CO_2 molecule, as was the case with the partial desolvation of the framework to yield the hydrate. The significant changes in the unit cell are listed in Table 7.

Table 7. Selected information about the phase change of **IMMOF-2** upon sCO_2 exchange.

	IMMOF-2	**IMMOF-2$_{sCO2}$**
Space group	*P*2/*n*	*P*2$_1$/*n*
Unit cell parameters	*a* = 16.805(1) Å, *b* = 7.787(1) Å, *c* = 22.035(2) Å β = 107.831(1)° *V* = 2744.8(3) Å^3	*a* = 8.346(2) Å, *b* = 15.505(3) Å, *c* = 19.208(4) Å β = 100.174(3)° *V* = 2446.6(9) Å^3
Guest molecules	One DMF and one water molecule per asymmetric unit	Half of a CO_2 molecule per asymmetric unit

The entrapped CO_2 molecules are situated between two neighbouring 2D layers of the host framework (Figure 33).

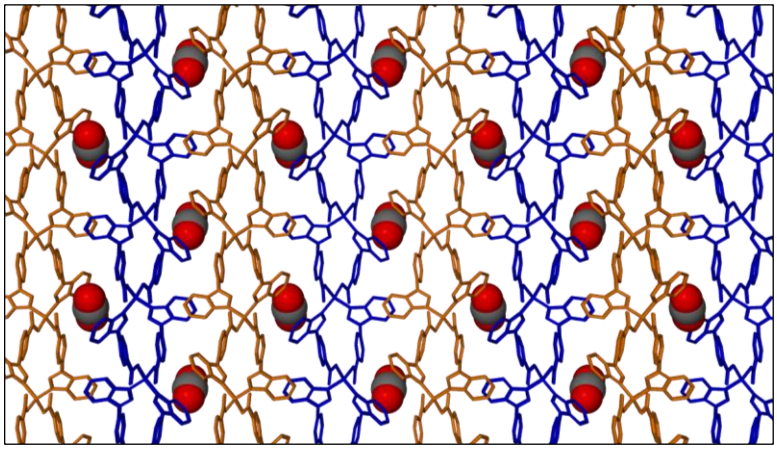

Figure 33. The **IMMOF-2** framework with entrapped CO_2 viewed along [100]. The CO_2 molecules are shown in space-filled representation and the 2D sheets of the framework are shown in blue and orange. Hydrogen atoms have been omitted for clarity.

Structural analysis revealed that the CO_2 is stabilised by host-guest interactions with the benzimidazole moieties of the host framework (Figure 34). Each CO_2 molecule is situated in a 65 $Å^3$ pocket surrounded by four benzimidazole moieties acting as two pairs of "molecular tweezers". The first pair of "tweezers" is positioned at either end of the CO_2 molecule. There are hydrogen bonding interactions between the benzimidazole protons and the oxygen atoms of the CO_2 molecule (C···O distance = 3.385(7) Å). The second pair of "tweezers" is located on either side of the central carbon atom of the CO_2 molecule. Here, a π-π interaction exists between the π-electron system of the benzimidazole group and the π electrons of the CO_2 molecule (centroid···C distance = 3.482(4) Å).

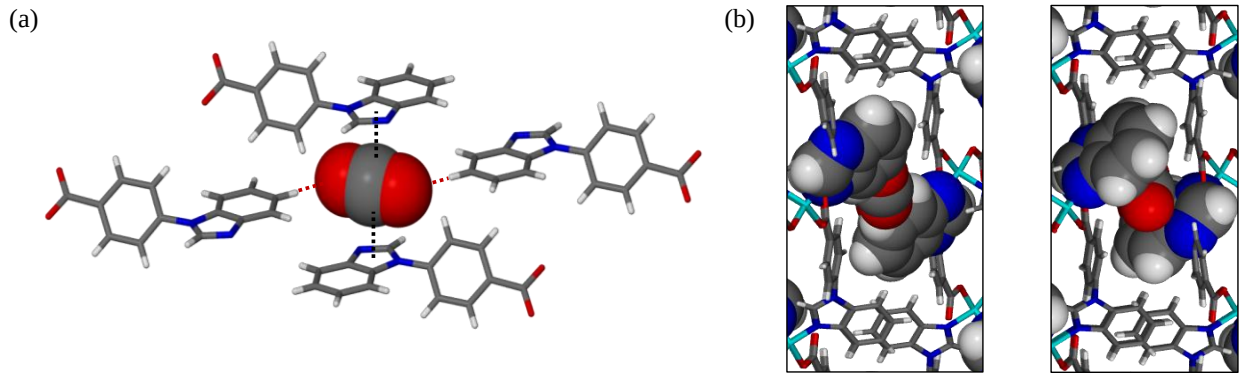

Figure 34. (a) The CO_2 molecule is stabilised by C-H···O hydrogen bonds (shown as dashed red lines) between the protons of the benzimidazole moiety and the oxygen atom of the CO_2 as well as π-π interactions (shown as dashed black lines) between the benzimidazole π-electron system and the CO_2 π electrons. (b) The benzimidazole moieties act as molecular tweezers holding the CO_2 in place.

The TGA trace of **IMMOF-2$_{sCO2}$**, shown in Figure 35, does not show a stepwise loss of CO_2 molecules but a gradual decrease in the weight of the sample is apparent. Based on the stoichiometry of the SCD structure a weight loss of 3.9% would account for all of the CO_2 molecules. This amount of weight loss is achieved at a temperature of ~100 °C, however the TGA trace shows further gradual decrease in weight until decomposition at ~400 °C. The small additional weight loss from 100 °C to 400 °C (~4%) is perhaps associated with slow decomposition of the sample prior to 400 °C, over a broad temperature range.

PXRD patterns were measured prior to and after sCO_2 exchange (Figure 36). From the results it was deduced that an almost complete phase conversion of the original **IMMOF-2** framework to **IMMOF-2$_{sCO2}$** can be achieved in a bulk sample.

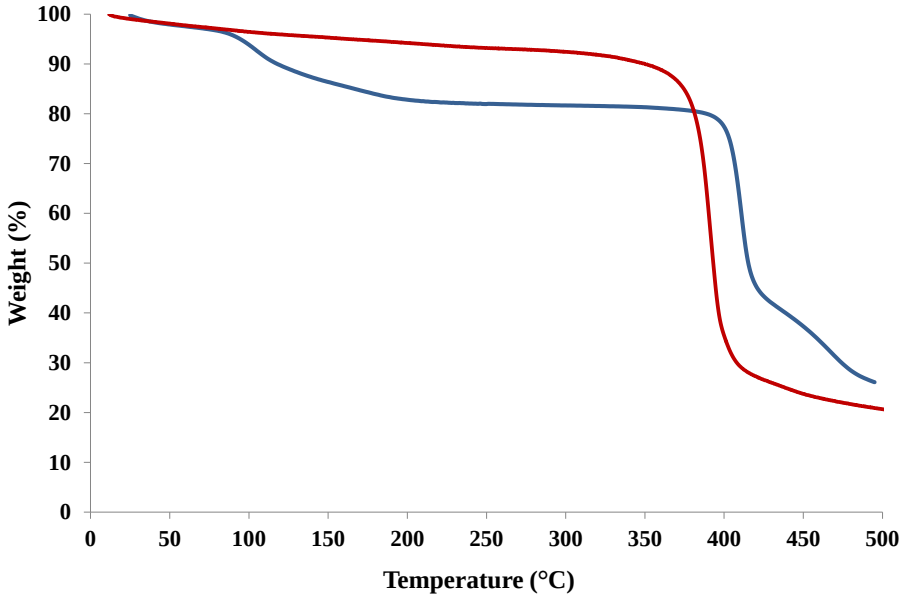

Figure 35. The TGA trace of **IMMOF-2** containing DMF and water (blue) compared to the TGA trace after sCO_2 exchange (red).

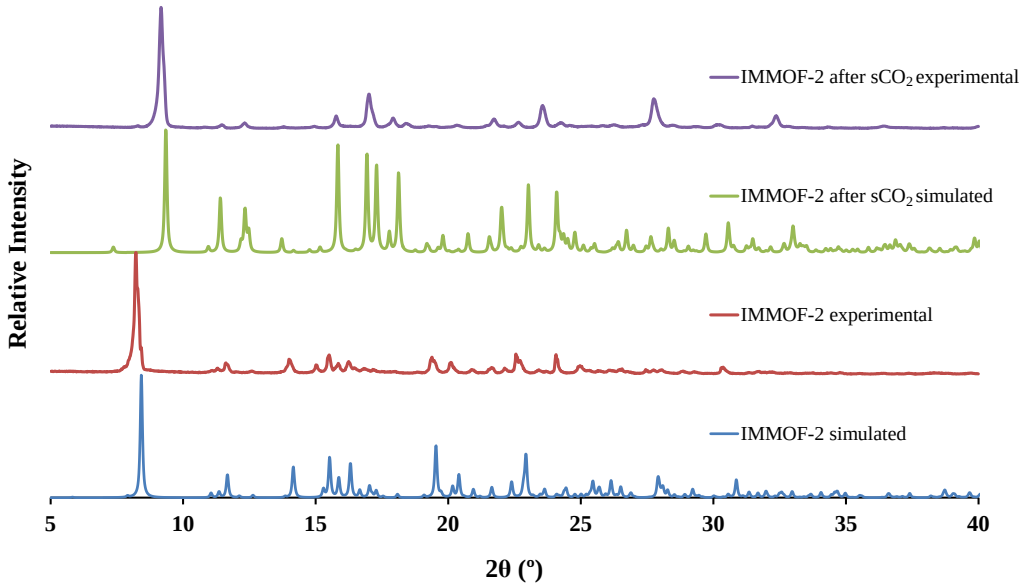

Figure 36. The simulated and experimental PXRD patterns of **IMMOF-2** before and after sCO_2 exchange.

IR spectra were recorded in the 4000–400 cm^{-1} region, using a Nexus 670 FT–IR instrument (Thermo Nicolet Instruments, USA) with a Golden Gate ATR accessory to provide further proof of CO_2 inclusion in **IMMOF-2** (Figure 37). In the IR spectrum of **IMMOF-2$_{sCO2}$** there is an additional large absorption band at 2332 cm^{-1}. The strong vibrational band is red shifted from the centre of the P and R bands of pure gaseous CO_2 (2303 cm^{-1}) and does not have fine rotational structure, as would be anticipated for a free gas.[56]

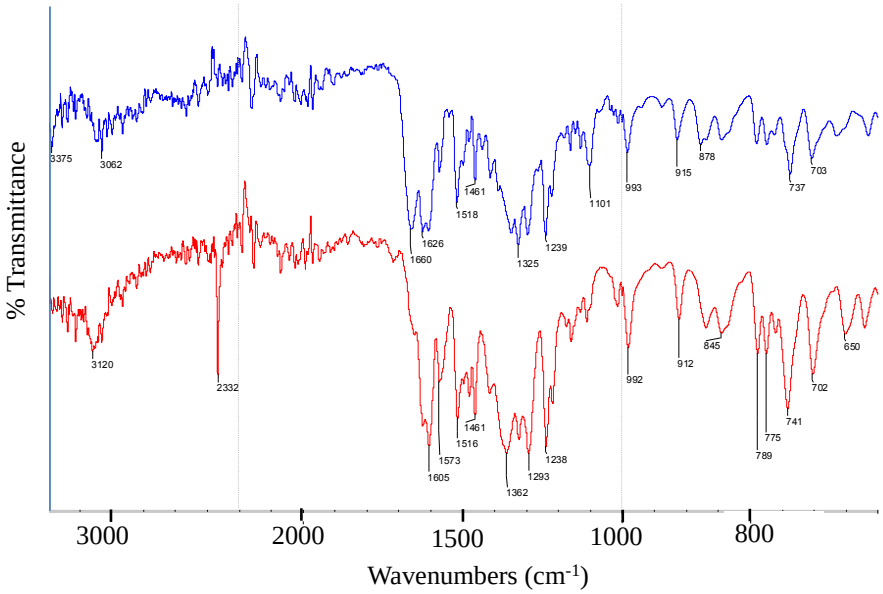

Figure 37. IR spectra of **IMMOF-2** (blue) and **IMMOF-2$_{sCO2}$** (red).

The band in the IR spectrum diminishes and is completely absent five days (Figure 38). Desorption of the CO_2 is believed to occur over several hours when the material is a powder (to be discussed later).

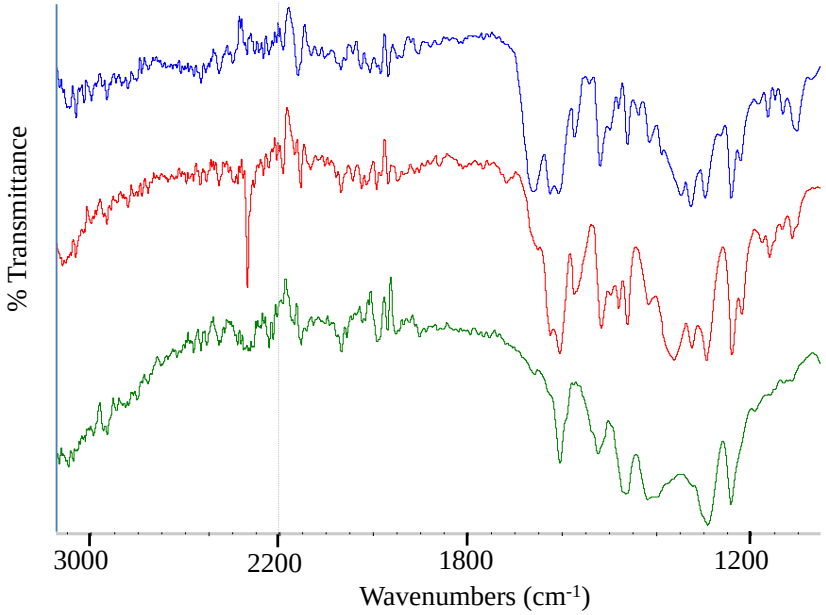

Figure 38. IR spectrum of **IMMOF-2** (blue), **IMMOF-2$_{sCO2}$** (red) and **IMMOF-2$_{sCO2}$** five days after the exchange (green).

As might be expected, large single crystals retain the CO_2 for a much longer time. A SCD structure was determined three days after sCO_2 exchange and the occupancy of the CO_2 molecule refined to 60% of the original occupancy. When a structure was collected eighteen days after the sCO_2 exchange, the material was completely desorbed, leaving the empty host.

The structure of the empty host is not significantly different from that of **IMMOF-2$_{sCO2}$**, with a small reduction in the unit cell volume from 2446.6(9) Å^3 to 2426.5(8) Å^3, which is associated with a reduction in the volume of the solvent-accessible space to 57 Å^3. A SQUEEZE electron count of 2 electrons per 57 Å^3 void was calculated, indicating that the voids are essentially empty. A summary of selected information for the SCD structures of **IMMOF-2** is shown in Table 8.

Table 8. Selected structural information about all the **IMMOF-2** structures.

Structure	Space group	Unit cell parameters				Unit cell volume (Å^3)	Void volume (Å^3)	Electron count per void (SQUEEZE[36,37])
		a (Å)	*b* (Å)	*c* (Å)	*β* (°)			
IMMOF-2	*P2/n*	16.805(1)	7.7867(5)	22.035(2)	107.831(1)	2744.8(3)	239	84
IMMOF-2$_{water}$	*P2$_1$/n*	8.257(2)	15.751(3)	19.109(4)	102.336(4)	2427.9(8)	54	13
IMMOF-2$_{sCO2}$	*P2$_1$/n*	8.346(2)	15.505(3)	19.208(4)	100.174(3)	2446.6(9)	65	18
IMMOF-2$_{sCO2\ 3daysafter}$	*P2$_1$/n*	8.332(2)	15.514(3)	19.170(4)	101.017(3)	2432.2(8)	59	9
IMMOF-2$_{apohost}$	*P2$_1$/n*	8.327(2)	15.520(3)	19.158(4)	101.455(3)	2426.5(8)	57	2

The TGA trace on a powdered sample of **IMMOF-2$_{apohost}$** shows a very small and gradual decrease in weight as the temperature is ramped (Figure 39). The percentage weight loss of 1.13% is believed to be due to air that the material absorbs under ambient conditions.

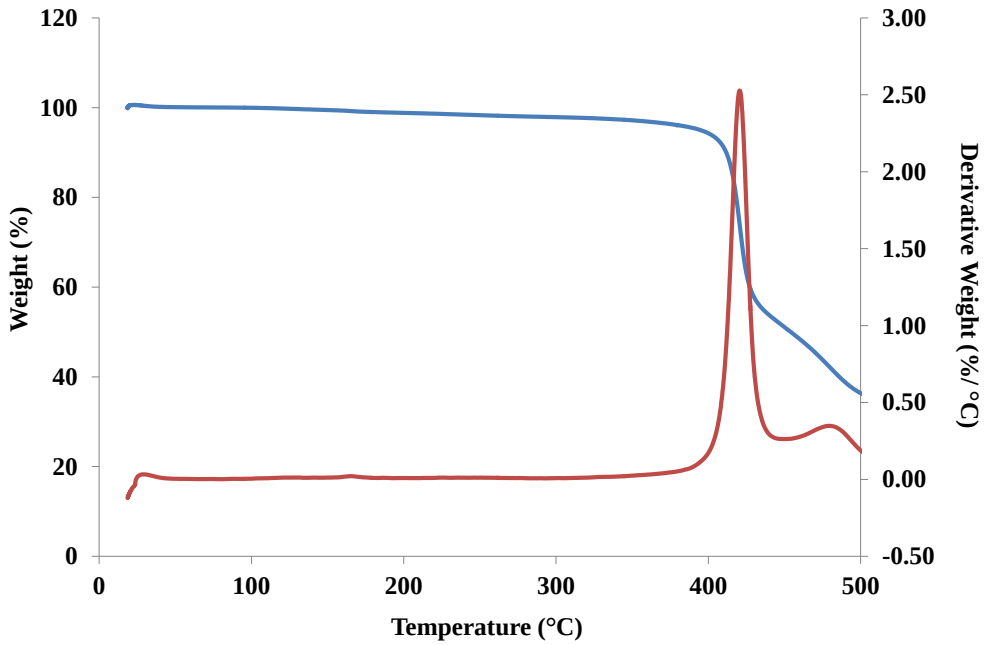

Figure 39. TGA trace of **IMMOF-2$_{apohost}$** (blue) and the derivative of the weight as a function of temperature (red).

A bulk sample of **IMMOF-2$_{apohost}$** can be prepared by a supercritical CO_2 exchange process followed by exposure to vacuum for 2 days. It is evident that CO_2 can pass through the framework and, consequently, CO_2 sorption studies were carried out next. Since the evacuated crystals retain their single crystallinity, a single crystal of **IMMOF-2$_{apohost}$** was mounted in a gas cell for structural studies under controlled atmospheres.

3.6.2 Single-crystal to single-crystal phase transition during CO_2 sorption at high pressures

A gas sorption isotherm with CO_2 was measured on the IGA at 25 °C (Figure 40). The ~57 Å^3 discrete cavities of the apohost are gradually filled to 74% occupancy at 20 bar CO_2 pressure.

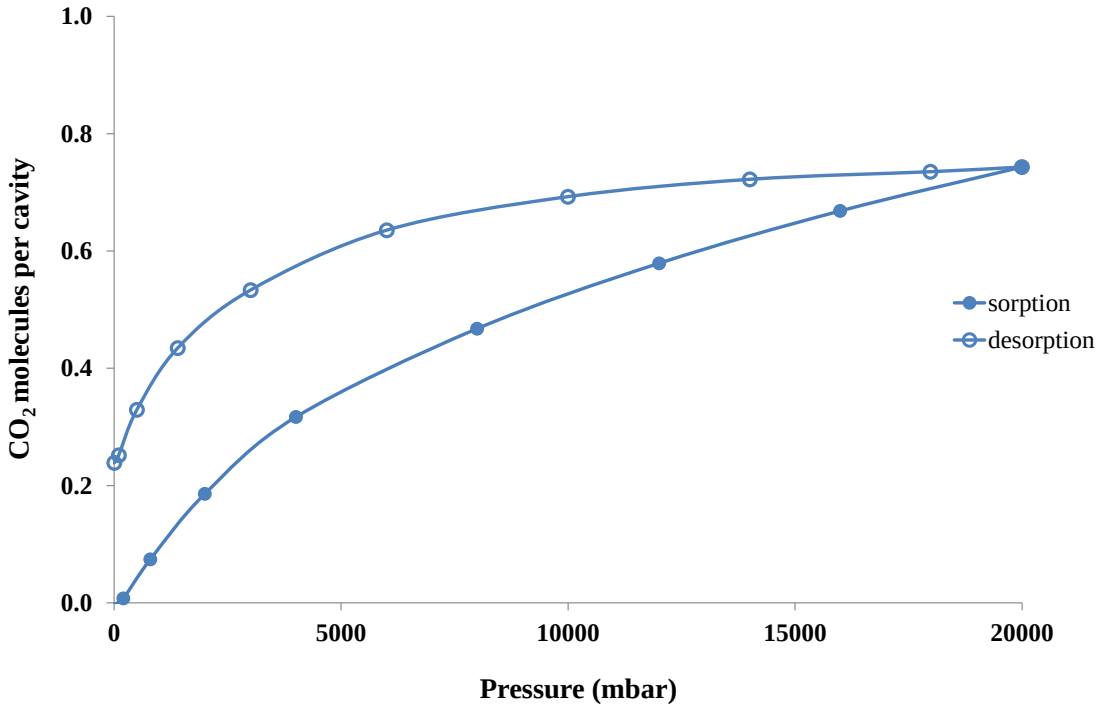

Figure 40. The CO_2 sorption isotherm of **IMMOF-2$_{apohost}$** measured at 25 °C on the IGA.

The sorption isotherm does not plateau completely, which might indicate that further sorption is possible at higher pressures. There is large amount of hysteresis in the desorption of CO_2, most likely owing to the confinement of the gas in discrete pockets by favourable interactions with the benzimidazole groups of the framework ligands.

IMMOF-2 has an expandable void space owing to its 2D structure with layers that can move closer or further apart. It is, therefore, possible that the framework might expand at high gas pressures to include more guest molecules. HPDSC measurements were carried out with a 35 mg

sample using a Setaram μDSC7 Evo module equipped with a high pressure sample holder (described in section 2.10). The HPDSC trace has an exothermic event at ~3 bar CO_2 pressure as well as a large exothermic event that starts at a pressure of 25 bar and reaches a maximum at 32 bar pressure (Figure 41). The first event is believed to signify the sorption of CO_2 to a maximum occupancy of ~0.74 to 1 CO_2 per void, while the second exothermic event with a much larger peak area represents a structural change and gate-opening pressure for the sorption of additional CO_2 molecules. An SCD structure was determined with a single crystal under 32 bar CO_2 pressure, revealing that the CO_2 occupancy had doubled from the original occupancy at lower pressure (more details to follow). Upon desorption, there is an endotherm apparent between 15 and 12 bar pressure, which suggests that the additional CO_2 molecules are retained for a large pressure range (from 36 to 15 bar).

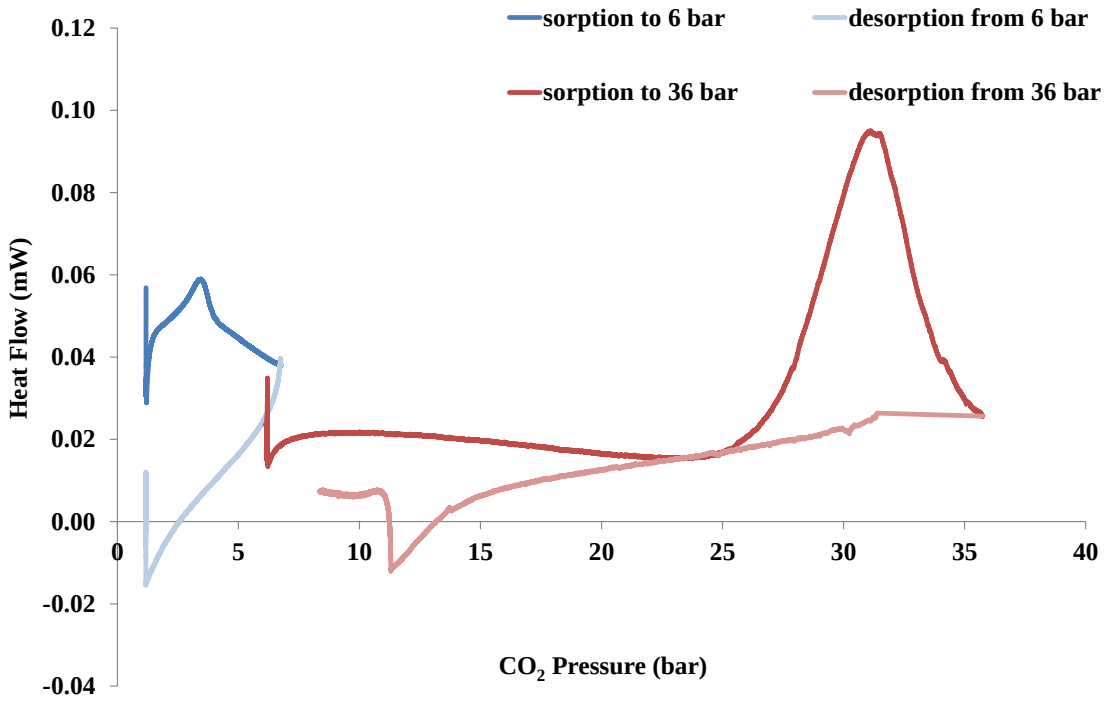

Figure 41. HPDSC trace of **IMMOF-2$_{apohost}$** with CO_2 measured at 25 °C.

The HPDSC measurements were repeated at the same temperature (25 °C) with nitrogen (N_2) and methane (CH_4), Figure 42 and Figure 43. It is probable that the phase transformation might occur at higher pressures for N_2 and CH_4, therefore, the pressure was increased to 60 bar N_2 and 54 bar CH_4 respectively. Three separate runs were carried out with each gas, owing to the fact that each run needs to start with a non-zero pressure and the initial pressure determines the pressure range and maximum pressure that the syringe pump can generate. Neither trace shows exothermic events corresponding to sorption or structural changes.

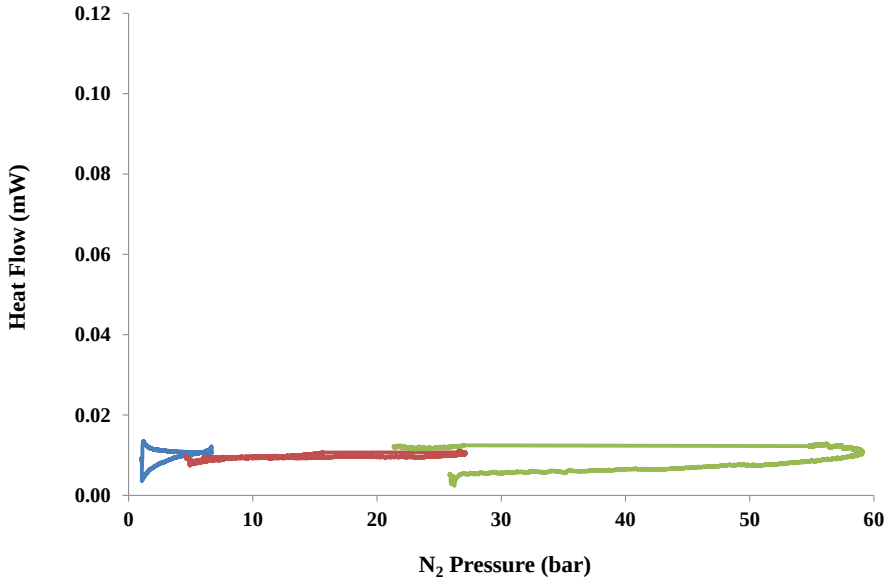

Figure 42. HPDSC trace of **IMMOF-2$_{apohost}$** with N_2 from 1 to 6 bar (blue) and 6 to 26 bar (red) and 26 to 60 bar (green) measured at 25 °C. For the purpose of comparison, the scale for the y-axis is consistent with that of Figure 41.

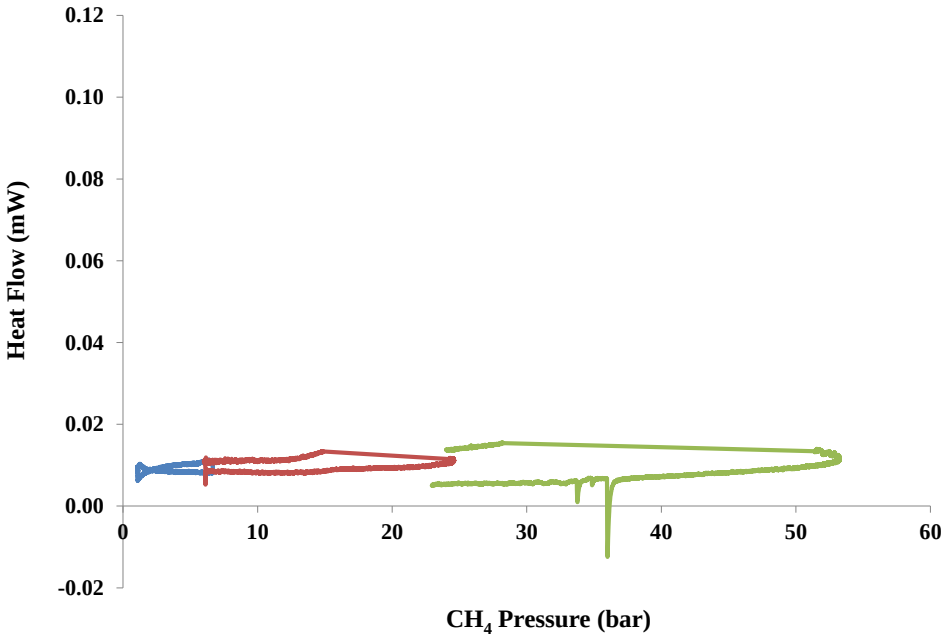

Figure 43. HPDSC trace of **IMMOF-2$_{apohost}$** with CH_4 from 1 to 6 bar (blue) and 6 to 26 bar (red) and 26 to 54 bar (green) measured at 25 °C. For the purpose of comparison, the same scale for the y-axis is consistent with that used in Figure 41.

PXRD patterns were measured with **IMMOF-2$_{apohost}$** sealed in a gas cell and the PXRD instrument in the capillary configuration (Figure 44). The PXRD patterns were measured with the powder under vacuum, 20 bar CO_2 pressure and 32 bar CO_2 pressure. At 20 bar CO_2 pressure, the pattern matches that simulated for the **IMMOF-2$_{sCO2}$** structure in which there is a

half of a CO_2 molecule per asymmetric unit (one CO_2 molecule per cavity). At 32 bar pressure there is indeed a structural change, as suggested by the HPDSC experiment.

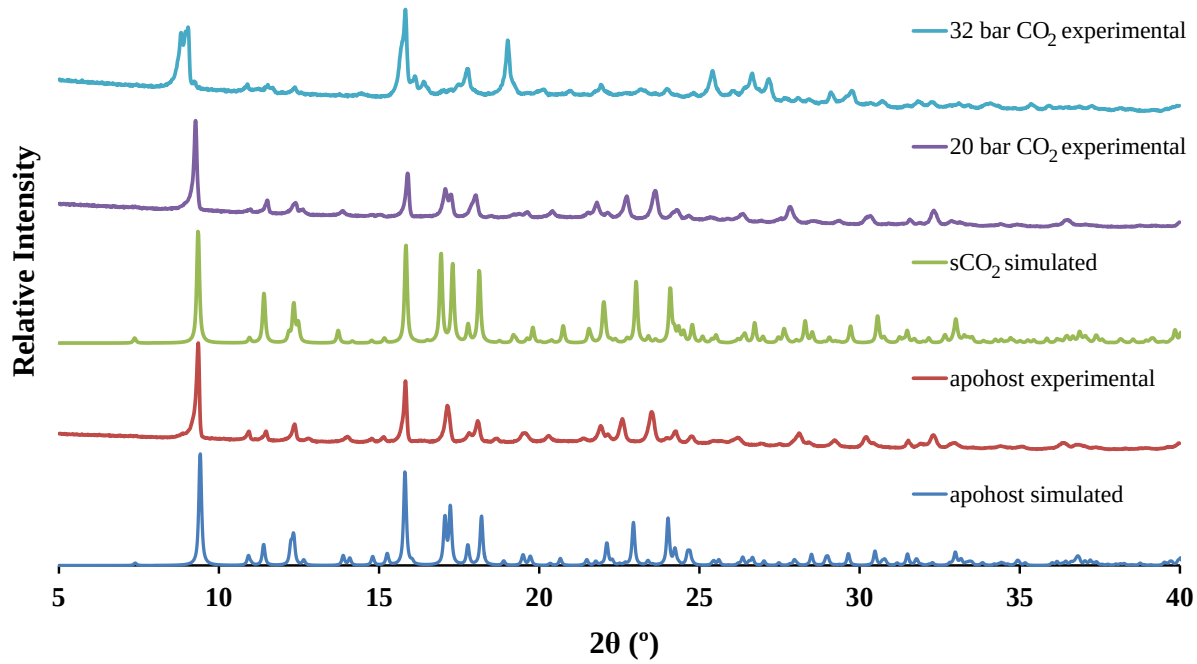

Figure 44. Simulated PXRD patterns of **IMMOF-2$_{apohost}$** and **IMMOF-2$_{sCO2}$** are compared with experimental PXRD patterns with the sample under vacuum and exposed to 20 and 32 bar CO_2 pressure.

The structure reverts back to the original phase when the CO_2 pressure is reduced to ambient pressure. However, there is still CO_2 entrapped in the void space when the pressure is reduced. A PXRD pattern measured at 20 bar CO_2 pressure has a characteristic double peak at $2\theta = 17.2°$, which serves as a confirmation of the presence of CO_2 in the cavities (Figure 45). From Figure 45, it is clear that, in the simulated PXRD pattern of **IMMOF-2$_{apohost}$**, the two peaks at $2\theta = 17.2°$ are closer together than in the simulated PXRD pattern of **IMMOF-2$_{sCO2}$**. The extent of peak splitting is related to the adjustment of the crystal structure to accommodate the CO_2 molecule. In the experimental PXRD pattern of the apohost framework the peak at 17.2° is single, given the resolution of the instrument. The CO_2 gas was exhausted from the gas cell and a PXRD pattern was collected at ambient conditions, exactly 1 hour and 20 minutes after the removal of the CO_2. The two peaks at $2\theta = 17.2°$ are still present, they are slightly less resolved, indicating that the framework stores the CO_2 for at least 1 hour and 20 minutes. In a second PXRD pattern that was measured 4 hours and 30 minutes after the removal of CO_2, the two peaks had merged into a single peak, signifying that the apohost framework was regenerated. It has thus been demonstrated that desorption of CO_2 occurs over a period of several hours.

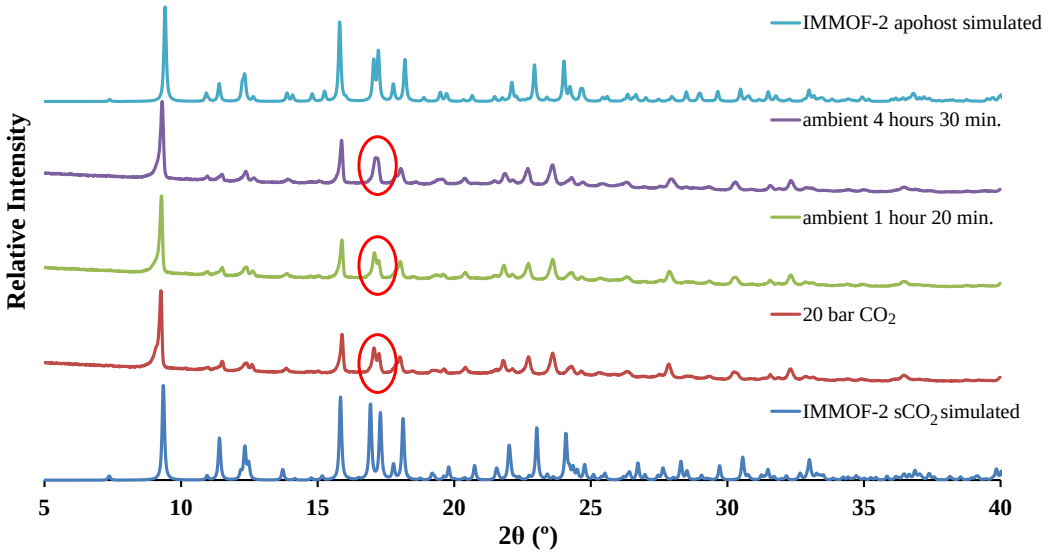

Figure 45. The experimental PXRD pattern of a sample of **IMMOF-2** exposed to 20 bar CO_2 pressure . Two more experimental PXRD patterns were measured on the same sample at different times following the removal of CO_2 pressure. The experimental PXRD patterns are compared to the simulated patterns of **IMMOF-2$_{sCO2}$** and **IMMOF-2$_{apohost}$**. The peaks of interest that serve as confirmation of CO_2 occupancy have been encircled (2θ = 17.2°).

As a control, PXRD diffractograms were also measured with **IMMOF-2$_{apohost}$** under 60 bar N_2 and 60 bar CH_4 pressure and no change in the pattern was observed (Figure 46). It can be concluded that the uptake of gas and the concurrent structural change occurs selectively with CO_2 at 25 °C and within the pressure ranges that were tested.

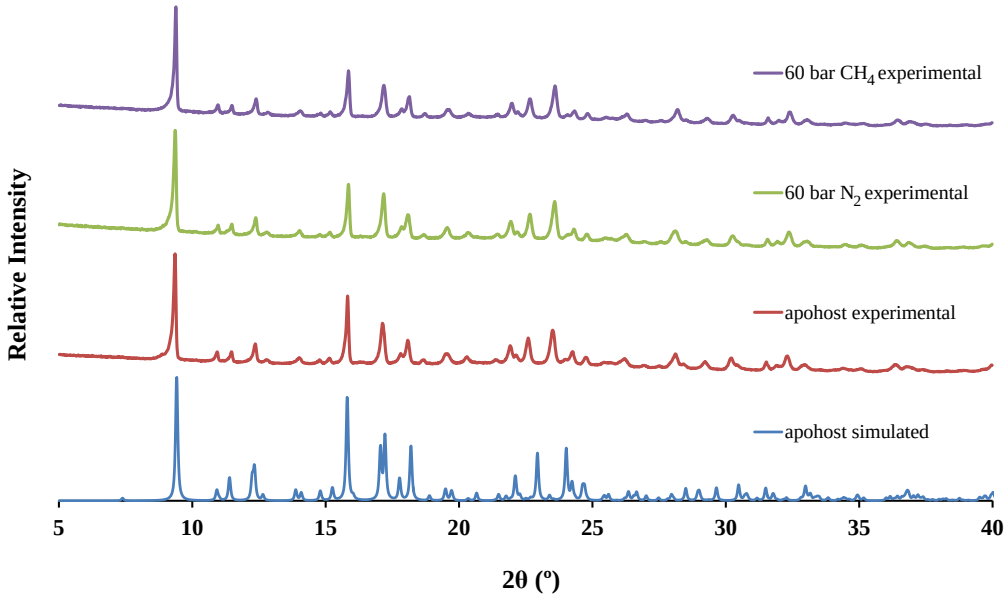

Figure 46. The experimental PXRD patterns of **IMMOF-2$_{apohost}$** under 60 bar N_2 and CH_4 pressures are the same as the experimental apohost pattern.

An environmental gas cell (see section 2.5) was used to collect single crystal X-ray data with a crystal under a specific gas pressure. A single crystal of **IMMOF-2$_{apohost}$** was mounted in the

gas cell and structural studies of the gate-opening mechanism at 32 bar CO_2 pressure attempted. The single crystal quality is reduced due to the structural transformation; nevertheless a structure of a gas inclusion complex at 32 bar CO_2 pressure (**IMMOF-2$_{32barCO2}$**) could be determined from the SCD data. The SCD data yielded a model with a large *R*-factor$_{all}$ of 0.17. The large R-factor is due to a twinning problem (evident from the reciprocal lattice) associated with an incomplete phase conversion in the single crystal. All attempts at obtaining SCD data from a crystal that was not twinned were unsuccessful. At high pressure, the structure transforms from the space group $P2_1/n$ to $P2/c$. Despite of the large *R*-factor, the restrained goodness of fit is satisfactory (*GooF* = 1.10) and the model still provides a significant level of information with regard to the structural transformation, the occupancy and location of the CO_2 molecules. The electron density peaks with approximately the correct bond distances for a CO_2 molecule aided in the credible modelling of the CO_2 position.

At 32 bar CO_2 pressure the 2D layers of the framework are displaced such that there are two voids of ~81 Å^3 each containing a CO_2 molecule, instead of one void of 60 Å^3 at a lower pressure (Figure 47).

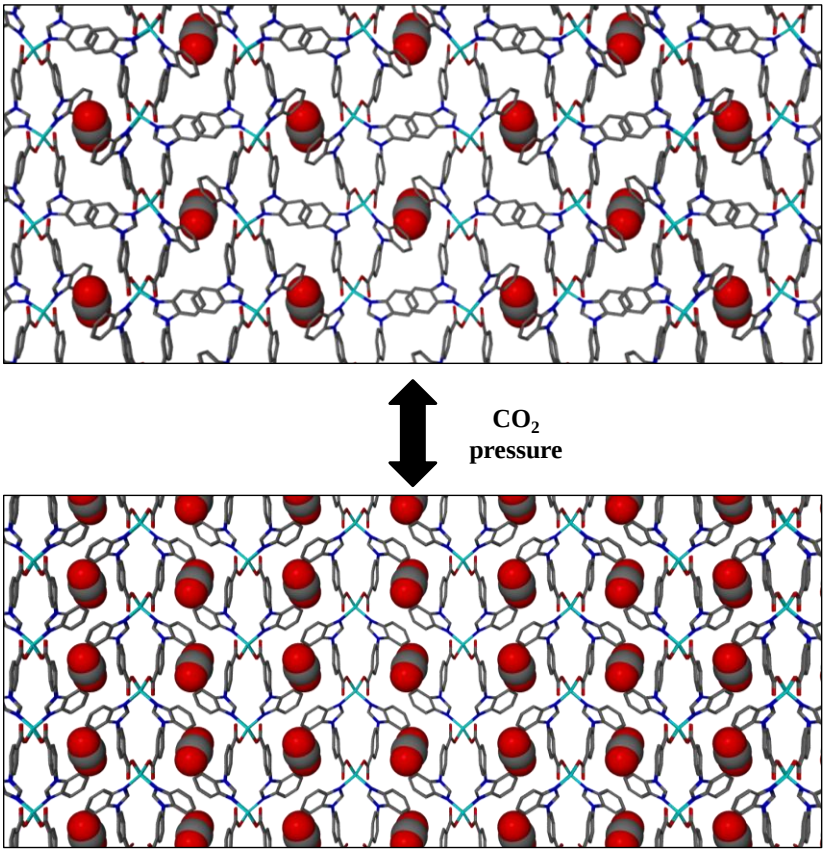

Figure 47. A comparison of the **IMMOF-2** framework at two different CO_2 pressures of 20 (top image) and 32 (bottom image) bar, respectively. The framework is viewed along [100] and the guest CO_2 molecules are shown in space-filled representation. Hydrogen atoms have been omitted for clarity. The framework can expand to double the CO_2 occupancy at ~32 bar pressure.

In effect, the void/total volume (%) increased from 5.3% to 12.5%. The occupancy of the framework doubles, so that it contains 8.2 wt% of CO_2 in comparison to the original 4.1 wt% at lower pressure. The CO_2 molecules are located in discrete cavities, confined by the benzimidazole moieties of two adjacent 2D layers (Figure 48).

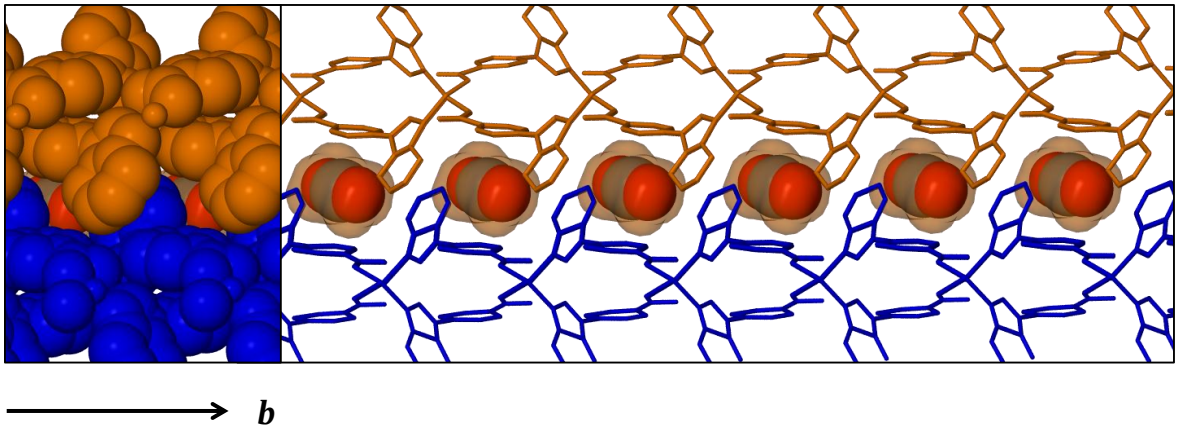

Figure 48. A view of the discrete cavities that extend along [010] of **IMMOF-2$_{32barCO2}$**. The ~80 Å of solvent-accessible space, mapped with MSROLL[39] (probe radius 1.4 Å), is shown as a semi-transparent orange surface and the adjacent 2D layers are shown in orange and blue. Hydrogen atoms have been omitted for clarity.

There are short contacts between the benzimidazole moiety and the CO_2 molecule (C···O distance = 3.36(3) Å); i.e. weak hydrogen bonds between the slightly negatively charged oxygen atom of the CO_2 and the benzimidazole protons (Figure 49a). The ligand benzene rings of two adjacent 2D sheets form a π-π interaction with the π system of the CO_2 molecule (C···centroid distance = 3.54(4) Å, Figure 49b).

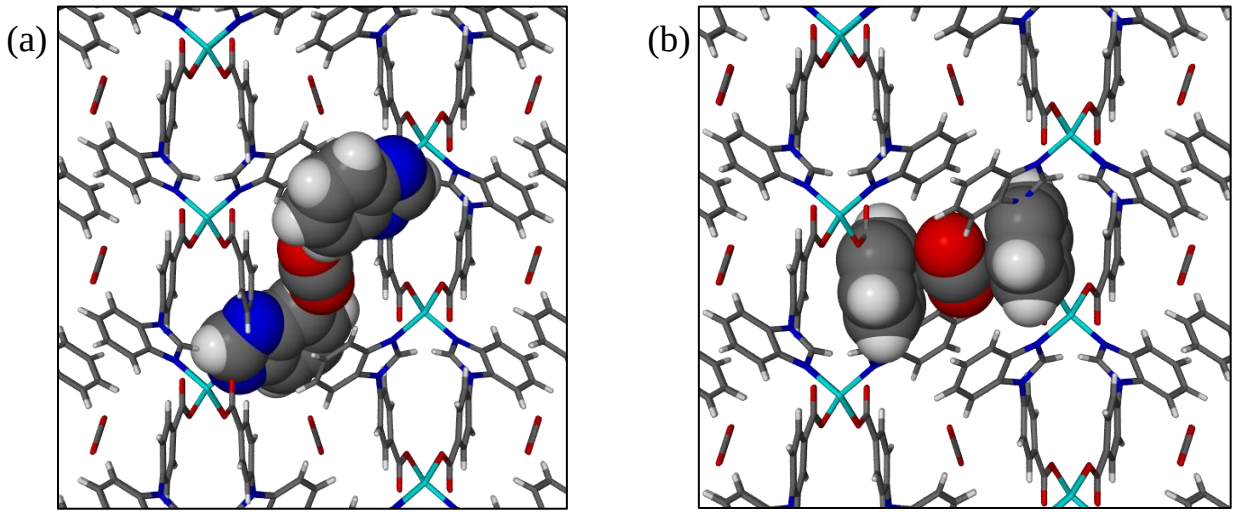

Figure 49. The confinement of CO_2 in discrete cavities occurs by close contacts with (a) the benzimidazole groups and (b) π-π interactions with the benezene rings of the ligands in adjacent 2D layers.

The structural transformation from the low pressure phase (**IMMOF-2$_{sCO2}$**) to the high pressure phase (**IMMOF-2$_{32barCO2}$**) occurs with an increase in the distance between successive layers denoted by an increase in the length of the *c* axis by 1.21(2) Å and the interatomic Zn···Zn separation between layers by 1.69(1) Å. The unit cell parameters and Zn···Zn distances of the apohost and the low and high pressure structures are summarised in Table 9. There is also a lateral shift in the positions of the layers relative to one another. The framework expands by a significant amount during the single-crystal to single-crystal transformation (Figure 50).

Table 9. Selected structural information for **IMMOF-2$_{apohost}$, IMMOF-2$_{sCO2}$ and IMMOF-2$_{32\ bar\ CO2}$.**

Structure	Space group	Unit cell parameters				Unit cell volume (Å^3)	Void volume (Å^3)	Zn···Zn distance * (Å)
		a (Å)	*b* (Å)	*c** (Å)	*β* (°)			
IMMOF-2$_{apohost}$	$P2_1/n$	8.327(2)	15.520(3)	19.158(4)	101.455(3)	2426.5(8)	57	8.946(2)
IMMOF-2$_{sCO2}$	$P2_1/n$	8.346(2)	15.505(3)	19.208(4)	100.174(3)	2446.6(9)	65	9.082(2)
IMMOF-2$_{32barCO2}$	$P2/c$	8.458(9)	7.734(9)	20.42(2)	104.41(1)	1294(2)	81	10.78(1)

*The Zn···Zn distance between adjacent 2D layers is reported. The successive 2D layers are stacked along the *c* axis, therefore there is a correlation between the increase in the *c*-axis length and the increase in the distance between the Zn atoms of adjacent layers.

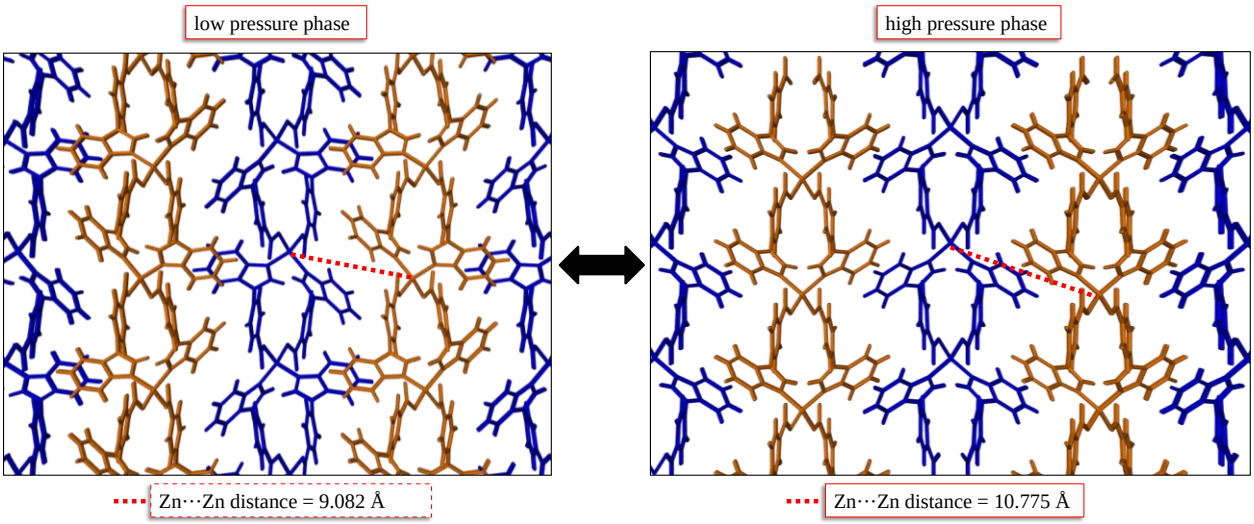

Figure 50. The expansion and contraction of **IMMOF-2** along [001] when it reversibly interconverts between the high and low pressure phases is shown. The successive 2D layers of the framework are shown in blue and orange and the interatomic Zn···Zn separation is represented as a dashed red line.

To support the credibility of the SCD structure, a PXRD pattern was simulated from the SCD model. The experimental PXRD pattern of the high pressure phase measured at 32 bar CO_2 pressure agrees well with the PXRD pattern simulated from the SCD model (Figure 51).

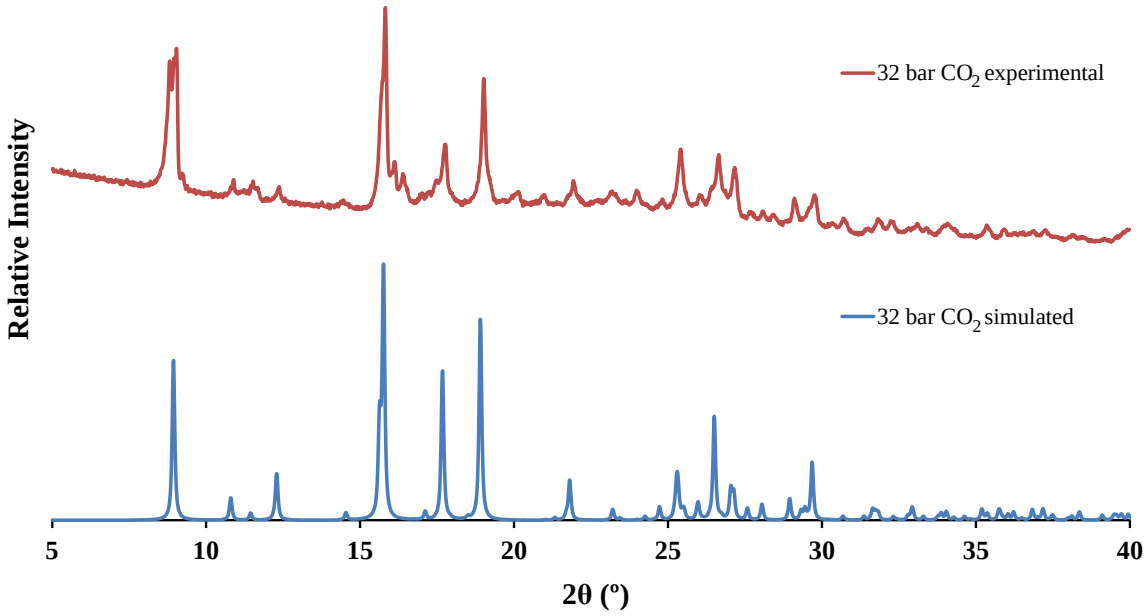

Figure 51. The PXRD pattern of **IMMOF-2** simulated from the SCD structure collected with the crystal exposed to 32 bar CO_2 pressure corresponds well with the experimental pattern that was measured with a bulk sample under 32 bar pressure.

After data collection at 32 bar pressure, the pressure in the gas cell was incrementally decreased and SCD structures were collected at variable pressures.

3.6.3 Structural study of CO_2 desorption by SCD methods

The CO_2 sorption isotherm of **IMMOF-2** measured on the IGA showed considerable hysteresis during desorption, alluding to a very high affinity for CO_2. The question arises whether the affinity for the additional CO_2 is sustained at high pressures. In the HPDSC trace (Figure 41) there is an endotherm during desorption in the 10 to 15 bar pressure range, which is believed to signify the phase transformation from double CO_2 occupancy to single occupancy. SCD structures were collected with a single crystal exposed to an initial gas pressure of 32 bar, which was decreased to 20, 10 and finally 0 bar. A minimum equilibration time of 12 hours was allowed between successive datasets. The objective was to determine over what pressure range the high pressure phase, **IMMOF-2$_{32barCO2}$**, exists as well as to follow the desorption process structurally. The structure remains approximately consistent from 32 to 10 bar. A summary of selected crystallographic information pertaining to the SCD structures measured at variable pressures is shown in Table 10. The unit cell parameters of the structures determined from data collected at 32, 20 and 10 bar are comparable and the space group, *P*2/*c*, is maintained. The electron count calculated using SQUEEZE regime remains approximately constant (19/22/18

electrons per void). As was the case with the structure collected at 32 bar, the data obtained at 20 and 10 bar were also twinned, resulting in SCD models with large *R*-factors.

Table 10. Selected structural information for **IMMOF-2$_{32barCO2}$** after a stepwise decrease in pressure.

Structure	Space group	Unit cell parameters				Unit cell volume (Å^3)	Void volume (SQUEEZE[36,37])	Electron count per void (SQUEEZE[36,37])
		a **(Å)**	***b*** **(Å)**	***c*** **(Å)**	***β*** **(°)**			
32 bar CO_2	*P*2/*c*	8.458(9)	7.734(9)	20.42(2)	104.41(1)	1294(2)	81	19
20 bar CO_2	*P*2/*c*	8.42(1)	7.70(1)	20.33(3)	104.63(1)	1274(3)	74	21
10 bar CO_2	*P*2/*c*	8.443(5)	7.723(5)	20.36(1)	104.308(8)	1286.4(2)	75	18
0 bar	$P2_1/c$	8.302(3)	15.488(5)	19.464(7)	102.191(4)	2446(1)	60	9

It appears that the transformation to the high pressure phase is only reversed once the pressure is reduced to less than 10 bar. The reversion occurs as a single-crystal to single-crystal transformation and the double reflections caused by twinning at 32 bar once again become single reflections. The structural change and its concomitant effect on the crystal's reciprocal lattice are thus reversible. The structure determined at 0 bar, is similar to that of **IMMOF-2$_{sCO2}$**, implying that the CO_2 occupancy in the crystal is halved. The CO_2 molecules are now located in 60 Å^3 void spaces. The CO_2 molecule was modelled with 40% occupancy per cavity, which is in agreement with the SQUEEZE electron count, which averages to 9 electrons per cavity. The sorption isotherm measured on the IGA also suggests that at 0 bar approximately 30% of the void volume still includes CO_2.

It has been demonstrated that **IMMOF-2** is an example of a soft porous material that can transform its structure and gas sorption capacity with the application of high pressure as the stimulus. **IMMOF-2** is transiently porous, i.e. it has discrete voids and no channels, yet gas is able to diffuse into and out of the framework. The diffusion of CO_2 out of the framework is less favoured, as indicated by the hysteresis in the sorption isotherm as well as the fact that the high pressure phase is maintained for a large pressure range (from 32 to 10 bar CO_2 pressure). **IMMOF-2** is selective for CO_2, relative to N_2 and CH_4, and it displays an extraordinary affinity for the molecule. This study shows that transformable and dynamic 2D MOFs can be applied for CO_2 sorption and storage purposes regardless of whether or not the MOF is permanently porous.

3.7 SUMMARY AND CONCLUSIONS

A number of MOFs were prepared from the solvothermal reactions of **L1** to **L7** with transition metal salts. Of the various MOFs that were prepared, only three were studied further owing to their ability to undergo single-crystal to single-crystal transformations. The two MOFs prepared with **L6** are 2D and transformable, resulting in unique sorption properties. The third MOF synthesised with **L7**, which is 3D and permanently porous, is described in detail in the following chapter. The SCD data after transformations yielded an abundance of structural information about the solid-state dynamics of the MOFs.

IMMOF-1 and **IMMOF-2**, incorporating **L6**, are 2D MOFs that have layers that can undergo mutual displacement to increase or decrease the solvent-accessible space. Both are examples of third generation MOFs or soft porous materials. **IMMOF-2** originally includes DMF and water, which can be exchanged for CO_2, or the DMF can be removed to yield the hydrate. When the DMF situated in between the 2D layers is removed, the layers move closer together with a concomitant shrinkage in the unit cell volume by 300 $Å^3$ (CO_2) or 317 $Å^3$ (H_2O). After the transformation, both the CO_2 and H_2O inclusion complexes have small discrete cavities between the 2D layers instead of continuous 1D channels between the layers, as in **IMMOF-2$_{DMF,water}$**. The CO_2 is retained for approximately three days in a large single crystal or several hours in polycrystalline material. When **IMMOF-2$_{apohost}$** is exposed to CO_2, one molecule per 57 $Å^3$ cavity is absorbed between 0 - 20 bar pressure. The CO_2 occupancy is doubled at 32 bar pressure with a simultaneous phase transformation to a more "open" phase that now has two discrete cavities instead of one in an equivalent amount of framework volume. The open phase is once again formed by the displacement of the 2D layers. **IMMOF-2** is selective for CO_2 uptake and has different CO_2 sorption capacities depending on the pressure to which it is exposed. **IMMOF-2** has dynamic and transformable porosity.

3.8 EXPERIMENTAL SECTION

3.8.1 Synthesis of L6

All chemicals used in these experiments were purchased from Merck or Aldrich. Thin layer chromatography (TLC) was carried out on aluminium-backed Merck silica gel 60 F_{254} plates. Visualisation was with a UV lamp or iodine. All ^{1}H and ^{13}C nuclear magnetic resonance spectra were obtained using a 300 MHz Varian VNMRS (75 MHz for ^{13}C) or a 400 MHz Varian Unity Inova (100 MHz for ^{13}C) using *d*-chloroform as the solvent. Chemical shifts (δ) were recorded using the residual solvent signal as reference. All chemical shifts are reported in ppm and all spectra were obtained at 25 °C. The NMR spectra are included in Appendix A. Melting points were obtained using a Gallenkamp Melting Point Apparatus and are uncorrected. Infrared spectra were obtained using a Nexus Thermo-Nicolet FT-IR using an ATR Golden Gate attachment. High resolution mass spectrometry was carried out by the Central Analytical Facility at Stellenbosch University using a Waters API Q-TOF Ultima spectrometer.

The two steps of the procedure are summarised in Scheme 4.

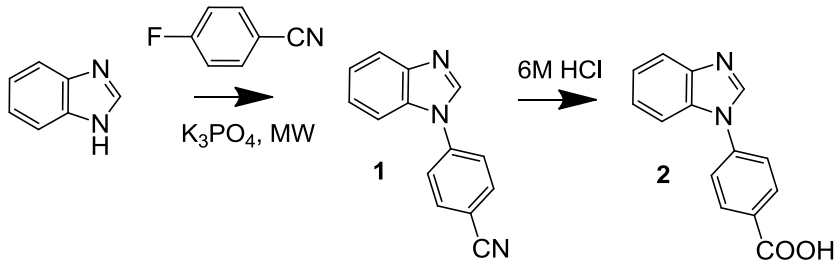

Scheme 4. The synthesis of 4-(1*H*-benzo[d]imidazole-1-yl)benzoic acid.

4-(1*H*-benzo[d]imidazole-1-yl)benzonitrile – (**1**)

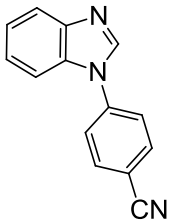

Benzimidazole (353 mg, 2.99 mmol, 1 eq), 4-fluorobenzonitrile (362 mg, 2.99 mmol, 1 eq), K_3PO_4 (1587 mg, 7.48 mmol, 2.5 eq) and dry DMF (13 ml) were added to a microwave reaction vessel (20 ml). The flask was sealed and heated under microwave radiation for 30 minutes at 160°C, following which the solvent was removed under reduced pressure. Further purification was not carried out and the crude mixture was used in the following reaction.

4-(1*H*-benzo[d]imidazole-1-yl)benzoic acid – (**2**)

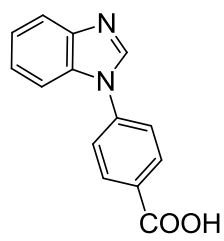

Crude reaction mixture **1** (presumed 2.99 mmol), concentrated HCl (100 ml) and H_2O (50 ml) were added to a round-bottom flask (250 ml) and the mixture was heated to reflux overnight. The flask was cooled to room temperature, the white solid was removed by filtration, suspended in H_2O (50 ml) and the pH of the mixture adjusted to 7 using $NaHCO_3$. After stirring for 30 minutes the resulting white solid was collected via filtration, washed with water and dried under reduced pressure, yielding a white powder (478 mg, 2.01 mmol, 67% yield from benzimidazole).

R_f: 0.31 (MeOH/DCM: 1/9).

MP: 244 °C.

IR υ_{max} (ATR)/cm^{-1}: 2455, 1698, 1605, 1519, 1456, 1290, 1175, 732.

^{1}H NMR (HCl salt) (400 MHz, DMSO-d_6) δ ppm 8.66 (s, 1 H, N=C*H*-N), 8.16 (dt, *J*=8.8, 2.0 Hz, 2 H, Ar*H*), 7.85 (dt, *J*=8.8, 2.0 Hz, 2 H, Ar*H*), 7.71 – 7.82 (m, 2 H, $Ar_{Benzimid}H$), 7.30 - 7.40 (m, 2 H, $Ar_{Benzimid}H$).

^{13}C NMR (75MHz, DMSO-d_6): δ ppm 166.60, 144.01, 143.21, 139.59, 132.61, 131,23, 129.57, 123.83, 123.18, 122.88, 120.13, 110.94.

3.8.2 Crystallographic tables

	IMMOF-1	**IMMOF-1$_{MeOH,water}$**	**IMMOF-2**	**IMMOF-2$_{water}$**
Empirical formula	$C_{34}H_{40}CuN_6O_{10}$	$C_{31}H_{31}CuN_4O_{10}$	$C_{62}H_{52}N_{10}O_{11}Zn_2$	$C_{28}H_{18}N_4O_5Zn$
Formula weight	378.13	341.57	1243.88	555.83
Temperature/K	100(2)	100(2)	100(2)	100(2)
Wavelength/Å	0.71073	0.71073	0.71073	0.71073
Crystal system	monoclinic	monoclinic	monoclinic	monoclinic
Space group	$P2_1/n$	$P2_1/n$	$P2/n$	$P2_1/n$
a /Å	9.9316(9)	9.677(19)	16.8047(11)	8.2576(16)
b /Å	16.4081(15)	16.18(3)	7.7867(5)	15.751(3)
c /Å	11.3246(10)	10.94(2)	22.0350(15)	19.109(4)
α /°	90.00	90.00	90.00	90.00
β /°	106.5050(10)	112.574(15)	107.8310(10)	102.336(4)
γ /°	90.00	90.00	90.00	90.00
Volume/Å^3	1769.4(3)	1582(5)	2744.8(3)	2427.9(8)
Z	2	2	2	4
Calculated density/g cm^{-3}	1.419	1.434	1.505	1.521
Absorption coefficient (mm^{-1})	0.683	0.753	0.949	1.060
F_{000}	790	708	1284	1136
Reflections collected	10050	3551	28384	2223
Independent reflections	3804 [R_{int} = 0.0341]	2530 [R_{int} = 0.0159]	5601 [R_{int} = 0.0225]	1803 [R_{int} = 0.0272]
Data/restraints/parameters	3804 / 4 / 222	2530 / 7 / 220	5601 / 13 / 423	1803 / 0 / 339
Goodness-of-fit on F^2	1.041	1.047	1.077	0.990
Final R indices [$I>2\sigma(I)$]	$R1$ = 0.0419, $wR2$ = 0.1123	$R1$ = 0.0599, $wR2$ = 0.1506	$R1$ = 0.0305, $wR2$ = 0.0703	$R1$ = 0.0436, $wR2$ = 0.1005
R indices (all data)	$R1$ = 0.0539, $wR2$ = 0.1211	$R1$ = 0.0719, $wR2$ = 0.1600	$R1$ = 0.0342, $wR2$ = 0.0721	$R1$ = 0.0583, $wR2$ = 0.1106

	IMMOF-2$_{sCO2}$	**IMMOF-2$_{apohost}$**	**IMMOF-2$_{CO2_32bar}$**	**IMMOF-2$_{CO2_20bar}$**
Empirical formula	$C_{57}H_{36}N_8O_{10}Zn_2$	$C_{28}H_{18}N_4O_4Zn$	$C_{29}H_{18}N_4O_6Zn$	$C_{29}H_{18}N_4O_6Zn$
Formula weight	1123.68	539.83	583.84	583.84
Temperature/K	100(2)	100(2)	295(2)	295(2)
Wavelength/Å	0.71073	0.71073	0.71073	0.71073
Crystal system	monoclinic	monoclinic	monoclinic	monoclinic
Space group	$P2_1/n$	$P2_1/n$	$P2/c$	$P2/c$
a /Å	8.3463(17)	8.3268(15)	8.458(9)	8.415(11)
b /Å	15.505(3)	15.520(3)	7.734(9)	7.695(10)
c /Å	19.208(4)	19.158(4)	20.42(2)	20.33(3)
α /°	90.00	90.00	90.00	90.00
β /°	100.174(3)	101.455(3)	104.405(12)	104.632(14)
γ /°	90.00	90.00	90.00	90.00
Volume/Å^3	2446.6(9)	2426.5(8)	1294(2)	1274(3)
Z	2	4	2	2
Calculated density/g cm^{-3}	1.525	1.478	1.499	1.522
Absorption coefficient (mm^{-1})	1.053	1.055	1.002	1.017
F_{000}	1148	1104	596	596
Reflections collected	5373	4835	3831	3059
Independent reflections	3622 [R_{int} = 0.0265]	3421 [R_{int} = 0.0180]	2018 [R_{int} = 0.0417]	1877 [R_{int} = 0.0487]
Data/restraints/parameters	3622 / 0 / 349	3421 / 0 / 334	2018 / 0 / 184	1877 / 0 / 173
Goodness-of-fit on F^2	1.067	1.198	1.156	1.128
Final R indices [$I>2\sigma(I)$]	$R1$ = 0.0452, $wR2$ = 0.0988	$R1$ = 0.0507, $wR2$ = 0.1168	$R1$ = 0.1323, $wR2$ = 0.3196	$R1$ = 0.1451, $wR2$ = 0.3768
R indices (all data)	$R1$ = 0.0656, $wR2$ = 0.1069	$R1$ = 0.0576, $wR2$ = 0.1197	$R1$ = 0.1751, $wR2$ = 0.3518	$R1$ = 0.1791, $wR2$ = 0.4021

	IMMOF-2$_{CO2_10bar}$	**IMMOF-2$_{CO2_0bar}$**
Empirical formula	$C_{29}H_{18}N_4O_6Zn$	$C_{28.20}H_{18}N_4O_{4.40}Zn$
Formula weight	583.84	548.66
Temperature/K	295(2)	295(2)
Wavelength/Å	0.71073	0.71073
Crystal system	monoclinic	monoclinic
Space group	*P*2/*c*	*P*2$_1$/*c*
a /Å	8.443(5)	8.302(3)
b /Å	7.723(5)	15.488(5)
c /Å	20.358(14)	19.464(7)
α /°	90.00	90.00
β /°	104.308(8)	102.191(4)
γ /°	90.00	90.00
Volume/Å^3	1286.4(15)	2446.4(13)
Z	2	4
Calculated density/g cm^{-3}	1.507	1.490
Absorption coefficient (mm^{-1})	1.007	1.049
F_{000}	596	1122
Reflections collected	6254	17204
Independent reflections	2351 [R_{int} = 0.0598]	4824 [R_{int} = 0.0510]
Data/restraints/parameters	2351 / 0 / 184	4824 / 1 / 339
Goodness-of-fit on F^2	1.113	1.178
Final *R* indices [$I>2\sigma(I)$]	*R*1 = 0.1187, *wR*2 = 0.2975	*R*1 = 0.0802, *wR*2 = 0.1912
R indices (all data)	*R*1 = 0.1369, *wR*2 = 0.3105	*R*1 = 0.1062, *wR*2 = 0.2045

CHAPTER 4

METAL-ORGANIC FRAMEWORKS: PERMANENT POROSITY

MOFs with permanent porosity possess either one-, two- or three-dimensional channels that allow unhindered guest transport. Permanent porosity usually exists in second generation materials with rigid frameworks that retain their crystallinity when the guest is no longer included within the pores. A 3D MOF that is extremely robust and that possesses 1D channels was synthesised, using the organic ligand **L7**, described in the previous chapter. The MOF is capable of guest exchange as a series of single-crystal to single-crystal transformations and has interesting gas and vapour sorption properties. In addition, it was discovered that the MOF has very unique thermal expansion properties that can be altered by guest inclusion.

4.1 MOFS PREPARED WITH L7

L7 was designed to extend the work already carried out with **L6**. It was rationalised that the introduction of an extensive π-electron system using the aromatic naphtha(2,3-*d*)imidazolyl moiety of the ligand would result in framework assemblies consisting of the same type of layered 2D grid structure with transformable void spaces such as those obtained with **L6**. Another benzene ring was added to the ligand in order to engineer a larger transformable void space. The flexible or shape-responsive void could then expand or contract owing to sliding motions between superimposed sheets of ligands associated by weak π-π interactions only. Crystallisation of **L7** with copper and zinc nitrate salts resulted in 2D and 3D frameworks, respectively. The 2D Cu-containing MOF contains transformable void space. Partial desolvation was achieved as a single-crystal transformation with a significant change in the framework and unit cell dimensions owing to horizontal displacement of the alternating layers. However the Cu-containing MOF has similar properties to those of **IMMOF-2**, which is discussed in the previous section, and an in-depth study was not undertaken. Instead, the 3D framework, hereafter named **IMMOF-3**, synthesised from **L7** and $Zn(NO_3)_2$ proved to be extremely robust, retaining its porosity upon guest removal. The permanent porosity of **IMMOF-3** was thus studied in more detail.

$\{[Zn(L7)_2(OH)_2]\cdot CH_3OH\}_n$ or IMMOF-3

Synthesis

The reaction of **L7** with Zn(II) nitrate resulted in the formation of a 3D framework (Scheme 5). The framework crystallises in the space group $I\bar{4}$ (tetragonal crystal system). The as-synthesised framework includes methanol molecules within well-defined channels.

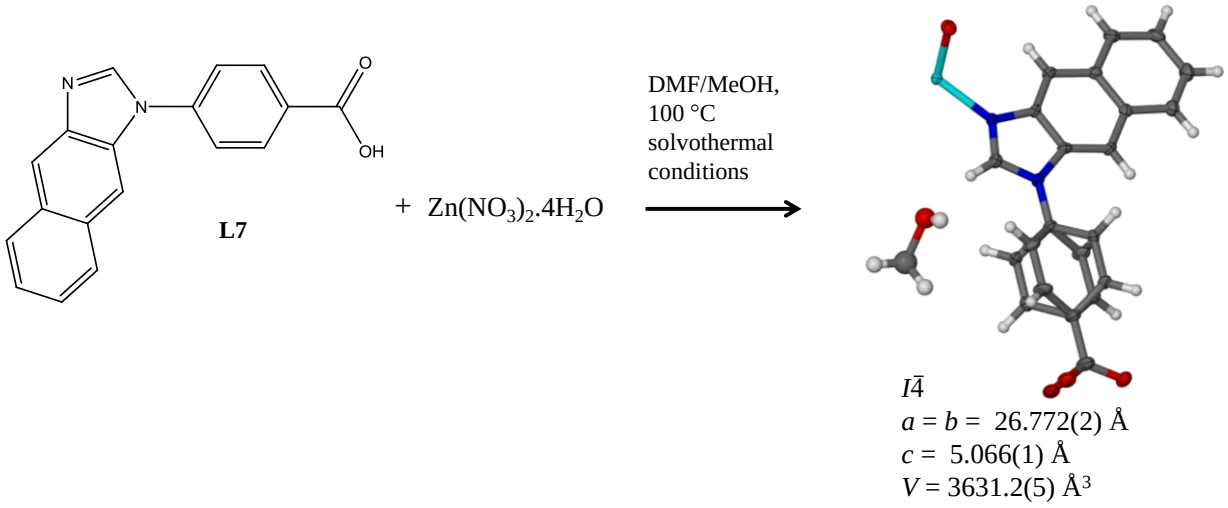

Scheme 5. The solvothermal synthesis of **IMMOF-3** from a combination of **L7** with $Zn(NO_3)_2$. The asymmetric unit (with thermal ellipsoids) of the resultant MOF is shown with hydrogen bonds represented as dashed red lines.

Metal Geometry

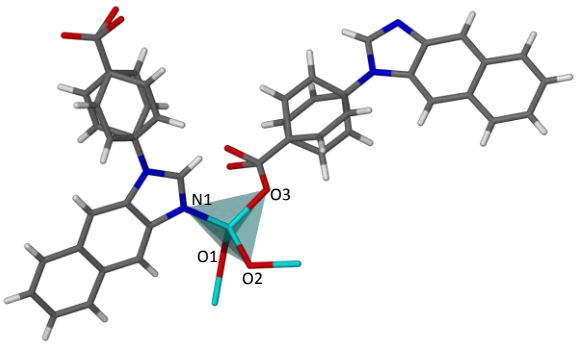

Figure 52. Tetrahedral metal geometry of **IMMOF-3**.

The Zn(II) metal has tetrahedral coordination geometry (Figure 52). Two ligands (**L7**) and two hydroxyl groups (anions) are coordinated to the metal. The hydroxyl groups interconnect the metal centres along the direction of the crystallographic *c* axis. The coordination environment comprises two hydroxyl oxygen atoms (bond lengths = 1.917(2) and 1.940(2) Å), an oxygen atom from the carboxyl moiety of one ligand (bond length = 1.976(2) Å) and a nitrogen atom

from an imidazolyl-moiety of a second ligand (bond length = 2.008(2) Å). The metal geometry is distorted from that of a perfect tetrahedron, with an O1-Zn-O2 angle of only 103.68(6)°. The distortion occurs as a result of hydrogen bonding interactions between coordinating groups, as described in the next section.

Framework interactions and topology

The 3D framework consists of grids/nets stacked on top of one another and interconnected by polymeric Zn-hydroxy-Zn coordination along the *c* axis. Successive hydroxyl oxygen atoms are separated by a distance of 3.033(9) Å and participate in weak hydrogen-bonding interactions along the $[Zn\text{-}OH\text{-}]_n$ chain (Figure 53). A carboxyl oxygen atom is coordinated to Zn and acts as a hydrogen bond acceptor to the coordinated hydroxyl groups (D···A distance = 2.81(1) Å).

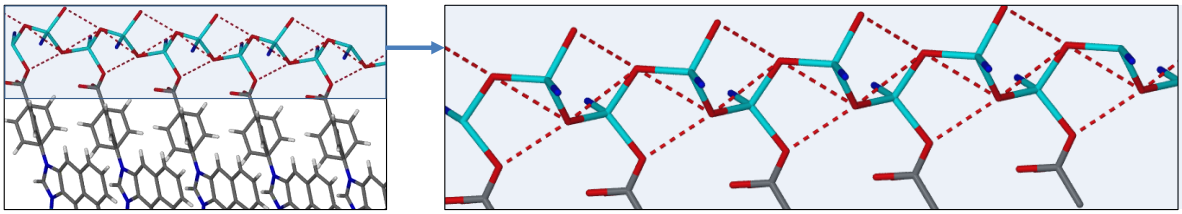

Figure 53. The $[Zn\text{-}OH\text{-}]_n$ chain along the crystallographic *c* axis of **IMMOF-3**. There are strong hydrogen bonds between coordinated carboxyl-oxygen atoms and the hydroxyl bridges, as well as weaker hydrogen bonding between successive hydroxyl bridges.

Soft π-π interactions are believed to play a role in the self-assembly of the MOF (Figure 54). There are parallel stacking interactions (centroid-centroid distance = 3.8(1) Å) as well as weak edge-to-face interactions (carbon-centroid distance = 4.4(1) Å) between the layers of aromatic naphtha(2,3-*d*)imidazolyl moieties superimposed on one another along the *c* axis.

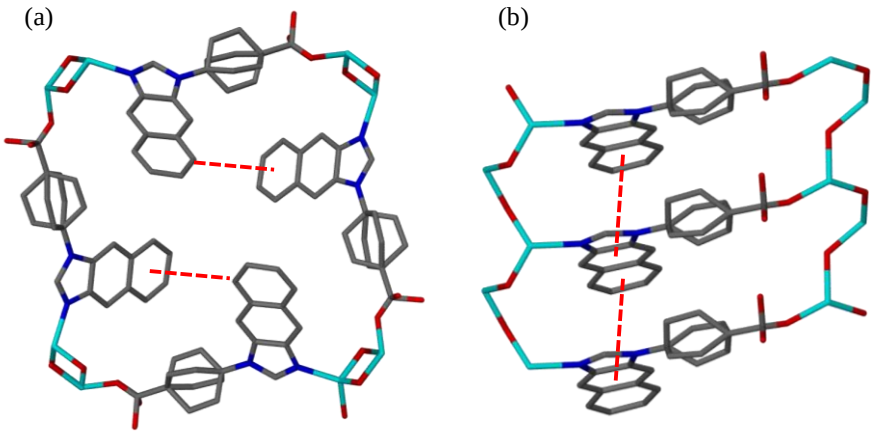

Figure 54. (a) Edge-to-face π-π interactions and (b) π-π stacking interactions between the ligands incorporated in **IMMOF-3**. Hydrogen atoms have been omitted for clarity.

Porosity

The structure has one-dimensional square-shaped channels (Figure 55 and Figure 56) with a cross-sectional width of approximately 6 Å. In the as-synthesised framework the channels contain methanol molecules, several of which hydrogen bond to the oxygen atoms of the carboxylate moieties of **L7**.

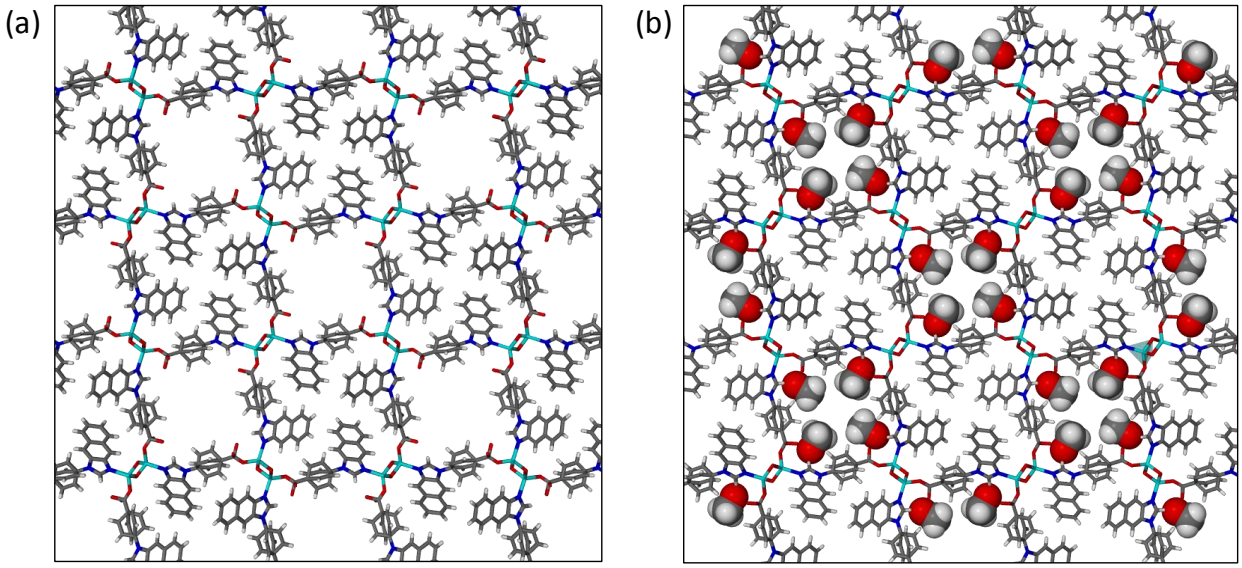

Figure 55. The **IMMOF-3** framework viewed along [001] with (a) solvent molecules omitted and (b) with the solvent methanol molecules shown.

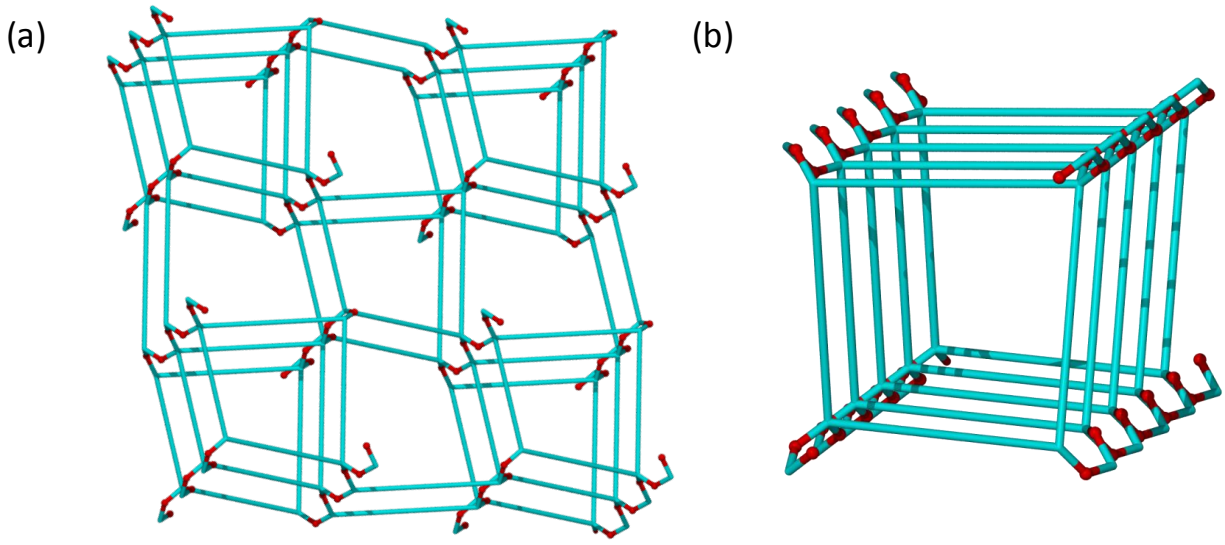

Figure 56. Topological representations of (a) the **IMMOF-3** framework and (b) one of the square-shaped channels. Blue lines represent the ligands that interconnect the metal centres. The hydroxyl oxygen atoms are shown in red.

Incommensurate guest inclusion

It is worth noting that it is not always possible to model all the guest molecules situated within the channels of **IMMOF-3**. The SQUEEZE electron count of 178 electrons per channel section with a volume of 297 $Å^3$ is indicative of a much higher guest occupancy than was modelled. Based on the solvent system used during the synthetic procedure, water and DMF may be included in addition to methanol. Only four methanol molecules that hydrogen bond to the framework were modelled. Initially it was thought that the positions of the remaining guest molecules are uncertain as a result of positional disorder. However, it was later determined that some of the guest molecules within the channels are positioned with a periodicity that is incommensurate with that of the framework. An oscillation frame (rotation of the *phi* axis of the SCD instrument) was recorded with the crystal mounted such that the direction of the channel (*c* axis) is parallel to the oscillation axis and perpendicular to the X-ray beam (Figure 57).

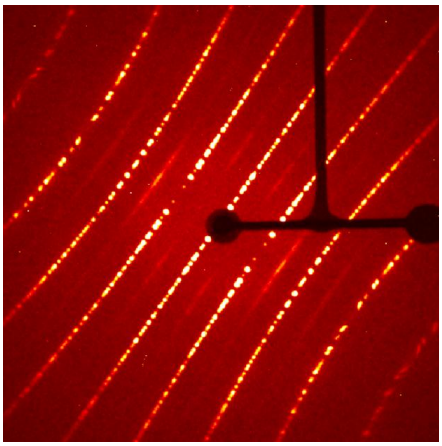

Figure 57. Phi-rotation (oscillation) frame recorded at 100 K.

The oscillation frame has lines of diffuse scattering between the layer lines of the host-dominated Bragg reflections. These are most likely due to the presence of a guest substructure; i.e. the guest molecules that are ordered in one dimension along the channel axis with a periodicity that is different from that of the host channel (Figure 58).

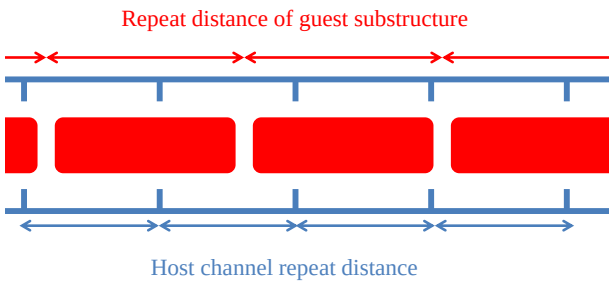

Figure 58. A schematic illustration of a host channel (blue) with a periodicity that is different to that of the guest molecules (red).

A modulated guest periodicity in channel compounds usually occurs in cases of very dense packing of the guest molecules resulting from strong guest-guest interactions. Methanol and water are capable of forming hydrogen bonded motifs (spirals or chains) along the length of the channel. These motifs may have a periodicity that does not match the repeat distance of the host channel itself (the *c* axis has a length of approximately 5.2 Å). Incommensurate inclusion is a well-studied occurrence amongst the family of urea channel compounds.[57] These materials comprise a urea channel host structure and a guest substructure (usually long alkane molecules) that is incommensurate along the channel direction, similar to that of **IMMOF-3**. Incommensurate compounds form part of a class of aperiodic crystals. Generally, aperiodic crystals are defined as materials that do not have three-dimensional translational symmetry. This feature distinguishes them from conventional crystals, giving them unique properties, including optical activity and birefringence.[57] A computational study carried out by Harris *et al.* has theoretically proven that a feature of incommensurate channel inclusion compounds is that diffusion of the guest molecules along the channels is, in principle, associated with no energy barrier, which is an important component for unidirectional guest exchange.[58] Indeed, **IMMOF-3** readily exchanges its original guest molecules for other guests, as will be demonstrated.

IMMOF-3 has 16.5% guest-accessible space based on the void volume (~600 $Å^3$) per unit cell (~3630 $Å^3$). The channels have an irregular shape with periodic undulations (Figure 59). There are bulges of solvent-accessible space near the carboxyl-groups where the guests form hydrogen bonding interactions with the channel walls.

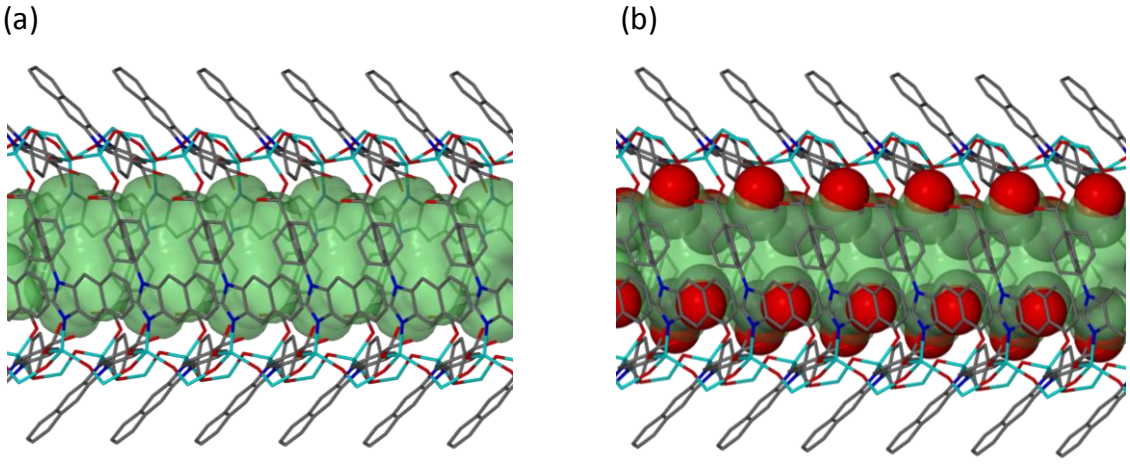

Figure 59. Perspective view of the channel of **IMMOF-3**; viewed perpendicular to [001]. (a) The solvent-accessible volume (Connolly surface mapped using MSROLL[39]) is shown in green (probe radius = 1.4 Å) and (b) the methanol guest molecules can be seen protruding through this surface owing to strong hydrogen bonding interactions with the framework. Hydrogen atoms have been omitted for clarity.

Disorder of the ligand

The disorder of the organic ligand is an important aspect of the **IMMOF-3** framework. The phenylene ring of the organic ligand is disordered over two positions, and the site occupancy factor (SOF) refines to ~50% for each position (Figure 60).

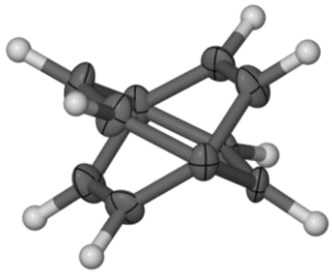

Figure 60. The disorder of the phenylene ring (thermal ellipsoids shown), which forms part of ligand **L7** in **IMMOF-3**.

At 100 K the small thermal ellipsoids of the carbon atoms imply that the disorder is static. At higher temperatures (more than 200 K) the thermal ellipsoids appear more enlarged than the rest of the ligand atoms, implying that the disorder becomes dynamic at elevated temperatures. The static disorder at 100 K is caused by the presence of two different conformations of the ligand. Since SCD methods only provide a model derived from the average unit cell for the whole crystal, the "real" positions of the atoms in any given unit cell are impossible to determine experimentally.

Computational study of the disorder of the phenylene ring

There are a number of possible situations that will result in the observed static disorder, but the energies of the following five models were calculated:

(a) All the phenylene rings are in the horizontal conformation (i.e. the conformation with the smallest torsion angle relative to the naphtha(2,3-*d*)imidazolyl group (Figure 61a);

(b) All of the phenylene rings are in the vertical conformation (i.e. the conformation with the larger torsion angle relative to the naphtha(2,3-*d*)imidazolyl group (Figure 61b);

(c) Opposite sides of the channel have the same conformation (Figure 61c);

(d) Two neighbouring sides have the same conformation, (Figure 61d);

(e) The phenylene rings of alternating layers along the *c* axis have different conformations (Figure 61e).

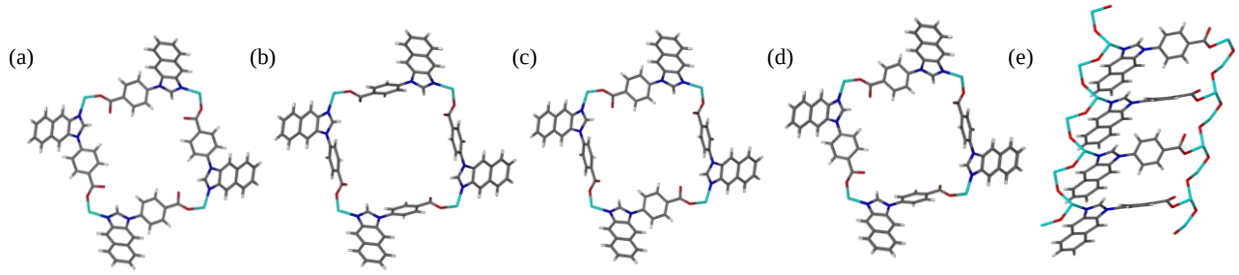

Figure 61. The five different models [(a) – (e)] of the structure that were optimised. Only (c), (d) and (e) would result in the observed static disorder of the phenylene ring in **IMMOF-3**.

Model (a) and (b) will not result in the observed disorder of the phenylene ring, but were optimised for comparison's sake. Molecular mechanics geometry optimisations were carried out using Materials Studio V4.3 employing the Forcite module. Calculations were performed on a non-periodic super-cell (1 × 1 × 4) of the framework. The positions of all atoms were fixed except those of the uncoordinated carboxyl oxygen atom and the hydrogen atoms. Charges were assigned using the charge equilibration method. Only the Universal and Dreiding forcefields are compatible with the zinc, and it of these two forcefields, the latter best describes the intermolecular interactions. The energy values per unit cell are summarised in Table 11.

Table 11. The energy values calculated for the five different models.

Model	Total Energy (kcal mol^{-1} per unit cell)	Valence energy (kcal mol^{-1} per unit cell)				Non-bond energy (kcal mol^{-1} per unit cell)		
		Bond	Angle	Torsion	Inversion	Hydrogen bond	van der Waals	Electrostatic
(a)	-273.9252	2.3903	22.7568	16.4108	1.9688	-11.4118	48.7120	-354.7518
(b)	-145.3790	2.1218	21.0590	29.0345	20.8833	-11.2863	100.9230	-308.1143
(c)	-85.6731	1.8238	21.1403	29.9893	16.7213	-10.4998	77.7635	-222.6113
(d)	-168.6439	1.8095	21.0878	22.4140	11.1548	-10.4185	73.0858	-287.7770
(e)	-251.9596	1.6130	16.2798	22.5460	11.2118	-10.3443	71.7498	-251.4843

The two lowest energy conformations are with all the phenylene rings parallel to each other, i.e. model (a) or with alternating layers of stacked rings having opposite conformations as described by model (e). Model (a) results in the smallest torsional strain on the ring, the smallest inversion energy valence term, as well as the lowest attractive electrostatic non-bonded energy. Having all the rings in the vertical conformation, model (b), is an unstable conformation owing to the strain caused by the larger torsion angle of the ring, as well as the significantly larger van der Waals repulsive non-bonded energy term. Since disorder is observed in the SCD structure, the calculations suggest that it is most likely that the orientation of the ring varies in each layer in

an …*abab*… arrangement. Even though there is slightly more van der Waals repulsion in model (e) and the attractive electrostatic energy is slightly less favourable than in model (a), it is stabilised by interactions between the layers. There are edge-to-face π-π (centroid to centroid distance = 5.06 Å) and CH- π (centroid to carbon (CH) distance = 3.79 Å) interactions between the layers, which the Dreiding forcefield does not describe very accurately (Figure 62).

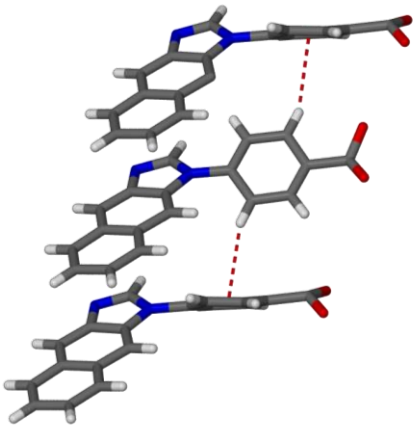

Figure 62. CH-π interactions between alternating layers of ligands stacked along [001] in **IMMOF-3**.

Thermal Analysis and Desorption

The thermogram shows that solvent loss starts at room temperature and is almost complete at approximately 150 °C (Figure 63). The framework is very stable and decomposition only starts at approximately 300 °C.

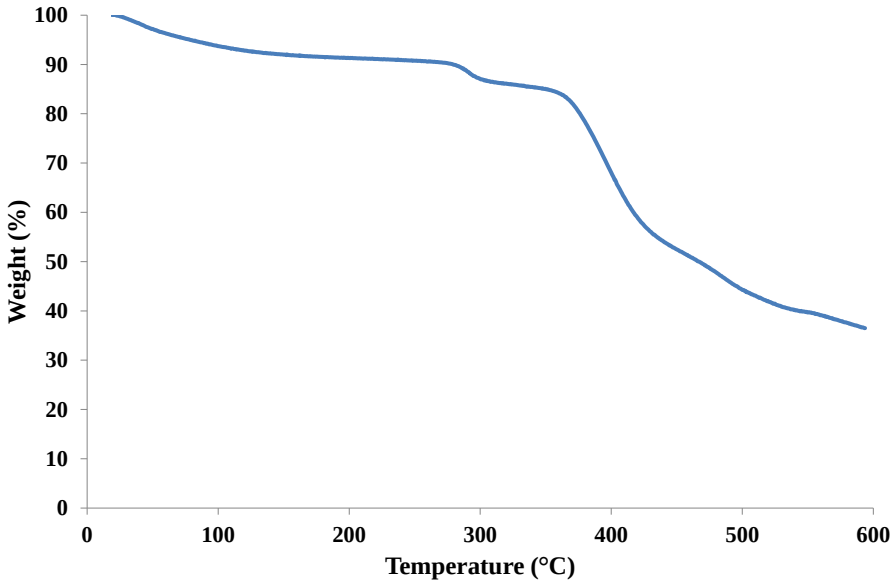

Figure 63. TGA of **IMMOF-3**.

The single crystals remain transparent and of diffraction-quality after guest removal. An SCD dataset was collected for an evacuated crystal sealed in the gas cell and placed under static vacuum. There were slight changes in the unit cell parameters and the electron density within the channel was reduced from 178 electrons per 297 $Å^3$ to 13 electrons per 324 $Å^3$ void (the difference in channel volume is due to the first dataset having been collected at 100 K, while the vacuum structure was determined from data collected at room temperature). The empty channels of the desolvated structure are shown in Figure 64.

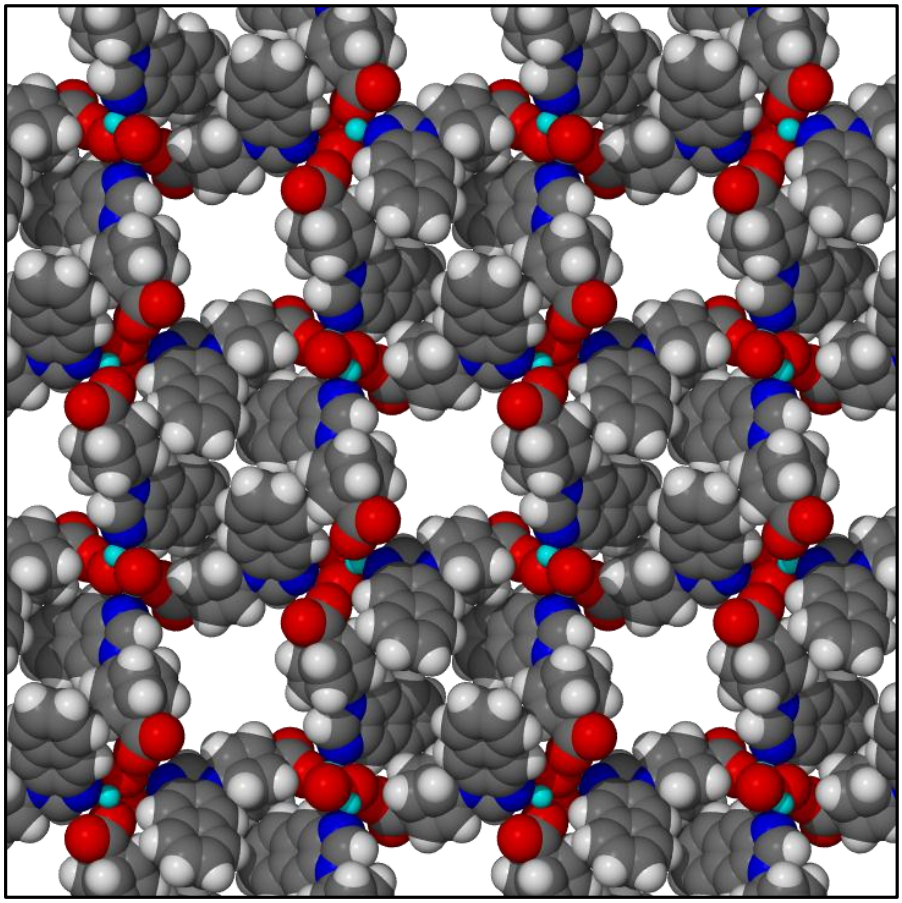

Figure 64. A space-filled representation of the empty **IMMOF-3** framework viewed along [001]. The appreciable void space is clearly visible.

PXRD data were recorded on the as-synthesised material prior to and after emptying the channels by heating the sample to 150 °C under reduced pressure. In Figure 65 it can be seen that there are some differences in the PXRD patterns of the as-synthesised and empty frameworks. These differences result from the small changes in the unit cell parameters or the presence of the guest-substructure. The bulk phase purity is maintained. The experimental and simulated powder patterns correspond well. The material maintains permanent porosity after desorption.

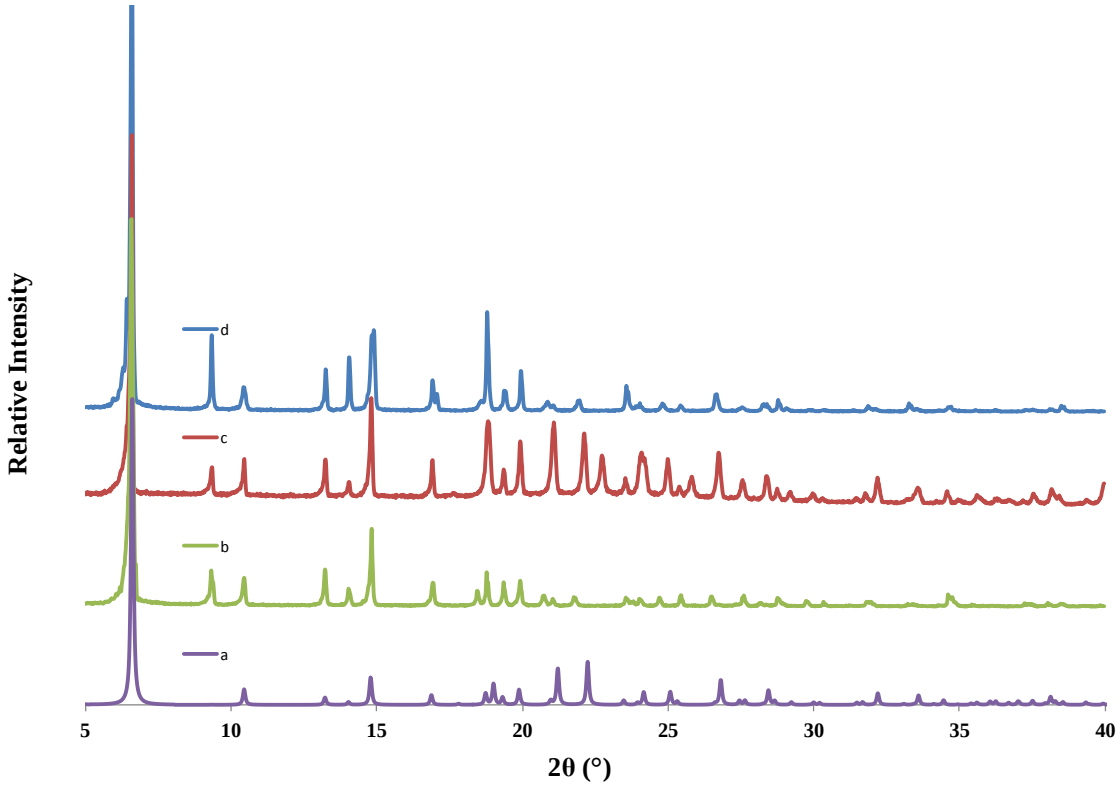

Figure 65. (a) Simulated PXRD pattern of the as synthesised compound, (b) the experimental PXRD pattern of a powdered sample of **IMMOF-3** (c) simulated PXRD pattern generated from a structure of an evacuated crystal collected whilst under reduced pressure and (d) experimental PXRD pattern from the same sample after heating it to 150°C under reduced pressure for four hours.

Generating the apohost using supercritical CO_2

Single crystals of **IMMOF-3** were subjected to supercritical CO_2 conditions using a critical point dryer (*SAMDRI-PVT-3D* from *Tousimis*). This procedure resulted in removal of the original methanol molecules from the channels. SCD structure determination revealed that two water molecules were included per ~300Å^3 channel section (twelve water molecules represent full occupancy of the channel). It was therefore concluded that the methanol was exchanged for CO_2 under the high pressure conditions and when the CO_2 pressure was reduced and eventually absent, the gas diffused out of the channels. The inclusion of water molecules is probably due to the exposure of the crystal to atmospheric moisture, and it is likely that the channel is hygroscopic.

4.2 SINGLE-CRYSTAL TO SINGLE-CRYSTAL TRANSFORMATIONS OF A POROUS AND DYNAMIC ZN(II) FRAMEWORK

Guest removal or desolvation of a solvate usually occurs via a phase transition to a more stable close-packed molecular assembly. Even in the case where guest loss does not result in a phase transition or significant structural changes, the integrity of the single crystal is likely to be disturbed by the rapid diffusion of guest molecules through the host lattice or by the harsh conditions (heat and vacuum) that are applied in order to remove them. Consequently, desolvation is almost invariably associated with the loss of single crystallinity and/or an increase in crystal mosaicity. In exceptional cases guest removal and exchange processes occur as single-crystal to single-crystal transformations that can be studied directly using SCD.[19] Single crystallinity is not essential for guest sorption/desorption processes, but it is of substantial value with regard to the acquisition of structural information by SCD methods.[10c]

The structural features of **IMMOF-3** that are thought to play a role in the crystals being extraordinarily robust are:

a) the framework is three-dimensional;

b) it is stabilised by collective π-π interactions and hydrogen bonds;

c) there are no discernable steric restraints for guest diffusion through the large and open channels;

d) the host is dynamic and flexible in a concerted fashion, as will become apparent.

On an atomic scale, noticeable structural changes occur when the host framework accommodates different guest molecules without an increase in the crystal mosaicity. It is thought that these changes occur in a concerted fashion to preserve the macroscopic integrity of the crystal.

4.2.1 Guest-exchange experiments

Guest-exchange experiments were carried out by immersion of single crystals in different solvents and/or the diffusion of volatile guests into the crystals (Table 12). These processes occurred as single-crystal to single-crystal transformations. In each guest-exchange experiment, a single crystal of **IMMOF-3** was placed in a vial containing a small volume of solvent for two weeks prior to structure determination from SCD data. The experiment was monitored visually to ensure that dissolution and recrystallization from the solvent did not occur. The original guest molecules (methanol) were exchanged without a decline in the single-crystal quality.

In the host-guest complexes with strong host-guest interactions (hydrogen or halogen bonds), the positions of the guest molecules are fixed and easily modelled. In the host-guest complexes containing weakly bound and disordered guest molecules, the exact occupancy per channel section cannot be modelled directly from the diffraction data. In these cases, the SQUEEZE electron count was used as a means of determining the occupancy per channel section or void space. This method was validated by the fact that the electron counts per channel section correspond almost exactly to the models for the structures where guest molecules could be modelled, namely those where guests formed hydrogen bonds with the host framework (i.e. water, ethanol, *n*-propanol and *iso*-propanol complexes).

Table 12. The occupancies of various guest molecules determined using the SQUEEZE[37] routine in Platon[36].

Guest	Electrons per molecule	Guest volume from van der Waals surface (Å^3)	Void volume from SQUEEZE (Å^3)	SQUEEZE electron count per void	Occupancy per void from SQUEEZE	Modelled guest occupancy per void
methanol	18	38.8	297	178	10	4
water	10	19.4	298	122	12	12
ethanol	26	54.0	297	105	4	4
n-propanol	34	70.7	316	121	4	4
iso-propanol	34	69.1	342	134	4	4
acetone	32	62.6	300	107	3	2
dichloromethane	42	58.7	317	127	3	2
chloroform	58	71.2	299	120	2	2
carbon tetrachloride*	74	86.2	295	56*	-	-
Benzene*	42	86.0	296	109*	-	-
acetonitrile	22	46.16	301	71	3	-
Toluene*	50	97.1	303	112*	-	-

* These structures contained water molecules as the guest instead of the solvent that it was submerged in. The highest electron density peaks are within hydrogen bonding distances from each other (2.700 – 2.730 Å) and correspond to the positions of the water molecules in **IMMOF-3$_{water}$**.

From the abovementioned results it is clear that **IMMOF-3** is capable of accommodating a wide variety of guest molecules with different H:G ratios, thus establishing its versatility as a porous material.

Inclusion of water and hydroxyl-functionalised guest molecules

The methanol molecules were successfully exchanged for water, ethanol, *n*-propanol and *iso*-propanol (Figure 66). In these four cases, the numbers of guest molecules that were modelled and the SQUEEZE electron count in the channel section correlate exactly.

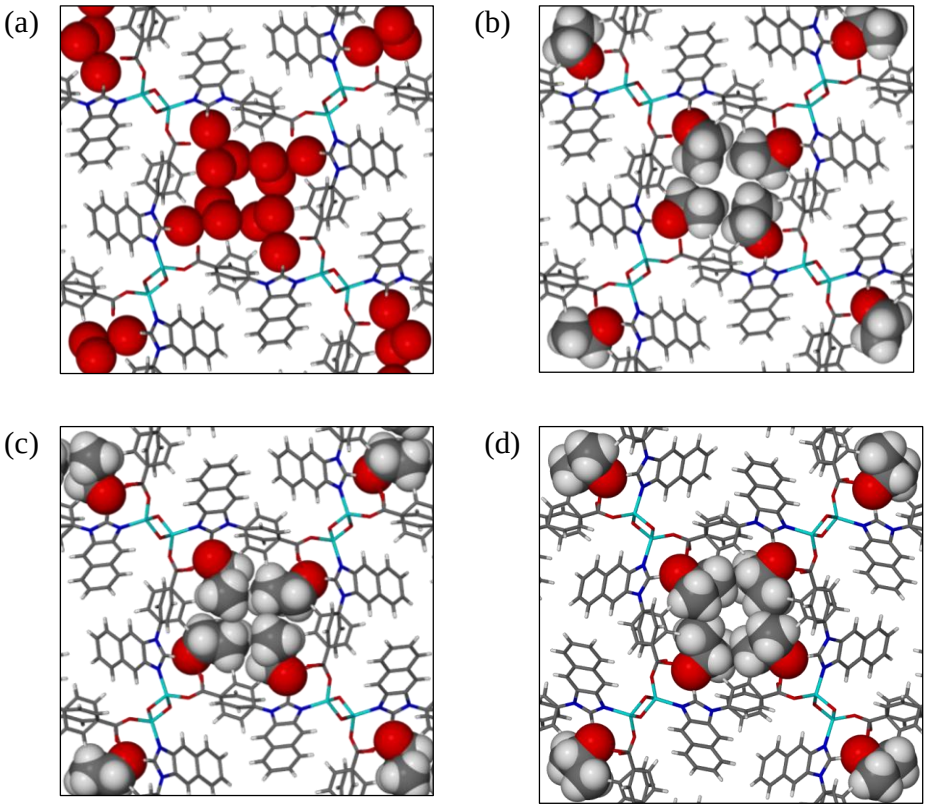

Figure 66. (a) The water, (b) ethanol, (c) *n*-propanol and (d) *iso*-propanol inclusion complexes of **IMMOF-3**. The high packing density of *n*-propanol in (c) is clearly visible. The hydrogen atoms of the hydroxyl moieties and the water molecules were not modelled.

The guest molecules pack very efficiently into the ~300 $Å^3$ channel section, with a packing coefficient [(number of molecules × van der Waals volume)/void volume] of 0.78 for water, 0.73 for ethanol, 0.89 for *n*-propanol and 0.81 for *iso*-propanol inclusion. Considering that the close packing of identical hard spheres results in a packing coefficient of 0.74 (cubic lattice) and that most organic crystals have packing coefficients of between 0.65 and 0.77,[59] it is clear that these polar solvents occupy almost all of the available void space. In the case of the *n*-propanol

inclusion complex, the methyl groups of neighbouring *n*-propanol molecules point in opposite directions in order to fit into the solvent-accessible space. Water molecules as well as the -OH groups of methanol, ethanol, *n*-propanol and *iso*-propanol all act as hydrogen bond donors towards the uncoordinated carboxyl oxygen atom of the ligand incorporated in the framework (Figure 67).

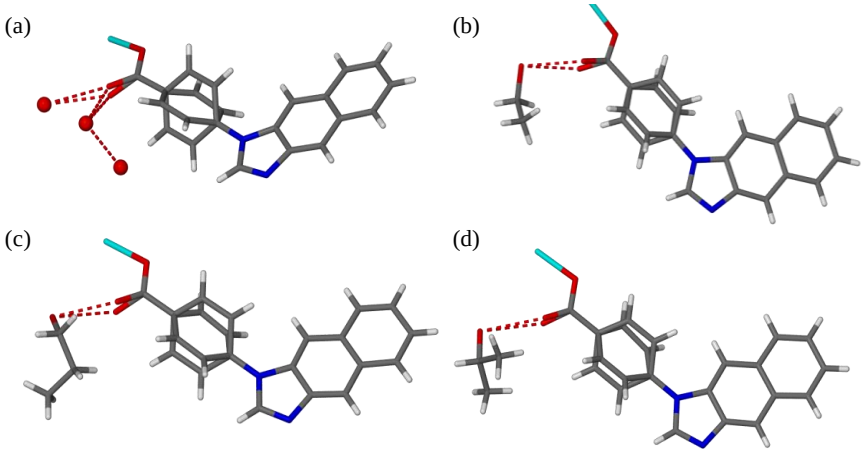

Figure 67. The hydrogen bonds (red dotted lines) between the uncoordinated carboxylate oxygen atom of the **IMMOF-3** framework and (a) water, (b) ethanol, (c) *n*-propanol and (d) *iso*-propanol. The hydrogen atoms of the hydroxyl moieties and the water molecules were not modelled.

The carboxylate oxygen atom is disordered over two positions (as is the phenylene ring of the ligand) with equal occupancy and therefore two hydrogen bonding distances to each guest molecule are reported in Table 13.

Table 13. Hydrogen bonding distances obtained from structural data.

Guest	O···O hydrogen bond distance # 1 (Å)	O···O hydrogen bond distance # 2 (Å)
methanol	2.692(8)	2.727(8)
Water*	2.70(1), 2.74(1)	2.870(9), 3.00(2)
ethanol	2.68(1)	2.767(9)
n-propanol	2.711(8)	2.783(7)
iso-propanol	2.758(5)	2.81(4)

* bifurcated hydrogen bonding

Porous materials with hydrogen-bonding sites are rare owing to the fact that the incorporation of structure-directing hydrogen bonding in solid-state assemblies usually limits pore size as a result of the close packing of the host itself.

Inclusion of chlorinated guest molecules

The crystals were also immersed in dichloromethane, chloroform and carbon tetrachloride. Only dichloromethane and chloroform were included whilst carbon tetrachloride was excluded. The

structure determined from the crystal that was immersed in carbon tetrachloride contained water molecules. The other chlorinated solvents participate in halogen bonds to the electronegative oxygen atom of the ligand. Only two molecules of dichloromethane or chloroform are included in each ~300 $Å^3$ channel section with low packing coefficients of 0.37 and 0.49, respectively (Figure 68). The reduced occupancy as compared to the hydroxyl-functionalised molecules could be a reflection of the weaker host-guest interactions or stronger guest-guest repulsion.

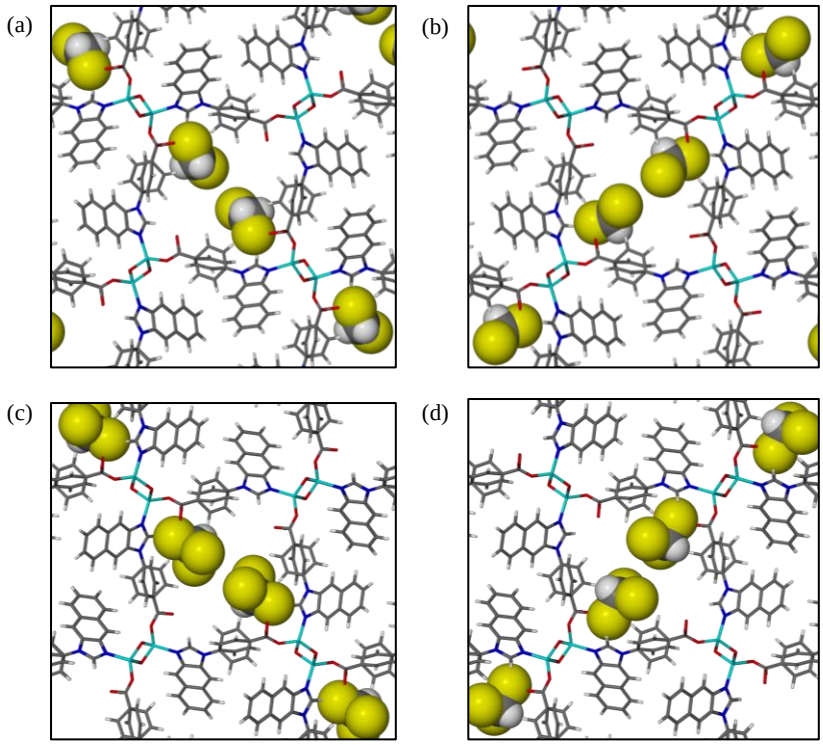

Figure 68. IMMOF-3 inclusion complexes with dichloromethane (a and b) and chloroform (c and d). Due to the four-fold symmetry of the channel each of the four symmetry-related positions in the channel is half occupied by the guest molecule. The guest molecules are likely to be situated either at the positions indicated in (a) and (c) or (b) and (d).

Guest molecules that were not included or could not be modelled due to disorder

Structures determined from crystals that were immersed in benzene, toluene and carbon tetrachloride contained water and not the parent solvent. **IMMOF-3** appears to be selective for water (an impurity in the parent solvent or a constituent of the air above the solvent) over these molecules. Benzene, toluene and carbon tetrachloride have large molecular volumes of 86.0, 97.1 and 86.2 $Å^3$, respectively and are non-polar. The size and non-polarity of these solvents may prevent their accommodation in the hydrophilic channels of **IMMOF-3**.

The acetone and acetonitrile inclusion complexes have diffuse electron density within the channels. The peaks of highest electron density are not within hydrogen bonding distances from each other and it is thus assumed that the guest molecules are not water. Acetone and acetonitrile

are not (strong) hydrogen or halogen bond donors and do not form stabilising interactions with the channel wall. Consequently, their positions could not be modelled at all. Since these included molecules cannot be directly observed by SCD methods, other techniques such as the measurement of sorption isotherms and TGA are necessary to confirm their presence within the channels. The TGA experiments did not aid in the determination of the H:G ratios since solvent loss occurs at room temperature and thus also during sample preparation. Consequently, vapour sorption experiments were carried out in order to determine precise H:G ratios.

4.2.2 Vapour sorption

In order to test the sorption capabilities and selectivity of **IMMOF-3**, vapour sorption kinetics were measured on the microbalance described in Section 2.9. Vapour sorption with a range of different organic solvents was carried out on the microbalance at 25 °C and the results are summarised in Table 14 and Figure 69.

Water is included with the highest H:G ratio of 9 molecules per ~300 $Å^3$ channel section (or 18 molecules per unit cell). The occupancy decreases in the order; water > acetone > methanol = ethanol > dichloromethane = chloroform = acetonitrile > *n*-propanol = *iso*-propanol.

Table 14. The maximum guest occupancies of **IMMOF-3** determined from vapour sorption experiments, compared with various physical properties of the solvent adsorbates.

Guest	Guest volume from van der Waals surface ($Å^3$)	Boiling point (°C)	Vapour pressure at 25 °C (mbar)	Kinetic diameter*[60] (Å)	Dipole moment[60] (D)	Occupancy from vapour sorption
water	19.4	100.0	31.7	2.641	1.85	9
methanol	38.8	64.7	169	3.626	1.70	4
ethanol	54.0	78.5	78.7	4.530	1.69	4
n-propanol	70.7	97.0	26.7	4.700	1.68	1
iso-propanol	69.1	82.5	58.7	4.800	1.66	1
acetone	62.6	56.3	308	4.600	2.88	5
dichloromethane	58.7	39.8	582	4.898	1.60	2
chloroform	71.2	61.2	262	5.389	1.04	2
carbon tetrachloride	86.2	76.7	152	5.947	0	0
benzene	86.0	80.1	127	5.850	0	0
acetonitrile	46.1	81.6	119	-	3.92	2

* The kinetic diameter is a reflection of the smallest effective dimension of a given molecule for permeation purposes.

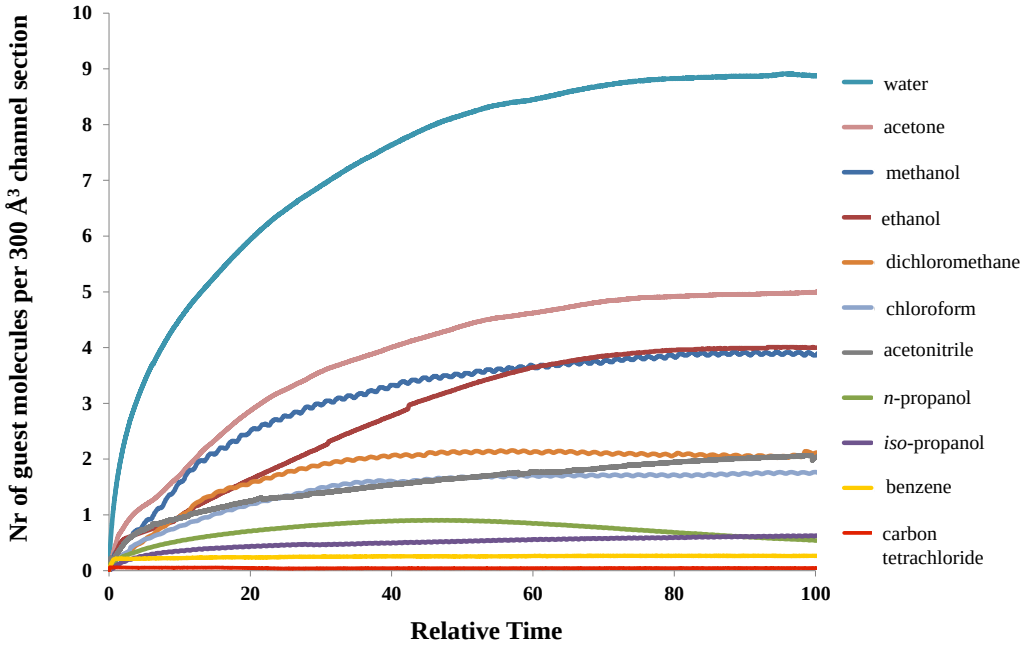

Figure 69. Vapour sorption experiments measured at 25 °C. Each of the different vapour sorption curves reached saturation (plateaued) at different times. In order to plot all of the data on one graph, the relative time (time as a percentage of the saturation time) was calculated.

IMMOF-3 is not likely to be utilised as a storage material as the guest uptake is low with weight/weight (%) and volume/volume (%) uptake of below 20% in all cases (Figure 70). Instead it may be useful in the selective uptake of vapour for separation purposes.

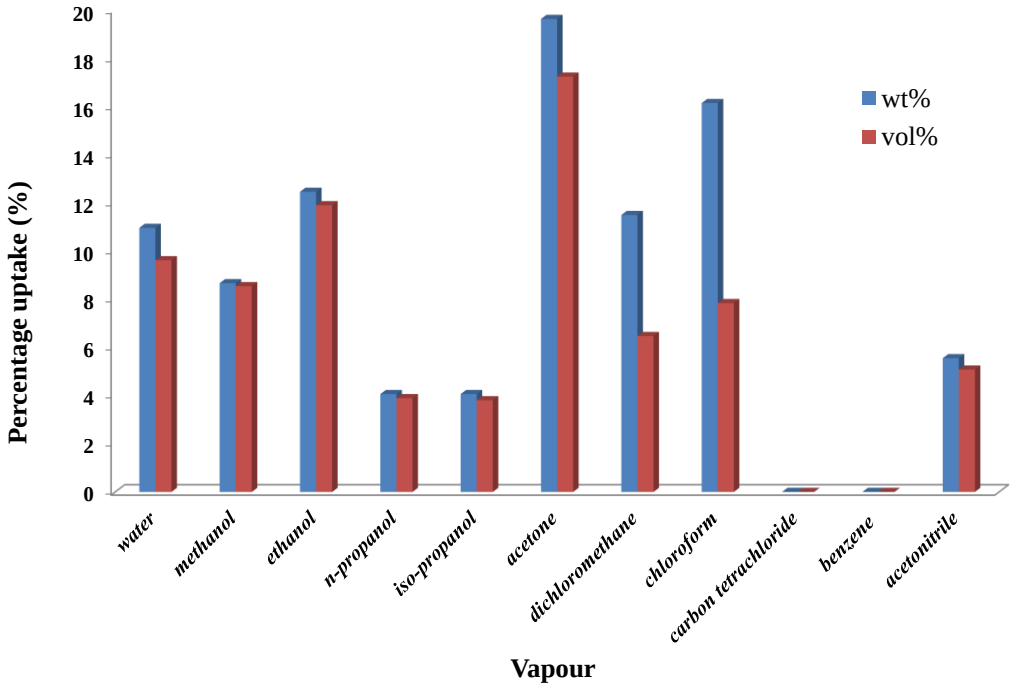

Figure 70. The percentage uptake by weight and volume of **IMMOF-3**.

The vapour sorption experiments confirmed that carbon tetrachloride and benzene molecules are excluded by **IMMOF-3**. The exclusion of carbon tetrachloride and benzene is likely to be caused by a combination of size/shape exclusion and the fact that there are fewer favourable interactions between the non-polar guest molecules and the pore surface. Thus one can conclude that, molecules with a kinetic diameter larger than that of chloroform, i.e. 5.389 Å or a molecular volume of more than 71.2 $Å^3$ do not diffuse into the approximately 6 Å × 6 Å square channels of **IMMOF-3**. Neither carbon tetrachloride nor benzene have dipole moments and do not form favourable interactions with the hydrophilic channels. The uncoordinated carboxylate oxygen atoms embedded in the channel wall participate in electrostatic interactions with molecules with a dipole moment (the dipole moments of the solvents are listed in Table 14).

The results of the vapour sorption experiments were also used to confirm the occupancy of the various different guest molecules from the SQUEEZE electron counts derived from the SCD structures, Table 15.

Table 15. The occupancy (number of guest molecules per ~300 $Å^3$) derived from the SCD structures compared to that of the vapour sorption experiments.

Guest	Modelled occupancy from SCD structure	Occupancy from vapour sorption
water	12	9
methanol	4	4
ethanol	4	4
n-propanol	4	1
iso-propanol	4	1
acetone	3*	5
dichloromethane	2	2
chloroform	2	2
carbon tetrachloride	0	0
benzene	0	0
acetonitrile	3*	2

* Occupancy from SQUEEZE electron count.

The guest occupancy determined from vapour sorption and the guest-exchange experiments with single crystals correlate in the cases of water, methanol, ethanol, dichloromethane and chloroform sorption. In some cases, such as that of *n*-propanol and *iso*-propanol sorption, the H:G ratio obtained from vapour sorption was much less (1 molecule per ~300 Å channel section) than that of the SCD structure following guest exchange (4 molecules per ~300 Å channel

section). Full immersion of the crystals within a solvent over a prolonged time period (2 weeks) during the guest exchange process clearly enhances the likelihood of guest uptake in these cases.

MOFs offer new opportunities for sorption technology since these materials can have selective sorption properties that are afforded by specific pore sizes and controllable host-guest interactions. The fact that **IMMOF-3** absorbs water, methanol and ethanol vapour to a much greater extent than *n*-propanol and *iso*-propanol vapour could have an application in the purification of alcohol mixtures. Bio-alcohols are being considered as an alternative to fossil fuels and the purification of alcohols from water is a challenge for making bio-fuels a viable alternative.[61] The kinetics of water, methanol, ethanol, *n*-propanol and *iso*-propanol sorption are shown in Figure 71.

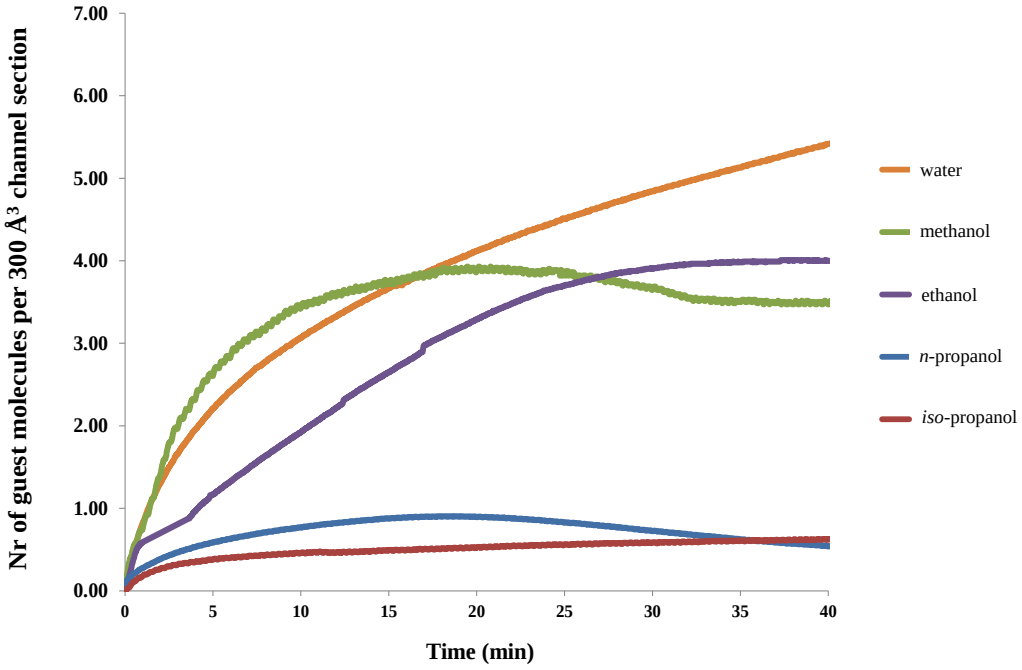

Figure 71. Vapour sorption of water, methanol, ethanol, *n*-propanol and *iso*-propanol by **IMMOF-3** measured at 25 °C. The water sorption experiment only reached saturation after 250 minutes (10 molecules per ~300 Å^3 section).

Clearly, there are different rates of uptake of water, methanol and ethanol vapour. At the same time *n*-propanol and *iso*-propanol appear to be slightly excluded. A vapour sorption isotherm utilising the IGA instrument could only be measured with methanol since there were difficulties obtaining suitable partial pressures of ethanol, *n*-propanol and *iso*-propanol. The vapour sorption isotherm measured on the IGA confirms that four methanol molecules are sorbed per ~300 Å^3 channel section (Figure 72). There is a significant amount of hysteresis during the desorption of methanol, owing to the hydrogen bonding interactions between the methanol and the host framework. Even at 0 bar pressure, two methanol molecules remain stored

in the **IMMOF-3** channels. The ability of **IMMOF-3** to retain alcohol guest molecules makes it an attractive material for alcohol separation purposes.

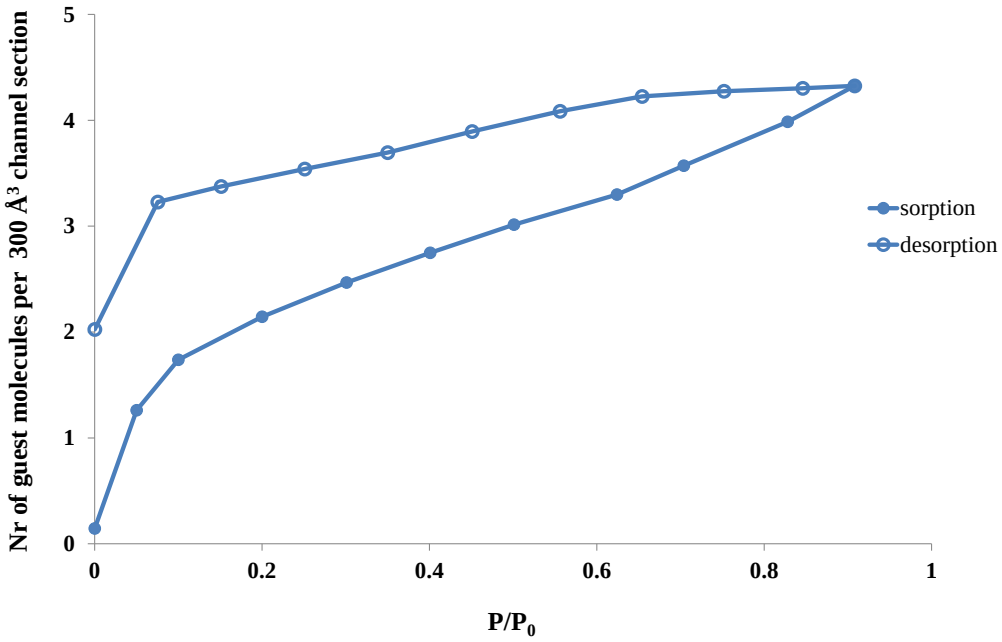

Figure 72. The methanol sorption isotherm of **IMMOF-3** at 25 °C measured on the IGA.

In principle, **IMMOF-3** is capable of selectively absorbing the water, methanol and ethanol components from a mixture of alcohols and water. It can also be postulated that the water, methanol and ethanol components will be retained within the solid material for different lengths of time. As a result, **IMMOF-3** can perhaps be applied as a stationary phase for the gas chromatographic (GC) separation of a mixture of water, methanol, ethanol, *n*-propanol and *iso*-propanol. Similar studies have been carried out by Zhu *et al*. The authors tested the ability of a micoporous MOF to separate alcohols from water in a gas chromatographic separation. A 180 x 2 mm column was packed with single crystals that have a diameter of between 20-50 µm.[61] GC separation studies with **IMMOF-3** can form part of potential future work.

4.2.3 Diffusion of volatile guests into a single-crystal

As previously mentioned, the crystals are remarkably robust and remain transparent after removal of the methanol molecules at 150°C under reduced pressure. Empty crystals of **IMMOF-3** were exposed to two volatile solids iodine and naphthalene (at STP conditions) but only iodine could be observed directly using SCD methods.

Iodine inclusion

Single crystals were placed on a glass slide and enclosed within a petri dish that contained iodine crystals. The petri dish was heated slightly (30-40 °C) on a hotplate. The diffusion of iodine into the crystals could be followed visually (Figure 73), as the light-brown crystals darkened and became almost black after exposure to iodine vapour for approximately four weeks.

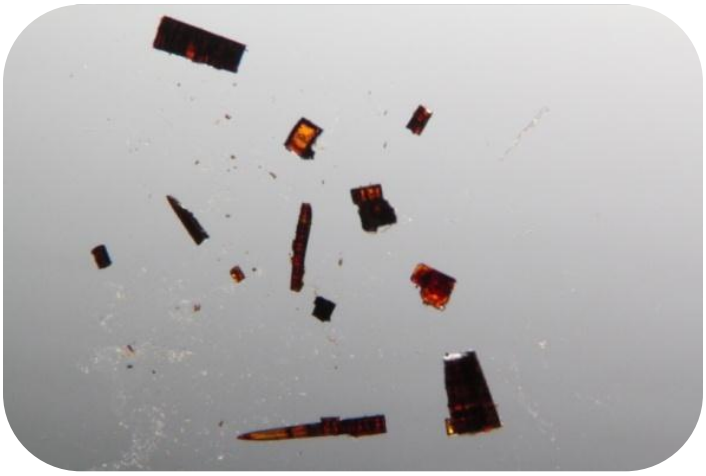

Figure 73. Photograph of **IMMOF-3** crystals that have been exposed to iodine vapour for four weeks.

Iodine can be modelled with half occupancy at each of four positions in a 327 $Å^3$ section of the channel. The SQUEEZE electron count of 204 electrons per 327 $Å^3$ channel section is approximately consistent with the inclusion of two iodine molecules (106 electrons each) in the channel section. The two molecules are disordered over four positions (Figure 74). The two most likely positions of the iodine molecules in the channel section are shown in Figure 74b and c. The possibility that there are two molecules that form a T-shaped interaction can be discounted because the measured intermolecular distance is too short (3.288 Å). I-I contacts are usually in the range of 3.4-3.9 Å (the van der Waals distance is 4.3 Å) and at 3.4-3.7 Å the contact may be considered as a secondary bond.[62]

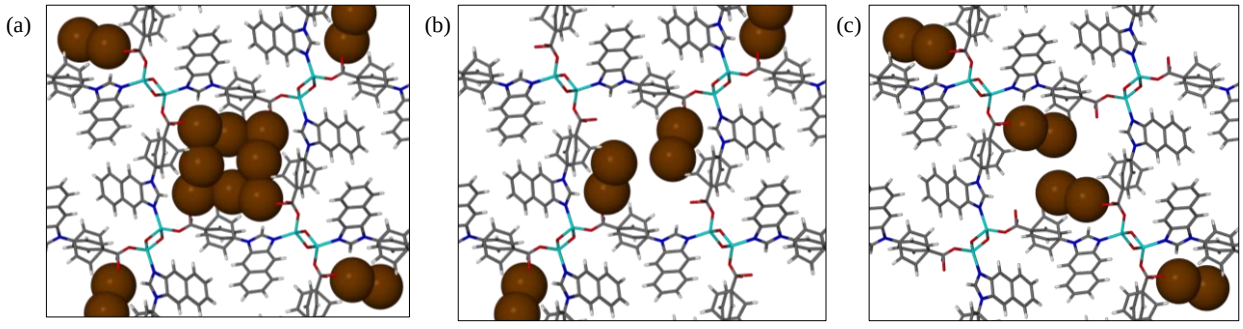

Figure 74. (a) The four half-occupied symmetry-related positions of the iodine molecules within a channel of **IMMOF-3**, viewed along [001], with the actual positions most likely being those shown in (b) and (c).

Assuming that equilibrium had been reached after exposure to iodine for four weeks, the inclusion of iodine occurs with a low packing coefficient of 0.37. There is a halogen bond (previously termed a charge-transfer interaction) between the uncoordinated oxygen atom of the carboxyl-group and iodine (average I···O distance of 2.84 Å), Figure 75. There are 16 CSD entries with a halogen bond between an iodine molecule and an oxygen atom, with a minimum I···O distance of 2.778 Å, a maximum distance of 3.459 Å and a mean distance of 3.104 Å. The CSD entry with an I···O distance of 2.826 Å between an oxygen atom of a 3D MOF, $Mn_3(HCOO)_6$ and iodine and the distance of 2.808 Å of an iodine complex with 1,4-dioxane are the most similar to the I···O distance of **IMMOF-3$_{iodine}$**.[63]

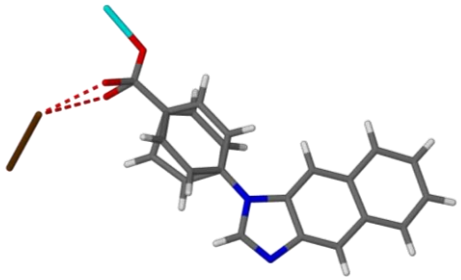

Figure 75. Halogen bond between the carboxylic oxygen atom of **IMMOF-3** and iodine.

The isotropic thermal parameter of the iodine atom that is not halogen bonded to the framework is very high (0.68), most likely because it is not interacting with the framework and is probably disordered over several positions, as illustrated in Figure 76.

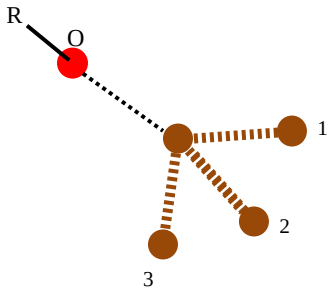

Figure 76. An illustration of the probable disorder of the iodine atom (positions 1, 2 and 3) that is not halogen bonded to the **IMMOF-3** oxygen atom.

The shortest distance between iodine atoms stacked along the channel is 5.24 Å (also the *c*-axis length and the distance between carboxyl-moieties along the channel wall), which is significantly longer than the van der Waals contact distance of 4.3 Å, Figure 77. The intermolecular distance between parallel-stacked iodine molecules in solid iodine is 4.268 Å.[62] The I···O halogen bond to the channel (host-guest) thus appears to be the dominant interaction

involved in the stabilisation of the iodine molecules within the channels (as opposed to the possibility of I···I interactions (guest-guest) between neighbouring iodine molecules in the continuous channels).

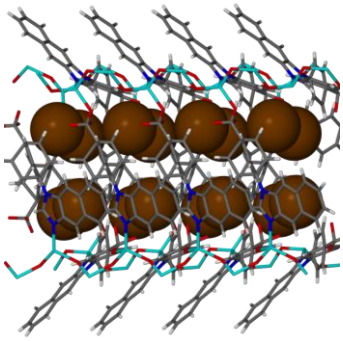

Figure 77. Parallel orientation of iodine molecules along the **IMMOF-3** channel, viewed perpendicular to [001].

4.2.4 Gas sorption

Gas sorption isotherms with a range of gases were measured at 25 °C on the IGA (Figure 78 and Table 16).

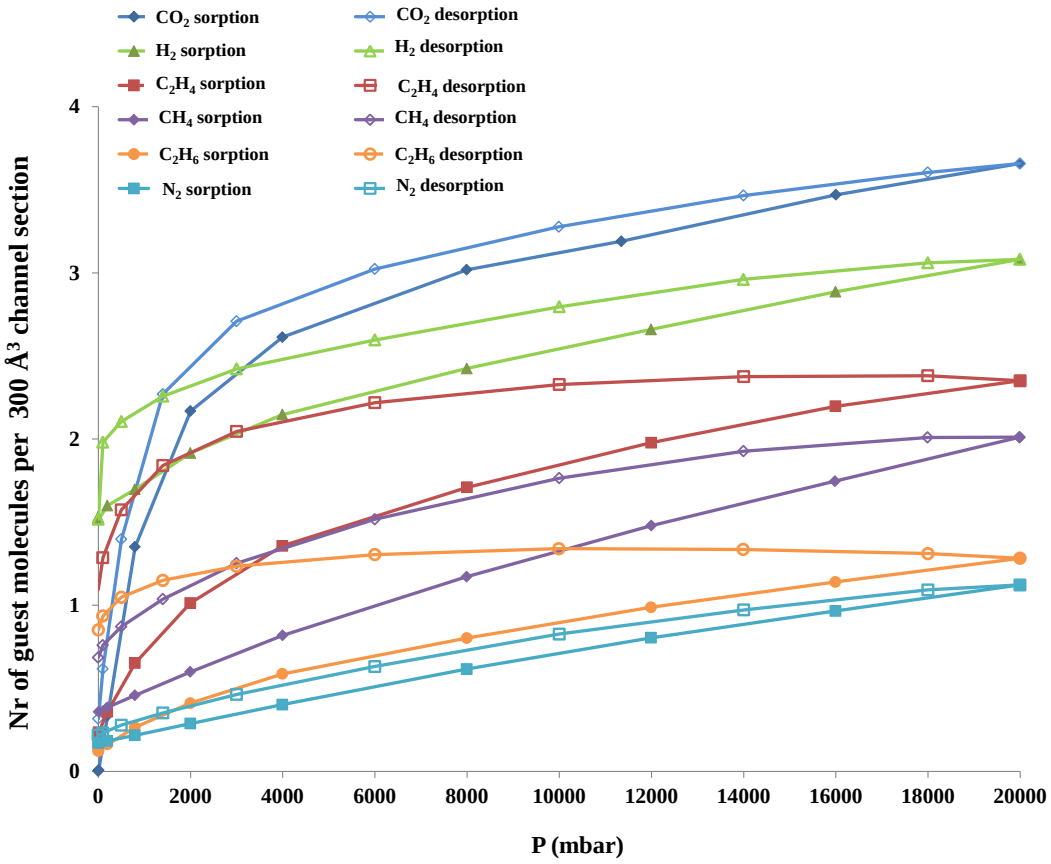

Figure 78. Gas sorption isotherms of **IMMOF-3** measured at 25 °C on the IGA.

Table 16. The maximum occupancy of various gases during gas sorption experiments with **IMMOF-3** and selected information about the gases.

Gas	Gas molecular formula	Molecular volume of gas from van der Waals surface ($Å^3$)	Kinetic diameter[60] (Å)	Polarizability[60] × 10^{25} (cm^3)	Maximum occupancy from gas sorption (molecules per ~300 $Å^3$ channel section)
carbon dioxide	CO_2	35.33	3.3	29.11	3.7
hydrogen	H_2	10.01	2.83-2.89	8.042	3.1
ethylene	C_2H_4	43.29	4.163	33.3-39.3	2.4
methane	CH_4	29.68	3.758	25.93	2.0
ethane	C_2H_6	50.65	4.443	44.3-44.7	1.3
nitrogen	N_2	22.23	3.64-3.80	17.403	1.1

The framework is selective for carbon dioxide and the occupancy (H:G ratio) decreases in the order carbon dioxide (CO_2) > hydrogen (H_2) > ethylene (C_2H_4) > methane (CH_4) > ethane (C_2H_6) > nitrogen (N_2), Table 16. There is a small amount of hysteresis during the desorption of CO_2 and H_2. In the cases of C_2H_4, C_2H_6 and CH_4 the hysteresis is more substantial and is thought to be a consequence of favourable host-guest interactions. C_2H_4, C_2H_6 and CH_4 are capable of participating in weak hydrogen bonds with the channel wall. The uptake of hydrogen is not significant (1.7 wt%) if one considers that the target set by the US Department of Energy for hydrogen storage is 6 wt%.[17]

The CO_2 occupancy tends to four molecules per ~300 $Å^3$ channel section, which might suggest that the CO_2 molecules interact with the four uncoordinated oxygen atoms of the host carboxyl groups embedded in the channel wall. Information about the host-guest interactions between gaseous guests and **IMMOF-3** can only be obtained from SCD structures determined with the single crystal under controlled atmospheres.

4.2.5 Gas inclusion complexes

An environmental gas cell (see section 2.5) was used to collect single crystal X-ray data with a crystal under a specific gas pressure. All of the single-crystal X-ray datasets for different gases were collected using the same single crystal mounted in the gas cell. Using a gas-inlet attachment, gas was introduced into the system, which was then sealed off from the atmosphere to allow the crystal to equilibrate for approximately 24 hours. After data collection, the gas was released and the crystal placed under dynamic vacuum for 24-48 hours in order to once again obtain the guest-free crystal.

The guest-free structure had a residual electron density of 13 electrons per 324 $Å^3$ void space. This is equivalent to 3 electrons per asymmetric unit, which is negligible compared to the as-synthesised structure (178 electrons per void). All attempts to reduce this electron count further were unsuccessful. The residual electron density might be ascribed to the disorder of the organic ligand (phenylene ring and coordinated carboxylic acid moiety), which forms part of the framework and channel wall. Data were collected with the guest-free crystal placed under specific gas pressures at room temperature and at low temperature. Gases with heavy atoms were chosen for these experiments as the increased electron density may assist in modelling the gas position. The low temperatures at which data were collected were chosen based on the physical properties of the respective gases in order to prevent condensation of the gas within the gas cell.

At room temperature, the gaseous molecules have high thermal motion and only diffuse electron density could be observed within the channels. Even at decreased temperatures, the gas molecules tend to be disordered if they do not interact strongly with the host framework. However, the increased SQUEEZE electron count within the channels at low temperature suggests that a greater number of gas molecules diffuse into the channels when the temperature is reduced.

Owing to the tetragonal symmetry (space group $I\bar{4}$) and the large volume of the channels (which allows for significant thermal motion), modelling the positions of the gas molecules was only possible in some cases. However, the occupancy can be deduced from the SQUEEZE electron count per void volume, by comparing it to that of the vacuum structure, Table 17.

Table 17. Structural data for a crystal under various controlled atmospheres.

		Room temperature					
Gas and loading pressure	**Electrons per molecule**	***a*-, *b*-axes (Å)**	***c*-axis (Å)**	**Unit cell volume (Å^3)**	**Void volume (Å^3)**	**Platon[36] SQUEEZE[37] electron count**	**Occupancy deduced from electron count**
Vacuum (no guest)	-	26.452(1)	5.287(3)	3698.9(3)	324	13	-
CO_2, 20 bar	22	26.544(2)	5.2750(3)	3716.8(4)	-	-	-
C_2H_2, 4 bar	14	26.5097(8)	5.2457(2)	3686.5(2)	307	39	2.79
CO, 20 bar	14	26.5219(5)	5.2453(1)	3689.6(1)	315	27	1.93
CH_3Br, 3 bar	44	26.555(5)	5.2242(9)	3684(1)	309	104	2.36
C_2H_3F, 15 bar	24	26.5120(9)	5.2509(2)	3690.8(2)	313	28	1.17
C_2H_3Cl, 3 bar	32	26.523(2)	5.2472(4)	3691.2(5)	310	24	0.75
C_2H_3Br, 1 bar	50	26.4984(8)	5.2598(2)	3693.2(2)	313	37	0.74
$ClCF_3$, 10 bar	50	26.590(4)	5.1957(8)	3674(1)	304	59	1.18
		Low temperature					
CO_2, 10 bar, 233 K	22	26.633(4)	5.2100(8)	3695(1)	299	104	4.73
C_2H_2, 4 bar, 220 K	14	26.558(1)	5.1974(2)	3665.8(2)	298	88	6.36
CO, 13 bar, 100 K	14	26.636(1)	5.1199(2)	3632.5(3)	291	89	6.36
CH_3Br, 3 bar, 273 K	44	26.56(3)	5.214(4)	3678(4)	347	122	2.77
C_2H_3F, 15 bar, 250 K	24	26.552(4)	5.2208(8)	3681(1)	303	43	1.72
C_2H_3Cl, 3 bar, 273 K	32	26.554(1)	5.222(1)	3682(1)	301	23	0.56
C_2H_3Br, 1 bar, 220 K	50	26.5447(9)	5.2079(2)	3669.6(2)	298	85	1.70
$ClCF_3$, 10 bar, 273 K	50	26.590(3)	5.2138(7)	3686.2(8)	310	61	1.22

Based on the occupancy values deduced from the SQUEEZE electron count, the highest occupancy values per host-channel section were achieved for (and in the order): acetylene (C_2H_2) > carbon monoxide (CO) > carbon dioxide (CO_2) > methyl bromide (CH_3Br) > vinyl fluoride (C_2H_3F) > vinyl bromide (C_2H_3Br) > freon-13 ($ClCF_3$) > vinyl chloride (C_2H_3Cl). These occupancy values, deduced from the electron counts, are as would be expected based on the increasing molecular volume of the guest molecules across the series, and taking into account which molecules would form the most favourable host-guest interactions.

Atomic coordinates could only be determined for carbon dioxide, acetylene, methyl bromide, vinyl fluoride and vinyl bromide. In these cases the guest molecules participate in favourable host-guest interactions that help to anchor the guest molecules in the channel.

Carbon dioxide inclusion

IMMOF-3 includes four CO_2 molecules per ~300 $Å^3$ channel section. The H:G ratio has been confirmed by the measurement of a CO_2 sorption isotherm on the IGA (see section 3.2.4).

In the **CO_2-IMMOF-3*** structure determined at 20 bar CO_2 pressure and room temperature (295 K), the CO_2 molecules are located at slightly different atomic positions to those determined for **CO_2-IMMOF-3** at 10 bar pressure and 233 K. The varying positions of the CO_2 molecules in the two structures are shown in Figure 79.

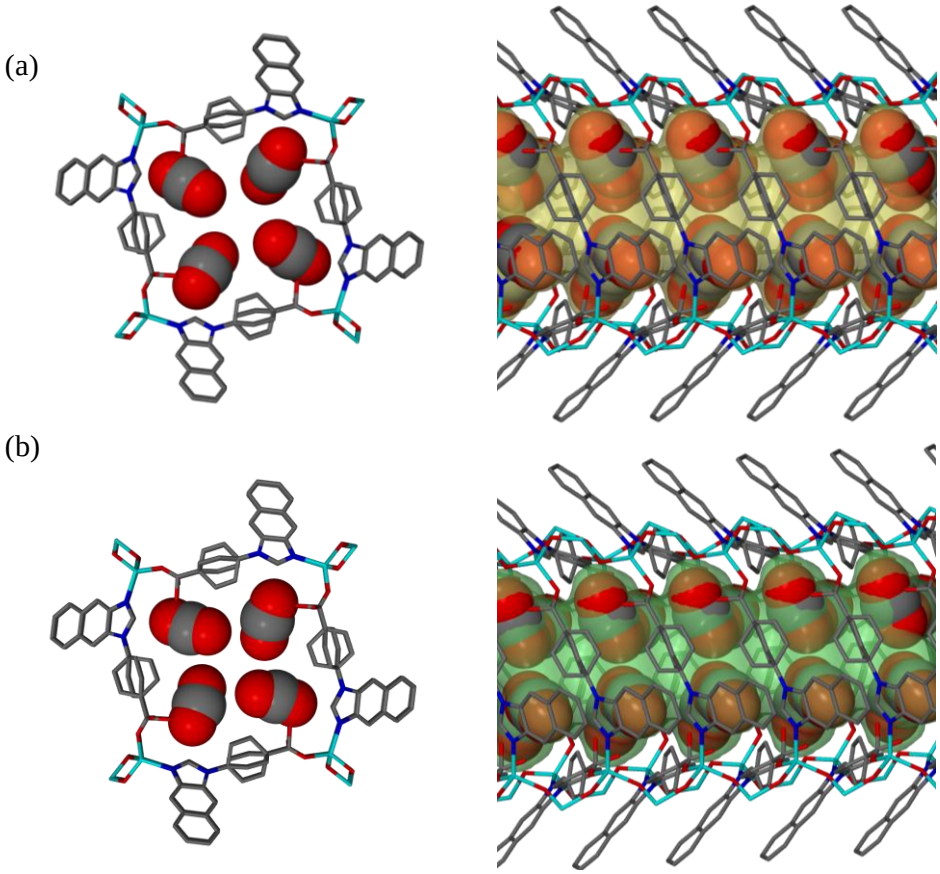

Figure 79. (a) Parallel and perpendicular views of an **IMMOF-3** channel occupied by CO_2 molecules (a) at 295 K and (b) at 233 K. Hydrogen atoms have been omitted for clarity. The solvent accessible space (semi-transparent yellow and green surfaces) was mapped with MSROLL[39] using a probe radius of 1.4 Å.

The CO_2 molecules situated at the four symmetry-related positions are less densely packed at 295 K than at 233 K. At 295 K there is a short contact distance resulting from an electrostatic

*The gas inclusion complexes have the molecular formula of the gas preceding the name of the host. This was done to distinguish between the structures determined from data collected using the environmental gas cell and the structures of the various solvates of **IMMOF-3** after guest-exchange experiments.

interaction between the slightly positively charged central carbon atom of the CO_2 with the uncoordinated carboxyl-oxygen atom of the ligand (O···C distance of 2.80(5) Å). No significant guest-guest interactions between two neighbouring molecules are discernible at room temperature. CO_2 is known to form T-shaped guest-guest interactions between the partially positive charge of the central carbon of one CO_2 molecule and the partially negative charge of the terminal oxygen of the neighbouring CO_2. At 295 K the O···C distance between two neighbouring CO_2 molecules is 4.49(7) Å. At 233 K, the CO_2 is orientated with a terminal oxygen atom at a distance of 2.74(5) Å or 2.90(5) Å from the framework's carboxyl-oxygen atom (two distances due to the disorder of the carboxyl-oxygen atom over two positions, with equal occupancy for each position), while the central carbon of the CO_2 is situated at a distance of 2.93(4) Å and 3.06(6) Å from it. At low temperature, neighbouring CO_2 molecules form slightly more pronounced T-shaped interactions with an O···C distance of 4.02(8) Å. Parallel stacking of the CO_2 molecules at room temperature is at a repeat distance of 5.275(1) Å and at 233 K the repeat distance is 5.210(1) Å.

Acetylene inclusion

The **C_2H_2-IMMOF-3** structure was determined from data collected with the crystal under 4 bar acetylene pressure at 220 K. There are two positions with half occupancy for the acetylene molecules in the asymmetric unit (Figure 80).

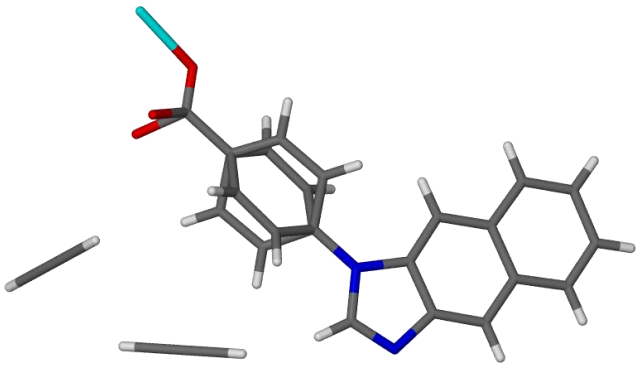

Figure 80. The asymmetric unit of the acetylene inclusion complex (**C_2H_2-IMMOF-3**).

The acetylene molecules cannot occupy both positions in the asymmetric unit concurrently as shown in Figure 81a. They can either occupy the four positions shown in Figure 81b or the positions shown in Figure 81c within a 298 $Å^3$ channel section. In Figure 81b there is host-guest hydrogen bonding between the donor (acetylene guest) and the carboxyl-oxygen acceptor (C···O

distance = 2.89(3) Å or 2.81(3) Å). In Figure 81c the strong semi-parallel π-π interactions and CH-π interactions[54] between guest molecules result in the formation of a spiral of acetylene molecules that extends along the channel direction. In addition, there are also weak CH-π interactions between the acetylene and the disordered phenylene ring of the host framework.

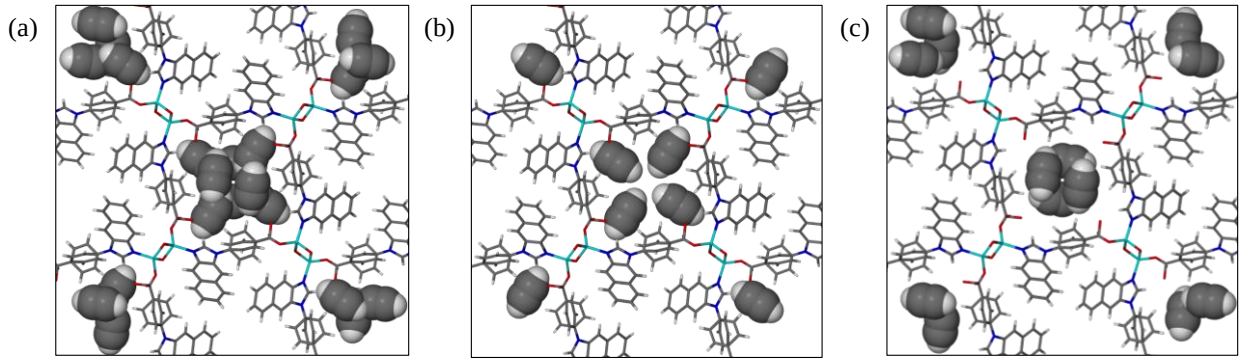

Figure 81. (a) The eight half-occupied positions for the acetylene molecules (space-filled representation) in **C_2H_2-IMMOF-3**, viewed along [001]. The molecules either form host-guest hydrogen bonds as shown in (b) or they form a spiral down [001] as shown in (c).

Halogenated guest molecules

In the structures that include CH_3Br, C_2H_3F and C_2H_3Br, the halogen atom of the guest has more electrophilic character than the uncoordinated oxygen atom of the carboxyl group of the framework, resulting in halogen bonds. These halogen bonds permit modelling of the guest molecules since they anchor the guest at one of the four symmetry-related positions per ~300 $Å^3$ channel section. Each of the respective guest molecules has less than full occupancy owing to the steric constraints imposed on it by the channel (topology), guest size and limited diffusion.

Methyl bromide inclusion

The framework includes methyl bromide when exposed to 3 bar of gas pressure. Although the methyl bromide molecules can only be modelled at low occupancy (20%), the average electron count within the channel section corresponds to approximately two molecules per ~300 Å channel section. That is, the occupancy suggests that two methyl bromide molecules are disordered over the four symmetry-related positions within the channel section. A comparison of the structure collected at 298 K with that of the structure collected at 273 K reveals that changes in the host-guest interaction distances occur.

In contrast to the CO_2-included structures, the methyl bromide guest molecules are not closer to one another or more densely packed at a lower temperature. Instead, the guest molecules are situated closer to the framework owing to stronger host-guest interactions. The solvent-accessible space within the channel was mapped using MSROLL, and is shown in Figure 82. The Br atoms protrude more extensively from the Connolly surface (solvent-accessible space) at 273 K than at 298 K. This is due to the fact that at 273 K the halogen bonding distance, i.e. the O···Br distance, is slightly shorter (2.76(2) Å) than at 298 K (2.89(4) Å). Studies of the temperature dependence of halogen bonds are rare but a study on organic non-porous crystals has been conducted, where a difference of between 0.030-0.059 Å was reported for Ar-N···I, Ar-O···I and Ar-N···Br interaction distances (Ar is a perfluorinated aromatic residue).[64]

Interestingly, the framework also appears to respond to the difference in the guest positions, as the channel volume (Platon, SQUEEZE) increases from 309 $Å^3$ at 298 K to 347 $Å^3$ at 273 K.

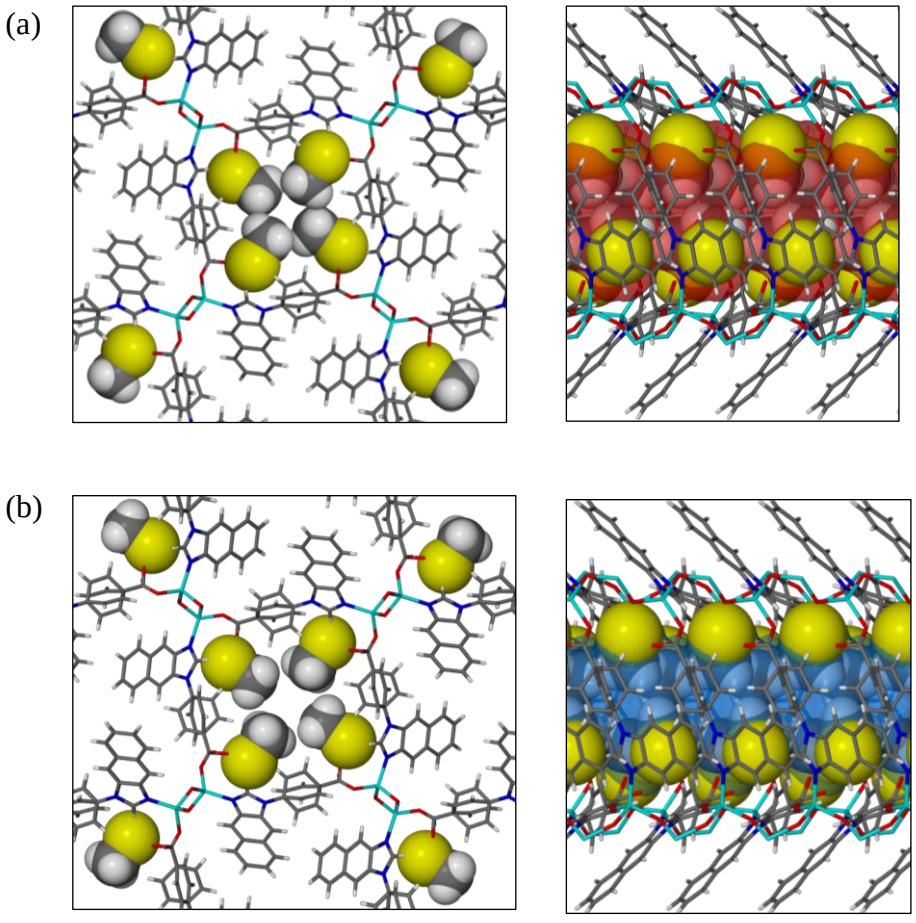

Figure 82. The methyl bromide molecules in the channel of **CH_3Br-IMMOF-3**, viewed along the *c* and *a* axes at (a) 298 K and (b) 273 K. In the views along [100] the Connolly surface (in red and blue) was mapped using MSROLL[39] (probe radius of 1.4 Å).

Vinyl halogen inclusion

When the crystal was allowed to equilibrate under atmospheres of vinyl fluoride, vinyl chloride, and vinyl bromide, only vinyl fluoride and vinyl bromide were included in an appreciable amount. Moreover, the electron count within the channel suggests low average occupancies of 1.72 and 1.70 molecules per ~300 $Å^3$ channel section, respectively.

The vinyl fluoride molecules are disordered over the four symmetry-related positions as directed by the location of the four interaction sites on the channel wall (Figure 83). The symmetry-related positions of the vinyl fluoride molecules within the channel only differ slightly between the structures determined at 298 and 250 K. Again, the temperature-dependent halogen bond distance decreases from 2.93(4) Å at 298 K to 2.87(4) Å at 250 K.

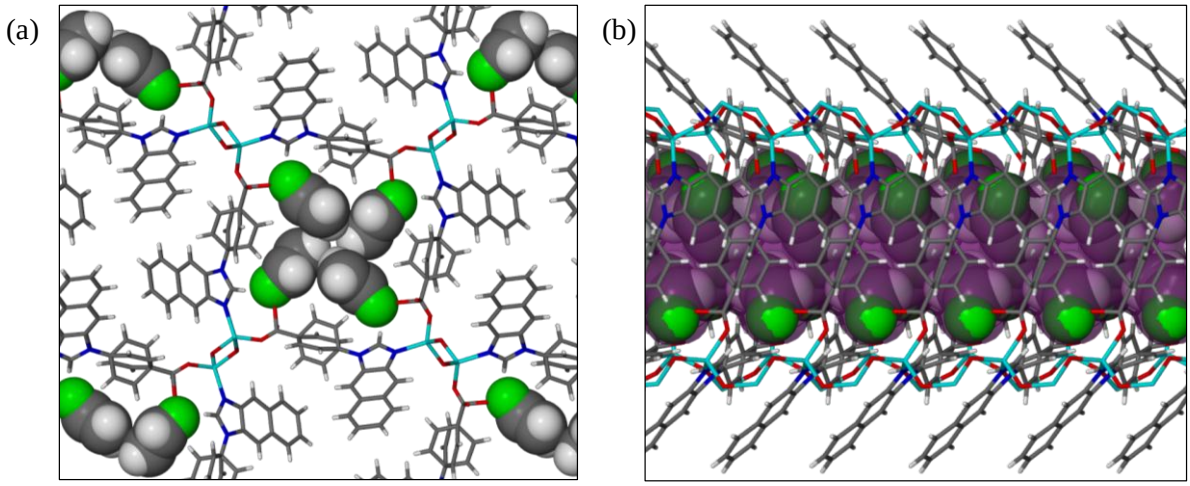

Figure 83. (a) Vinyl fluoride included within the channels of **C_2H_3F-IMMOF-3**, viewed along [001] and (b) perpendicular to [001]. The Connolly surface, mapped using MSROLL[39], is shown in purple (probe radius of 1.4 Å).

The orientation and position of vinyl bromide within the channel are different to those of vinyl fluoride because of the larger atomic radius of the bromine atom (Figure 84).

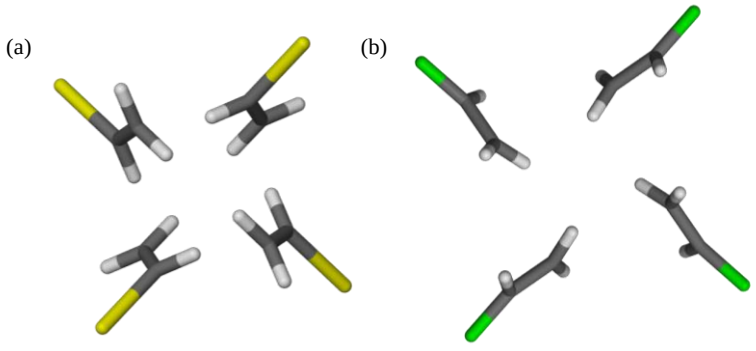

Figure 84. The four symmetry-related positions of (a) vinyl bromide and (b) vinyl fluoride within a channel section of **IMMOF-3**.

Vinyl bromide, with the softer electrophilic halogen atom, should participate in a stronger halogen bond with the carboxyl-oxygen atom of the framework than vinyl fluoride. Indeed a short O···Br contact of 3.02(4) Å that is 0.35 Å shorter than the sum of the van der Waals radii (3.37 Å) occurs (Figure 85), as opposed to the O···F distance of 2.87(4) Å, which is only 0.12 Å shorter than the sum of the van der Waals radii (2.99 Å). The average interaction distances are shown in Figure 85.

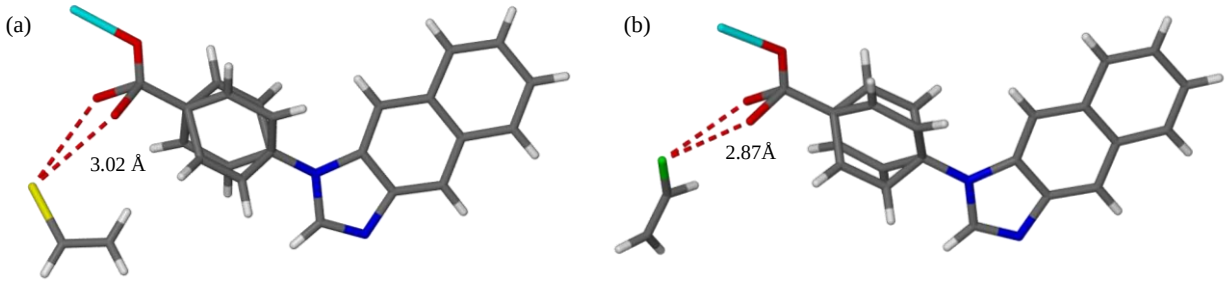

Figure 85. Halogen bonding distances shown (dashed red lines) of (a) vinyl bromide (**C_2H_3Br-IMMOF-3**) and (b) vinyl fluoride (**C_2H_3F-IMMOF-3**) at 220 and 250 K, respectively.

Exclusion of vinyl chloride

Interestingly, vinyl chloride does not appear to enter the channels and this interesting observation prompted a computational study. Molecular mechanics calculations using a script designed to imitate the diffusion of a guest molecule through a channel section was performed using the Forcite module in Materials Studio V4.3. A supercell (1 × 1 × 4 the unit cell axes) that represents one channel was constructed from the apohost crystal structure and defined as a non-periodic superstructure. The uncoordinated oxygen atom and hydrogen atom positions were geometrically optimised and charges were assigned to all the constituent atoms of the framework using the charge equilibration method. Following this procedure, an optimised guest molecule was translated through the channel (Figure 86). The position of the halogen atom (the heaviest atom) was fixed and translated down the middle of the channel while the rest of the guest molecule's atoms were allowed to optimise in order to allow rotational motion of the molecule.

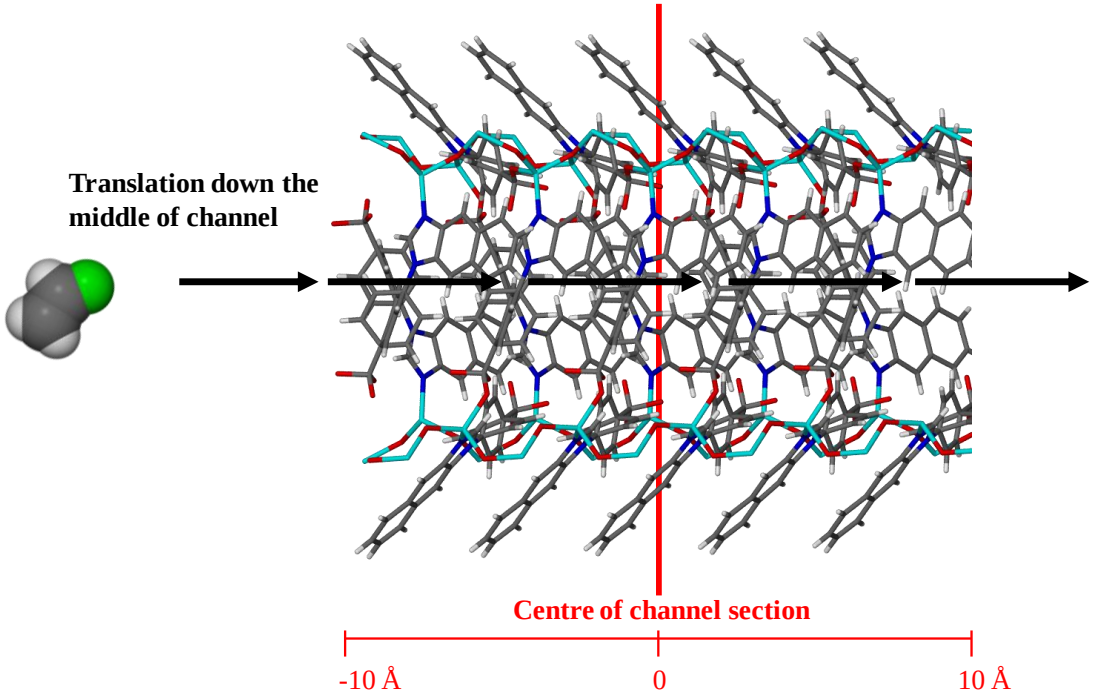

Figure 86. A graphical representation of the model used for single-point energy calculations that were performed as the guest is located at a specific distance from the centre of the **IMMOF-3** channel section. The guest vinyl fluoride molecule (space-filled representation) is translated down the middle of the channel section (capped stick representation, ~20 Å in length).

The single-point energy (Dreiding forcefield) of the system was initially calculated at 1 Å translational increments and at 0.5 Å increments once the guest was located further inside the channel. The results of the calculations are shown in Figure 87.

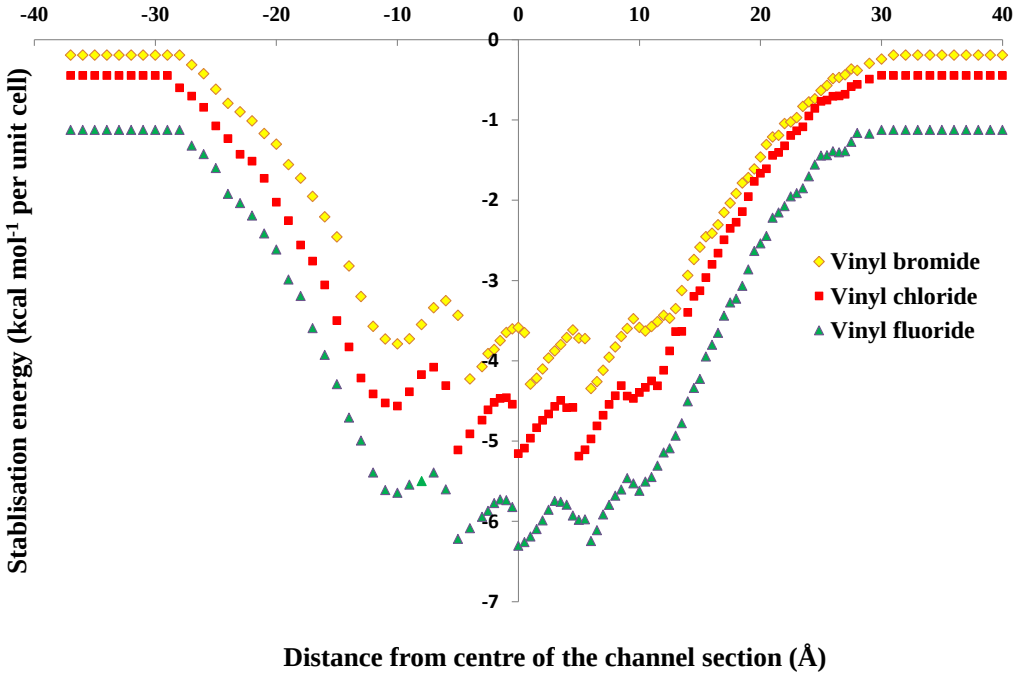

Figure 87. Energy curves for the diffusion of vinyl fluoride, vinyl chloride and vinyl bromide through a channel of **IMMOF-3**.

Vinyl fluoride is most stabilised within the channel owing to its involvement in the most favourable electrostatic interactions with the framework, followed by vinyl chloride and then vinyl bromide. The minima in the energy curves correspond to when the guest molecule is the closest to the carboxyl groups of the host framework, which are periodically positioned every ~5 Å (or the *c*-axis length) along the channel length.

The calculations show that inclusion of vinyl chloride does stabilise the system and should occur thermodynamically if vinyl bromide is able to diffuse into the channels. The calculations were, however, only performed with one guest molecule, and the kinetics of the diffusion process as well as the effect of guest-guest interactions were not taken into account. The fact that vinyl chloride could not be observed within the channels could be ascribed to extremely slow diffusion kinetics, i.e. that equilibrium had not been reached after approximately 12 hours of exposure to the gas.

In conclusion, accurate determination of the atomic coordinates of gas molecules in the crystal requires a favourable interaction with the host lattice or framework. A smaller void space and low symmetry (such as a triclinic space group) would also aid in resolving guest positions within a porous lattice. While sorption isotherms are useful in terms of the determination of the capacity of the framework, the structural data provide valuable information concerning the host-guest interactions that might be involved in selectivity for one gas over another.

4.2.6 Structural response to the guest

Significant structural changes to the **IMMOF-3** framework occur upon the inclusion of a variety of guest molecules, whilst the crystal retains its single-crystal nature. The void space of the channel can expand volumetrically by 15.2% from its original size when it includes larger guests such as *iso*-propanol. Much larger swelling of hybrid frameworks has been reported previously, the highest "breathing amplitude" being approximately 70% by MIL-88, as reported by Férey *et al.*[65] However, the breathing of MIL-88 does not occur as a single-crystal transformation, as is the case with **IMMOF-3**. To elucidate the mechanism of the expansion observed with MIL-88, the authors had to make use of synchrotron PXRD and computational methods. In the present case, the SCD datasets provide all the necessary evidence for the mechanism involved in the structural response.

Solvent inclusion, as opposed to gas inclusion, resulted in size- and shape-responsive fitting of the guest within the channel. Whilst maintaining the original symmetry, the unit cell dimensions are subject to considerable changes when the framework accommodates guest molecules of different size, shape and polarity (Table 18). The *a* and *b* unit cell axes vary in length between 26.192(2) and 26.772(2) Å, and the *c* axis between 5.0662(4) and 5.3960(4) Å.

Table 18. Unit cell parameters and void volumes for different inclusion complexes at 100 K.

Guest	*a*, *b* axes (Å)	*c* axis (Å)	Volume (Å^3)	Void volume Platon, SQUEEZE[36,37] (Å^3)	void/volume ratio
methanol	26.772(2)	5.0662(4)	3631.2(5)	297	8.18%
water	26.701(6)	5.123(1)	3653(1)	299	8.19%
ethanol	26.713(4)	5.0883(8)	3631(1)	297	8.18%
n-propanol	26.742(4)	5.1504(8)	3683(1)	316	8.58%
iso-propanol	26.192(2)	5.3960(4)	3701.7(5)	342	9.23%
acetone	26.722(2)	5.0968(4)	3639.4(5)	301	8.27%
dichloromethane	26.722(4)	5.1135(7)	3651.3(9)	317	8.68%
chloroform	26.579(7)	5.081(1)	3590(2)	299	8.33%
carbon tetrachloride*	26.666(4)	5.1006(7)	3626.9(9)	304	8.36%
benzene*	26.683(3)	5.0972(6)	3629.1(7)	296	8.16%
acetonitrile	26.703(2)	5.0928(3)	3631.4(4)	301	8.29%
toluene*	26.654(5)	5.1138(9)	3633(1)	303	8.34%
iodine	26.472(6)	5.244(1)	3675(1)	327	8.90%

* Includes water molecules and not the guest molecule listed.

The void/volume ratio increases from 8.18% for the methanol inclusion complex to 9.23% for the *iso*-propanol inclusion complex. The framework therefore responds to the guest size and shape by not only expanding as a whole but also by adjusting the atomic positions relative to one another within the unit cell. Nevertheless, there is a direct relationship between the void volume and *c*-axis length as a result of the inclusion of different guest molecules, as is evidenced by the plot shown in Figure 88.

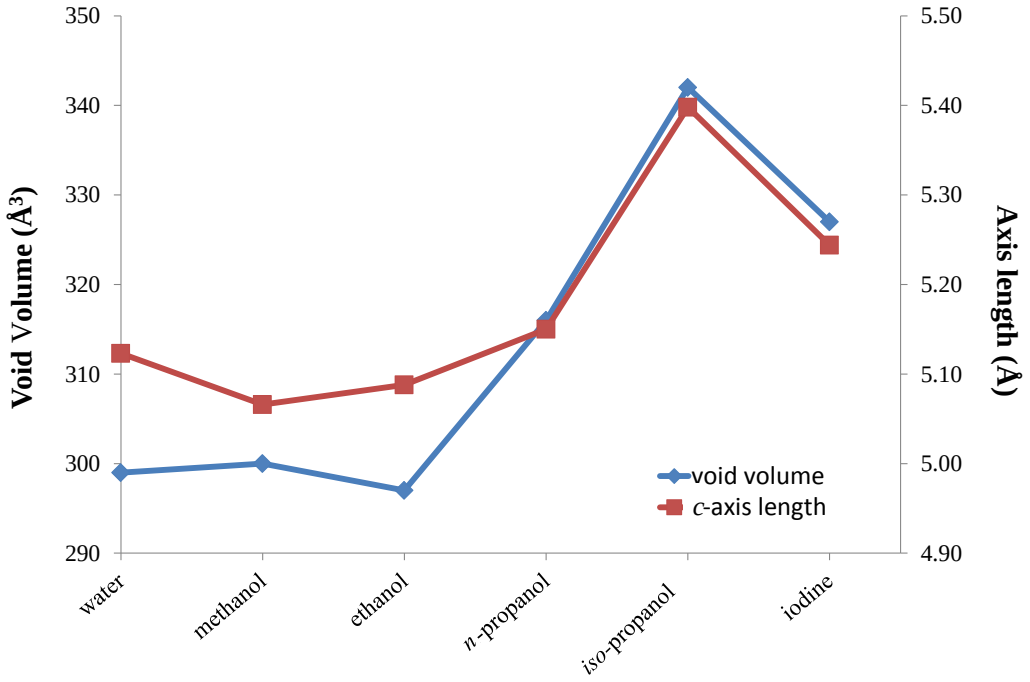

Figure 88. A plot of the void volume and *c*-axis length of different **IMMOF-3** inclusion complexes.

The channel increases in volume, expanding along its length when the steric bulk of the guest substituent is increased (Figure 89).

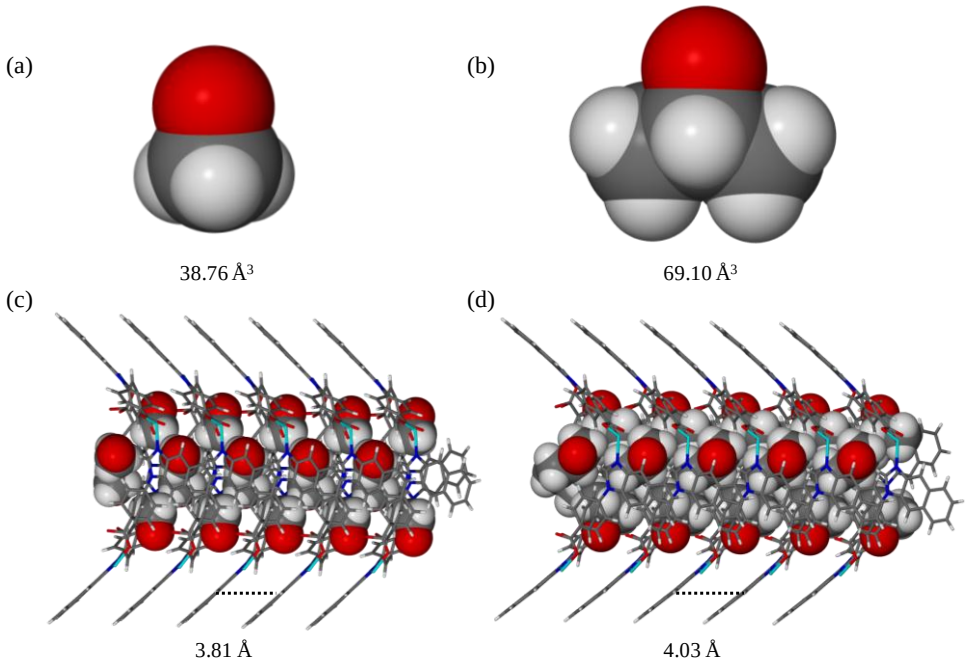

Figure 89. The volume of (a) methanol and (b) *iso*-propanol calculated from the van der Waals surface of each molecule (the hydrogen atoms bound to the hydroxyl-oxygen atoms have been omitted from the graphical representation but not from the calculation of the volume of the molecules). A channel section of (c) the methanol inclusion complex and (d) the *iso*-propanol inclusion complex of **IMMOF-3** with the π-bond interaction distance between stacked naphtha-imidazolyl moieties represented by a black dashed line.

The series of inclusion complexes formed with the alcohols best displays the trend of expansion along the *c* axis. Across this particular series the guest occupancy is approximately constant (four molecules per ~300 $Å^3$ channel section), even with an increase in the size of the guest. Structural analysis of these complexes, as well as those incorporating water and iodine, revealed that there are several changes to the host framework that are induced upon inclusion. The structural characteristics involved with the expansion along the *c* axis are summarised in Table 19.

Table 19. Summary of the structural features involved in the linear expansion of the channel.

Guest	Guest molecular volume[a] ($Å^3$)	*c* Axis (Å)	Void volume Platon[36], SQUEEZE[37] ($Å^3$)	Zn···(OH) ···Zn distance (Å)	Zn-O(H)-Zn angle (°)	O_{carb}[b]-Zn-O_{hydr} angle (°)	O_{carb}···O_{hydr} framework hydrogen bond distance (Å)	Offset π-bond distance (Å)
water	19.4	5.123(1)	299	3.4095(7)	124.0(1)	107.4(1)	2.828(3)	3.82
methanol	38.8	5.0662(4)	300	3.4006(5)	123.7(1)	108.2(1)	2.820(4)	3.81
ethanol	54.0	5.0883(8)	297	3.4008(7)	123.8(2)	108.7(1)	2.812(5)	3.83
n-propanol	70.7	5.1504(8)	316	3.4142(6)	124.6(1)	109.0(1)	2.835(3)	3.85
iso-propanol	69.1	5.3960(4)	342	3.4678(6)	127.4(1)	115.9(1)	2.901(4)	4.03
iodine	61.3	5.244(1)	327	3.446(2)	127.3(5)	110.3(6)	2.92(2)	3.97

[a] The guest molecular volume was calculated using Materials Studio V4.3 from the van der Waals surface (i.e. the surface that intersects with the van der Waals radii of the atoms in the structure) using geometrically optimised models of the molecules.
[b] O_{carb} is the oxygen atom of the carboxyl group of the ligand that is coordinated to the metal

The expansion of the channel is facilitated by a Zn-O(H)-Zn angle deformation, as shown in Figure 90. In other words, it is the flexibility of the hydroxyl-bridges that facilitates guest-responsive enlargement of the channel along its length.

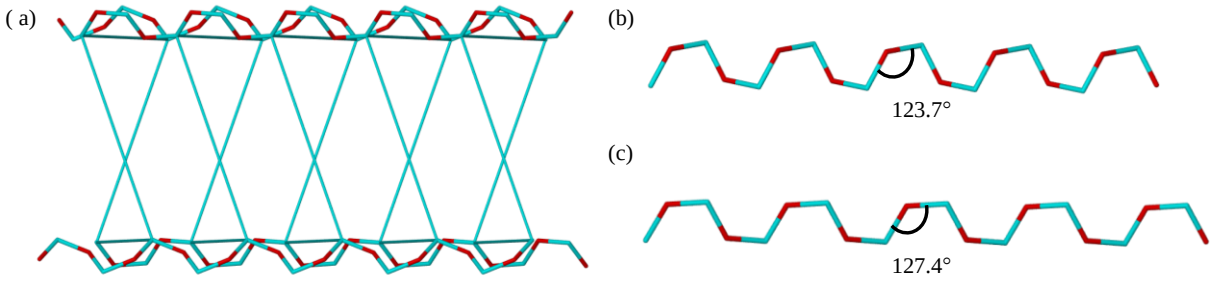

Figure 90. (a) The topology of a channel section of **IMMOF-3** (connections between metal nodes) with the hydroxyl oxygen atoms that bridge metal centres along the *c* axis also shown. The Zn-O(H)-Zn angle in (b) the methanol inclusion complex and (c) the *iso*-propanol inclusion complex.

The angle deformation is accompanied by a simultaneous increase in the Zn···(OH)···Zn distance. Two of these angles span one unit cell length and this effect is thus duplicated, resulting in the large expansion along the *c* axis (Figure 91).

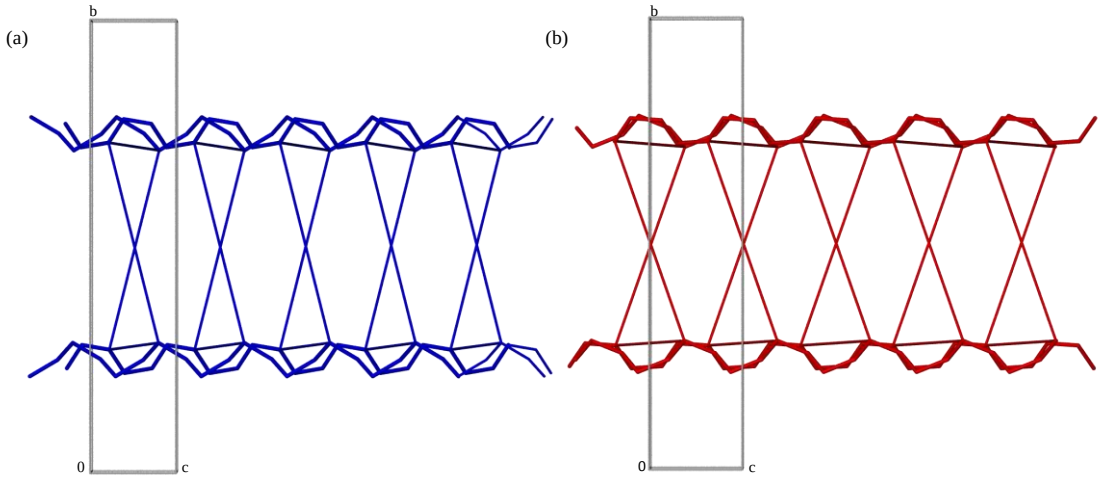

Figure 91. Topological representations of the channels of (a) the methanol inclusion complex and (b) *iso*-propanol inclusion complexes of **IMMOF-3**, viewed along [100]. The positions of the hydroxyl bridges lining the channel are subject to the most change.

As the *c* axis increases in length, the *a* and *b* axes of the unit cell are reduced from 26.772(2) Å in the original methanol-containing complex to 26.192(2) Å in the *iso*-propanol inclusion complex. In other words, the channel becomes narrower as it is elongated. A structural overlay of a cross-section through the channels of the methanol and *iso*-propanol inclusion complexes is shown in Figure 92.

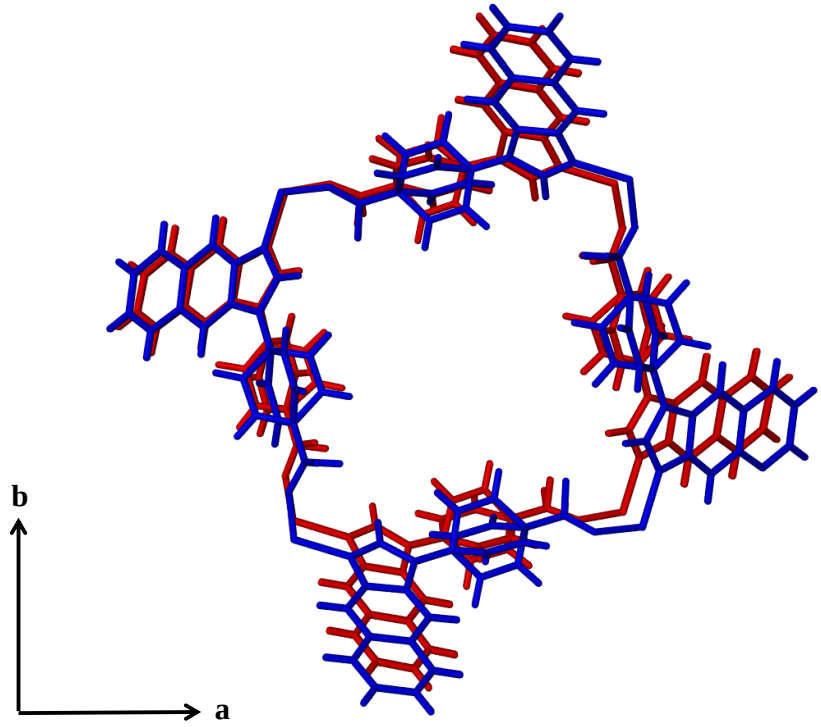

Figure 92. A structural overlay of the methanol (blue) and *iso*-propanol (red) inclusion complexes of **IMMOF-3**.

The guest-shape-responsive fitting that necessitates expansion along one direction and contraction along the perpendicular direction are responsible for changes in the coordination geometry around the metal centre. Coordination bond lengths remain approximately the same, but there are changes in the coordination angles upon guest inclusion that require less energy (Table 20).

Table 20. The variation of the unit cell parameters and the coordination angles of different inclusion complexes of **IMMOF-3**.

Guest	*a*, *b* axes (Å)	*c* axis (Å)	N-Zn-O_{carb} (°)	O_{carb}-Zn-OH1 (°)	N-Zn-OH1 (°)	O_{carb}-Zn-OH2 (°)	N-Zn-OH2 (°)	O(H1)-Zn-OH2 (°)
water	26.701(6)	5.123(1)	112.4(1)	107.4(1)	115.9(1)	105.3(1)	110.6(1)	104.45(6)
methanol	26.772(2)	5.0662(4)	111.3(1)	108.2(1)	117.3(1)	106.62(9)	109.0(1)	103.68(6)
ethanol	26.713(4)	5.0883(8)	110.9(1)	108.8(1)	117.3(2)	106.5(1)	108.7(1)	103.88(8)
n-propanol	26.742(4)	5.1504(8)	112.3(1)	109.0(1)	116.3(1)	105.2(1)	109.2(1)	104.06(6)
iso-propanol	26.192(2)	5.3960(4)	110.6(1)	115.9(1)	113.8(1)	101.2(1)	108.5(1)	105.82(6)
iodine	26.472(6)	5.244(1)	113.3(5)	110.5(5)	114.5(5)	104.2(5)	109.6(5)	104.0(3)

The angular deformations bring about concerted shifting of all of the atomic positions to yield a more strained high-energy state. The high-energy state is stabilised by the favourable interaction energy of the guest with the host framework. Another noticeable effect of the strain the guest imposes on the framework pertains to the disorder of the phenylene ring of the ligand. The larger the volume of the guest, the smaller the angle between the planes of the two disordered phenylene rings (Figure 93 and Table 21).

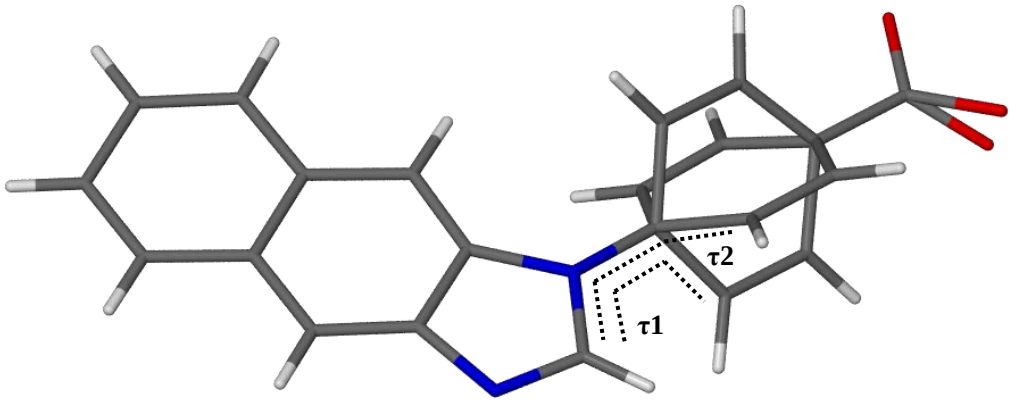

Figure 93. The disorder of the phenylene ring of **IMMOF-3** with two torsion angles τ1 and τ2 (listed in Table 21) between the naphtha-imidazolyl and phenylene groups shown with dotted black lines.

Table 21. The disorder of the phenylene ring in different inclusion complexes.

Guest	Angle between two disordered rings (°)	τ1 (°)	τ2 (°)
water	79.3	37.6(6)	-41.2(6)
methanol	70.1	30.7(6)	-36.8(6)
ethanol	66.2	34.6(8)	-30.2(8)
n-propanol	65.0	29.9(6)	-35.0(6)
iso-propanol	57.9	25.0(5)	-27.0(2)
iodine	66.3	25.0(2)	-36(2)

The lattice enthalpy values of the various inclusion complexes were calculated using Materials Studio V4.3. Geometry optimisations (Dreiding forcefield) were performed with the positions of all the atoms of the crystal structure fixed except those of the hydrogen atoms and the uncoordinated oxygen atom of the carboxyl group on the ligand. The guest molecules were deleted from the structure in order to obtain the enthalpy for the framework only and to allow direct comparison between the different complexes.

The results confirmed the premise that inclusion of larger sized guest molecules results in a more strained framework with higher lattice enthalpy values. It follows that the interaction energy of these guests with the framework needs to be more stabilising (i.e. more negative) than that of the original methanol guest in order to compensate for the destabilising transformations in the framework. It must also be noted that, since the original methanol molecules can be exchanged for larger molecules, the original framework is not necessarily in its lowest energy state. The lattice enthalpy values plotted in Figure 94 are not absolute energy values.

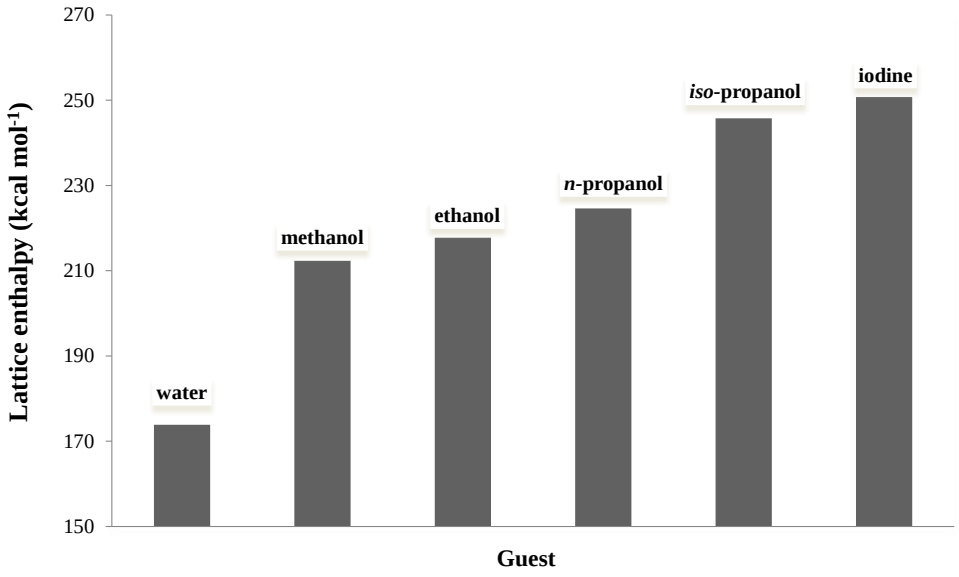

Figure 94. Lattice enthalpy values calculated for different inclusion complexes of **IMMOF-3**.

The structural response to other halogenated guest molecules

The inclusion of halogenated solvents such as dichloromethane (55.8 $Å^3$), chloroform (70.1 $Å^3$) and/or acetone and acetonitrile did not induce the same type of expansion of the channel with increasing guest size. In the case of dichloromethane and chloroform the occupancy is only two molecules per ~300 $Å^3$ such that expansion is not necessary. Acetone and acetonitrile do not occupy the four symmetry-related interaction sites within the channel as efficiently as the hydroxyl-functionalised guests, thus resulting in disordered models. The different packing of these guest molecules in the channels does not appear to necessitate a significant change in the framework structure. The halogenated guest molecules participate in halogen bonding interactions with the framework. This type of host-guest interaction is weaker than the hydrogen bonding interactions that occur with hydrogen bond donors such as alcohols and water. Therefore, it seems that the extent and type of change induced in the framework does not only depend on the size and shape of the molecules, but also the electrostatic topology and type of host-guest interactions that are at play. The framework is able to include larger sized guests and undergo destabilising transformations only when there is a strong interaction such as a hydrogen bond between the host framework and guest molecules.

During the study of the various host-guest adducts of **IMMOF-3** it was noticed that the unit cell dimensions are not only guest dependant but also temperature dependant. The discovery prompted further studies of the thermal response of the framework when it does not include any guest molecules, as well as when it includes guest molecules, in order to gain a molecular level understanding of its thermal expansion behaviour under different conditions.

4.3 ANISOTROPIC THERMAL EXPANSION OF A POROUS ZN(II) FRAMEWORK

4.3.1 Isotropic and anisotropic thermal expansion

When a material is heated it normally experiences positive thermal expansion (PTE) along all three dimensions, owing to an increase in the anharmonic vibrations of the constituent atoms, molecules or ions. The PTE of solids is mostly caused by collective atomic motions resulting from bond-bending and bond-stretching vibrations.[66] These vibrations have the largest effect on intermolecular interaction distances. Weak intermolecular forces have shallow interatomic potential wells, which give rise to greater amplitudes of anharmonic vibration, while covalent bonds have a steeper potential well and smaller changes in the covalent bond lengths are observed upon temperature fluctuations.[67] In rare cases, specific structural features or packing arrangements in the solid state may give rise to anomalous thermal expansion behaviour such as unusually large positive thermal expansion (PTE), zero thermal expansion (ZTE) and negative thermal expansion (NTE). The thermal response may be isotropic, with expansion or contraction occurring along all three unit cell axes (e.g. in cubic systems), or anisotropic, when the thermal expansion is not uniform in all three dimensions. PTE and NTE can be quantified in terms of the linear expansion coefficient, conveniently expressed in relation to the three crystallographic axes. In the present investigation, the unit cell parameters of a single crystal of **IMMOF-3** were measured at 15 K intervals and the linear thermal expansion coefficient, $\boldsymbol{\alpha}$, for each of the axes *a*, *b* and *c* was calculated using equation (2):

$$\propto = \frac{\Delta L}{L_0 \Delta T} \qquad (2)$$

where ΔL is the difference in length of the crystallographic axis over a specified temperature range (although $\boldsymbol{\alpha}$ can also be calculated using the change in the length of the crystal itself), L_0 is the initial length of the axis at the initial (lower) temperature, T_0, and ΔT is the change in temperature. The volumetric expansion coefficient, $\boldsymbol{\alpha_V}$, can be calculated using a modified form of equation (2) (i.e. by substituting ΔV for ΔL and V_0 for L_0). The PTE coefficients for most common materials (glass, metals and ceramics) are usually in the range of 4×10^{-6} K^{-1} (glass) to 24×10^{-6} K^{-1} (aluminium) (Figure 95).

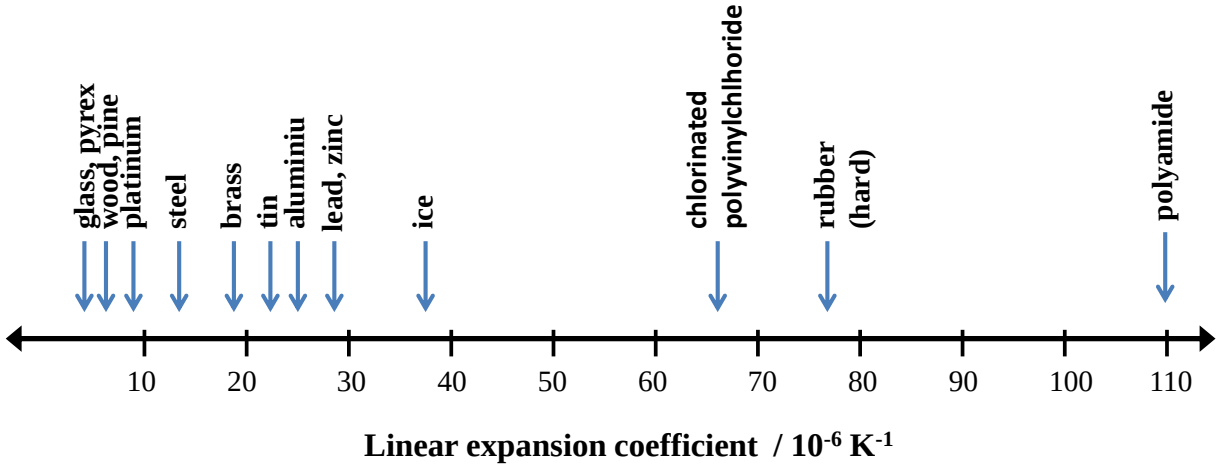

Figure 95. The positive linear expansion coefficients of a range of common materials.

Materials with PTE coefficients larger than 10^{-4} K^{-1} have previously been described as having "colossal" thermal expansion (e.g. $Ag_3[Co(CN)_6]$ and other Prussian blue analogues).[68] The mechanisms at work in materials displaying colossal thermal expansion are very different from the usual vibrational mechanism found in materials with small to medium expansion coefficients (and are not yet well understood). The elucidation of such a mechanism provides insight for the design of thermo-responsive materials that can be used in sensors and actuators. In some cases colossal PTE is accompanied by NTE along a different axis. NTE in itself is a very interesting phenomenon. There have been many reports in the recent literature of NTE in inorganic oxides and zeolites.[69] However, it is rare for purely organic materials to display NTE and compounds such as (S,S)-octa-3,5-diyne-2,7-diol,[70] methyl paraben, 4,4′-diiodobiphenyl and 4-iodobenzoic acid have been studied in this regard.[71] The mechanisms responsible for anisotropic NTE are usually related to a specific structural feature such as a flexible metal-organic framework with hinged motion around a metal centre. A specific packing arrangement that can undergo concerted molecular motion due to expansion of an intermolecular interaction distance along one direction that necessitates the contraction of intermolecular distances in the opposite direction can also result in anisotropic NTE. Furthermore, there are many reported mechanisms of NTE such as magnetic ordering, electron transfer, and vibrational mechanisms, including transverse vibrations[72] (Figure 96). Other suggested mechanisms of NTE are associated with phase transitions; e.g. the temperature dependence of the unit cell parameters of $PbTiO_3$ as it approaches its ferroelectric-paraelectric phase transition at 490 °C.[69a]

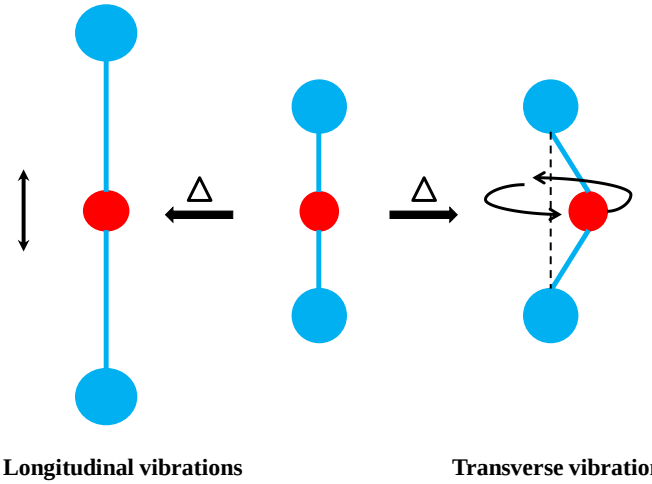

Figure 96. Longitudinal vibrations result in PTE, while transverse "guitar string" vibrations may cause NTE.

4.3.2 Anomalous thermal expansion of metal-organic frameworks

Metal-organic frameworks (MOFs) have recently emerged as a new class of thermo-responsive materials with anomalous thermal expansion behavior. Anisotropic and exceptionally large thermal expansion, in the order of that of $Ag_3[Co(CN)_6]$ and other Prussian blue analogues[68] ($>10^{-4}$ K^{-1}), has been reported for the flexible HMOF-1, which has a lattice-fence topology and hinged motion around the metal centre.[66] Other types of framework materials known to display isotropic NTE include the cyanide bridged coordination polymers,[68c,73] the isoreticular IRMOFs, the NASICON (sodium super-ionic conductor) or NZP (sodium zirconium phosphate) family based on the $NaZr_2(PO_4)_3$ structure type[69a] and $Cu_3(btc)_2$ where btc = 1,3,5-benzenetricarboxylate.[72] $Cu_3(btc)_2$ displays isotropic NTE owing to the transverse vibration of the entire btc linker. Frustration due to metal connectivity leads to libration of the benzene linker, which is necessary for concerted vibrational modes.[72] In certain zeolites[69b,74] and AM_2O_8, AM_2O_7, $A_2M_3O_{12}$ (principally A = Zr, Hf, M = W, Mo) NTE is caused by the contraction of the metal-oxygen-metal (M-O-M) bridges, causing a concomitant contraction of the metal-to-metal (M-M) distance. These transverse vibrations result in the rotation and translation of metal-coordination polyhedra that counteract the higher energy longitudinal vibrations that cause bond-length expansion.[75] The low-energy transverse vibrational modes result in the overall NTE of the zeolitic material.

Quite recently MOF-research has branched from exclusively focusing on porosity to the exploration of anomolous thermal expansion, temperature-shock resistance, compressibility and other interesting mechanical properties of these self-assembled frameworks.[76]

4.3.3 Anisotropic thermal expansion behaviour of IMMOF-3

Porous **IMMOF-3** displays unusually large anisotropic thermal expansion, a property that can be considered additional evidence of the material's dynamic nature. A crystal of the apohost framework (**IMMOF-3$_{apohost}$**) placed under static vacuum (within a gas cell) exhibits exceptionally large uniaxial PTE with $\boldsymbol{\alpha}_c$ = 123 × 10^{-6} K^{-1} along the *c* axis, measured over a temperature range of 100-370 K. The PTE along the *c* axis is accompanied by biaxial NTE along the *a* and *b* axes with $\boldsymbol{\alpha}_{a,b}$ = –21 × 10^{-6} K^{-1} for the same temperature range. The exceptional PTE along the *c* axis, which is an order of magnitude larger than conventional PTE, results in an equally impressive overall volumetric expansion of $\boldsymbol{\alpha}_V$ = 87 × 10^{-6} K^{-1} (calculated from the unit cell volume over a temperature range of 100-370 K, Table 22).

Table 22. Unit cell determination at variable temperatures.

	Unit cell parameters			
Temperature (K)	***a, b* axis (Å)**	***c* axis (Å)**	**Volume (Å^3)**	**Crystal mosaicity (°)**
100	26.54(2)	5.151(3)	3625(7)	0.65
115	26.54(2)	5.165(3)	3640(8)	0.64
130	26.54(2)	5.180(3)	3650(8)	0.64
145	26.54(2)	5.191(4)	3655(9)	0.64
160	26.50(2)	5.200(4)	3652(9)	0.63
175	26.50(2)	5.215(4)	3662(8)	0.62
190	26.50(2)	5.228(4)	3672(10)	0.62
205	26.49(2)	5.241(4)	3679(10)	0.63
220	26.48(2)	5.248(4)	3680(9)	0.63
235	26.48(2)	5.262(3)	3691(8)	0.63
250	26.46(2)	5.268(4)	3688(10)	0.63
265	26.43(2)	5.272(4)	3684(9)	0.64
280	26.41(2)	5.280(4)	3681(10)	0.64
295	26.41(2)	5.289(4)	3689(10)	0.64
310	26.43(2)	5.296(5)	3699(12)	0.63
325	26.41(2)	5.302(5)	3697(11)	0.63
340	26.39(2)	5.308(4)	3698(8)	0.64
355	26.40(2)	5.3153)	3703(9)	0.64
370	26.40(2)	5.328(4)	3712(9)	0.65

Standard deviation calculated from unit cell refinement within the APEX II software suite.

Surprisingly, the crystal mosaicity is not affected by the temperature or the anisotropic expansion itself (Table 22). The plots of the unit cell parameters and unit cell volume, show small deviation from linearity at approximately 180 K and 250 K (Figure 97 and Figure 98). The

non-linearity in the thermal response is believed to be a structural phenomenon or property of the host framework that merits further investigation.

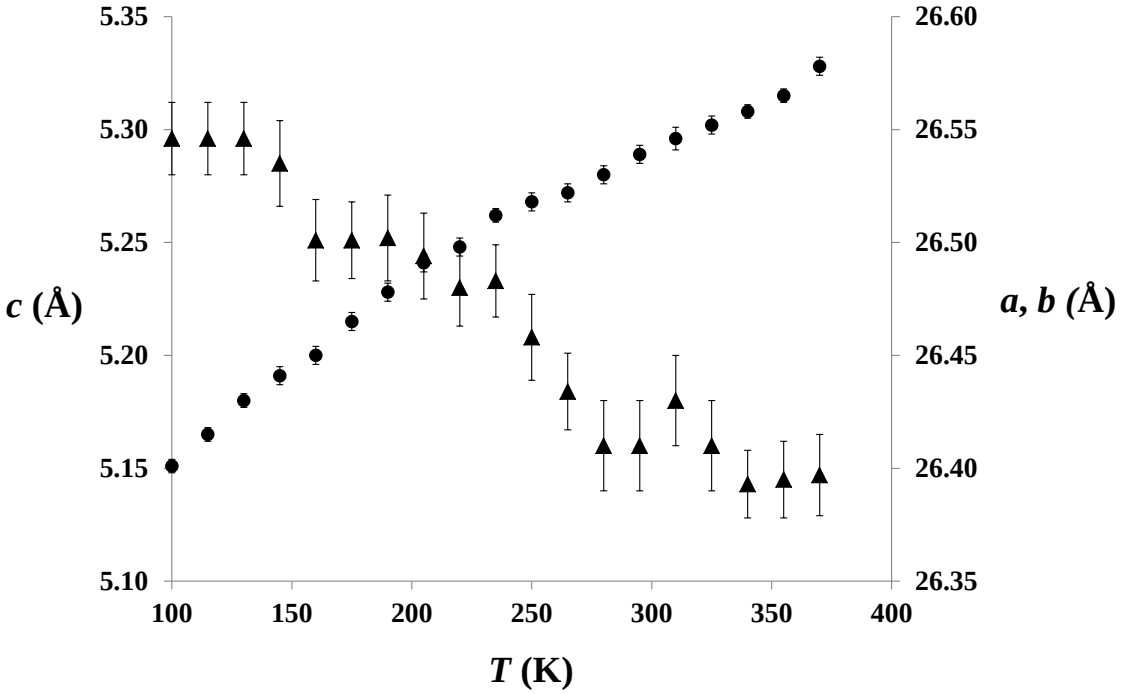

Figure 97. The thermal expansion and contraction of unit cell axes of a single crystal of **IMMOF-3$_{apohost}$** placed under static vacuum within the gas cell and determined at increasing temperatures (circles = *c* axis and triangles = *a* and *b* axes). The error bars represent the estimated standard deviations of the values and were obtained from unit cell refinement with the APEX II software suite.

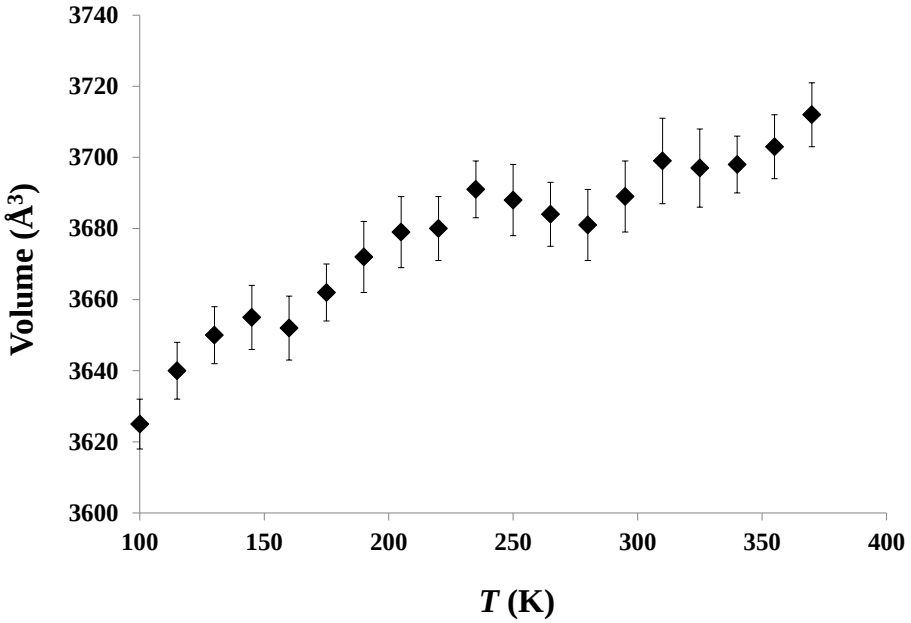

Figure 98. A plot of the volumetric thermal expansion of **IMMOF-3$_{apohost}$** in the 100-370 K temperature range. The estimated standard deviations of the values obtained from unit cell refinement with the APEX II software suite are shown.

Table 23 lists the expansion coefficients for the *a*, *b* and *c* axes calculated for each of the 15 K increments. The statistical average of the **α** values in the table ($\alpha_{a,b}$ = -20 × 10^{-6} K^{-1}, α_c = 125 × 10^{-6} K^{-1}) compares well with **α** calculated over the entire 100-370 K temperature range ($\alpha_{a,b}$ = -21 × 10^{-6} K^{-1}, α_c = 123 × 10^{-6} K^{-1}), however there is significant standard deviation from the average value, which could indicate non-linear behaviour. This behaviour is probably due to the interplay between different thermal response mechanisms in the material and in the energy barriers associated with specific structural transformations. Another possibility is that there is an order-disorder transition that occurs at a specific temperature, which results in the deviation from non-linearity. To monitor whether such a transition might be occurring, recording solid-state NMR at variable temperatures might yield some insight. Solid-state NMR can also be employed for the elucidation of the thermal response mechanism itself and can form part of future studies.

Table 23. The linear thermal expansion coefficients of **IMMOF-3$_{apohost}$** calculated at 15 K intervals.

Temperature (K)	***a*- & *b*-axis length (Å)**	**$\alpha_{a,b}$ x10^6 (K^{-1})**	***c*-axis length *(Å)***	**α_c x 10^6 (K^{-1})**
100	26.54(2)	-	5.151(3)	-
115	26.54(2)	0	5.165(3)	181
130	26.54(2)	0	5.180(3)	193
145	26.54(2)	0	5.191(4)	141
160	26.50(2)	-100	5.200(4)	115
175	26.50(2)	0	5.215(4)	192
190	26.50(2)	0	5.228(4)	166
205	26.49(2)	-25	5.241(4)	165
220	26.48(2)	-25	5.248(4)	89
235	26.48(2)	0	5.262(3)	177
250	26.46(2)	-59	5.268(4)	76
265	26.43(2)	-76	5.272(4)	51
280	26.41(2)	-50	5.280(4)	101
295	26.41(2)	0	5.289(4)	113
310	26.43(2)	50	5.296(5)	88
325	26.41(2)	-50	5.302(5)	75
340	26.39(2)	-50	5.308(4)	75
355	26.40(2)	25	5.3153)	88
370	26.40(2)	0	5.328(4)	163
	Average	**-20**	**Average**	**125**
	Std Dev	**37**	**Std Dev**	**47**

Since the mechanical response to temperature does not result in the loss of single-crystal quality of the material, structure determinations from SCD at regular temperature intervals can afford the necessary information to determine the mechanism involved. Single crystal X-ray

diffraction data were collected at 100, 190, 280 and 370 K with a guest-free crystal kept under static vacuum for the duration of the experiment. Structural analysis revealed that changes in the metal geometry and intra-framework hydrogen bond distances are involved with the anisotropic thermal expansion observed. There are also changes in the atomic displacement parameters (ADPs) due to the temperature-dependent increase in the amplitudes of atomic and overall framework vibrations. Although the changes in the lengths of the coordination bonds are minimal, a number of coordination angles change considerably. The three coordination angles that are subject to most of the temperature-dependent variation are shown in Figure 99 and the structural data are summarised in Table 24.

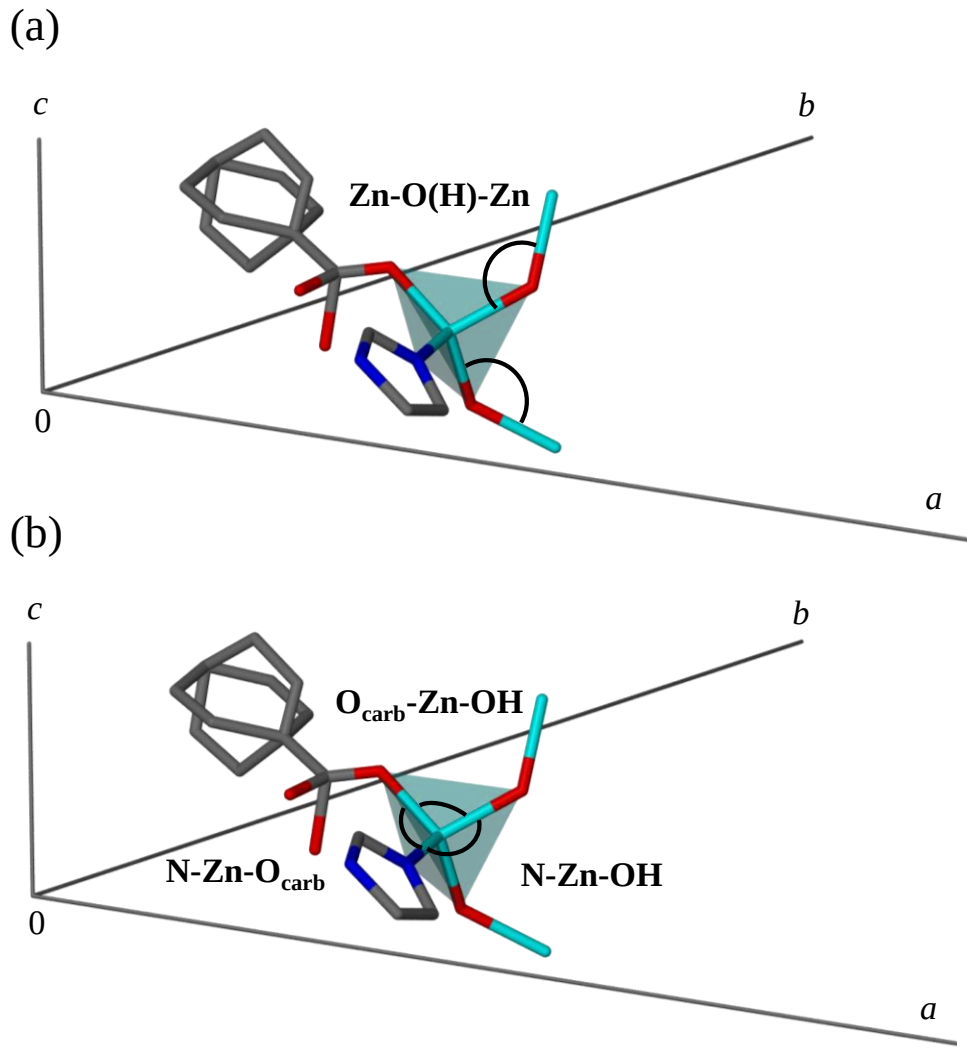

Figure 99. The coordination environment around the tetrahedral Zn^{II} node in **IMMOF-3$_{apohost}$**, in relation to the unit cell axes. (a) The polymeric Zn-O(H)-Zn angles that expand with increasing temperature along [001] are shown. (b) The O_{carb}-Zn-OH, N-Zn-O_{carb} and the N-Zn-OH angles that are approximately in the *ab* plane, contract upon heating. Hydrogen atoms have been omitted for clarity.

Table 24. Temperature-dependent structural data for **IMMOF-3$_{apohost}$**.

	Unit cell parameters			PTE		NTE			
T (K)	*a*, *b* axes (Å)	*c* axis (Å)	Void volume Platon[36], SQUEEZE[37] (Å^3)	Zn-O(H)-Zn angle (°)	Zn···(O)···Zn distance (Å)	N-Zn-OH angle (°)	N-Zn-O$_{carb}$* angle (°)	*O$_{carb}$-Zn-OH angle (°)	Zn···(L)···Zn distance (Å)
100	26.594(1)	5.1462(2)	291	126.7(1)	3.4313(4)	115.4(1)	111.6(1)	105.9(1)	12.1969(6)
190	26.5112(9)	5.2351(1)	300	128.5(1)	3.4551(4)	108.7(1)	112.0(1)	105.0(1)	12.2056(6)
280	26.4574(9)	5.2854(2)	312	129.6(2)	3.4683(5)	109.5(2)	112.4(1)	104.6(2)	12.1958(6)
370	26.4366(9)	5.3287(2)	336	130.7(2)	3.4816(6)	109.6(2)	113.5(3)	104.2(2)	12.1926(7)

* O_{carb} is the oxygen atom of the carboxylate group of the ligand.

The anomalously large PTE results directly from the large increase in the Zn-O(H)-Zn angle. The angle increases by 4.0° over the 100-370 K temperature range, resulting in an increase in the distance between two Zn atoms across the hydroxyl bridge. The Zn···Zn separation increases from 3.431 Å to 3.482 Å. The difference of 0.051 Å corresponds to an expansion coefficient of 55×10^{-6} K^{-1}. There are two Zn–O(H)–Zn angles along the *c* axis of the unit cell and the combined effect corresponds to an overall Zn···Zn expansion coefficient of 110×10^{-6} K^{-1} which is close to the coefficient determined for the *c* axis (123×10^{-6} K^{-1}). The Zn-O(H)-Zn bridges form a polymeric chain along the *c* axis and the enlargement of this angle results in the "colossal" PTE along that direction, Figure 100. The distance between two Zn-atoms interconnected by a ligand (Zn···(L)···Zn) in the *ab* plane decreases with increasing temperature with a coefficient of -2.4×10^{-6} K^{-1} (per unit cell), a value much smaller than the NTE coefficient determined for the *a* and *b* axes (-21×10^{-6} K^{-1}). The NTE effect is therefore not related to a decrease in the Zn···Zn separation across the length of the rigid ligand, but it is caused by the out-of-plane relocation of the ligand due to the changes in the coordination angles around the metal node. There is a reduction in the N–Zn–OH and O_{carb}–Zn–OH angles by 5.8° and 1.7°, respectively (Table 24). The N–Zn–OH, N–Zn–O_{carb} and O_{carb}–Zn–OH angles are approximately in the *ab* plane and it is believed that their distortion leads to the observed NTE along these directions.

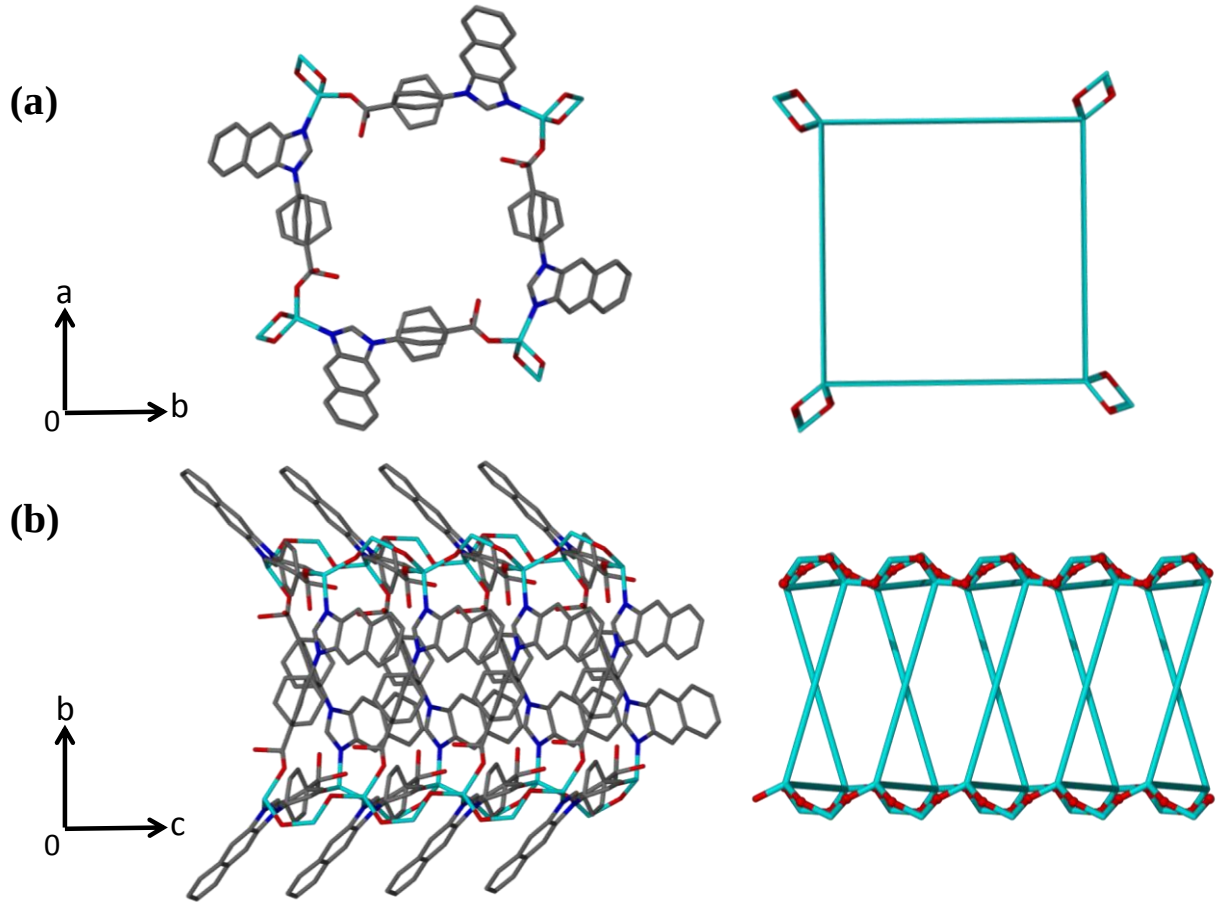

Figure 100. (a) A section of the empty **IMMOF-3**$_{\text{apohost}}$ framework viewed along [001], illustrating the Zn···(L)···Zn vector. (b) A section of a framework channel viewed along [100] showing the Zn···(OH)···Zn distances across the hydroxyl bridges. Hydrogen atoms have been omitted for clarity.

It has not yet been determined whether the NTE results from geometric frustration caused by the colossal PTE or whether an additional vibrational mechanism is at play. By studying the atomic displacement parameters (ADPs) of the constituent atoms of the framework more closely, useful information about vibrational mechanisms can be obtained. The out-of-plane libration of the phenylene ring of the organic ligand rapidly increases in magnitude when the crystal is heated. This is apparent from the thermal ellipsoids of the phenylene ring carbon atoms, which increase in size at a greater rate as opposed to the thermal ellipsoids of the rest of the ligand atoms (Figure 101). The large thermal ellipsoids of the phenylene ring imply dynamic disorder at elevated temperatures. The libration of the phenylene ring is a transverse vibration that may contribute to the observed NTE along the *a* and *b* axes (i.e. along the length of the ligand). The libration of the ring may also contribute to the expansion in the direction perpendicular to the plane of the ring (i.e. expansion between successive layers stacked along the *c* axis).

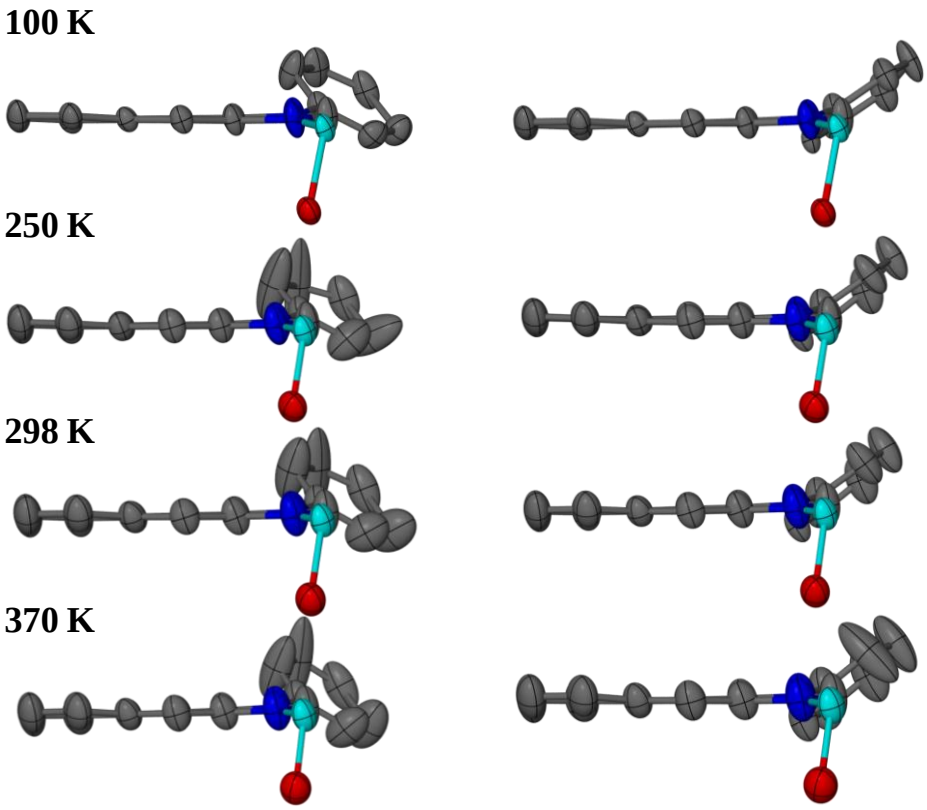

Figure 101. The effect of increasing temperatures on the thermal ellipsoids of the ligand coordinated to the Zn metal centre in **IMMOF-3$_{apohost}$**. The two positions over which the phenylene ring is disordered (approximately 50% probability for each position) are shown.

Using the SCD data a structural model can be constructed in order to explain the thermal response of the material. The model is reminiscent of the 3D lattice-fence topology found in HMOF-1 (assembled from meso-tetra-(4-pyridyl)porphine and CdI_2) in which a hinged motion around the metal node results in an anisotropic and exceptionally large thermal expansion.[66] In the case of **IMMOF-3$_{apo}$**, the enlargement of the Zn-O(H)-Zn angle at elevated temperatures leads to elongation of the framework along the *c* axis, analogous to the stretching of an accordion (Figure 102).

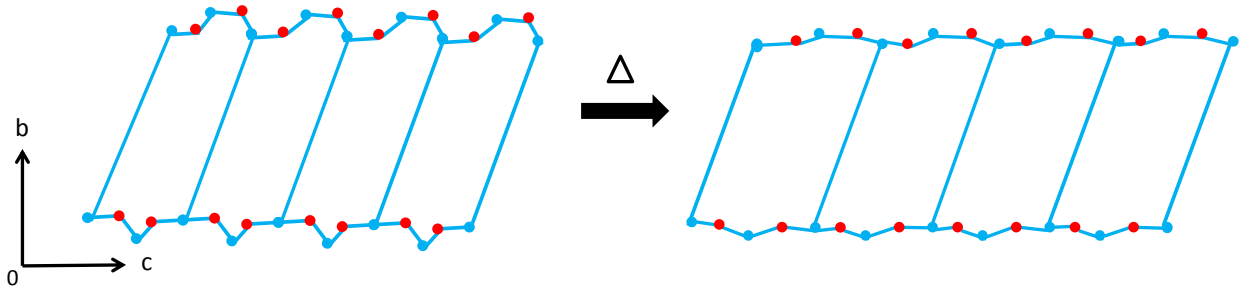

Figure 102. A schematic two-dimensional representation of the **IMMOF-3** topology with the Zn metal centres depicted as blue circles and the hydroxyl bridges as red circles.

Owing to their large thermal vibrations, intermolecular interactions are subject to more thermal expansion than covalent or coordination bonds. The larger thermal vibrations are a consequence of these interactions, having a shallower potential energy well. There are strong hydrogen-bonding interactions along the $[Zn–OH–]_n$ chain (Figure 103). The hydrogen bond distance between the hydroxyl group and the coordinated carboxyl oxygen atom increases from 2.875(3) Å at 100 K to 3.065(8) Å at 370 K. The concomitant increase in the hydrogen-bond distances and the changes in the coordination angles around the Zn^{II} node are both responsible for the anisotropic thermal expansion observed. That is, the expansion of the intermolecular framework interactions and the lability of the coordination angles are both requirements for the large PTE and NTE effects.

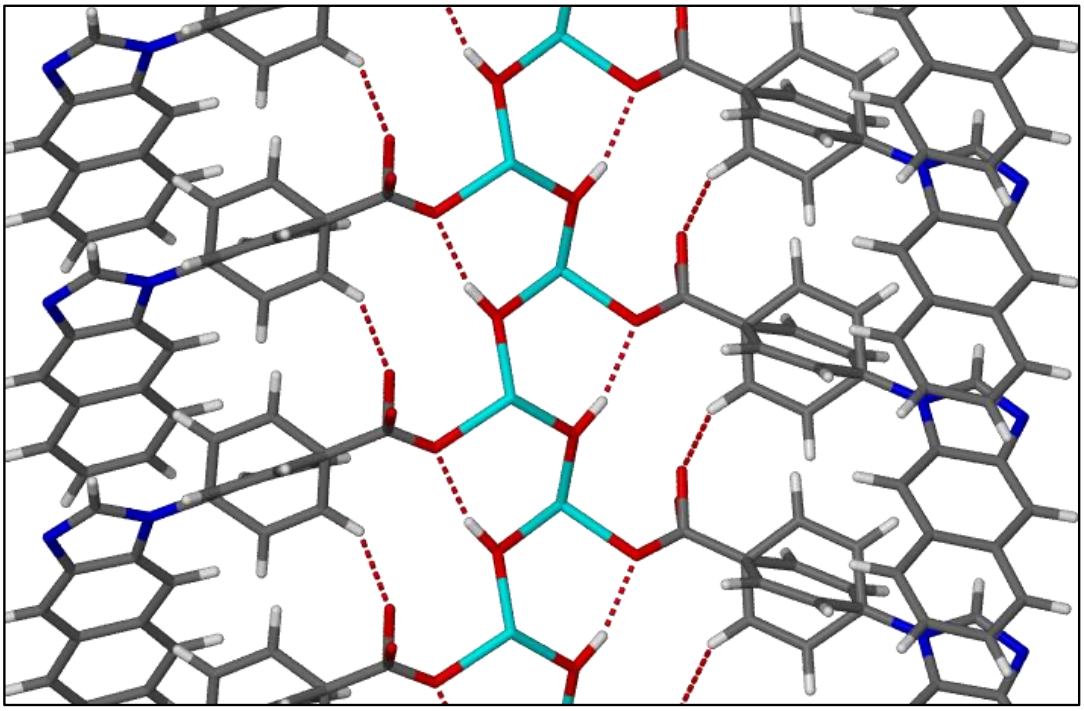

Figure 103. Hydrogen bonding interactions in **IMMOF-3$_{apohost}$** that are approximately parallel to [001] are shown as dashed red lines.

To ascertain whether the anomalous thermal expansion observed in a single crystal also manifests in the bulk material, PXRD patterns of the desolvated material were measured at various temperatures (Figure 104 and Figure 105).

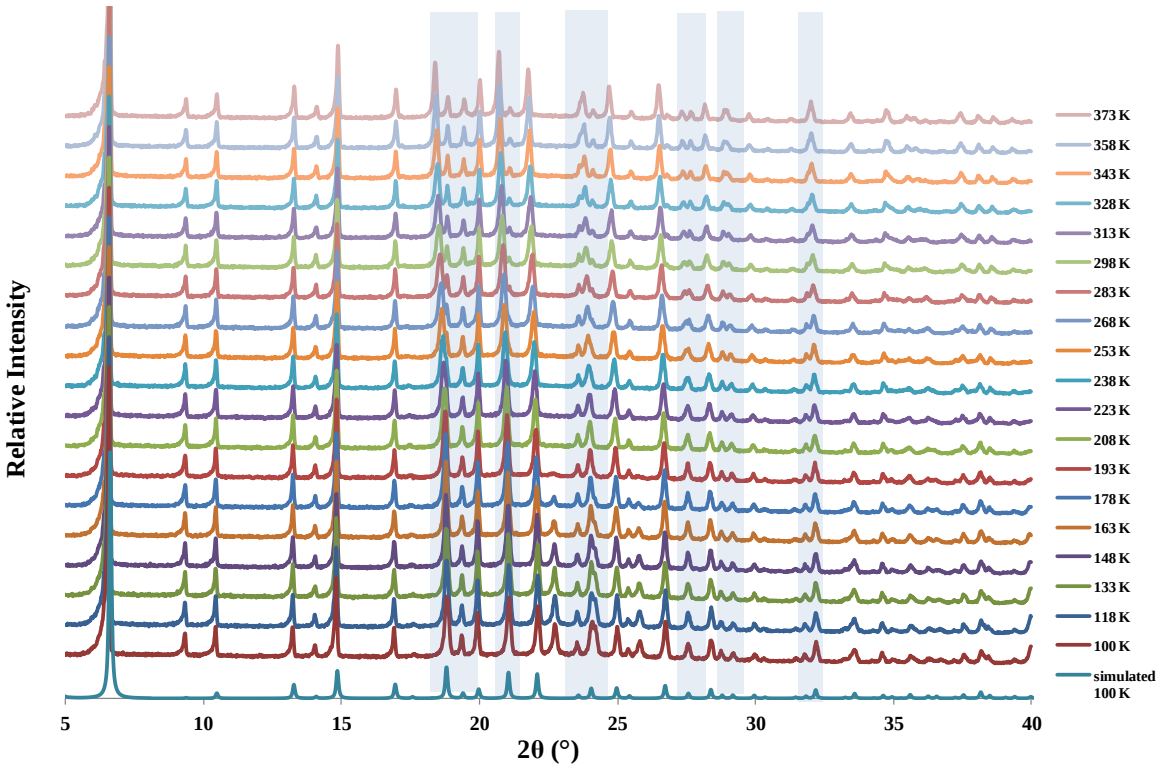

Figure 104. Simulated and experimental PXRD patterns measured at 15 K intervals for **IMMOF-3$_{apohost}$**. The subtle differences between the patterns are highlighted in light blue.

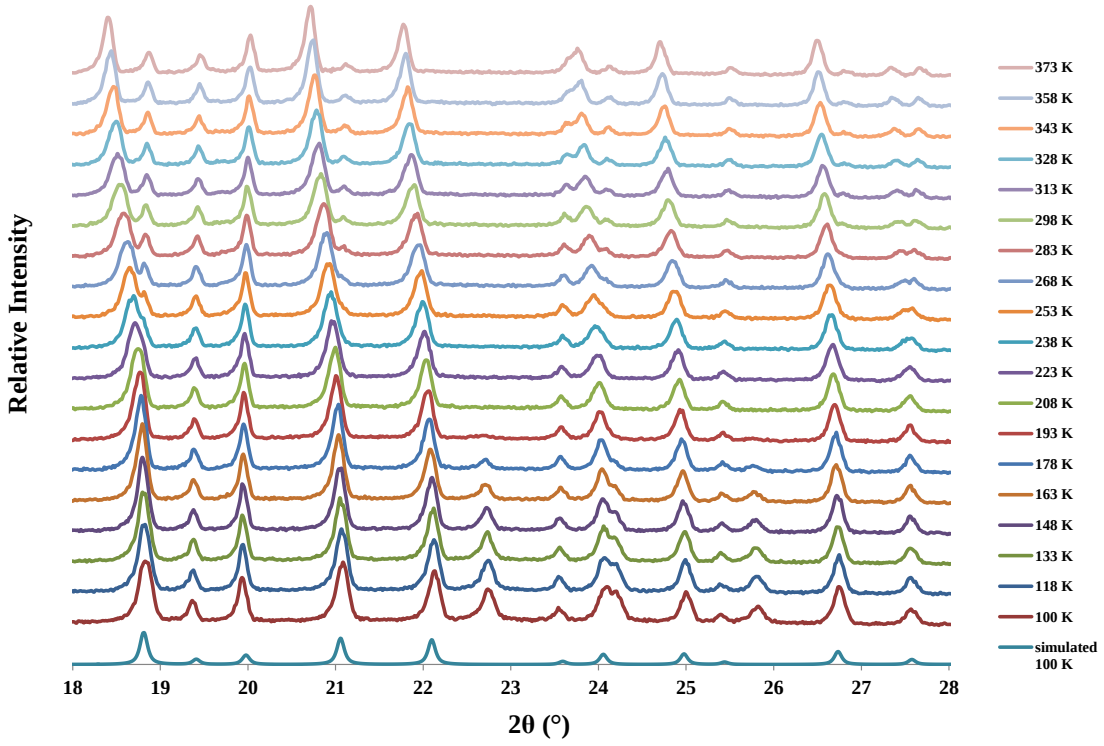

Figure 105. Simulated and measured PXRD patterns for **IMMOF-3$_{apohost}$** (see Figure 104) in the range 2Θ = 18° to 28°.

Certain peaks, such as those initially occurring at 2Θ-angles of approximately 19.9°, 23.7°, 25.4° and 27.6°, shift to the right owing to the NTE, i.e. in the opposite direction to which they would shift if the material displayed only PTE (Figure 105). It is important to point out that the unusually large peak shifts in the powder patterns measured at different temperatures of a material with NTE should not be mistaken for polymorphic transitions or impurities. The peaks at 2Θ = 23.6°and 25.8°, which are not present in the simulated pattern, are due to ice that formed on the surface of the capillary during cooling. Indexing of the patterns confirmed that the bulk material of **IMMOF-3** has the same thermal expansion properties as the single crystal used for the acquisition of SCD data.

4.3.4 Thermal response of guest-included framework

Since the material is porous, it affords the unique opportunity to study the effects that guest molecules situated within the channels may have on its thermal expansion. If the single-crystal quality of a material is maintained during a guest exchange experiment, (as is the case with **IMMOF-3**), the changes in host mechanics of different host-guest inclusion complexes as a function of temperature can be studied systematically. This study demonstrates that host-guest materials can have controllable physical properties if the guest component can be removed and/or exchanged.

Similar to IRMOF MCF-18(L,M), constructed from a tripodal-pyridyl-dicarboxylate ligand and 9-connected, tricapped trigonalprismatic $Ni_3(\mu_3\text{-}OH)(O_2CR)_6(py)_3$ clusters, controllable thermal expansion behaviour is realised in **IMMOF-3** due to the fact that abnormal thermal expansion and guest-induced framework breathing coexist and couple in the structure.[77] An example of a potential benefit of this coupling of properties occurring in a single crystal is that it can be used as a thermo-mechanical actuator or sensor in a single-crystal device.

When the original guest molecules in **IMMOF-3** (which will henceforth be referred to as **IMMOF-3$_{MeOH}$**) are replaced there is a noticeable effect on the host mechanics, resulting in an alteration of the thermal expansion properties of the material. This study of the thermal expansion coefficients of different inclusion complexes of the host MOF involved systematic alteration of guest size, i.e. methanol, ethanol, *n*-propanol and *iso*-propanol, showing that fine control can be achieved over the thermal expansion coefficients and that the coefficients can be correlated with the size of the guest.

Single crystals of **IMMOF-3$_{MeOH}$** were suspended in vials containing ethanol, *n*-propanol or *iso*-propanol for two weeks prior to SCD structure determination. After initial structure determination at 100 K in each case to confirm guest exchange, the unit cell parameters were measured at 15 K intervals upon heating to 370 K (Figure 106). Please refer to Appendix B for tables containing the unit cell data for the various solvates.

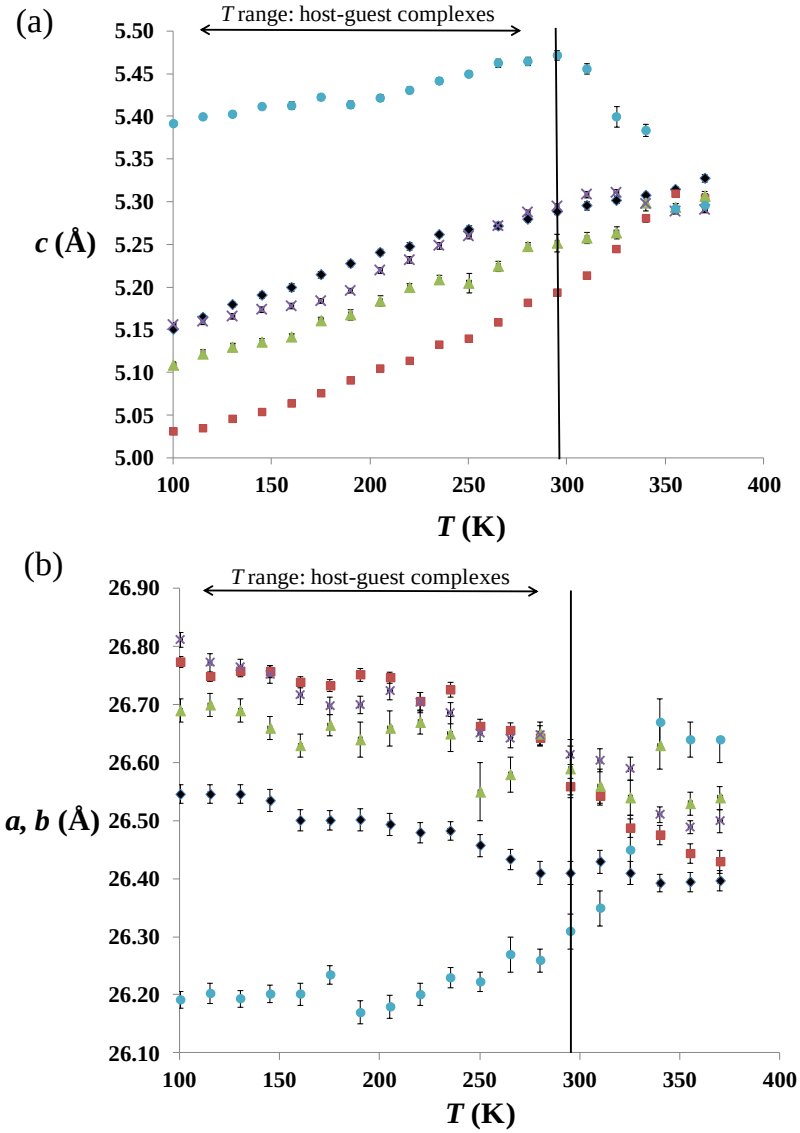

Figure 106. The temperature-dependent (a) *c* and (b) *a*=*b* unit cell parameters of **IMMOF-3$_{MeOH}$** (red squares), **IMMOF-3$_{EtOH}$** (green triangles), **IMMOF-3$_{n\text{-}PrOH}$** (purple crosses), **IMMOF-3$_{apohost}$** (black diamonds) and **IMMOF-3$_{iso\text{-}PrOH}$** (blue circles). Error bars show the estimated standard deviations

In addition, videos of the **IMMOF-3$_{MeOH}$** crystal were also recorded at 15 K intervals. The most accurate measurement of the crystal dimensions could be obtained from indexing of the crystal faces. Videos were not recorded with the guest-free crystal (**IMMOF-3$_{apohost}$**) placed under vacuum within the gas cell, as the glass capillary obscures the view of the crystal and thus

accurate determination of the crystal dimensions by face-indexing is not possible. At 100 K the crystal dimensions of **IMMOF-3$_{MeOH}$** were 0.218 × 0.229 × 1.095 mm and at 370 K the crystal dimensions are 0.214 × 0.220 × 1.161 mm (Figure 107).

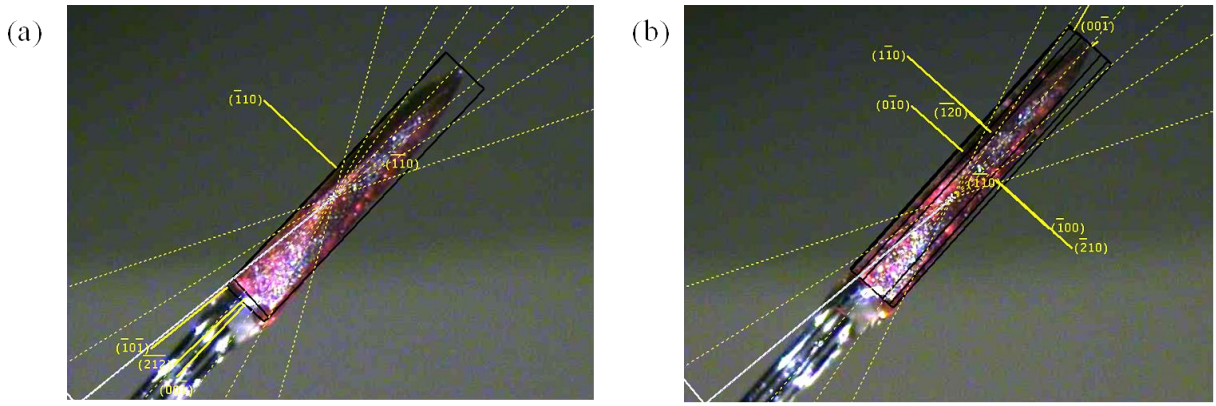

Figure 107. Face-indexing of **IMMOF-3$_{MeOH}$** at (a) 100 K and (b) 370 K using the APEX II software suite.

As anticipated, the length of the needle-shaped crystal of **IMMOF-3$_{MeOH}$** in Figure 108 increases from 1.095 mm to 1.161 mm upon heating from 100 K to 370 K. The macroscopic increase in length corresponds with α_c of 202 × 10^{-6} K^{-1} calculated from the unit cell parameters for the 100–370 K temperature range. At the same time the width decreases to a lesser extent owing to the NTE along the *a* and *b* axes. It is remarkable that the crystal stays intact despite the large magnitude of thermal expansion. However fracture lines can be observed on the crystal at 370 K (Figure 108).

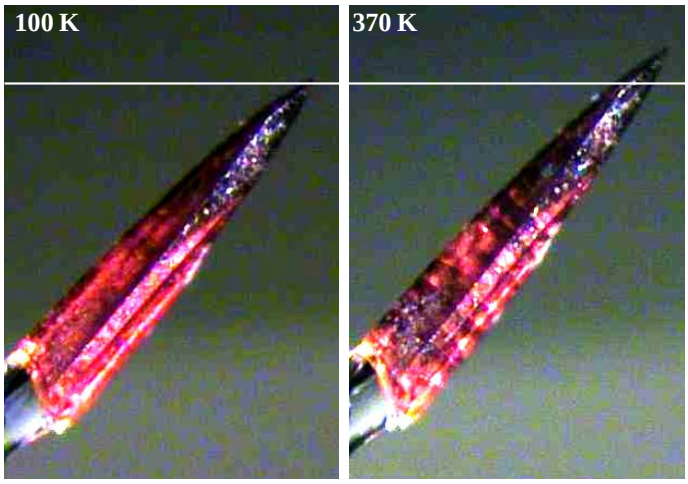

Figure 108. Photographs of an **IMMOF-3$_{MeOH}$** crystal mounted on a glass fibre recorded at 100 and 370 K, respectively. The PTE along [001] (parallel to the length of the shard) is clearly visible.

Across this series of alcohol solvates the guest occupancy is the same (four molecules of guest per ~300 $Å^3$ channel section or one guest molecule per asymmetric unit), even with an

increase in the size of the guest. Thermogravimetric analysis of the as-synthesized material (**IMMOF-3$_{MeOH}$**, Figure 63, Section 4.1), showed that guest-loss occurs at room temperature and therefore the unit cell parameters of **IMMOF-3$_{MeOH}$** start to converge with those of **IMMOF-3$_{apohost}$** from 295 K onwards. However, all of the host-guest inclusion complexes are stable over the temperature range of 100–295 K.

Relative to **IMMOF-3$_{apohost}$** there is an increase in the already unusually large PTE and NTE coefficients in the presence of methanol, ethanol and *n*-propanol guest molecules (**IMMOF-3$_{MeOH}$, IMMOF-3$_{EtOH}$** and **IMMOF-3$_{n\text{-}PrOH}$**) while the bulky *iso*-propanol molecules (**IMMOF-3$_{iso\text{-}PrOH}$**) suppress the extent of thermal expansion. The PTE and NTE coefficients for the various solvates are summarised in Table 25. More significantly, the PTE coefficients for the different guests correlate to the size (van der Waals volume) of the guest involved. Table 26 summarizes the PTE coefficients for the host material when it includes guests of increasing van der Waals volume; the Zn–O(H)–Zn angles at 100 K are also listed. The PTE coefficient decreases in the order: **1$_{MeOH}$ >1$_{EtOH}$ >1$_{n\text{-}PrOH}$ > 1$_{apohost}$ >1$_{iso\text{-}PrOH}$.**

Table 25. PTE and NTE coefficients for the different host-guest complexes for the 100-295 K temperature range**.**

Solvate	Guest volume (Å^3)	α_c ×10^6 (K^{-1})	$\alpha_{a,b}$ ×10^6 (K^{-1})
MeOH	38.8	166(4)	-41(3)
EtOH	54.0	144(5)	-17(5)
n-PrOH	70.7	138(4)	-38(4)
apohost	–	137(5)	-26(5)
iso-PrOH	69.1	76(6)	23(6)

Table 26. PTE coefficients and selected structural information of the host-guest complexes.

Solvate	Guest volume (Å^3)[a]	α_c ×10^6 (K^{-1})[b]	Zn–O(H)–Zn (°)	H-bond (Å)[c]
MeOH	38.8	166(4)	123.7(1)	2.808(4)
EtOH	54.0	144(5)	123.8(2)	2.812(5)
n-PrOH	70.7	138(4)	124.6(1)	2.832(8)
apohost	–	137(5)	126.7(1)	2.875(3)
iso-PrOH	69.1	76(6)	127.4(1)	2.915(3)

[a] The guest volume was calculated using the van der Waal's surface.

[b] α_c was calculated for the temperature range 100–295 K.

[c] The intra-framework hydrogen-bond distance between the hydroxyl group and the coordinated carboxyl-oxygen atom at 100 K (as shown in Figure 104).

The guest size, shape and the hydrogen-bonding interactions with the host framework concurrently have an effect on the host mechanics, as is evidenced by the differing coordination

environment around the Zn(II) nodes and the different strengths of the intra-framework hydrogen bonds in the different solvates. As was discussed in Section 4.2.6, there is an induced fit of the guest within the framework channels, i.e. the framework has the ability to adjust its metal geometry and channel size according to the size of the guest molecules. The guest molecules participate in hydrogen-bonding interactions with the host framework and it is believed that these host-guest interactions alter the host mechanics. The differences in the metal geometry and the intra-framework hydrogen bonding distances at 100 K relative to the apohost framework (listed in Table 26) ultimately result in the different responses to temperature. At 100 K the Zn–O(H)–Zn angle of **IMMOF-3$_{MeOH}$**, **IMMOF-3$_{EtOH}$** and **IMMOF-3$_{n\text{-}PrOH}$** is smaller than that of **IMMOF-3$_{apohost}$** resulting in a shorter *c* axis of the unit cell. These solvates are in a "contracted" state relative to the apohost framework. Effectively, the initial metal geometry at 100 K allows a greater extent of PTE to occur in these complexes. However, in **IMMOF-3$_{iso\text{-}PrOH}$** the Zn–O(H)–Zn angle is already enlarged due to the presence of the bulky guest, and the framework is already in a slightly "expanded" state, which renders it less flexible towards further thermal expansion. It is clear that the intermolecular host-guest interactions play a role in the apparent thermal expansion of host material.[78]

The magnified thermal response when there are certain guests within the channel is an unusual result. The guest-free frameworks of $Cu_3(btc)_2$ and cadmium cyanide ($Cd(CN)_2$) are known to display isotropic NTE, which is dampened by the presence of guest molecules such that only unremarkable PTE is observed.[72,79] In both of these materials, a purely vibrational mechanism involving transverse vibrations of the organic linkers is associated with the NTE and the authors report that open channels are necessary for the framework flexibility.[72] In contrast, in the case of **IMMOF-3$_{MeOH}$**, **IMMOF-3$_{EtOH}$** and **IMMOF-3$_{n\text{-}PrOH}$** the guest molecules enhance the flexibility of the framework by means of altering the coordination environment and the strength of framework interactions. The fact that the NTE effect is enhanced by guest inclusion in some cases (see Table 25) is evidence that the guest molecules do not simply act to increase the overall volume thermal expansion as was the case in the studies of $Cu_3(btc)_2$ and cadmium cyanide ($Cd(CN)_2$). Instead the NTE coefficient of **IMMOF-3$_{apohost}$**, $\alpha_{a,b} = -26(5) \times 10^{-6}$ K^{-1}, is increased to $\alpha_{a,b} = -41(3) \times 10^{-6}$ K^{-1} in **IMMOF-3$_{MeOH}$**, which suggests that host-guest interactions play a role in the thermal response of the various solvates.

A study of the effect of guest molecules on the apparent thermal expansion of a MOF has been reported by Omary *et al.* They observed an increase in the apparent NTE and PTE with the

sequential filling of the pores of a fluorous MOF (FMOF-1) with N_2 molecules.[78] In contrast to **IMMOF-3**, FMOF-1 displays unusual two-step breathing, involving a volumetric NTE process in one temperature range (90–119 K) and an overall PTE process in another temperature range (119–295 K). The anomalous thermal expansion was correlated to the location of the N_2 within the channels and the reversal in the thermal response was, in part, attributed to the localization of more N_2 guest molecules such that guest-guest repulsion becomes significant. In the case of **IMMOF-3$_{MeOH}$**, **IMMOF-3$_{EtOH}$**, **IMMOF-3$_{n\text{-}PrOH}$** and **IMMOF-3$_{iso\text{-}PrOH}$** an approximately linear trend is observed (Figure 109) and the initial guest occupancy is presumed to remain constant from 100 to ~295 K.

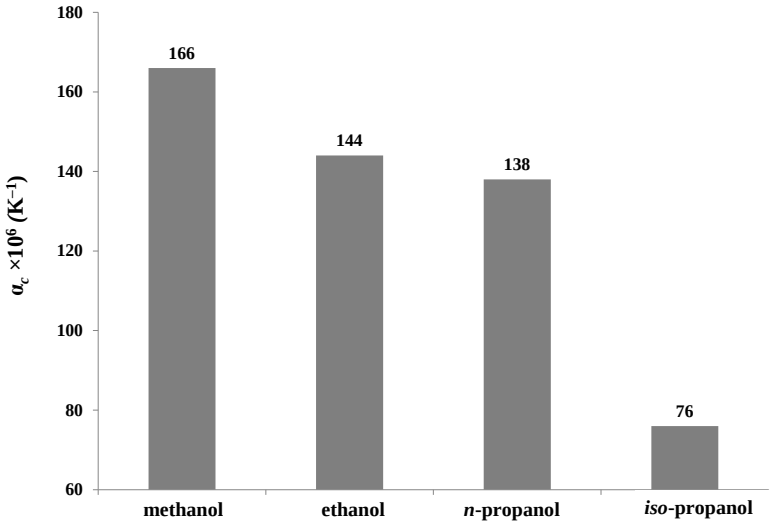

Figure 109. A plot of the PTE coefficients (α_c) of the various host-guest adducts of **IMMOF-3.**

To our knowledge, the current study is the first example of a controlled experiment in which a series of related guest molecules of increasing size is included with a constant host-guest ratio over a broad temperature range. The effect of temperature on the host mechanics was monitored by structural analyses.

In conclusion, it has been shown that **IMMOF-3** has the combined properties of being porous and having unusual anisotropic thermal expansion. It has been demonstrated that the choice of guest can alter the thermal expansion behaviour of a host material such that fine control over the thermal expansion coefficients can be achieved. The study also demonstrates that guest inclusion does not only alter the linear thermal expansion coefficient but it also creates an array of possible absolute physical dimensions of a single crystal by the control of two variables; the type of guest and the temperature. This study establishes a novel concept of guest-tunable thermal expansion, with implications for enhanced utility of materials based on 'single crystals'.

4.4 SUMMARY AND CONCLUSIONS

A number of MOFs were prepared from the solvothermal reactions of **L1** to **L7** with transition metal salts. In stark contrast to the soft porous MOFs described in the previous chapter, **IMMOF-3**, incorporating **L7**, is a 3D permanently porous framework with remarkable thermal and chemical stability. The framework dynamics are therefore more subtle, with small variations in the unit cell volume and dimensions depending on which guest the MOF includes in the continuous 1D channels. The MOF can accommodate a wider range of guest molecules than **IMMOF-2** owing to the presence of wide channels with approximately 6 × 6 Å dimensions. However, guest uptake still occurs selectively in some cases and is dependent on size/shape exclusion as well as the thermodynamics of forming the most stable host-guest adducts. The channels are hydrophilic and preferentially accommodate guest molecules that can form hydrogen bonds or other favourable electrostatic interactions with the host carboxylate groups.

In addition to its guest-inclusion properties, **IMMOF-3** also displays anisotropic thermal expansion. The mechanism of the unusual expansion was determined from SCD experiments carried out at regular temperature intervals. The guest-dependent thermal expansion behaviour when the framework includes a series of alcohols (methanol, ethanol, *n*-propanol and *iso*-propanol) was also studied. An approximately linear trend of increasing positive thermal expansion coefficients with increasing size of the guest molecules was established. The results prove that thermal expansion properties can be "fine-tuned" by guest inclusion.

MOFs do not only have interesting gas sorption and guest-inclusion properties but, owing to their inhomogeneity and structural diversity, many other properties can be discovered. SCD methods are extremely suitable for characterising the solid-state dynamics of structural transformations or incremental structural changes provided that the crystal remains intact during the process.

4.5 EXPERIMENTAL SECTION

4.5.1 Synthesis of L7

All chemicals used in these experiments were purchased from Merck or Aldrich. Thin layer chromatography (TLC) was carried out on aluminium-backed Merck silica gel 60 F_{254} plates. Visualisation was with a UV lamp or iodine. All ^{1}H and ^{13}C nuclear magnetic resonance spectra were obtained using a 300 MHz Varian VNMRS (75 MHz for ^{13}C) or a 400 MHz Varian Unity Inova (100 MHz for ^{13}C) using *d*-chloroform as the solvent. Chemical shifts (δ) were recorded using the residual solvent signal as reference. All chemical shifts are reported in ppm and all spectra were obtained at 25 °C. The NMR spectra are included in Appendix A. Melting points were obtained using a Gallenkamp Melting Point Apparatus and are uncorrected. Infrared spectra were obtained using a Nexus Thermo-Nicolet FT-IR using an ATR Golden Gate attachment. High resolution mass spectrometry was carried out by the Central Analytical Facility at Stellenbosch University using a Waters API Q-TOF Ultima spectrometer.

The three steps of the procedure are summarised in Scheme 6.

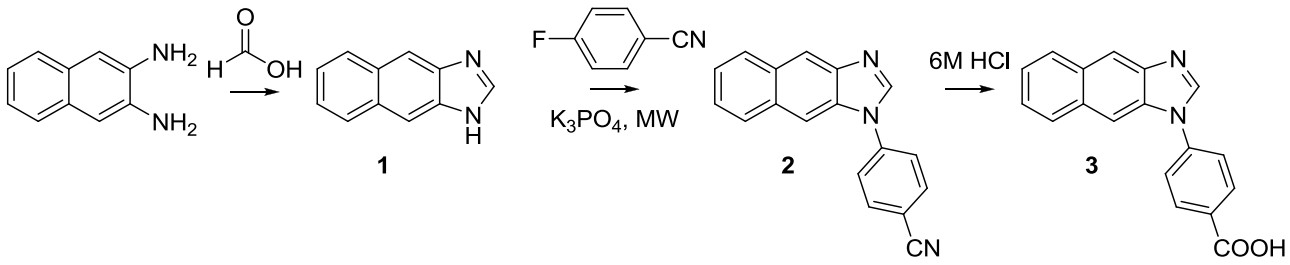

Scheme 6. The synthesis of 4-(1*H*-Naphtho[2,3-*d*]imidazol-1-yl)benzoic acid.

1*H*-Naphtho[2,3-*d*]imidazole – (**1**)

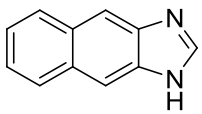

2,3-Diaminoanthracene (500mg, 3.16 mmol, 1 eq) and formic acid (10 ml, in excess) were added to a round-bottom flask (50 ml). The mixture was heated to reflux under an inert atmosphere (N_2) for 36 hours. The mixture was then cooled to room temperature and the contents poured into saturated Na_2CO_3 solution (60 ml). The resulting solid was collected by filtration, washed with H_2O (50 ml) and dried under reduced pressure to yield a brown powder (420 mg, 2.50 mmol, 79 %). Further purification was not required.

R_f: 0.25 (MeOH/DCM: 5/95).

MP: 218-220 °C.

^{1}H NMR (400 MHz, DMSO-d_6) δ ppm 12.54 (br. s. N*H*), 8.50 (s, 1 H, N=C*H*-N), 8.13 (br. s., 2 H, Ar*H*), 7.95 - 8.05 (m, 2 H, Ar*H*), 7.31 - 7.43 (m, 2 H, Ar*H*).

4-(1*H*-Naphtho[2,3-*d*]imidazol-1-yl)benzonitrile – (**2**)

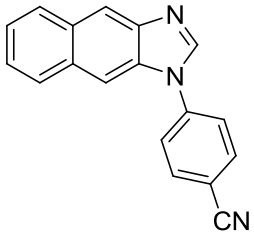

Napthaimidazole **1** (500 mg, 2.99 mmol, 1 eq) 4-fluorobenzonitrile (362 mg, 2.99 mmol, 1 eq) K_3PO_4 (1587 mg, 7.48 mmol, 2.5 eq) and dry DMF (13 ml) were added to a microwave reaction vessel (20 ml). The flask was sealed and heated under microwave radiation for 30 minutes at 160°C, following which the solvent was removed under reduced pressure. Further purification was not carried out and the crude mixture was used in the following reaction.

R_f: 0.60 (MeOH/DCM: 5/95).

MP: 219-221 °C.

IR υ_{max} (ATR)/cm^{-1}: 3092, 2919, 1606, 1518, 1444, 1195, 852.

^{1}H NMR (400 MHz, CHLOROFORM-*d*) δ ppm 8.37 (s, 1 H, N=C*H*-N), 8.32 (s, 1 H, Ar*H*), 8.02 - 8.07 (m, 1 H, $Ar_{Nap}H$), 8.01 (s, 1 H, $Ar_{Nap}H$), 7.90 - 7.96 (m, 3 H, $Ar_{Nap}H$, 2xAr*H*), 7.74 - 7.79 (m, 2 H, 2xAr*H*), 7.45 - 7.53 (m, 2 H, 2x$Ar_{Nap}H$).

^{13}C NMR (101 MHz, CHLOROFORM-*d*) δ ppm 145.04, 143.92, 140.26, 134.27, 132.84, 131.12, 130.63, 128.61, 127.59, 125.35, 124.45, 123.54, 118.43, 117.88, 111.20, 106.43

HRMS: calcd for $C_{18}H_{12}N_3$ 270.1031 found 270.1024 $(M+H)^+$.

4-(1*H*-Naphtho[2,3-*d*]imidazol-1-yl)benzoic acid – (**3**)

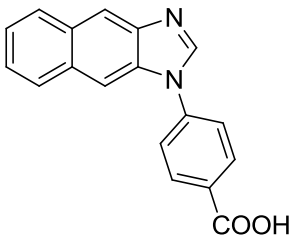

Crude reaction mixture **2** (presumed 2.99 mmol), concentrated HCl (100 ml) and H_2O (50 ml) were added to a round-bottom flask (250 ml) and the mixture was heated to reflux overnight. The flask was cooled to room temperature, the pale brown solid was removed by filtration, suspended in H_2O (50 ml) and the pH of the mixture adjusted to 7 using

$NaHCO_3$. After stirring for 30 minutes the resulting brown solid was collected via filtration and dried under reduced pressure, yielding a brown powder (803 mg, 2.78 mmol, 93% yield from napthaimidazole **1**).

R_f: 0.1 (MeOH/DCM: 1/9).

MP: >300 °C.

IR υ_{max} (ATR)/cm^{-1}: 3081, 1604, 1566, 1517, 1384, 847, 780.

^{1}H NMR (HCl salt) (400 MHz, DMSO-d_6) δ ppm 9.82 (s, 1 H, N=C*H*-N), 8.51 (s, 1 H, $Ar_{NAP}H$), 8.43 (s, 1 H, $Ar_{NAP}H$), 8.28 (d, *J*=8.6 Hz, 2 H), 8.21 (dd, *J*=6.3, 3.4 Hz, 1 H, $Ar_{NAP}H$), 8.16 (dd, *J*=6.3, 3.4 Hz, 1 H, $Ar_{NAP}H$), 8.05 (d, *J*=8.6 Hz, 2 H, Ar*H*), 7.54 - 7.60 (m, 2 H, $Ar_{NAP}H$), 5.63 (br. s., 1 H, NH^+).

^{13}C NMR (75MHz, DMSO-d_6): δ ppm 166.42, 146.38, 138.16, 135.34, 131.23, 131.15, 131.06, 131.02, 130.73, 128.25, 128.21, 125.79, 125.52, 124.50, 114.20, 109.15.

HRMS: calcd for $C_{18}H_{13}N_2O_2$ 289.0977 found 289.0971 $(M+H)^+$.

4.5.2 Crystallographic tables

	IMMOF-3	**IMMOF-3$_{sCO2}$**	**IMMOF-3$_{apohost}$**	**IMMOF-3$_{water}$**
Empirical formula	$C_{19}H_{15}N_2O_4Zn$	$C_{18}H_{13}N_2O_4Zn$	$C_{18}H_{11}N_2O_3Zn$	$C_{18}H_{11}N_2O_6Zn$
Formula weight	400.70	386.67	368.66	416.66
Temperature/K	100(2)	100(2)	295(2)	100(2)
Wavelength/Å	0.71073	0.71073	0.71073	0.71073
Crystal system	tetragonal	tetragonal	tetragonal	tetragonal
Space group	$I\bar{4}$	$I\bar{4}$	$I\bar{4}$	$I\bar{4}$
a /Å	26.772(2)	26.692(4)	26.4515(13)	26.701(6)
b /Å	26.772(2)	26.692(4)	26.4515(13)	26.701(6)
c /Å	5.0662(4)	5.1004(7)	5.2866(3)	5.1231(12)
α /°	90.00	90.00	90.00	90.00
β /°	90.00	90.00	90.00	90.00
γ /°	90.00	90.00	90.00	90.00
Volume/Å^3	3631.2(5)	3633.8(9)	3698.9(3)	3652.5(14)
Z	8	8	8	8
Calculated density/g cm^{-3}	1.466	1.414	1.324	1.515
Absorption coefficient (mm^{-1})	1.379	1.375	1.343	1.382
F_{000}	1640	1576	1496	1688
Reflections collected	11042	10976	11850	12017
Independent reflections	3963 [R_{int} = 0.0237]	3968 [R_{int} = 0.0261]	3794 [R_{int} = 0.0238]	4390 [R_{int} = 0.0351]
Data/restraints/parameters	3963 / 0 / 273	3968 / 3 / 278	3794 / 0 / 263	4390 / 0 / 290
Goodness-of-fit on F^2	1.055	1.117	1.038	1.061
Final R indices [$I>2\sigma(I)$]	$R1$ = 0.0338, $wR2$ = 0.0891	$R1$ = 0.0364, $wR2$ = 0.1032	$R1$ = 0.0411, $wR2$ = 0.1122	$R1$ = 0.0396, $wR2$ = 0.0939
R indices (all data)	$R1$ = 0.0357, $wR2$ = 0.0905	$R1$ = 0.0395, $wR2$ = 0.1055	$R1$ = 0.0467, $wR2$ = 0.1165	$R1$ = 0.0452, $wR2$ = 0.0973

	IMMOF-3$_{EtOH}$	**IMMOF-3$_{n\text{-}PrOH}$**	**IMMOF-3 $_{iso\text{-}PrOH}$**	**IMMOF-3$_{acetone}$**
Empirical formula	$C_{20}H_{17}N_2O_4Zn$	$C_{21}H_{19}N_2O_4Zn$	$C_{21}H_{19}N_2O_4Zn$	$C_{39}H_{28}N_4O_7Zn_2$
Formula weight	414.73	428.75	428.75	795.39
Temperature/K	100(2)	101(2)	100(2)	107(2)
Wavelength/Å	0.71073	0.71073	0.71073	0.71073
Crystal system	tetragonal	tetragonal	tetragonal	tetragonal
Space group	$I\bar{4}$	$I\bar{4}$	$I\bar{4}$	$I\bar{4}$
a /Å	26.713(4)	26.742(4)	26.1918(19)	26.722(2)
b /Å	26.713(4)	26.742(4)	26.1918(19)	26.722(2)
c /Å	5.0883(8)	5.1504(8)	5.3960(4)	5.0968(4)
α /°	90.00	90.00	90.00	90.00
β /°	90.00	90.00	90.00	90.00
γ /°	90.00	90.00	90.00	90.00
Volume/Å^3	3631.0(10)	3683.2(10)	3701.7(5)	3639.4(5)
Z	8	8	8	4
Calculated density/g cm^{-3}	1.517	1.546	1.539	1.452
Absorption coefficient (mm^{-1})	1.381	1.365	1.358	1.373
F_{000}	1704	1768	1768	1624
Reflections collected	10621	11035	14644	8855
Independent reflections	3888 [R_{int} = 0.0384]	4008 [R_{int} = 0.0260]	5188 [R_{int} = 0.0616]	2891 [R_{int} = 0.0271]
Data/restraints/parameters	3888 / 0 / 272	4008 / 3 / 271	5188 / 0 / 297	2891 / 6 / 277
Goodness-of-fit on F^2	1.050	1.030	1.100	1.063
Final *R* indices [$I>2\sigma(I)$]	$R1$ = 0.0469, $wR2$ = 0.1129	$R1$ = 0.0368, $wR2$ = 0.0950	$R1$ = 0.0453, $wR2$ = 0.1224	$R1$ = 0.0400, $wR2$ = 0.1151
R indices (all data)	$R1$ = 0.0551, $wR2$ = 0.1178	$R1$ = 0.0393, $wR2$ = 0.0968	$R1$ = 0.0483, $wR2$ = 0.1238	$R1$ = 0.0426, $wR2$ = 0.1173

	IMMOF-3$_{DCM}$	**IMMOF-3$_{CHCl3}$**	**[a]IMMOF-3$_{CCl4}$**	**[a]IMMOF-3$_{benzene}$**
Empirical formula	$C_{37}H_{24}Cl_2N_4O_6Zn_2$	$C_{37}H_{23}Cl_3N_4O_6Zn_2$	$C_{36}H_{22}N_4O_9Zn_2$	$C_{36}H_{22}N_4O_{11}Zn_2$
Formula weight	822.24	856.68	785.32	817.32
Temperature/K	100(2)	100(2)	100(2)	101(2)
Wavelength/Å	0.71073	0.71073	0.71073	0.71073
Crystal system	tetragonal	tetragonal	tetragonal	tetragonal
Space group	$I\bar{4}$	$I\bar{4}$	$I\bar{4}$	$I\bar{4}$
a /Å	26.722(4)	26.579(7)	26.666(4)	26.683(3)
b /Å	26.722(4)	26.579(7)	26.666(4)	26.683(3)
c /Å	5.1135(7)	5.0811(14)	5.1006(7)	5.0972(6)
α /°	90.00	90.00	90.00	90.00
β /°	90.00	90.00	90.00	90.00
γ /°	90.00	90.00	90.00	90.00
Volume/Å^3	3651.3(9)	3589.6(17)	3626.9(9)	3629.1(7)
Z	4	4	4	4
Calculated density/g cm^{-3}	1.496	1.585	1.438	1.496
Absorption coefficient (mm^{-1})	1.511	1.612	1.381	1.387
F_{000}	1664	1728	1592	1656
Reflections collected	8457	7983	11736	10977
Independent reflections	2748 [R_{int} = 0.0322]	2926 [R_{int} = 0.0589]	4381 [R_{int} = 0.0237]	3948 [R_{int} = 0.0228]
Data/restraints/parameters	2748 / 2 / 270	2926 / 6 / 281	4381 / 0 / 280	3948 / 0 / 280
Goodness-of-fit on F^2	1.077	1.030	1.095	1.073
Final *R* indices [$I>2\sigma(I)$]	$R1$ = 0.0674, $wR2$ = 0.1847	$R1$ = 0.0518, $wR2$ = 0.1304	$R1$ = 0.0399, $wR2$ = 0.1115	$R1$ = 0.0338, $wR2$ = 0.0929
R indices (all data)	$R1$ = 0.0697, $wR2$ = 0.1873	$R1$ = 0.0583, $wR2$ = 0.1361	$R1$ = 0.0426, $wR2$ = 0.1131	$R1$ = 0.0357, $wR2$ = 0.0941

[a] structure contains water and not the solvent that the crystal was immersed in.

	IMMOF-3$_{acetonitrile}$	**[a]IMMOF-3$_{toluene}$**	**IMMOF-3$_{iodine}$**	**CO_2-IMMOF-3$_{20bar_295K}$**
Empirical formula	[b]$C_{18}H_{11}N_2O_3Zn$	$C_{18}H_{11}N_2O_6Zn$	$C_{18}H_{11}IN_2O_3Zn$	$C_{37}H_{22}N_4O_8Zn_2$
Formula weight	368.66	416.66	495.58	781.33
Temperature/K	100(2)	101(2)	100(2)	295(2)
Wavelength/Å	0.71073	0.71073	0.71073	0.71073
Crystal system	tetragonal	tetragonal	tetragonal	tetragonal
Space group	$I\bar{4}$	$I\bar{4}$	$I\bar{4}$	$I\bar{4}$
a /Å	26.7029(17)	26.654(5)	26.472(6)	26.5444(15)
b /Å	26.7029(17)	26.654(5)	26.472(6)	26.5444(15)
c /Å	5.0928(3)	5.1138(9)	5.2438(11)	5.2750(3)
α /°	90.00	90.00	90.00	90.00
β /°	90.00	90.00	90.00	90.00
γ /°	90.00	90.00	90.00	90.00
Volume/Å^3	3631.4(4)	3633.1(11)	3674.7(13)	3716.8(4)
Z	8	8	8	4
Calculated density/g cm^{-3}	1.349	1.524	1.777	1.396
Absorption coefficient (mm^{-1})	1.368	1.389	3.034	1.345
F_{000}	1496	1688	1888	1584
Reflections collected	10612	7433	7295	8563
Independent reflections	3701 [R_{int} = 0.0249]	2279 [R_{int} = 0.0386]	2288 [R_{int} = 0.0349]	2694 [R_{int} = 0.0353]
Data/restraints/parameters	3701 / 0 / 263	2279 / 0 / 265	2288 / 6 / 198	2694 / 3 / 273
Goodness-of-fit on F^2	1.185	1.143	1.269	1.042
Final *R* indices [$I>2\sigma(I)$]	*R*1 = 0.0542, *wR*2 = 0.1613	*R*1 = 0.0449, *wR*2 = 0.1161	*R*1 = 0.0930, *wR*2 = 0.2689	*R*1 = 0.0453, *wR*2 = 0.1211
R indices (all data)	*R*1 = 0.0568, *wR*2 = 0.1641	*R*1 = 0.0482, *wR*2 = 0.1185	*R*1 = 0.1018, *wR*2 = 0.2805	*R*1 = 0.0563, *wR*2 = 0.1287

[a] structure contains water and not the solvent that the crystal was immersed in.
[b] acetonitrile molecule could not be modelled and therefore its molecular formula is not included in the molecular formula of the structure.

	CO_2-IMMOF-3$_{10bar_220K}$	**C_2H_2-IMMOF-3$_{4bar_298K}$**	**C_2H_2-IMMOF-3$_{4bar_220K}$**	**CO-IMMOF-3$_{20bar_273K}$**
Empirical formula	$C_{19}H_{11}N_2O_5Zn$	$C_{19}H_{12}N_2O_3Zn$	$C_{20}H_{13}N_2O_3Zn$	$C_{18}H_{11}N_2O_3Zn$
Formula weight	412.67	381.68	394.69	368.66
Temperature/K	233(2)	298(2)	219(2)	273(2)
Wavelength/Å	0.71073	0.71073	0.71073	0.71073
Crystal system	tetragonal	tetragonal	tetragonal	tetragonal
Space group	$I\bar{4}$	$I\bar{4}$	$I\bar{4}$	$I\bar{4}$
a /Å	26.633(4)	26.5097(8)	26.5579(10)	26.5219(5)
b /Å	26.633(4)	26.5097(8)	26.5579(10)	26.5219(5)
c /Å	5.2100(8)	5.2457(2)	5.1974(2)	5.24530(10)
α /°	90.00	90.00	90.00	90.00
β /°	90.00	90.00	90.00	90.00
γ /°	90.00	90.00	90.00	90.00
Volume/Å^3	3695.4(10)	3686.5(2)	3665.8(2)	3689.60(12)
Z	8	8	8	8
Calculated density/g cm^{-3}	1.483	1.375	1.430	1.327
Absorption coefficient (mm^{-1})	1.361	1.350	1.361	1.347
F_{000}	1672	1552	1608	1496
Reflections collected	2234	12925	14860	12224
Independent reflections	2234 [R_{int} = 0.0000]	4183 [R_{int} = 0.0201]	5212 [R_{int} = 0.0214]	3541 [R_{int} = 0.0300]
Data/restraints/parameters	2234 / 3 / 274	4183 / 1 / 270	5212 / 2 / 280	3541 / 0 / 264
Goodness-of-fit on F^2	1.100	1.043	1.065	1.124
Final *R* indices [$I>2\sigma(I)$]	*R*1 = 0.0484, *wR*2 = 0.1373	*R*1 = 0.0373, *wR*2 = 0.1058	*R*1 = 0.0369, *wR*2 = 0.1042	*R*1 = 0.0446, *wR*2 = 0.1352
R indices (all data)	*R*1 = 0.0542, *wR*2 = 0.1431	*R*1 = 0.0407, *wR*2 = 0.1084	*R*1 = 0.0426, *wR*2 = 0.1075	*R*1 = 0.0519, *wR*2 = 0.1391

	CO-IMMOF-3$_{13bar_100K}$	**CH_3Br-IMMOF-3$_{3bar_298K}$**	**CH_3Br-IMMOF-3$_{3bar_273K}$**	**C_2H_3F-IMMOF-3$_{15bar_298K}$**
Empirical formula	$C_{37}H_{22}N_4O_7Zn_2$	$C_{18.20}H_{11.60}Br_{0.20}N_2O_3Zn$	$C_{18.20}H_{11.60}Br_{0.20}N_2O_3Zn$	$C_{18.50}H_{11.75}F_{0.25}N_2O_3Zn$
Formula weight	765.33	387.65	387.65	380.17
Temperature/K	100(2)	299(2)	273(2)	298(2)
Wavelength/Å	0.71073	0.71073	0.71073	0.71073
Crystal system	tetragonal	tetragonal	tetragonal	tetragonal
Space group	$I\bar{4}$	$I\bar{4}$	$I\bar{4}$	$I\bar{4}$
a /Å	26.6362(12)	26.555(5)	26.562(18)	26.5120(9)
b /Å	26.6362(12)	26.555(5)	26.562(18)	26.5120(9)
c /Å	5.1199(2)	5.2242(9)	5.214(4)	5.2509(2)
α /°	90.00	90.00	90.00	90.00
β /°	90.00	90.00	90.00	90.00
γ /°	90.00	90.00	90.00	90.00
Volume/Å^3	3632.5(3)	3684.0(12)	3678(4)	3690.8(2)
Z	4	8	8	8
Calculated density/g cm^{-3}	1.399	1.398	1.400	1.368
Absorption coefficient (mm^{-1})	1.373	1.784	1.786	1.350
F_{000}	1552	1566	1566	1544
Reflections collected	14354	3374	7517	14882
Independent reflections	4977 [R_{int} = 0.0237]	1871 [R_{int} = 0.0344]	4036 [R_{int} = 0.0315]	5205 [R_{int} = 0.0246]
Data/restraints/parameters	4977 / 1 / 272	1871 / 1 / 258	4036 / 1 / 275	5205 / 2 / 273
Goodness-of-fit on F^2	1.092	1.117	1.097	1.024
Final *R* indices [$I>2\sigma(I)$]	*R*1 = 0.0359, *wR*2 = 0.1001	*R*1 = 0.0482, *wR*2 = 0.1361	*R*1 = 0.0521, *wR*2 = 0.1526	*R*1 = 0.0395, *wR*2 = 0.1064
R indices (all data)	*R*1 = 0.0398, *wR*2 = 0.1019	*R*1 = 0.0604, *wR*2 = 0.1435	*R*1 = 0.0616, *wR*2 = 0.1580	*R*1 = 0.0523, *wR*2 = 0.1136

	C_2H_3F-IMMOF-3_{15bar_250K}	**C_2H_3Br-IMMOF-3_{1bar_298K}**	**C_2H_3Br-IMMOF-3_{1bar_220K}**	**[b] C_2H_3Cl-IMMOF-3_{3bar_298K}**
Empirical formula	$C_{19}H_{12.50}F_{0.50}N_2O_3Zn$	[a] $C_{18}H_{11}N_2O_3Zn$	$C_{18.20}H_{11.30}Br_{0.10}N_2O_3Zn$	$C_{18}H_{11}N_2O_3Zn$
Formula weight	391.68	368.66	379.35	368.66
Temperature/K	250(2)	296(2)	220(2)	298(2)
Wavelength/Å	0.71073	0.71073	0.71073	0.71073
Crystal system	tetragonal	tetragonal	tetragonal	tetragonal
Space group	$I\bar{4}$	$I\bar{4}$	$I\bar{4}$	$I\bar{4}$
a /Å	26.552(4)	26.4984(8)	26.5447(9)	26.523(2)
b /Å	26.552(4)	26.4984(8)	26.5447(9)	26.523(2)
c /Å	5.2208(8)	5.2598(2)	5.2079(2)	5.2472(4)
α /°	90.00	90.00	90.00	90.00
β /°	90.00	90.00	90.00	90.00
γ /°	90.00	90.00	90.00	90.00
Volume/Å^3	3680.8(10)	3693.2(2)	3669.6(2)	3691.2(5)
Z	8	8	8	8
Calculated density/g cm^{-3}	1.414	1.326	1.373	1.327
Absorption coefficient (mm^{-1})	1.358	1.345	1.573	1.346
F_{000}	1592	1496	1536	1496
Reflections collected	14855	14961	14860	11375
Independent reflections	5183 [R_{int} = 0.0270]	5233 [R_{int} = 0.0226]	5208 [R_{int} = 0.0228]	4210 [R_{int} = 0.0230]
Data/restraints/parameters	5183 / 3 / 273	5233 / 0 / 264	5208 / 3 / 273	4210 / 0 / 264
Goodness-of-fit on F^2	1.006	1.048	1.066	1.029
Final R indices [$I>2\sigma(I)$]	$R1$ = 0.0397, $wR2$ = 0.1043	$R1$ = 0.0418, $wR2$ = 0.1148	$R1$ = 0.0379, $wR2$ = 0.1060	$R1$ = 0.0389, $wR2$ = 0.1091
R indices (all data)	$R1$ = 0.0506, $wR2$ = 0.1103	$R1$ = 0.0521, $wR2$ = 0.1212	$R1$ = 0.0452, $wR2$ = 0.1102	$R1$ = 0.0448, $wR2$ = 0.1131

[a] vinyl bromide molecule could not be modelled and therefore its molecular formula is not included in the molecular formula of the structure.

[b] The gas molecule was not included in the host framework.

	$ClCF_3$-IMMOF-3_{10bar_298K}	**$ClCF_3$-IMMOF-3_{10bar_273K}**	**IMMOF-$3_{apo\_100\ K}$**	**IMMOF-$3_{apo\_190\ K}$**
Empirical formula	$C_{18.25}H_{11}Cl_{0.25}F_{0.75}N_2O_3Zn$	$C_{18.25}H_{11}Cl_{0.25}F_{0.75}N_2O_3Zn$	$C_{18}H_{12}N_2O_3Zn$	$C_{18}H_{12}N_2O_3Zn$
Formula weight	394.77	394.77	369.67	369.67
Temperature/K	299(2)	273(2)	100(2)	190(2)
Wavelength/Å	0.71073	0.71073	0.71073	0.71073
Crystal system	tetragonal	tetragonal	tetragonal	tetragonal
Space group	$I\bar{4}$	$I\bar{4}$	$I\bar{4}$	$I\bar{4}$
a /Å	26.590(4)	26.590(3)	26.5937(11)	26.5112(9)
b /Å	26.590(4)	26.590(3)	26.5937(11)	26.5112(9)
c /Å	5.1957(8)	5.2138(7)	5.1462(2)	5.2351(2)
α /°	90.00	90.00	90.00	90.00
β /°	90.00	90.00	90.00	90.00
γ /°	90.00	90.00	90.00	90.00
Volume/Å^3	3673.5(10)	3686.2(8)	3639.5(3)	3679.5(2)
Z	8	8	8	8
Calculated density/g cm^{-3}	1.428	1.423	1.349	1.331
Absorption coefficient (mm^{-1})	1.398	1.394	1.365	1.350
F_{000}	1596	1596	1504	1496
Reflections collected	11352	11318	14398	14425
Independent reflections	4354 [R_{int} = 0.0224]	4235 [R_{int} = 0.0249]	5116 [R_{int} = 0.0245]	5190 [R_{int} = 0.0199]
Data/restraints/parameters	4354 / 10 / 279	4235 / 10 / 279	5116 / 1 / 268	5190 / 0 / 258
Goodness-of-fit on F^2	1.071	1.121	1.066	1.050
Final *R* indices [$I>2\sigma(I)$]	*R*1 = 0.0364, *wR*2 = 0.1035	*R*1 = 0.0358, *wR*2 = 0.1018	*R*1 = 0.0395, *wR*2 = 0.1089	*R*1 = 0.0439, *wR*2 = 0.1250
R indices (all data)	*R*1 = 0.0408, *wR*2 = 0.1064	*R*1 = 0.0388, *wR*2 = 0.1048	*R*1 = 0.0443, *wR*2 = 0.1116	*R*1 = 0.0496, *wR*2 = 0.1296

[a] The gas molecule was not included in the host framework.

	IMMOF-3 $_{apo\_280\ K}$	**IMMOF-3** $_{apo\_370\ K}$
Empirical formula	$C_{18}H_{11}N_2O_3Zn$	$C_{18}H_{11}N_2O_3Zn$
Formula weight	368.66	368.66
Temperature/K	280(2)	370(2)
Wavelength/Å	0.71073	0.71073
Crystal system	tetragonal	tetragonal
Space group	$I\bar{4}$	$I\bar{4}$
a /Å	26.4574(9	26.4366(9)
b /Å	26.4574(9	26.4366(9)
c /Å	5.2854(2)	5.3287(2)
α /°	90.00	90.00
β /°	90.00	90.00
γ /°	90.00	90.00
Volume/Å^3	3699.7(2)	3724.2(2)
Z	8	8
Calculated density/g cm^{-3}	1.324	1.315
Absorption coefficient (mm^{-1})	1.343	1.334
F_{000}	1496	1496
Reflections collected	13894	13359
Independent reflections	4790 [R_{int} = 0.0208]	4468 [R_{int} = 0.0801]
Data/restraints/parameters	4790 / 0 / 253	4468 / 1 / 249
Goodness-of-fit on F^2	1.042	1.015
Final *R* indices [$I>2\sigma(I)$]	$R1$ = 0.0457, $wR2$ = 0.1332	$R1$ = 0.0589, $wR2$ = 0.1558
R indices (all data)	$R1$ = 0.0510, $wR2$ = 0.1379	$R1$ = 0.0666, $wR2$ = 0.1609

CHAPTER 5

A METALLOCYCLIC MATERIAL: TRANSIENT POROSITY

A metallocycle is a discrete cyclic entity formed by the coordination of ditopic ligands to transition metal cations. A type of flexible ditopic ligand used to prepare metallocycles in our research group consists of an aromatic spacer with two imidazolyl moieties on either side of the spacer. When two of these ligands adopt a *C*-shaped conformation and coordinate to two metal cations, a metallocycle is formed (Figure 110).

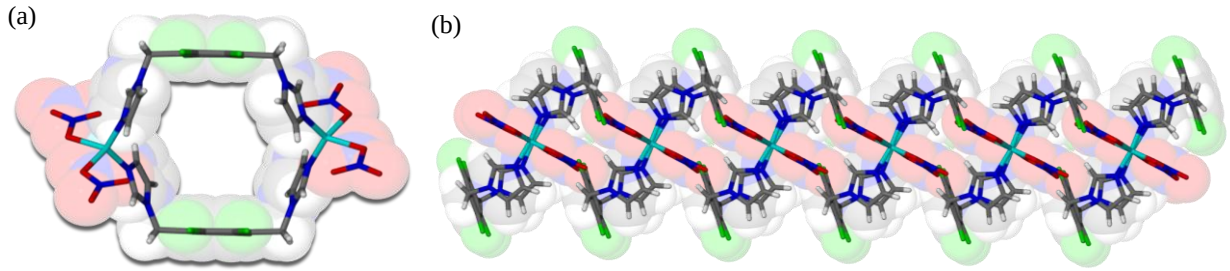

Figure 110. (a) The space-filled (semi-transparent) and capped stick representation of a metallocycle that consists of two ditopic ligands coordinated to two metal cations. Two nitrate anions coordinate to each of the the metal(II) centres. (b) A representation of a column of stacked metallocycles.

The metallocycle can enclose solvent molecules within the cavity of the ring-like complex. In some cases solvent can also be included in the interstices between the metallocycles. The metallocyclic units usually stack on top of each other in columns forming one-dimensional solvent-accessible channels or, in some cases, discrete solvent-accessible cavities. Once the solvent molecules are removed a porous system is produced if the supramolecular assembly remains intact. In a limited number of cases, the apohost crystals can be obtained without a loss of single crystallinity during the desolvation process. Our research group has reported several studies on the gas sorption and guest inclusion properties of these metallocyclic materials.[23] In the reported studies, SCD data are used to obtain structural information on the host-guest and guest-guest interactions in metalocyclic host-guest systems.

We make use of the fact that the "doughnut-shaped" cyclic complexes are unable to stack efficiently or interdigitate in the solid-state such that porous materials result. To this end, systematic studies have been carried out to find the ideal crystallisation technique and conditions for the self-assembly of metallocycles instead of close-packed one-dimensional coordination

polymers.[80] When a coordination polymer is formed, the ligand is generally in an *S*-shaped conformation instead of the *C*-shaped conformation found in metallocycles (Figure 111).

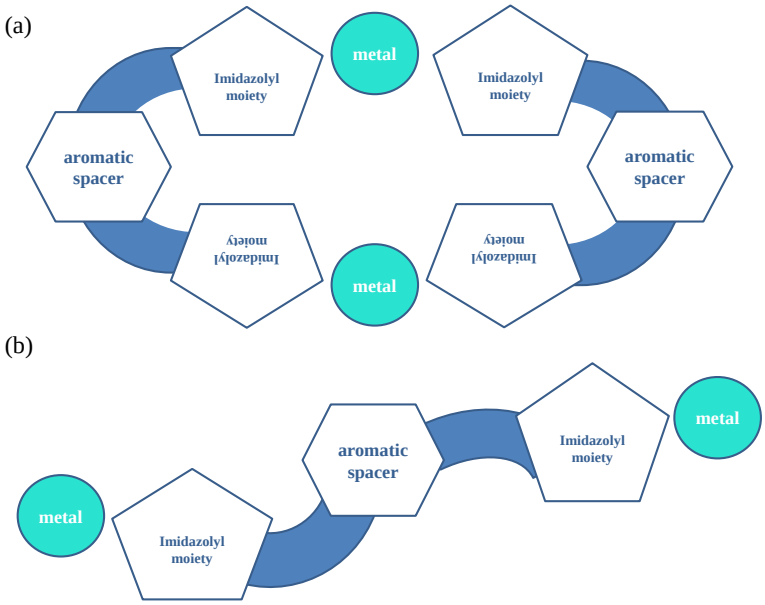

Figure 111. A schematic representation of (a) a ligand, consisting of an aromatic spacer and two imidazolyl coordinating moieties that adopts a *C*-shaped conformation to form a metallocycle and (b) a ligand in the *S*-shaped conformation that forms part of a 1D coordination polymer.

Layering the metal salt in a solvent (usually methanol or acetonitrile) on top of a solution of the ligand in another solvent (usually DCM) generally yields crystals of a metallocycle at the interface of the two solvents. Variation of the metal:ligand (M:L) ratio often yields different products and dilute solutions of the ligand and metal salt are more likely to form metallocycles. If a vial is left for a long time before the crystals are analysed various polymorphs or supramolecular isomers of the building blocks may form over time. This may occur due to varying solution concentration during the crystallisation, or due to the re-dissolving of the metal-organic products in the solution.

Various adaptations of the ditopic ligands have been studied previously.[80] However, in the current study, a fluorinated aromatic spacer (fluorinated at positions 2, 3, 5 and 6) with two imidazolyl moieties was crystallised with $Zn(NO_3)_2$ to form a novel metallocyclic material with discrete solvent-filled cavities. The dynamic nature of this material and its transiently porous properties were investigated and will be described in the following sections. During the course of these studies it became evident that the desolvation of a solvent-templated assembly of metallocycles may result in a metastable phase that can spontaneously rearrange in the solid state, as triggered by external stimuli such as gas pressure or temperature.

5.1 SYNTHESIS AND STRUCTURAL ANALYSIS OF A ZN(II) METALLOCYCLE

(The first synthesis of the ligand and the first crystallisation of the metallocycle were carried out by Storm Potts, a former PhD student in our research group)

The organic ligand, 1,1'-(perfluoro-1,4-phenylene)bis(methylene)bis(1*H*-imidazole) (Fbix) was synthesised following a procedure from the literature.[81] The authors report the structures of a metallocycle formed with the ligand and Ag(II) and a coordination network of the ligand with Co(II). The authors report that fluorination of the phenylene spacer prevents interpenetration from occurring and will increase the likelihood of enclathration of the guest. This is due to the fact that the electron-deficient tetrafluorophenylene spacer is involved with weaker intermolecular interactions than the electron-rich phenylene spacer. The electron-rich spacer participates in π-π stacking that constricts or interpenetrates the structure. In the present study the preparation and sorption properties of a novel metallocycle formed from the abovementioned ligand with $Zn(NO_3)_2.4H_2O$ were investigated.

The Zn(II) metallocycle, **MC1**, was prepared by layering 0.025 mmol (7.8 mg) Fbix, in 3 ml dichloromethane (CH_2Cl_2, DCM) with an equimolar amount of $Zn(NO_3)_2.4H_2O$ in 2 ml methanol (MeOH), Scheme 7. After one day single crystals suitable for single-crystal X-ray diffraction were obtained on the side of the vial at the DCM/MeOH interface.

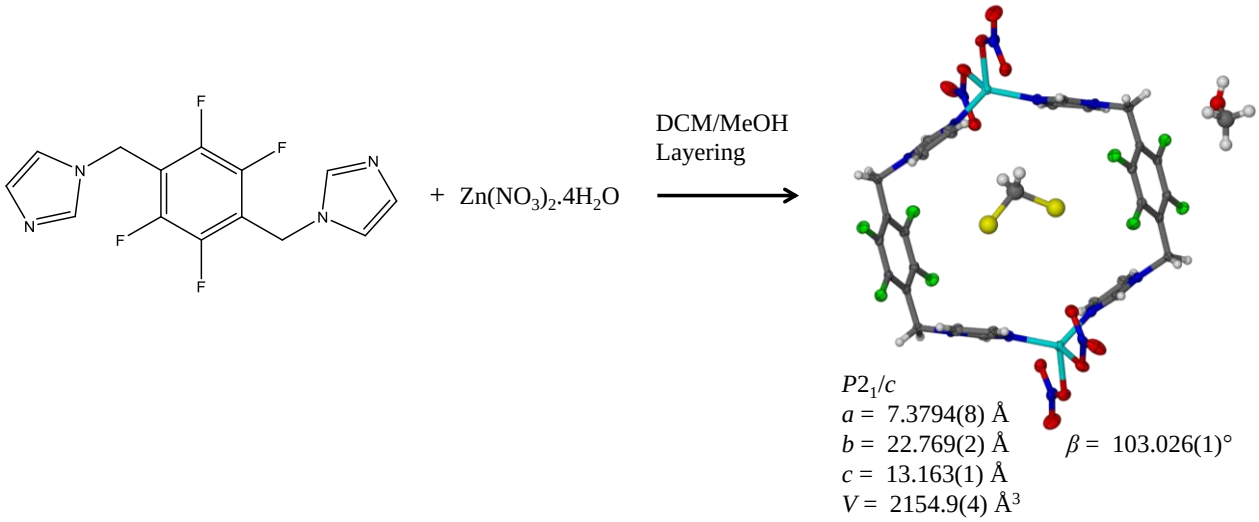

Scheme 7. The formation of **MC1** with selected crystallographic information.

Structure elucidation revealed the formation of discrete dinuclear metallocycles in which each zinc ion is coordinated to two monodentate nitrate anions and two ligands that are located *trans* with respect to each other to form a distorted tetrahedral coordination environment around

each metal centre. The ring-like complexes stack along the crystallographic *a* axis to form columns, which are arranged in a herringbone fashion when viewed along [100]. Interestingly, both reaction solvents are present in the crystal structure; each metallocycle encloses one DCM molecule disordered equally over two positions across a crystallographic inversion centre, and two MeOH molecules per metallocycle are located in the interstices between columns. Each methanol molecule accepts a hydrogen bond from a methylene carbon (C···O = 3.227(6) Å) and in turn donates a hydrogen bond to a coordinated nitrate ion (O···O = 3.228(6) Å), and adjacent columns are connected to one another by virtue of these weak hydrogen bonds (Figure 112).

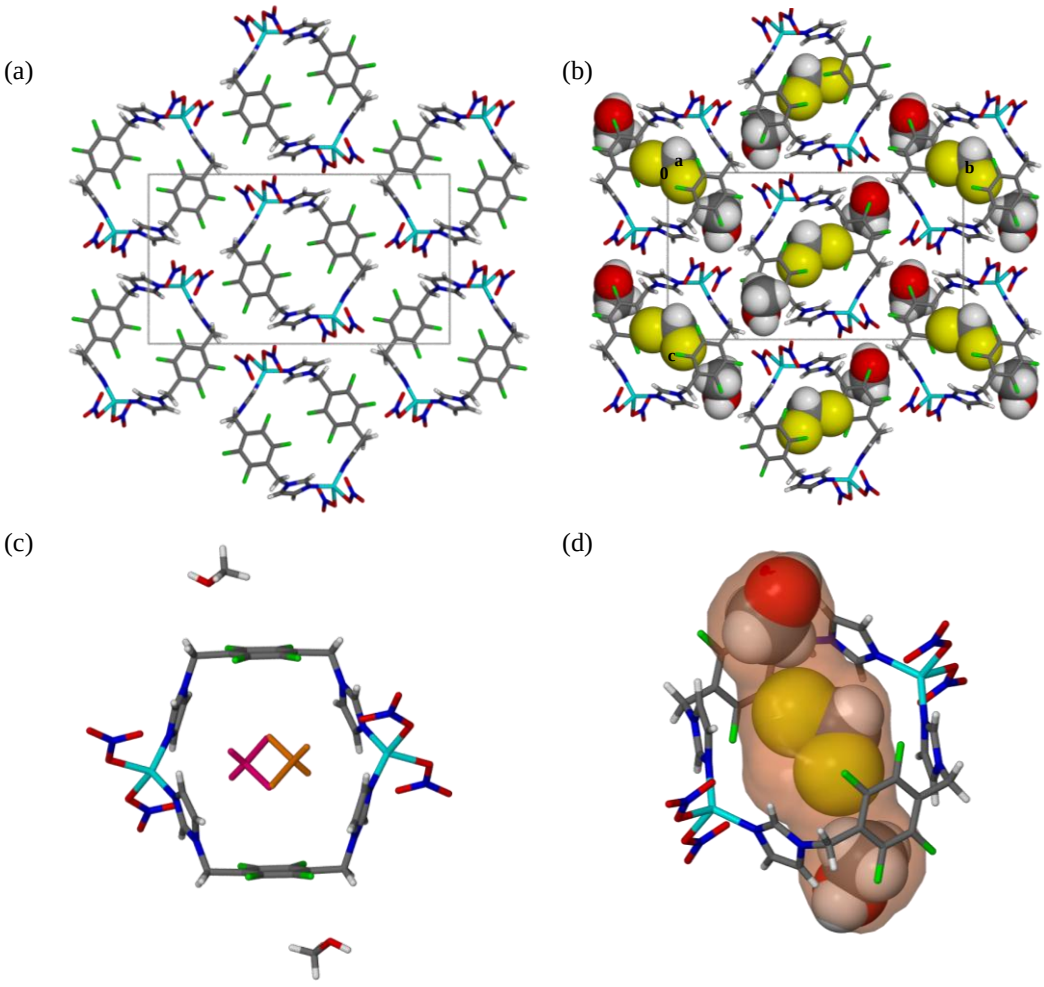

Figure 112 (a) The herringbone packing arrangement of adjacent columns of metallocycles viewed along [100] (solvent omitted). (b) The packing arrangement with the solvent molecules shown in space-filled representation. (c) A metallocycle enclosing a DCM molecule that is disordered equally over two positions (shown in green and pink). (d) The Connolly surface, mapped using MSROLL[39], of the solvent-accessible space occupied by one DCM and two methanol molecules per metallocycle.

The included DCM molecule is thought to template the formation of the metallocycle. Indeed, previous studies of the solvent-templating effect during the self-assembly of metallocycles have been reported.[82] Certain aspects of the included solvent, such as its molecular

shape, size and polarity, can play a role in the conformation of the ligand and thus direct the self-assembly process.

Previous reports of metallocycles of this kind have all shown that the columnar stacking arrangement of the metallocycles facilitates the formation of continuous 1D solvent-filled channels or discrete solvent-filled pockets. The solvent molecules of **MC1** are situated in discrete pockets, but unlike previous examples, the discrete pockets in **MC1** are not entirely localized within the column. A Connolly[39] surface analysis (using a probe radius of r_{probe} = 1.4 Å) revealed that the discrete pockets protrude outwards from the inner aperture of the metallocycle columns (Figure 113). This can be ascribed to interstitial methanol molecules, which are in van der Waals contact with the occluded DCM molecules. The total solvent-accessible volume (259 Å^3) is therefore significantly larger than the solvent-accessible volumes of metallocycles that have been previously reported by our research group.[23]

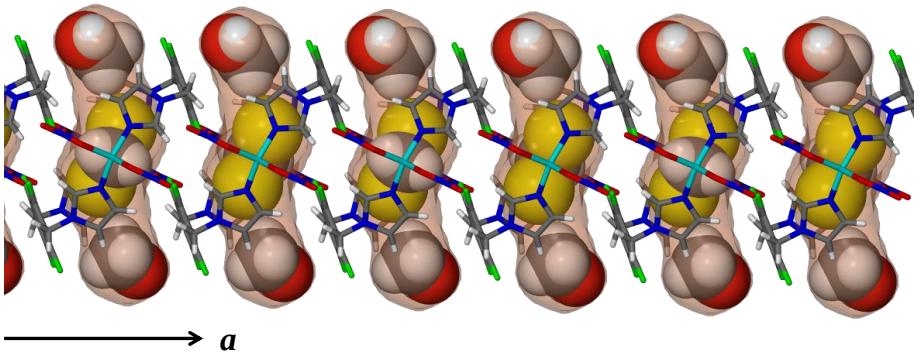

Figure 113. The columnar stacking of metallocycles along [100] (view along the Zn···Zn vector). The Connolly surface of the solvent-accessible space (259 Å^3), mapped using MSROLL[39] (probe radius = 1.4 Å), is shown in orange.

5.2 SUPRAMOLECULAR ISOMERISM

Supramolecular isomerism refers to the different host packing arrangements or crystalline products derived from the same building blocks. For our purposes, only structural supramolecular isomerism will be discussed. Structural supramolecular isomerism refers to different superstructures obtained from the same components, such that the superstructures have the same empirical formula.[83] During crystallization of **MC1** with a 1:1 metal:ligand ratio, a concomitant supramolecular isomer was obtained. The supramolecular isomer is a polymeric 2D MOF salt that will be referred to as coordination polymer (**CP**). Three ligand molecules and one nitrate anion coordinate to the metal centre in a tetrahedral coordination environment

(Figure 114). An uncoordinated nitrate anion and three water molecules are situated within 1D "channels" that occur along the *a* axis (Figure 115).

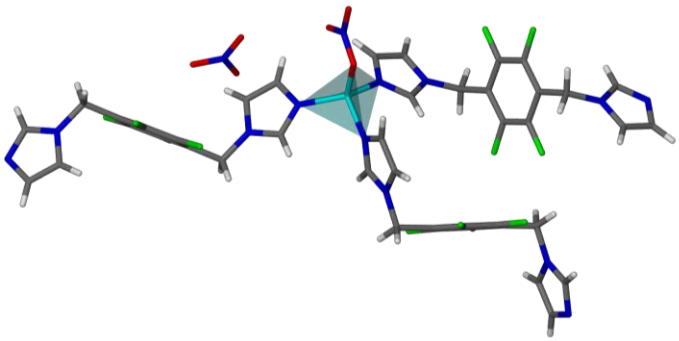

Figure 114. The tetrahedral coordination environment around the Zn(II) metal centre of **CP**. Three ligand molecules that are in the *S*-shaped conformation and one nitrate anion are coordinated to the metal centre. The included water molecules were omitted.

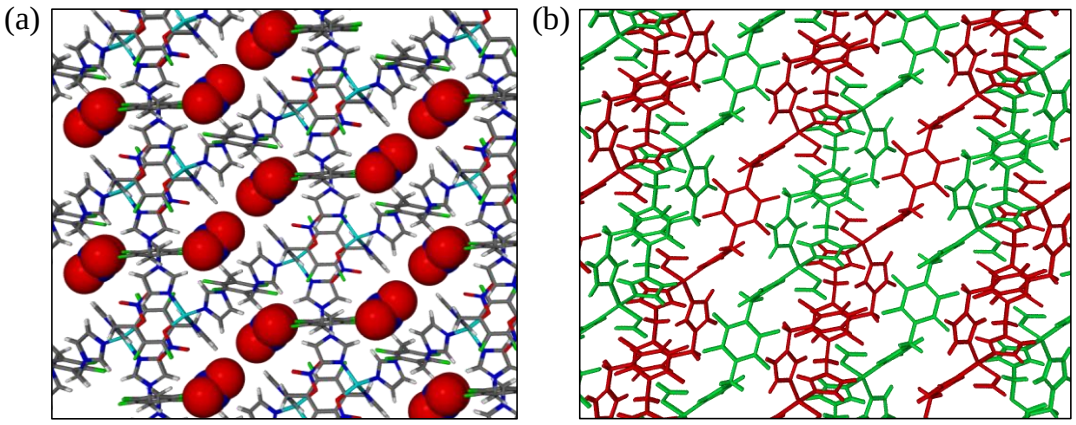

Figure 115. (a) The 2D **CP** formed with the Fbix ligand and $Zn(NO_3)_2$ viewed along [100]. The uncoordinated nitrate anion (shown in space-filled representation) and three water molecules (omitted) occupy the one dimensional channels along [100]. (b) The 2D layered structure of **CP** viewed along [010]. The 2D layers are coloured in green and red in order to distinguish between them.

A systematic variation of the M:L ratio during crystallisation and subsequent PXRD analysis revealed that when the $Zn(NO_3)_2$ salt is in excess (M:L ratio of 1.25:1, 1.5:1 and 2:1) the formation of the metallocyclic phase is favoured. When the ligand is in excess the polymeric 2D MOF phase, **CP**, starts to form concomitantly with **MC1 (**Figure 116**)**. Interestingly, if crystals of the **MC1** phase are not removed from the mother liquor directly after they form, they will "convert" to the polymeric phase over time, as evidenced by the PXRD patterns shown in Figure 117. It is believed that the **MC1** phase is a kinetic product and is soluble in the mother liquor under certain conditions. If the crystallization vial is disturbed, or if there are temperature variations, **MC1** dissolves and a presumably more stable thermodynamic product, namely **CP**, is formed.

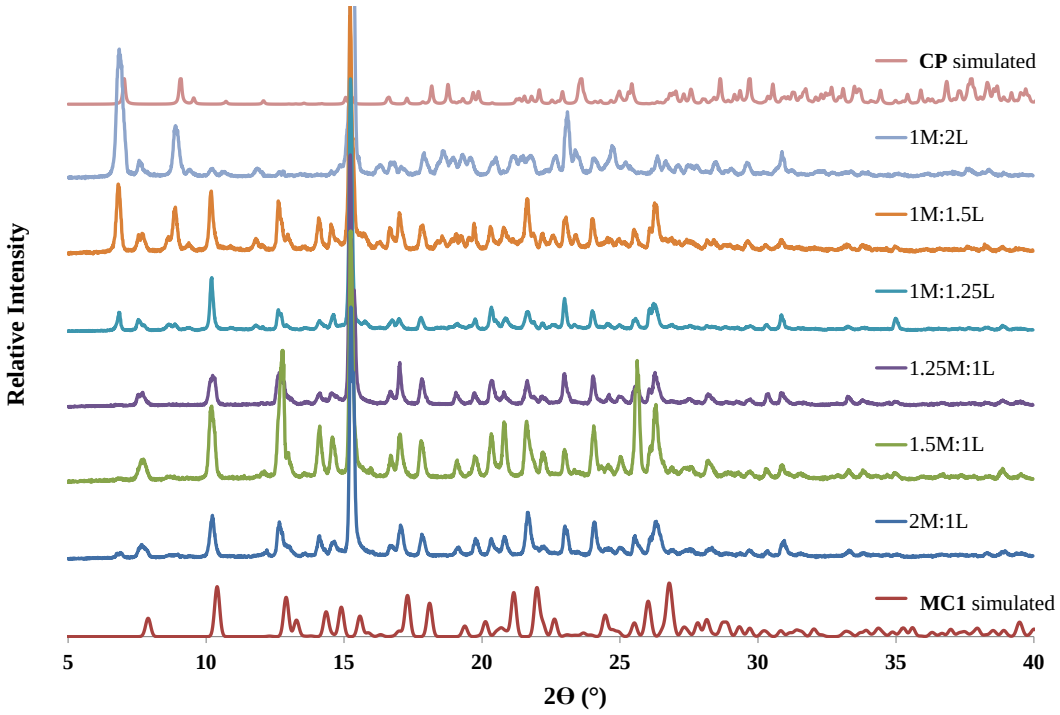

Figure 116. The experimental PXRD patterns obtained when the M:L ratio is varied during the crystallisation of **MC1**. The simulated PXRD patterns for **MC1** and the polymeric MOF, **CP**, are also shown in order to aid in the identification of the two supramolecular isomers in the experimental PXRD patterns.

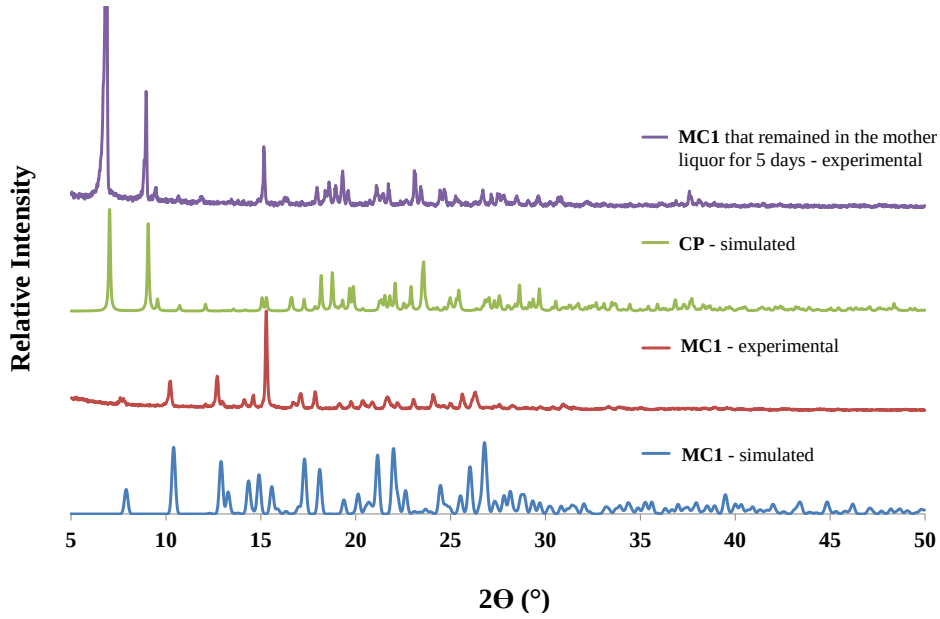

Figure 117. The PXRD pattern of crystallites of **MC1** (red) directly after it crystallised compares well with the simulated pattern of **MC1** (blue). However, the PXRD pattern that was measured on crystallites from the same vial of crystals that remained in the mother liquor for 6 days after the first batch of crystals were analysed (purple) correlates with the simulated PXRD pattern of the **CP** phase (green).

In addition to the phenomenon of supramolecular isomerism, metallocycles, like other inclusion compounds, can adopt the same packing arrangement whilst including a range of different guests. In this context the term "isoskeletal" refers to an identical host packing

arrangement that accommodates different guest molecules.[3] An isoskeletal solvatomorph of **MC1**, which will be referred to as **MC2**, was prepared using the same crystallization method used for **MC1** but with the $Zn(NO_3)_2.4H_2O$ salt dissolved in acetonitrile instead of methanol. The host packing arrangement is identical to that of **MC1**, i.e. isoskeletal, but different guest molecules are situated in the solvent-accessible spaces. In **MC2** three DCM molecules are included in the 272 $Å^3$ solvent-accessible space (with a packing coefficient of 0.64), Figure 118, in comparison to one DCM and two MeOH molecules included in the 259 $Å^3$ solvent-accessible spaces of **MC1** (with a packing coefficient of 0.53).

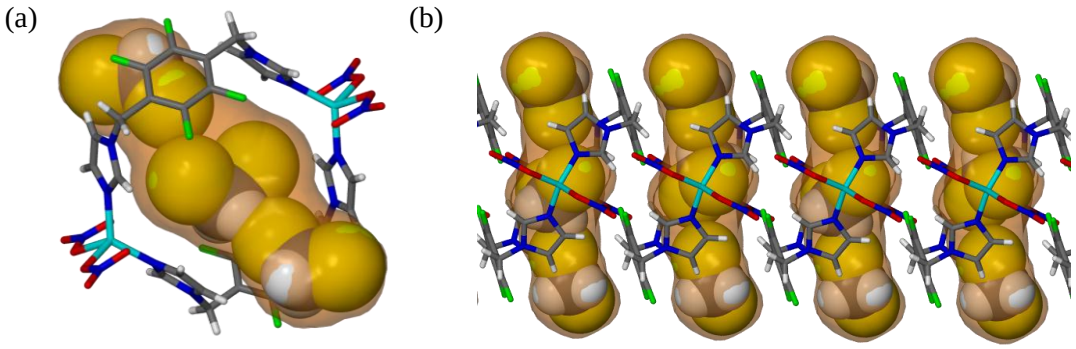

Figure 118. (a) The Connolly surface of the solvent-accessible space (272 $Å^3$), mapped using MSROLL[39] (probe radius = 1.4 Å), is shown in orange. The space is occupied by three DCM molecules per metallocycle. (b) The columnar stacking of metallocycles along [100] (view along the Zn···Zn vector).

Interestingly, acetonitrile is not included, perhaps owing to the fact that acetonitrile does not participate in the same type of stabilising interactions with the host. As was the case with methanol, the interstitial DCM molecule can act as a hydrogen bond acceptor for a methylene bridge hydrogen atom (C-H···Cl = 3.610(7) Å) and a hydrogen bond donor for the nitrate anion acceptor (C-H···O = 3.43(3) Å). The hydrogen-bond interactions between the interstitial DCM of **MC2** appear to be weaker than the interactions between the methanol molecules and the **MC1** host. This can be inferred from the longer donor···acceptor distances. The DCM molecules in **MC2** are more readily removed by heating than the guest molecules in **MC1**. This is apparent from the early onset of guest loss in **MC2** as compared to **MC1** in the TGA thermograms shown in Figure 119.

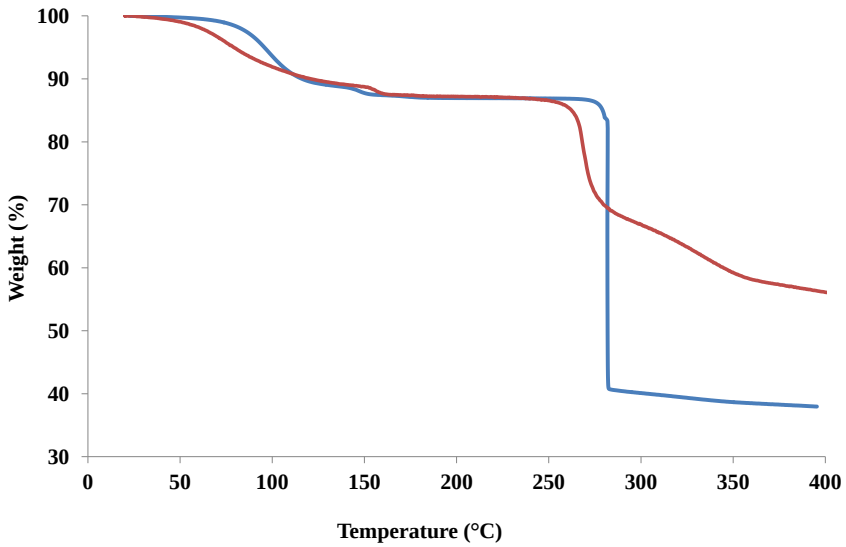

Figure 119. TGA of **MC1** (blue) and **MC2** (red).

The TGA trace of **MC2** is different to that of **MC1**, with an earlier onset of guest loss at room temperature in the case of **MC2**, whilst in **MC1** guest loss only occurs from 50 °C. Decomposition of **MC2** occurs at a lower temperature (~250 °C) than that of **MC1** (~270 °C). The different decomposition temperatures of **MC1** and **MC2** may be ascribed to the formation of unknown phases (described later in section 5.3.2) before decomposition. All further studies were carried out with the solvatomorph that was prepared first, namely **MC1**.

5.3 SINGLE-CRYSTAL TO SINGLE-CRYSTAL TRANSFORMATIONS

5.3.1 Guest-exchange experiments

The discrete pockets of space within the crystal structure are "closed off" or gated by the fluorinated benzene spacer of adjacent metallocycles (F···F distance: 3.160(5) Å where the sum of the van der Waals radii of two fluorine atoms is 2.94 Å), Figure 120.

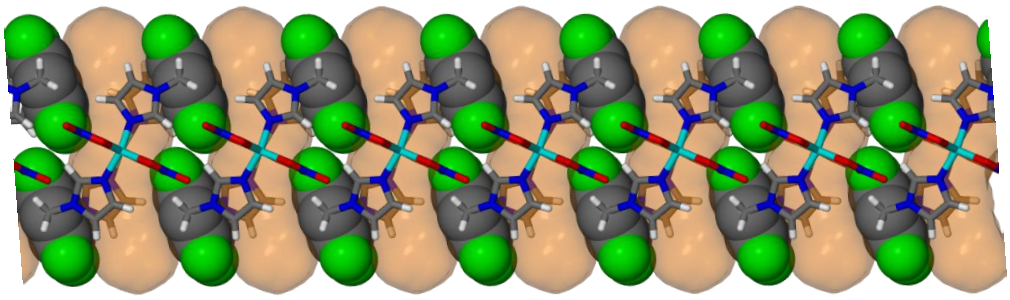

Figure 120. The fluorinated benzene spacers that guard the cavities (orange transparent surface, mapped using MSROLL[39]) are shown in space-filled representation. The solvent molecules are omitted for clarity.

It is believed that guest transport through the crystal is possible due to the rotational freedom of the fluorinated benzene spacer afforded by the flexible methylene bridges. The fluorinated benzene spacer can therefore rotate out of plane in order to allow the formation of a continuous undulating channel while the guest molecules are transported. The proposed transport mechanism is shown in Figure 121, but obtaining experimental evidence for this mechanism is not possible using X-ray diffraction techniques.

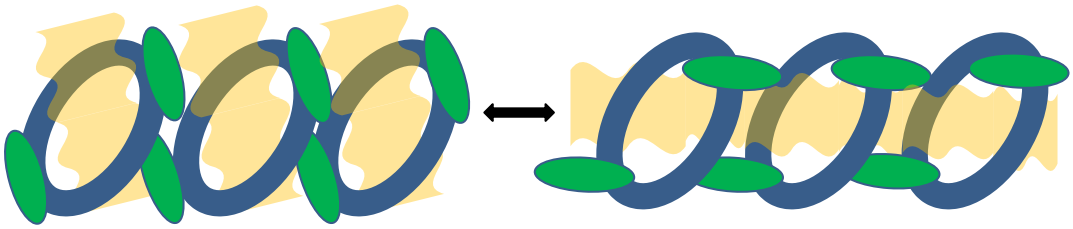

Figure 121. A schematic representation of the proposed guest transport mechanism in **MC1**. The fluorinated benzene spacers that gate the cavities are represented as green ovals. The semi-transparent orange surfaces represent the cavities that can interconvert to form continuous 1D channels during the diffusion of guest molecules through the metallocycle apertures.

Guest-exchange experiments were carried out in order to demonstrate that guest-transport is possible through the host structure. Single crystals dissolved in water and acetonitrile and became polycrystalline when immersed in methanol, benzene or ethanol. Vapour exchanges with the above-mentioned solvents did not yield diffraction quality single crystals either. Single crystals of **MC1** were also exposed to carbon disulphide (CS_2) vapours. The original DCM and methanol molecules contained in the structure were exchanged for carbon disulphide molecules in a single-crystal to single-crystal transformation. The inclusion complex of **MC1** with CS_2 will be referred to as **MC1·CS$_2$** and is shown in Figure 122. Guest exchange occurs without the presence of permanent channels in the structure. The material is thus flexible and atoms can move from their stable equilibrium positions in a concerted fashion in order to allow the diffusion of guest molecules. It is proposed that this can only be achieved with the stabilisation offered by favourable host-guest interactions.

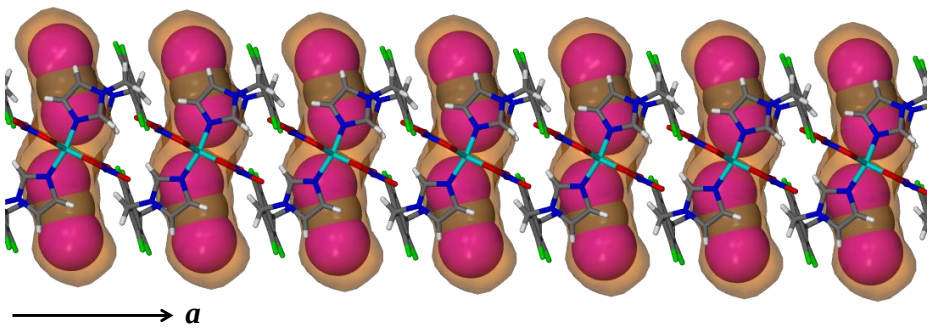

Figure 122. Two CS_2 molecules, shown in space-filled representation, are included per metallocycle in the solvent-accessible space of 253 Å^3 (orange, mapped using MSROLL,[39] probe radius = 1.4 Å).

Two CS_2 molecules (each with a molecular volume of 54.0 $Å^3$, calculated from the van der Waals surface in Materials Studio),[84] are included per metallocycle or per 253 $Å^3$ of solvent-accessible space. As is evident in Figure 122 the two molecules fit well into the irregularly shaped solvent-accessible space with a packing coefficient of 0.43. CS_2 molecules have a high polarizability (87.4-88.6 × 10^{25} cm^3)[60] which facilitates their transport and inclusion in **MC1·CS$_2$**. The TGA trace of **MC1·CS$_2$** shows that guest loss occurs from room temperature to 175 °C (6.35% weight), Figure 123. The stoichiometry of guest loss measured by TGA does not correlate with the SCD structure (13.22%) owing to guest loss occurring during sample preparation.

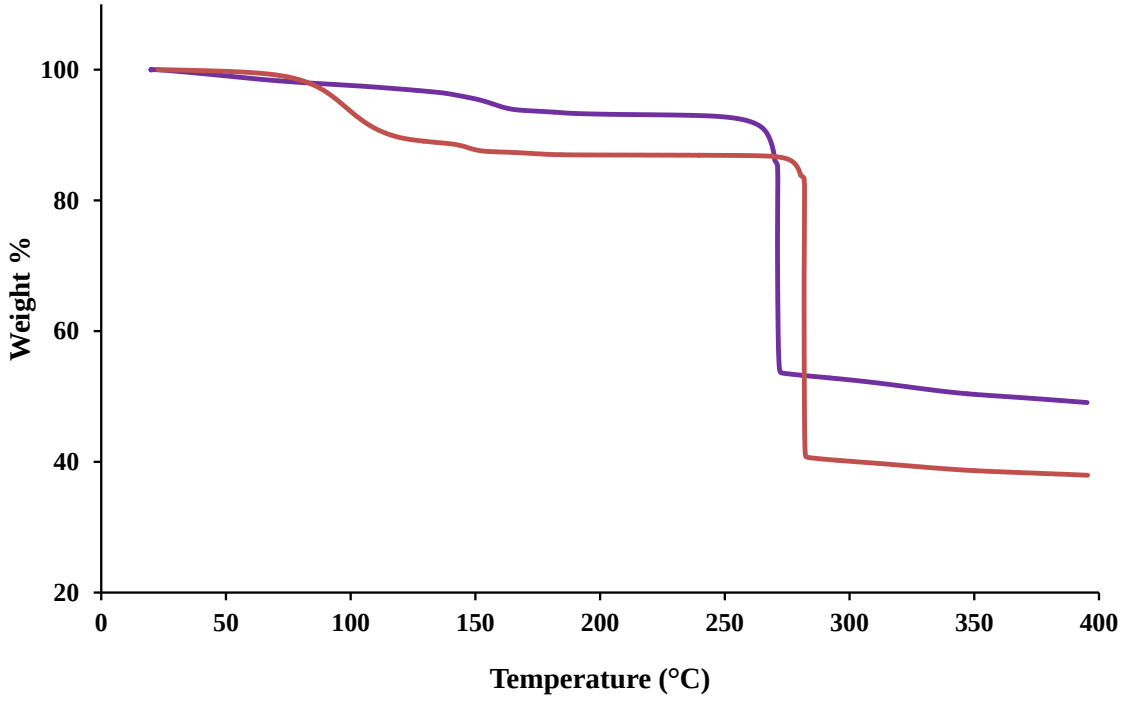

Figure 123. TGA of **MC1** (red) compared to **MC1·CS$_2$** (purple).

The inclusion of CS_2 molecules in a host system is an indication that further studies of CO_2 inclusion and sorption are merited. If CS_2 molecules with a larger molecular volume than CO_2 can be included, further gas sorption and gas cell studies will be appropriate. When crystals of **MC1** were subjected to exchange with CO_2 under supercritical CO_2 conditions, SCD analysis revealed that exchange did not take place. Therefore **MC1** needs to be desolvated prior to CO_2 inclusion and evacuation (discussed in the next section) needs to occur in a very specific manner.

5.3.2 Desolvation

The thermogram of **MC1** shown in Figure 124 reveals that the material starts losing solvent with an onset temperature of 50 °C. The overall mass loss of 12.9% between the temperatures of 50 °C and approximately 150 °C corresponds with the calculated mass loss for both the DCM and methanol guest molecules (12.9%).

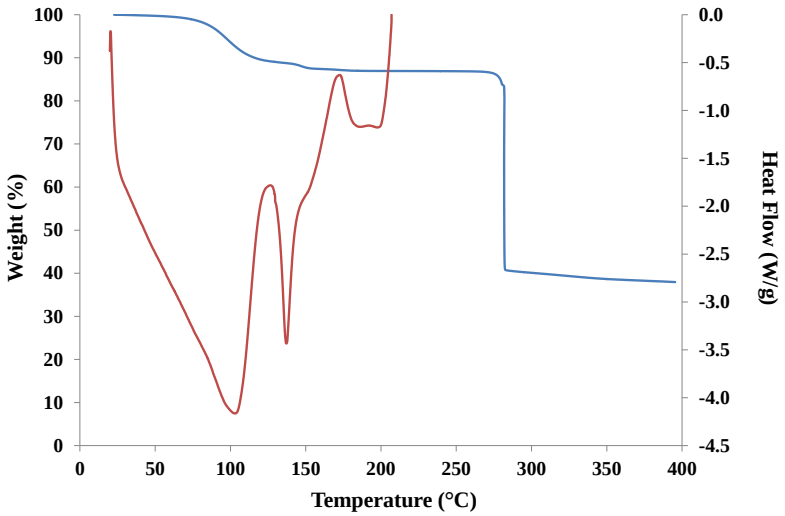

Figure 124. TGA of **MC1** (blue) with the differential scanning calorimetry (DSC) trace overlaid (red)

The DSC trace shows endotherms corresponding to the desolvation processes; however it is unclear from the DSC trace whether structural rearrangement occurs upon guest loss. Structural rearrangement (a phase change) is usually associated with an endo- or exothermic event and is difficult to distinguish from the endothermic desolvation process. Hot stage micrographs, shown in Figure 125, were taken in order to visualise the desolvation process and to establish whether the crystals remain single and/or of diffraction quality. The photographs reveal that **MC1** becomes opaque and polycrystalline during desolvation.

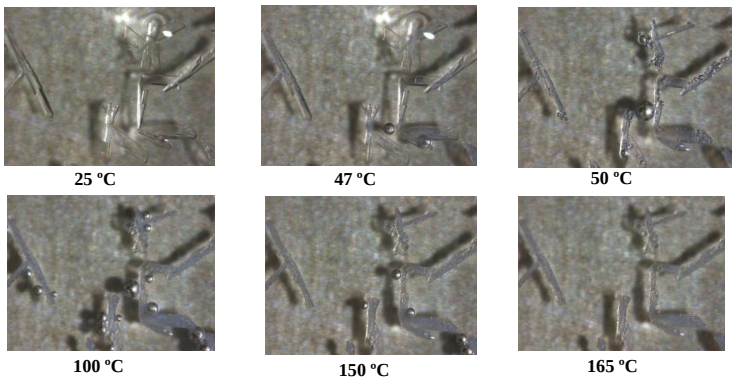

Figure 125. Hot stage microscopy of **MC1** reveals that the onset of desolvation occurs at 47 ºC and is complete at a temperature between 150 ºC and 165 ºC. The single crystals become polycrystalline during the desolvation process.

PXRD patterns were measured before and after desolvation. When the material is heated directly to 155 °C at a rate of ~15 °C min^{-1} a phase change occurs (Figure 126). However, if the material is heated in a stepwise manner, i.e. at a rate of ~15 °C min^{-1} to a temperature of 100 °C and held there for 20 minutes and then held at 155 °C for a further 20 minutes, the apohost is generated whilst maintaining the initial host packing arrangement (Figure 127).

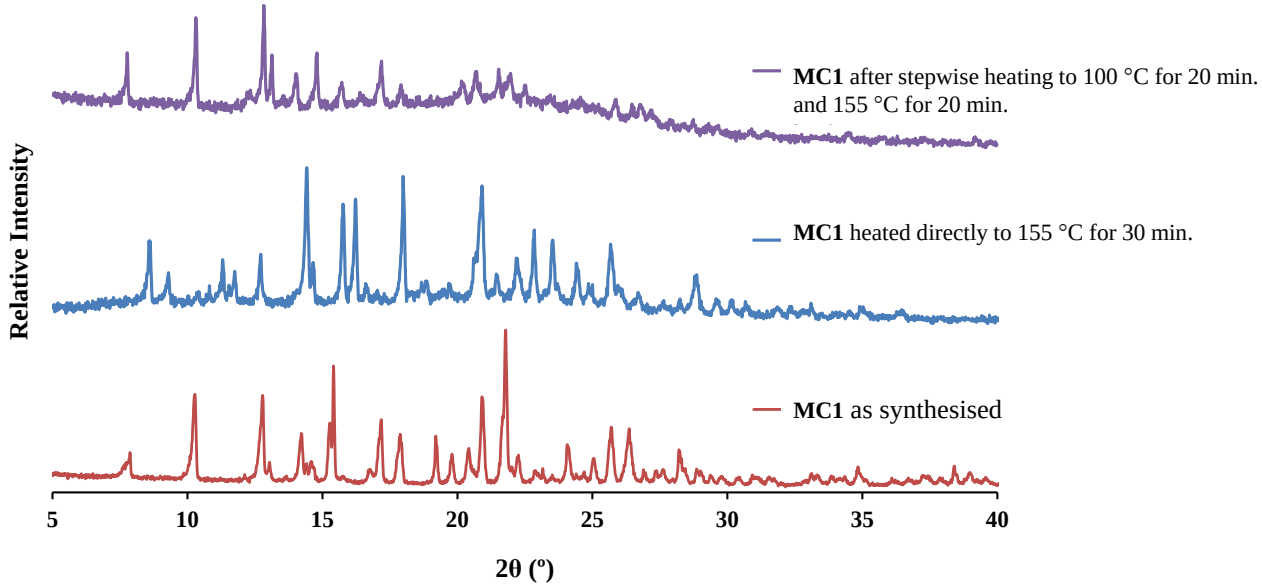

Figure 126. Experimental PXRD patterns of **MC1** are shown. Heating **MC1** directly to 155 °C results in a phase change to an unknown structure. However, stepwise heating to 100 °C and 155 °C results in the preservation of the original **MC1** structure.

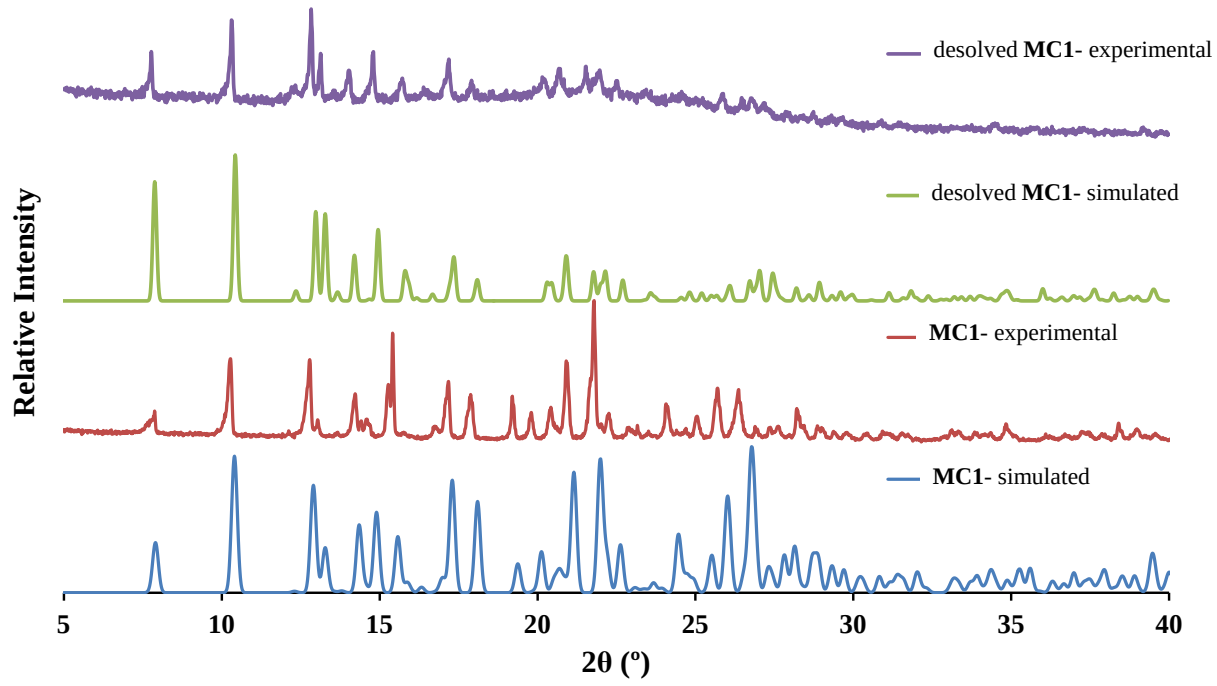

Figure 127. Experimental and simulated PXRD patterns of **MC1** prior to and after desolvation by stepwise heating.

Using the latter technique an empty single crystal was generated that was mounted within a gas cell for SCD structure determination whilst under controlled atmospheres. Similarly, a powdered sample was evacuated for gas sorption studies.

5.3.3 Gas sorption and single crystal X-ray diffraction under gas pressure

Gas sorption isotherms were measured at 20 °C on an evacuated sample of **MC1** using a gravimetric sorption analyser (IGA). A powdered sample of **MC1** absorbs more carbon dioxide (CO_2, ~2 molecules per metallocycle) than nitrogen (N_2,~0.7 molecules per metallocycle) and/or ethylene (C_2H_4,~0.5 molecules per metallocycle), Figure 128.

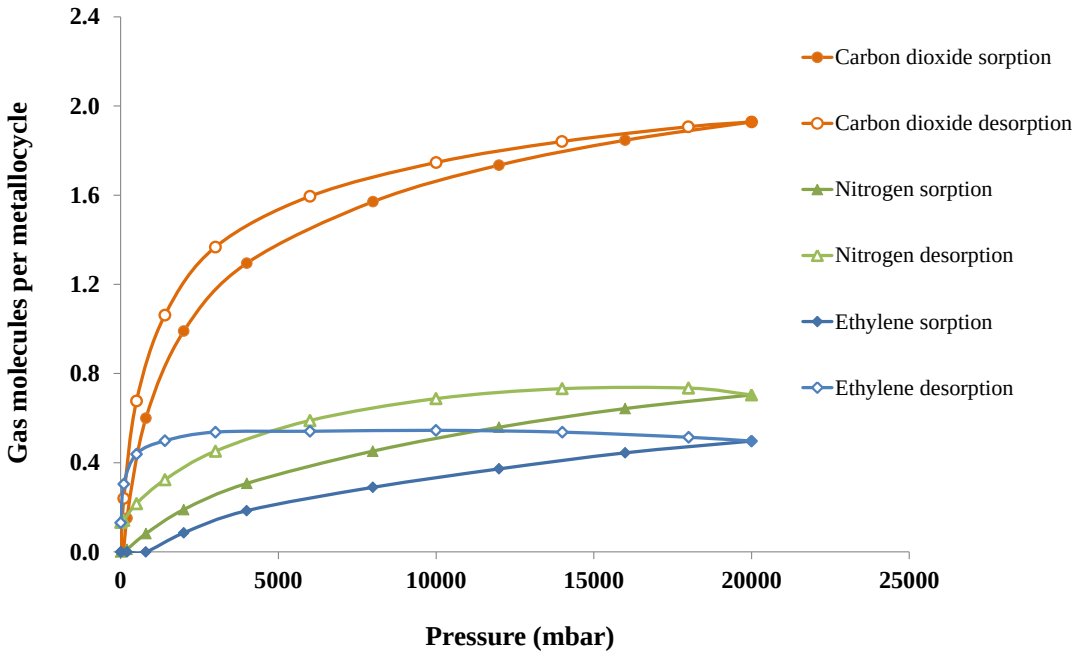

Figure 128. Gas sorption isotherms of **MC1** measured at 20 °C.

All three isotherms display hysteresis during desorption, which indicates favourable host-guest interactions. In particular, the desorption of C_2H_4 displays substantial hysteresis due to very slow diffusion kinetics. As the pressure was decreased, the IGA reached its time-out after 120 minutes of exposure to C_2H_4 at each specific pressure point. The amount of gas absorbed was then recorded despite the fact that the system did not reach equilibrium. Consequently, **MC1** was still absorbing C_2H_4 even though the pressure had been decreased. Of all three gases, C_2H_4 has the highest polarizability and kinetic diameter (listed in Table 27). These properties may cause the slow diffusion kinetics and hysteresis. A equilibration of several hours might be necessary at each pressure point. The hysteresis observed with N_2 sorption is surprising as N_2

does not normally interact strongly with microporous materials owing to its low polarizability (see Table 27). The hysteresis may be due to gas becoming entrapped in individual cavities to form stable host-guest adducts that have a lower lattice enthalpy than the apohost framework. The space filling role of the guest molecules probably lowers the lattice enthalpy substantially and thus diffusion of the guest out of the system is less favourable. This is true even in the case of N_2, where only weak van der Waals forces stabilise the host-guest adduct.

Table 27. The maximum occupancy of the three gases during gas sorption experiments with **MC1** and selected information about the gases.

Guest	Guest molecular formula	Guest volume from van der Waals surface (Å^3)	Kinetic diameter[60] (Å)	Polarizability[60] × 10^{25} (cm^3)	Maximum occupancy (molecules per metallocycle)
carbon dioxide	CO_2	35.33	3.3	29.11	1.9
ethylene	C_2H_4	43.29	4.163	33.3-39.3	0.5
nitrogen	N_2	22.23	3.64-3.80	17.403	0.7

The temperature dependence of the hysteresis is apparent in the CO_2 sorption isotherms measured at various temperatures (Figure 129). At 50 °C there is no hysteresis and the maximum occupancy is slightly reduced to ~1.8 CO_2 molecules per metallocycle, whilst at -5 °C the hysteresis is much more pronounced than at 20 °C. Some of the pressure points during sorption and desorption at -5 °C reached the time-out after 120 minutes, and the occupancy was recorded even though equilibrium had not been reached. The failure to reach equilibrium most likely caused the small inflection at ~11 bar in the sorption isotherm measured at -5 °C.

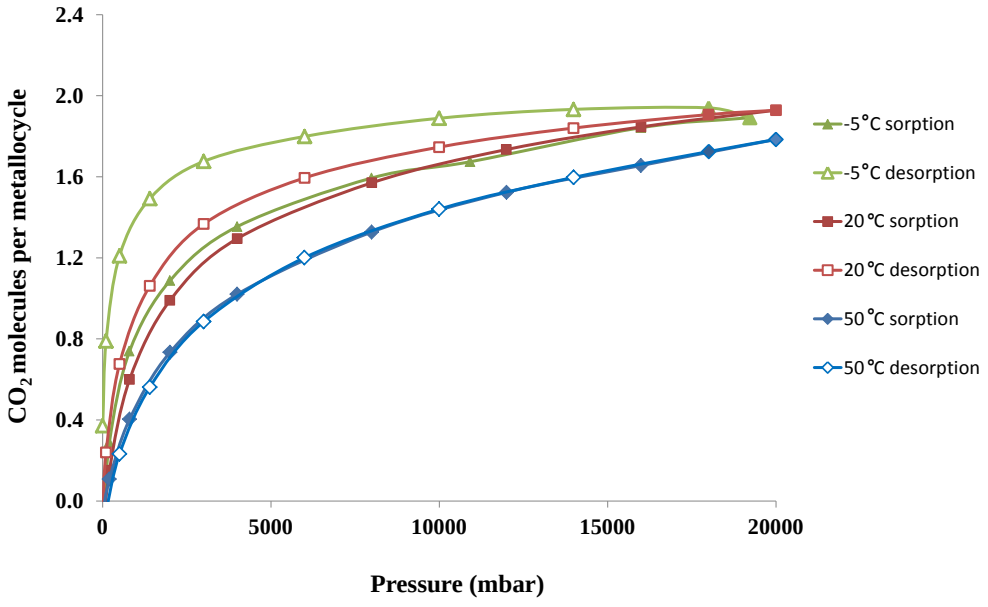

Figure 129. CO_2 sorption isotherms of **MC1** measured at -5 °C, 20 °C and 50 °C.

An HPDSC trace with **MC1** under increasing CO_2 pressure was measured at 20 °C in order to detect whether any structural changes occur concurrently with sorption at high CO_2 pressures (Figure 130). The first trace was measured from 1 to 10 bar CO_2 pressure and it shows an exothermic event that recedes gradually with increasing pressure. This exothermic event is likely due to CO_2 sorption and one cannot distinguish any unique thermal events relating to sudden structural changes. However the gradual descent to the baseline (wide exotherm) might be indicative of slow or ongoing dynamic structural changes that occur during the course of CO_2 transport. When a second DSC trace was measured from 10 to 40 bar CO_2 pressure, no further thermal events were recorded. **MC1** is therefore saturated with CO_2 and further increases in pressure do not appear to have a measurable effect on the structure.

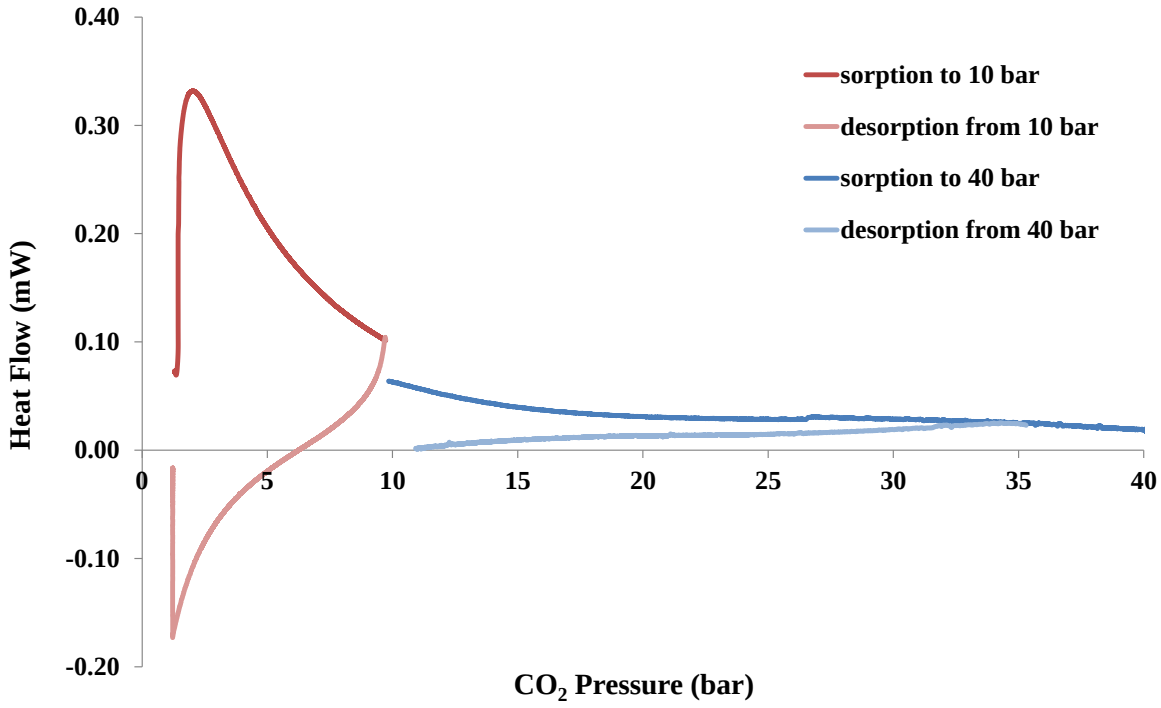

Figure 130. HPDSC trace of **MC1** with CO_2 at 20 °C. The red trace was measured from 1 - 10 bar (sorption and desorption) and the blue trace from 10 - 40 bar CO_2 pressure (sorption and desorption).

In order to understand which host-guest interactions may be involved with the inclusion of CO_2 and other gaseous guests in **MC1**, SCD data with a single crystal under controlled atmospheres were collected. The aim was to locate the positions of the guests within the metallocyclic framework in order to obtain information on the host-guest and guest-guest interactions. Simultaneously a comparison of the loaded and unloaded (apohost) material would reveal what deformation of the host is necessary to accommodate the guest molecules.

A structure of the apohost (**MC1·apohos**t) was determined from SCD data collected under vacuum in a sealed environmental gas cell. There are no continuous channels through the structure, but discrete cavities of ~238 $Å^3$ (determined using SQUEEZE) are present (Figure 131). The unoccupied space in the crystal is estimated to be approximately 22% of the total volume.

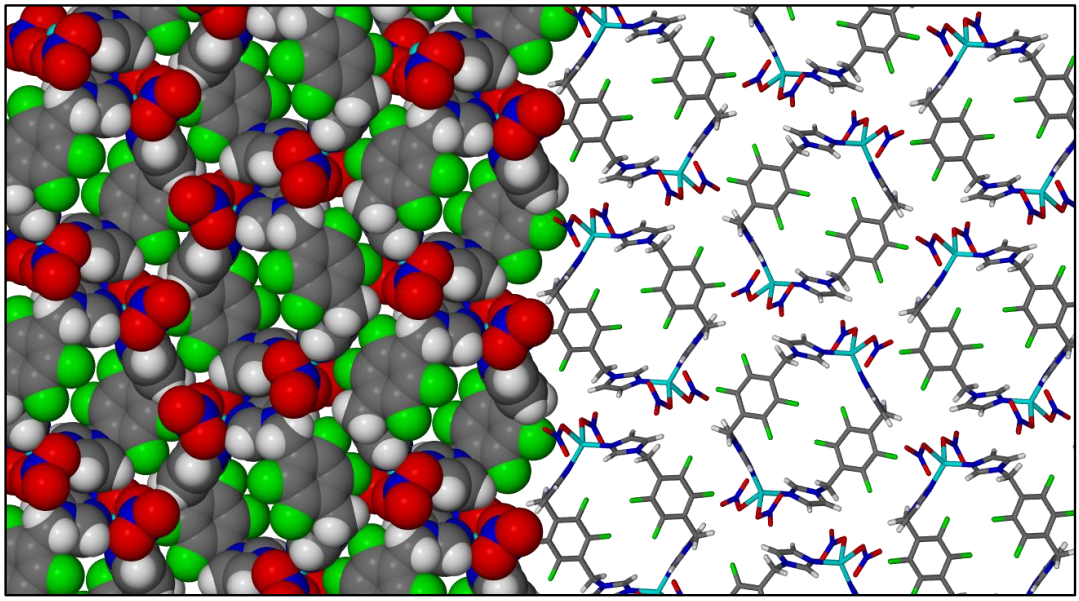

Figure 131. The herringbone packing arrangement of **MC1·apohost** viewed along [100]. Half of the image is in space-filled representation in order to demonstrate that there are no channels in the structure. Dynamic behaviour, such as the rotation of the fluorinated benzene spacer, is required for guest transport into the discrete voids.

The same crystal was exposed to 20 bar CO_2 pressure and a structure was collected at 268 K (-5 °C) to reduce the thermal motion and facilitate modelling of the guest. Three CO_2 molecules, each at full occupancy, were located within each cavity of **MC1·CO_2** (Figure 132). The bond lengths of the CO_2 molecules were restrained to 1.160(2) Å. The SQUEEZE electron count of 70 electrons per 253 $Å^3$ cavity is close to the expected total of 66 electrons for three CO_2 molecules.

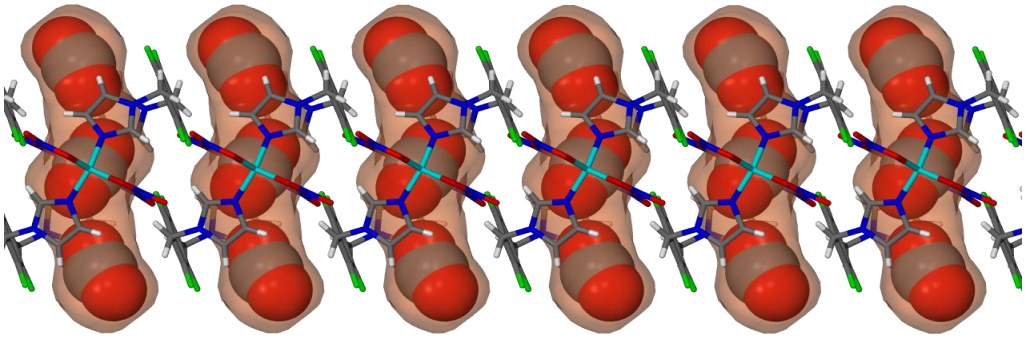

Figure 132. Three CO_2 molecules, shown in space-filled representation, are included per metallocycle in the guest-accessible space (semi-transparent orange surface mapped using MSROLL,[39] probe radius = 1.4 Å) of 253 $Å^3$.

When occupied by the gas molecules, the volume of the void increased to 253 $Å^3$ (from 238 $Å^3$ determined for the vacuum structure). The inclusion of CO_2 occurs with a packing coefficient of 0.42. Based on the SCD structure, **MC1** has a weight% CO_2 uptake of 13.26 wt% which is more than that of **IMMOF-3** (11.92%) despite the absence of channels in **MC1**. The sorption experiments with CO_2 imply a maximum occupancy of two molecules per metallocycle which is at odds with the SCD data. Possible reasons for the inconsistency are (i) the prolonged exposure of the single crystal to the CO_2 pressure both before (16 hours equilibration prior to data collection) and during data collection which may have led to increased sorption or (ii) the loss of crystallinity (and porosity) of a portion of the **MC1** powder upon desolvation or during the sorption experiments.

The two CO_2 molecules in the interstitial spaces between metallocycles appear to interact with the host via electrostatic interactions between the slightly negatively charged oxygen atom of a nitrate anion and the slightly positively charged central carbon atom of the CO_2 (O···C distance = 3.38(2) Å, Figure 133a). The "outermost" oxygen atom of the interstitial CO_2 molecule participates in a weak hydrogen bond with the methylene bridge hydrogen atoms of an adjacent metallocycle (O···C distance = 3.38(1) Å, Figure 133b).

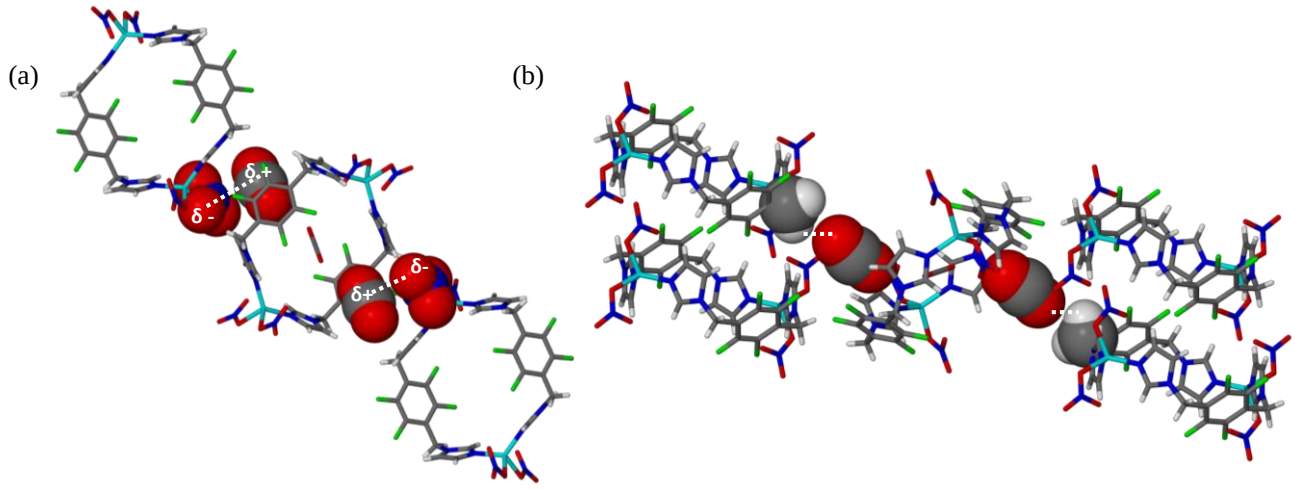

Figure 133. The CO_2 molecules located in the interstitial spaces between metallocycles are held in position by (a) electrostatic interactions with the nitrate anions as well as (b) weak hydrogen bonds with the hydrogen atoms of adjacent metallocyles.

The CO_2 molecule located within the cavity of the metallocycle can participate in weak electrostatic interactions with the fluorine atoms of the fluorinated benzene spacers that "gate" the cavity (C···F distance = 3.268(4) Å, Figure 134).

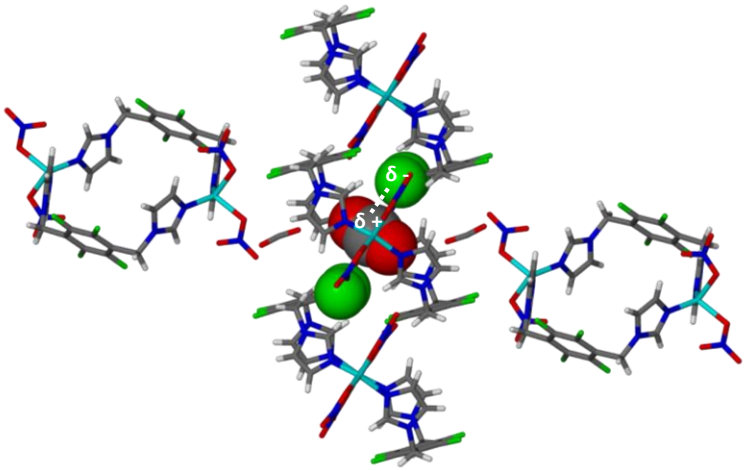

Figure 134. The CO_2 molecule in the centre of the metallocycle aperture is believed to be held in position by electrostatic interactions with the fluorine atoms of neighbouring metallocycles.

When the single crystal in the gas cell was placed under 20 bar ethylene (C_2H_4) pressure for data collection at 268 K, the crystal quality deteriorated during the measurement of the second batch of frames. Fortunately a structure of **MC1·C_2H_4** could be determined from the first 600 frames of diffraction data and two C_2H_4 molecules are included per metallocycle. The C=C bond lengths of the C_2H_4 molecules were restrained to 1.340(2) Å. The SQUEEZE electron count of 37 electrons per void confirms an occupancy of two C_2H_4 molecules. Once again, the occupancy does not correlate with the maximum occupancy of ~0.5 C_2H_4 molecule per metallocycle that was determined during the C_2H_4 sorption experiment on the IGA. The C_2H_4 molecules are disordered over four positions, two of which are symmetry-related. Each position was modelled with half occupancy (Figure 135).

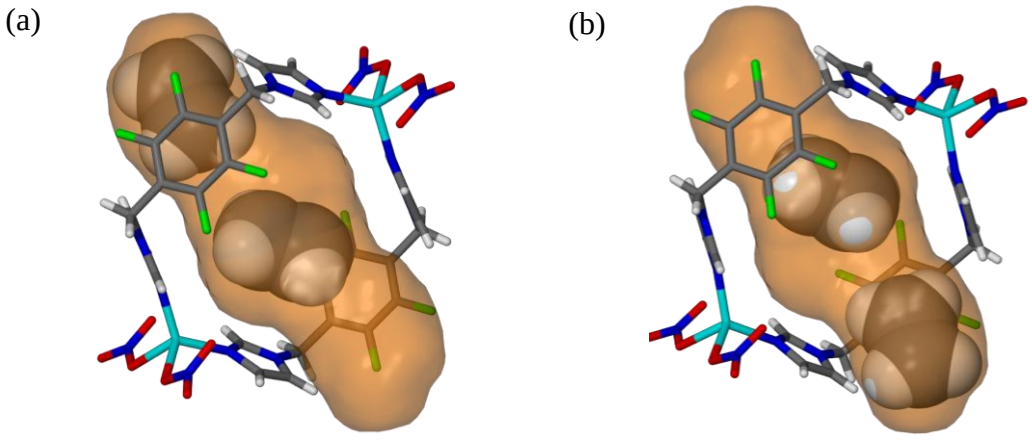

Figure 135. Two C_2H_4 molecules, shown in space-filled representation, are included per metallocycle in the guest-accessible space (semi-transparent orange surface, mapped using MSROLL,[39] probe radius = 1.4 Å) of 266 Å^3**.** The molecules are disordered over four positions with equal occupancy (50%). They are either located (a) in the top interstitial void and the aperture or (b) in the bottom of the interstitial space and the other symmetry-related position inside the aperture. The hydrogen atoms of the C_2H_4 molecules were simply added to generate the images and were not located in difference electron density maps.

When the C_2H_4 molecule is located at the far end of the elongated cavity (in the interstitial space) it forms a weak hydrogen bond with one of the oxygen atoms of the nitrate anion (C···O distance = 3.66(4) Å, Figure 136).

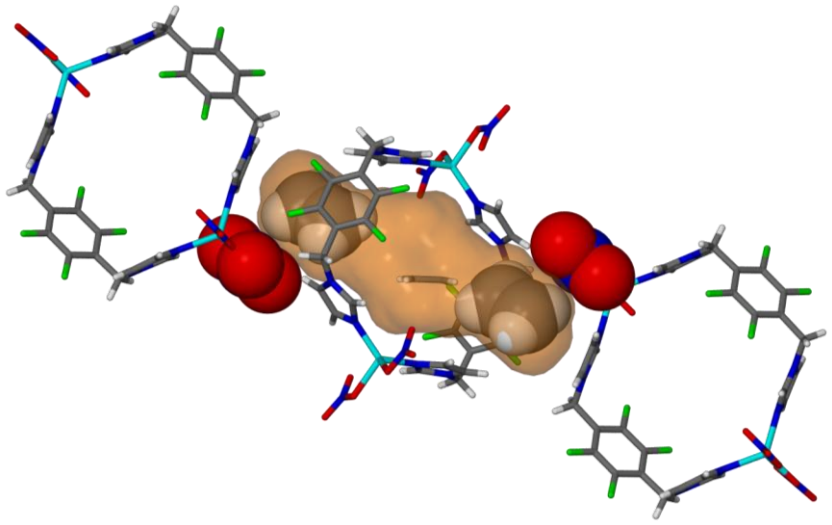

Figure 136. The C_2H_4 molecules (space-filled representation) located in the interstitial spaces between metallocycles are held in position by weak hydrogen bonds with the nitrate oxygen atoms (space-filled representation) of adjacent metallocyles. The hydrogen atoms of the C_2H_4 molecules were placed at positions that were not refined.

The C_2H_4 molecule in the centre of the cavity is able to participate in weak hydrogen bonding interactions with the fluorine atoms of adjacent metallocyles (shortest C···F distance = 3.37(4) Å, Figure 137).

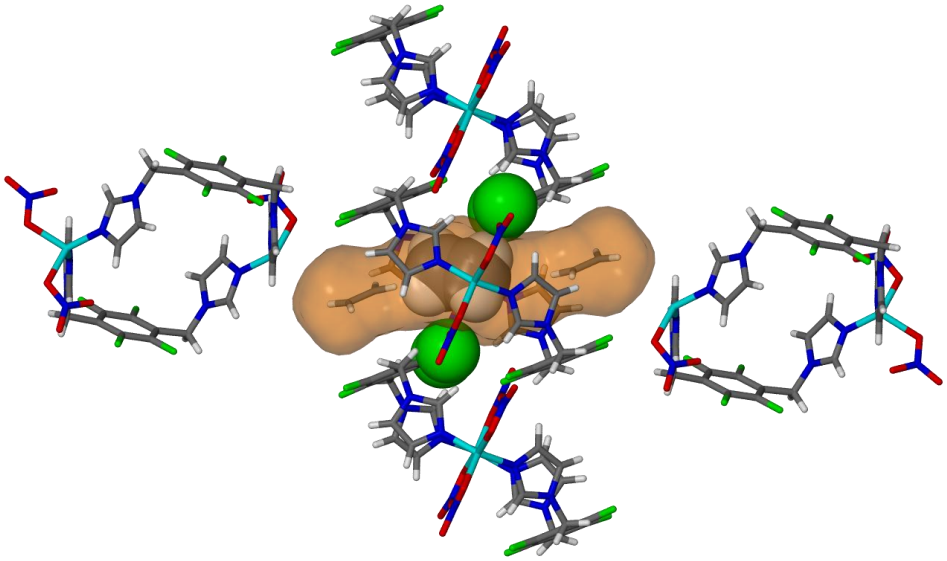

Figure 137. The C_2H_4 molecule in the centre of the metallocycle aperture (only one of the two symmetry-related positions is shown) is held in position by weak hydrogen bonds with the fluorine atoms of neighbouring metallocycles. The hydrogen atoms of the C_2H_4 molecules were placed at positions that were not refined.

Gas sorption isotherms with N_2 revealed that **MC1** includes a maximum of ~0.7 N_2 molecules per metallocycle at 20 °C and 20 bar pressure. The occupancy was confirmed with a structure that was determined from a single crystal exposed to 20 bar N_2 gas at 268 K. The site occupancy factor of the N_2 molecule refined to 78% and the molecule is disordered over two symmetry related positions within the 250 $Å^3$ metallocycle cavity (Figure 138 and Figure 139). The N≡N bond length was restrained to 1.140(5) Å.

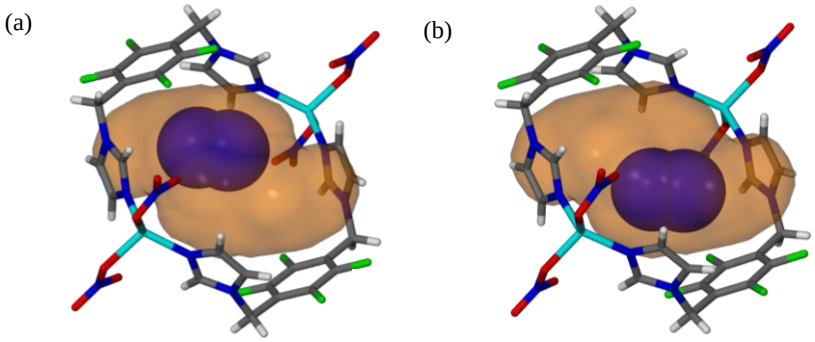

Figure 138. The confinement of one molecule of N_2 with 78% occupancy in the cavity of **MC1·N_2.** The two symmetry-related positions of the N_2 molecule are shown in (a) and (b). The guest-accessible space is shown in orange and was mapped using MSROLL[39] (probe radius = 1.4 Å).

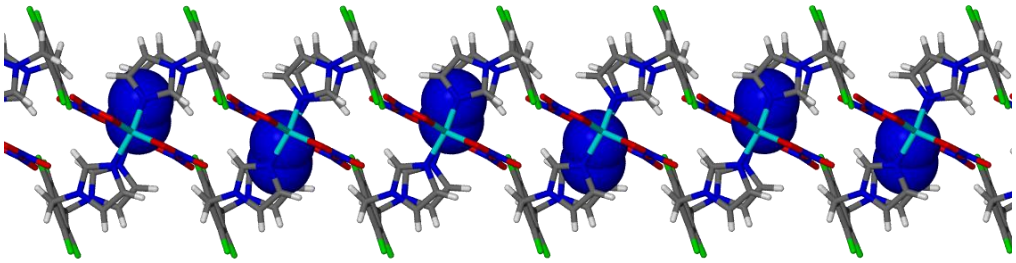

Figure 139. Only one molecule of N_2 with 78% occupancy is included per metallocycle even though the cavity has a volume of 250 $Å^3$. The nitrogen molecules are shown in space-filled representation and the symmetry-related positions are alternated along the column of stacked metallocycles.

There are no apparent host-guest interactions between the N_2 molecules and **MC1**. The packing coefficient for N_2 inclusion at 268 K is very low (0.09), and is related to the low polarizability, or more informally, the "non-sticky" nature of N_2 gas.

Structural analyses of the host framework when it includes different gaseous guests reveal that the void in the aperture of the metallocycle and the interstitial void deform to different extents depending on the type of gas molecules that are included, and where they are located. The two diameters across the oval-shaped metallocycle were measured, as well as the distance between adjacent metallocycles stacked along the *a* axis. The distances that were measured are shown in Figure 140 and Figure 141 and the results are tabulated in Table 28.

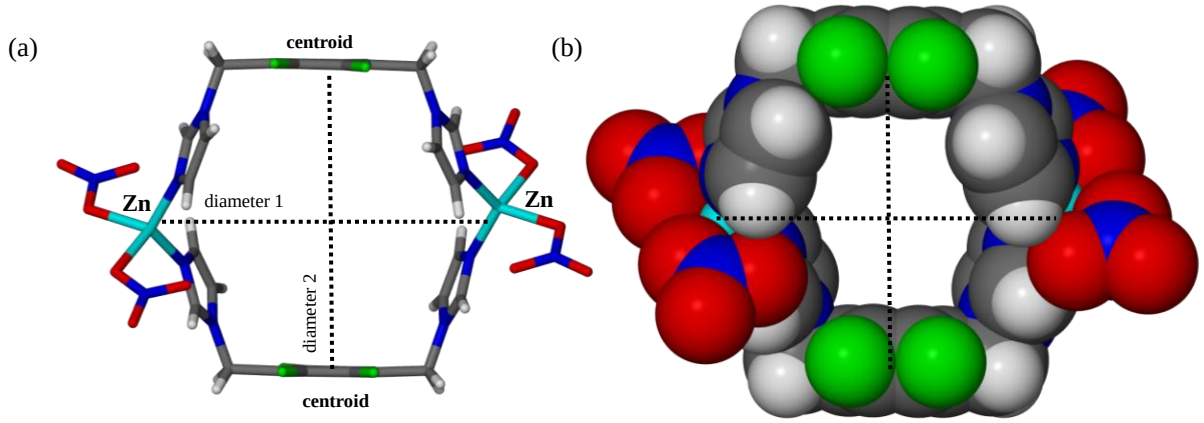

Figure 140. MC1·apohost in (a) capped-stick and (b) space-filled representation**.** The two diameters that are used to describe the shape of the metallocycle are shown as dashed black lines.

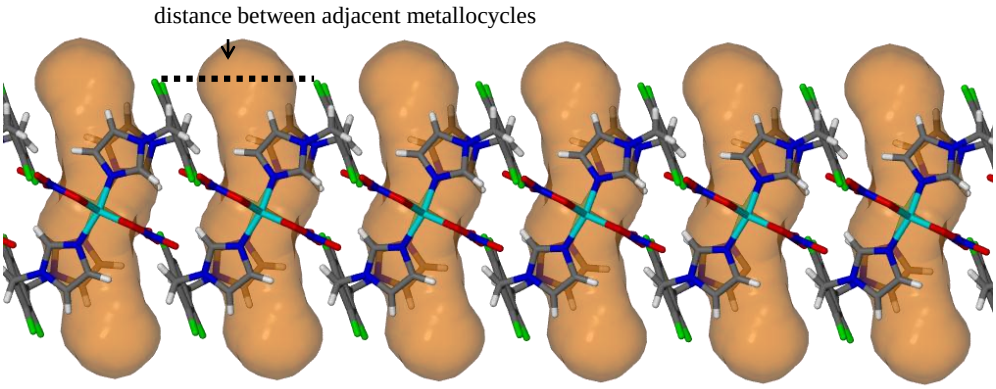

Figure 141. The distance between adjacent metallocycles that are stacked along [100] is shown.

Table 28. Selected structural information of the various gas inclusion complexes and the apohost material.

Structure at 268 K	Distance between adjacent metallocycles[a] (Å)	Metallocycle diameter 1[b] (Å)	Metallocycle diameter 2[c] (Å)
MC1·apohost	7.4130(4)	10.325(1)	9.906(1)
MC1·CO_2	7.466(1)	10.284(1)	9.952(1)
MC1·C_2H_4	7.498(1)	10.302(2)	9.919(2)
MC1·N_2	7.416(5)	10.311(2)	9.932(2)

[a] The length of the *a* unit cell parameter is equivalent to the distance between adjacent metallocycles stacked along the axis.

[b] The first diameter represents the Zn···Zn distance across the metallocycle aperture.

[c] The second diameter represents the centroid···centroid distance between the fluorinated benzene spacers.

In all three gas inclusion complexes the longest diameter (diameter 1) across the metallocycle cavity (Zn···Zn distance) is slightly narrowed as compared to **MC1·apohost**. However the shortest diameter (diameter 2) of the metallocycle, measured as the distance between two

centroids of the fluorinated benzene spacers, is widened relative to the apohost framework in all the inclusion complexes. In effect, the metallocycle becomes more rounded when it includes guest molecules. The distance between the fluorinated benzene spacer is the shortest in **MC1·C_2H_4**. The C_2H_4 molecule is disordered over a site within the metallocycle cavity (50% occupancy) and a site in the interstitial space (50% occupancy). The lower occupancy of the cavity (50%) as compared to the other structures (100% and 78% for CO_2 and N_2, respectively) could explain the narrower void. However, the contraction can also be a result of the previously mentioned weak hydrogen bonding interactions between the C_2H_4 molecule and the fluorine atoms of the benzene spacer. Similarly, in the structures where CO_2 and C_2H_4 are located in the interstitial voids, the distance between the stacked metallocycles is longer relative the apohost framework. The distance is the longest in the case of C_2H_4 inclusion, which could be a result of a combination of factors, such as (i) its large molecular volume and/or (ii) the fact that it forms weaker interactions with the adjacent metallocycles as compared to CO_2. The distance between the stacked metallocycles in the **MC1·N_2** is comparable to the distance in **MC1·apohost**, which supports the model in which N_2 is only located in the metallocycle aperture and not in the interstitial space.

5.3.4 The instability of MC1 as a porous material

As previously mentioned, the quality of the single crystal of **MC1** was significantly reduced during the third SCD data collection on the same crystal sealed within the gas cell. The crystal had already undergone two guest-exchange processes. The unit cell determined from the second batch of frames (a = 7.14(6) Å, b = 21.5(2) Å, c = 13.1(1) Å, β = 107.8(3)°, V = 1910(50) $Å^3$) has a much smaller volume (ca. 300 $Å^3$ reduction), which might suggest that structural collapse into a more dense phase had occurred despite the presence of C_2H_4 pressure. Unfortunately a structure could not be determined from the diffraction data after the crystal quality was reduced.

To test which external stimuli (temperature and/or pressure) could be responsible for the structural change, variable temperature PXRD patterns were measured with **MC1·apohost** powder (Figure 142). A DSC thermogram of **MC1·apohost** was also measured (Figure 143). The variable temperature PXRD patterns reveal that structural changes occur at ~100 °C and ~160 to 175 °C. In the DSC thermogram an endothermic event, directly followed by an exothermic event, is clearly present between 150 and 180 °C, which correlates with the structural change observed in the PXRD patterns measured at 160 and 175 °C.

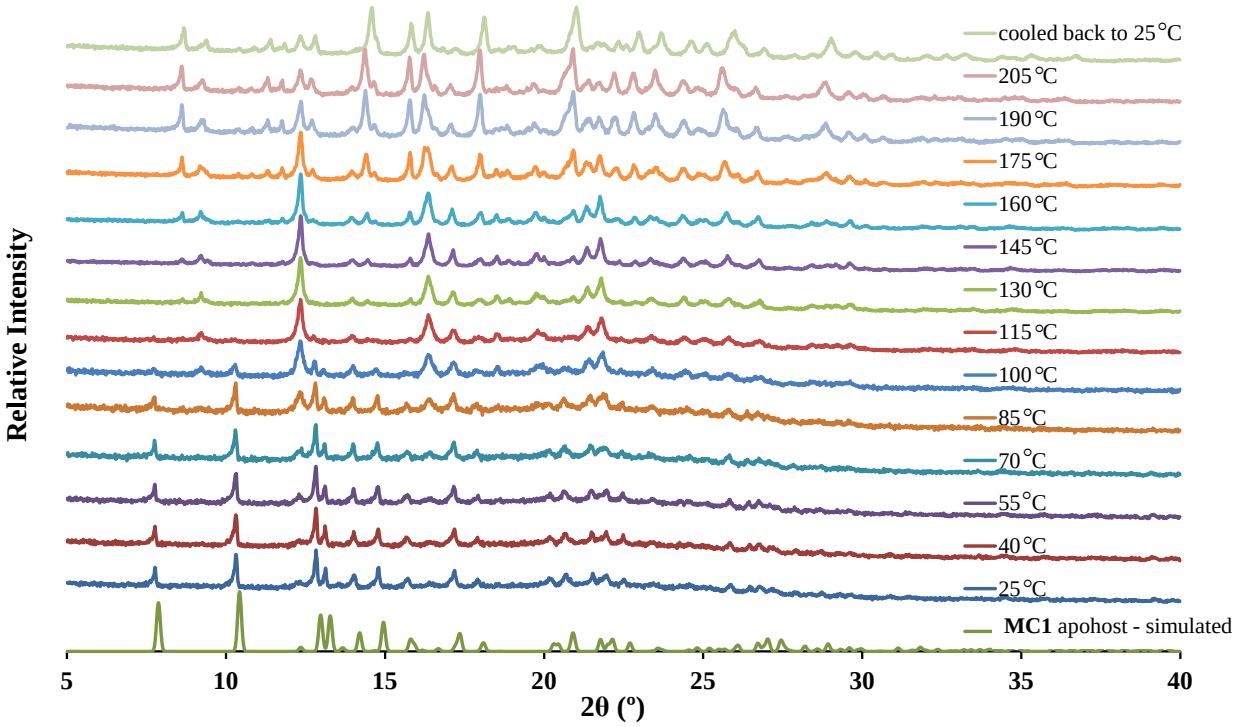

Figure 142. Variable temperature PXRD measurements with **MC1·apohost**. The first structural change is apparent at 100 °C and the second change occurs between 160 and 175 °C.

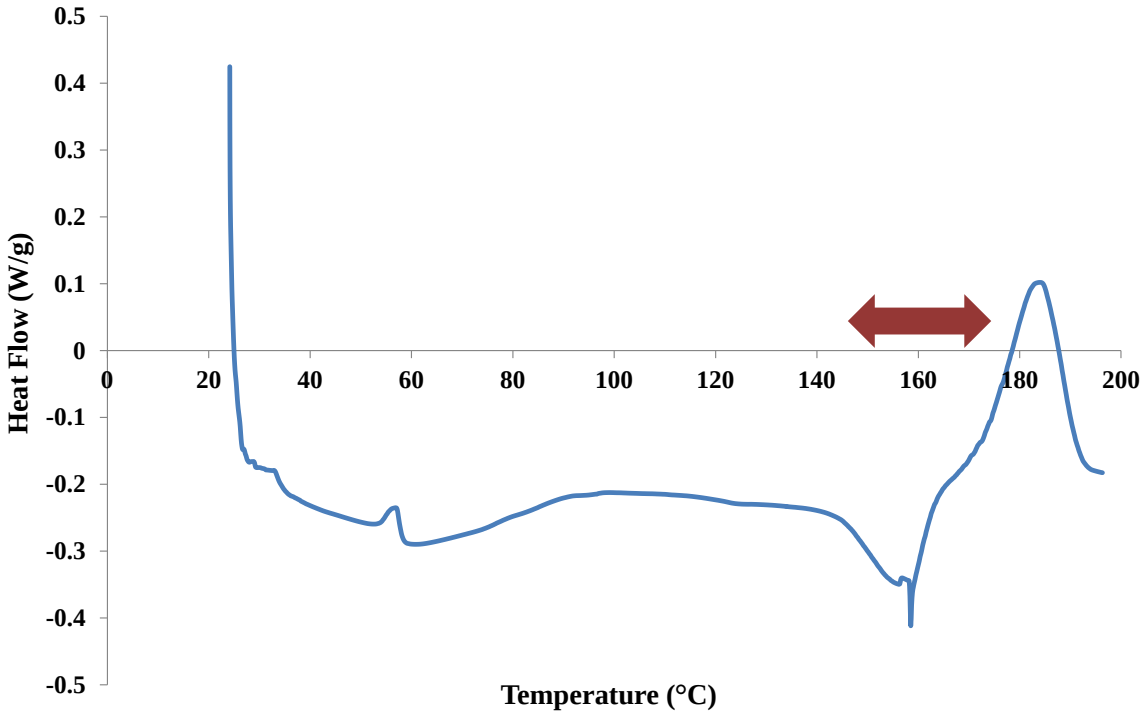

Figure 143. DSC trace of **MC1·apohost**. The temperature range of the major thermal event is indicated by an arrow.

After the temperature was increased to 205 °C, the sample was cooled back to 25 °C and another PXRD pattern was measured in order to show that the thermally-induced phase change is irreversible. PXRD patterns were then measured with samples of **MC1·apohost** under CO_2 and C_2H_4 pressures using a gas cell (Figure 144). The patterns show that the original phase was maintained after exposure to these gases for 2 hours. In both of the PXRD patterns that were measured under gas pressure, an additional peak is noticeable at 2θ = 14.5°. However, when a PXRD pattern was measured on the same sample (still under pressure) one month later, a phase change to an unknown phase had occurred.

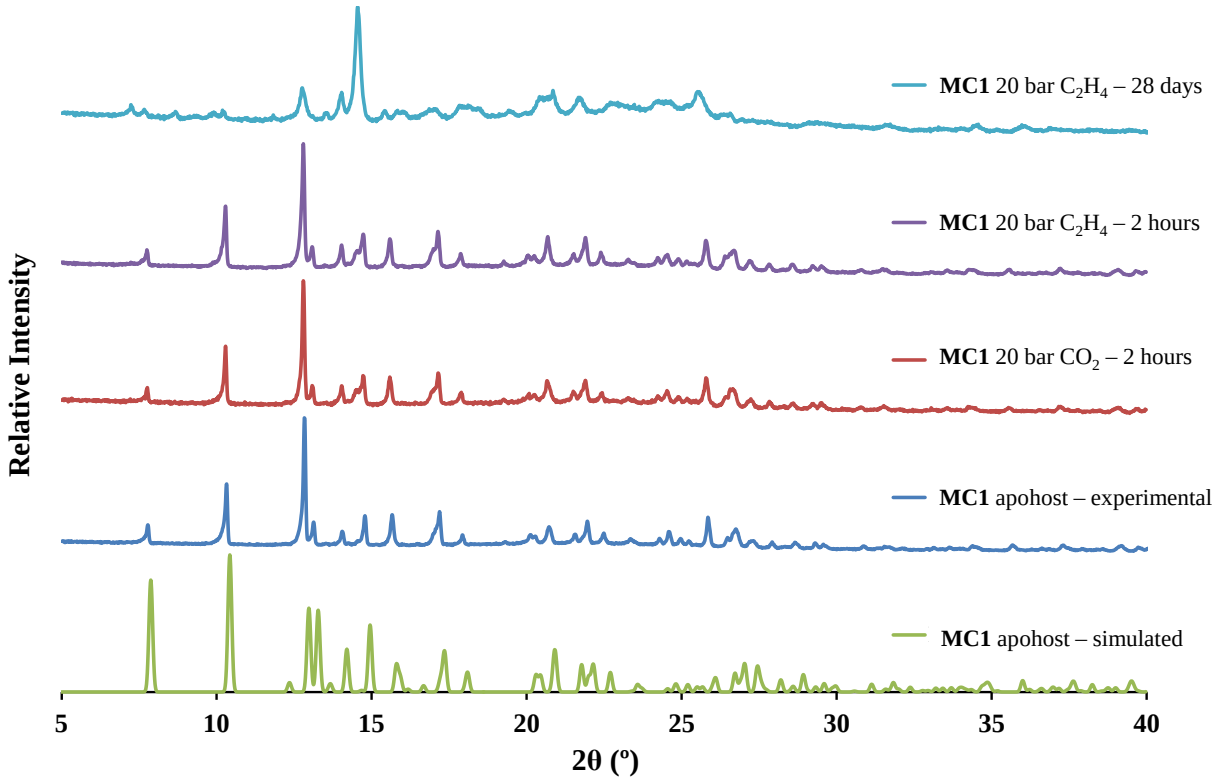

Figure 144. PXRD patterns of **MC1·apohost** that were measured with the sample in a gas cell and the instrument in capillary configuration. PXRD patterns with the sample under vacuum, 20 bar CO_2 and 20 bar C_2H_4 were measured. However a phase change could only be detected after 28 days of exposure to C_2H_4.

During the course of the studies carried out on **MC1** it was noted that, when a sample of **MC1** is removed from the mother liquor and left to stand, it spontaneously converts to a different phase within one month (Figure 145). This phase is different to **CP**, which was previously taken to be a thermodynamic product of the crystallization process. The PXRD pattern of the unknown phase in Figure 145 has some peaks in common with the unknown phase that was observed when **MC1** was exposed to C_2H_4 for 28 days (Figure 144). More importantly, the unknown phase is the same phase that can also be obtained by heating **MC1·apohost** to 175 °C.

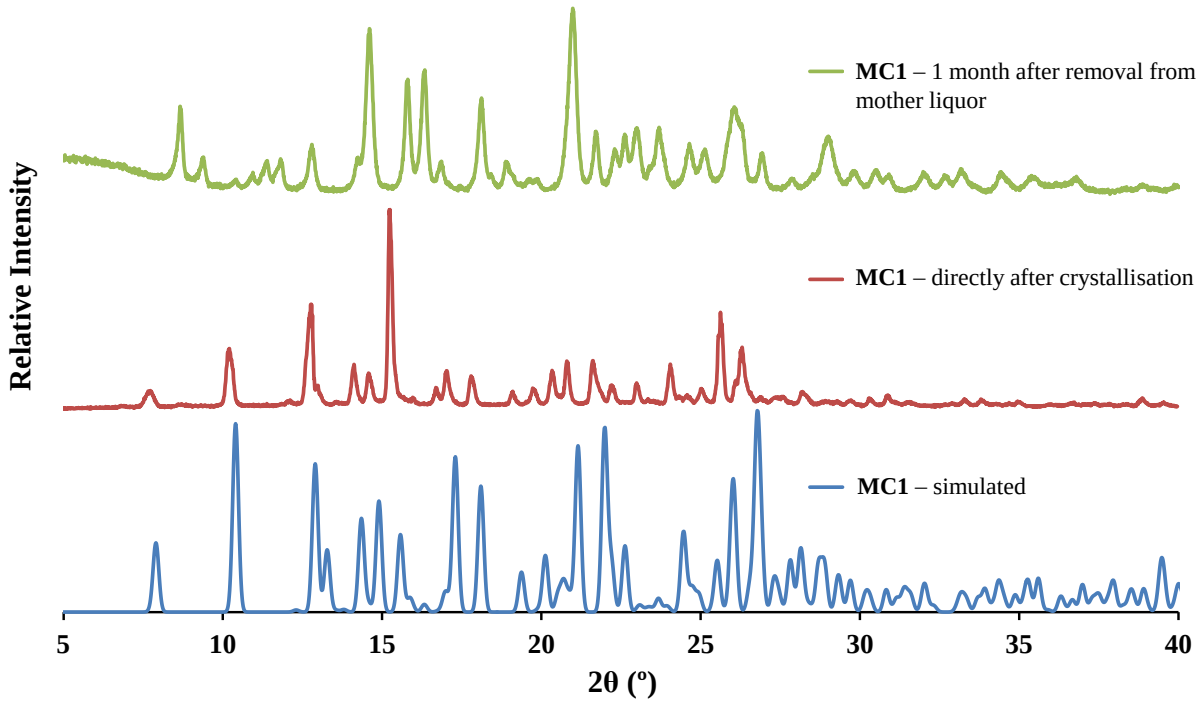

Figure 145. PXRD patterns of **MC1** directly after it crystallised and of the same sample after a phase change occurred whilst the sample was at ambient conditions (outside the mother liquor) for 1 month.

The phase change is irreversible and exposure to 20 bar of CO_2 pressure for 12 hours did not result in regeneration of **MC1**. The unknown phase is most likely another thermodynamically stable packing arrangement and is presumed to be a more dense (non-porous) than **MC1**. Unfortunately, the crystals were not of diffraction quality after the phase change and a structure could not be determined by SCD methods. **MC1·apohost** is not a robust porous material and does not maintain its structure for long. **MC1** crystallises overnight and if the crystallisation vial is left to stand, it reverts into a coordination polymer, **CP**, within the mother liquor. **MC1** appears to be the kinetic and not the thermodynamic product of the self-assembly process and, interestingly, it remains unstable even after it has been removed from the mother liquor. The **MC1·apohost** phase can only be maintained for one month before spontaneous conversion occurs to an unknown phase.

5.4 SUMMARY AND CONCLUSIONS

The preparation of a Zn(II) metallocycle (**MC1**), its concomitant coordination polymer phase (**CP**) and an isoskeletal solvate (**MC2**) were studied. The ideal crystallisation stoichiometry for the formation of **MC1** was determined by systematic variation of the metal:ligand ratio. Phase purity of **MC1** is achieved with a M:L ratio of 1.25:1 or 1.5:1. The permeability of **MC1** to guest molecules was studied further despite the fact that there are no apparent channels in the crystal structure. Movement of the fluorinated benzene spacers from their equilibrium positions is thought to aid the guest transport process. The permeability of **MC1** was demonstrated by the measurement of gas sorption isotherms on the IGA. The sorption isotherms with CO_2, C_2H_4 and N_2 were all type I, based on the IUPAC classification. Hysteresis was observed with all three gases, implying that there are appreciable host-guest interactions. A guest-exchange experiment with CS_2 as a single-crystal to single-crystal transformation was successful and paved the way for further studies with small gaseous molecules. The three gases for which sorption isotherms were measured were diffused into evacuated **MC1**·**apohost** crystals using an environmental gas cell. The single crystals remained of diffraction quality after exposure to 20 bar of CO_2, C_2H_4 and N_2 and the binding sites of the gases within the host cavities could consequently be determined.

Unfortunately the transient porosity of **MC1** is not a permanent property. Structural collapse occurs when the material is heated to above 100 °C or simply left to stand at ambient conditions for a long period of time. It is proposed that the less dense packing arrangement of the metallocycles creates inherent instability and structural collapse is inevitable, although temperature increases can accelerate the process.

In the context of the main aims of this dissertation, the structural changes involved in guest inclusion and dynamic responses to external stimuli such as temperature and pressure were studied. A surprising finding was that a transiently porous material (**MC1**) can include more CO_2 (by wt% and vol/vol) than a conventionally porous MOF with open channels (**IMMOF-3**). However, the 3D framework of **IMMOF-3** is significantly more stable towards temperature and pressure fluctuations and the structure is maintained for a much longer time. It can also be immersed in various solvents without dissolving, which is not the case for **MC1**.

5.5 EXPERIMENTAL SECTION

5.5.1 Crystallographic tables

	MC1	**CP**	**MC2**	**MC1·CS_2**
Empirical formula	$C_{30}H_{30}Cl_2F_8N_{12}O_{14}Zn_2$	$C_{21}H_{15}F_6N_8O_{8.50}Zn$	$C_{30}H_{26}Cl_6F_8N_{12}O_{12}Zn_2$	$C_{30}H_{20}F_8N_{12}O_{12}S_4Zn_2$
Formula weight	1148.31	694.78	1254.09	1151.57
Temperature/K	100(2)	100(2)	100(2)	100(2)
Wavelength/Å	0.71073	0.71073	0.71073	0.71073
Crystal system	monoclinic	triclinic	monoclinic	monoclinic
Space group	$P2_1/c$	$P\bar{1}$	$P2_1/c$	$P2_1/c$
a /Å	7.3794(8)	9.8377(18)	7.338(2)	7.3884(9)
b /Å	22.769(2)	11.124(2)	22.906(7)	22.477(3)
c /Å	13.1634(14)	13.609(3)	13.400(4)	13.2659(16)
α /°	90.00	109.197(2)	90.00	90.00
β /°	103.0260(10)	95.671(2)	102.461(6)	103.701(2)
γ /°	90.00	105.944(2)	90.00	90.00
Volume/Å^3	2154.9(4)	1322.7(4)	2199.3(12)	2140.4(4)
Z	2	2	2	2
Calculated density/g cm^{-3}	1.770	1.745	1.894	1.787
Absorption coefficient (mm^{-1})	1.351	1.036	1.564	1.424
F_{000}	1156	698	1252	1152
Reflections collected	13287	19752	17085	13068
Independent reflections	5095 [R_{int} = 0.0383]	7609 [R_{int} = 0.0238]	6127 [R_{int} = 0.0599]	5020 [R_{int} = 0.0464]
Data/restraints/parameters	5095 / 3 / 327	7609 / 0 / 406	6127 / 3 / 327	5020 / 0 / 308
Goodness-of-fit on F^2	1.060	1.064	1.028	1.049
Final R indices [$I>2\sigma(I)$]	$R1$ = 0.0594, $wR2$ = 0.1535	$R1$ = 0.0359, $wR2$ = 0.0950	$R1$ = 0.0844, $wR2$ = 0.2239	$R1$ = 0.0652, $wR2$ = 0.1712
R indices (all data)	$R1$ = 0.0761, $wR2$ = 0.1653	$R1$ = 0.0423, $wR2$ = 0.0985	$R1$ = 0.1253, $wR2$ = 0.2506	$R1$ = 0.0957, $wR2$ = 0.1898

	MC1·apohost	**MC1·CO_2**	**MC1·C_2H_4**	**MC1·N_2**
Empirical formula	$C_{28}H_{20}F_8N_{12}O_{12}Zn_2$	$C_{30}H_{20}F_8N_{12}O_{18}Zn_2$	$C_{32}H_{20}F_8N_{12}O_{12}Zn_2$	$C_{28}H_{20}F_8N_{15.12}O_{12}Zn_2$
Formula weight	999.29	1131.32	1047.33	1042.99
Temperature/K	100(2)	268(2)	268(2)	268(2)
Wavelength/Å	0.71073	0.71073	0.71073	0.71073
Crystal system	monoclinic	monoclinic	monoclinic	monoclinic
Space group	$P2_1/c$	$P2_1/c$	$P2_1/c$	$P2_1/c$
a /Å	7.3606(6)	7.4662(10)	7.4253(17)	7.416(5)
b /Å	22.4237(19)	22.503(3)	22.561(6)	22.606(14)
c /Å	13.3449(12)	13.4688(18)	13.431(3)	13.440(8)
α /°	90.00	90.00	90.00	90.00
β /°	103.2240(10)	102.809(2)	103.383(3)	103.456(8)
γ /°	90.00	90.00	90.00	90.00
Volume/Å^3	2144.2(3)	2206.6(5)	2188.9(9)	2191(2)
Z	2	2	2	2
Calculated density/g cm^{-3}	1.548	1.703	1.589	1.581
Absorption coefficient (mm^{-1})	1.221	1.207	1.200	1.201
F_{000}	1000	1132	1048	1044
Reflections collected	13131	10204	6130	7114
Independent reflections	5028 [R_{int} = 0.0334]	3106 [R_{int} = 0.0374]	4207 [R_{int} = 0.0352]	3144 [R_{int} = 0.0395]
Data/restraints/parameters	5028 / 0 / 280	3106 / 4 / 280	4207 / 2 / 297	3144 / 1 / 289
Goodness-of-fit on F^2	1.058	1.038	1.039	1.058
Final R indices [$I>2\sigma(I)$]	$R1$ = 0.0344, $wR2$ = 0.0785	$R1$ = 0.0545, $wR2$ = 0.1451	$R1$ = 0.0602, $wR2$ = 0.1383	$R1$ = 0.0490, $wR2$ = 0.1270
R indices (all data)	$R1$ = 0.0519, $wR2$ = 0.0855	$R1$ = 0.0734, $wR2$ = 0.1583	$R1$ = 0.1095, $wR2$ = 0.1599	$R1$ = 0.0734, $wR2$ = 0.1407

CHAPTER 6

CALIX[4]ARENE: GAS STORAGE IN A NON-POROUS MATERIAL

Work in the Barbour group on the encapsulation of small compounds by non-covalent molecular assemblies originated from an investigation of the seemingly non-porous van der Waals crystals of calix[*n*]arenes by Atwood *et al.*[85] Calix[*n*]arenes are organic macrocycles often used as platforms for the functionalisation of the upper and lower rims of their skeletons. The supramolecular assemblies formed by the calix[*n*]arene family of compounds have been thoroughly studied, with particular emphasis on their ability to form various host-guest adducts. It is the simple calix[4]arenes that have proven to be most interesting, in terms of the encapsulation and transport of guest molecules. The first single crystal X-ray diffraction structure of a calix[*n*]arene was published in 1979 by Andreetti *et al.*, and it served as a confirmation of the suspected bowl (or calix) shape of *p-tert*-butylcalix[4]arene.[86] In a crystal of the sublimed polymorph of *p-tert*-butylcalix[4]arene (in space group $P2_1/n$), the calix-shaped molecules are arranged in bilayers and there are voids of ~235 $Å^3$ between offset facing molecules in adjacent bilayers ("skewed capsules").[87] There are no permanent channels leading to the discrete void spaces because of the *tert*-butyl groups of the adjacent molecules occupying the potential channel space between capsules. However, transport of vinyl bromide and other guests through the crystal was demonstrated despite the absence of permanent channels in the structure.[85] The single-crystal to single-crystal transformation of a seemingly non-porous system to a phase that includes a guest was a noteworthy discovery at the time; however, the concept of flexible pores is rapidly becoming more well-established.

A parallel study of calix[4]arene (**C4**) as host material for small and volatile guest molecules was in progress at the same time.[88] Thermal analysis of various solvates showed extraordinary thermal stability of these host-guest assemblies. Guest molecules trapped in the lattice voids formed by the hexagonal close-packed (hcp) arrangement of **C4** trimers were retained well above their normal boiling points.[88] It was thus demonstrated that even organic materials with assemblies stabilised by relatively weak van der Waals interactions should not be overlooked as stable gas storage media.

Guest-free **C4** crystals can be grown by vacuum sublimation at 300 °C. Notably, the apohost crystallises in the same hexagonal space group, $P6_3/m$, as almost all of the solvates. However, the sublimed material has no guests in the ~141 $Å^3$ voids. The interstitial lattice voids result from

the slightly inefficient hcp arrangement of the spherical trimers formed by three **C4** molecules (Figure 146).

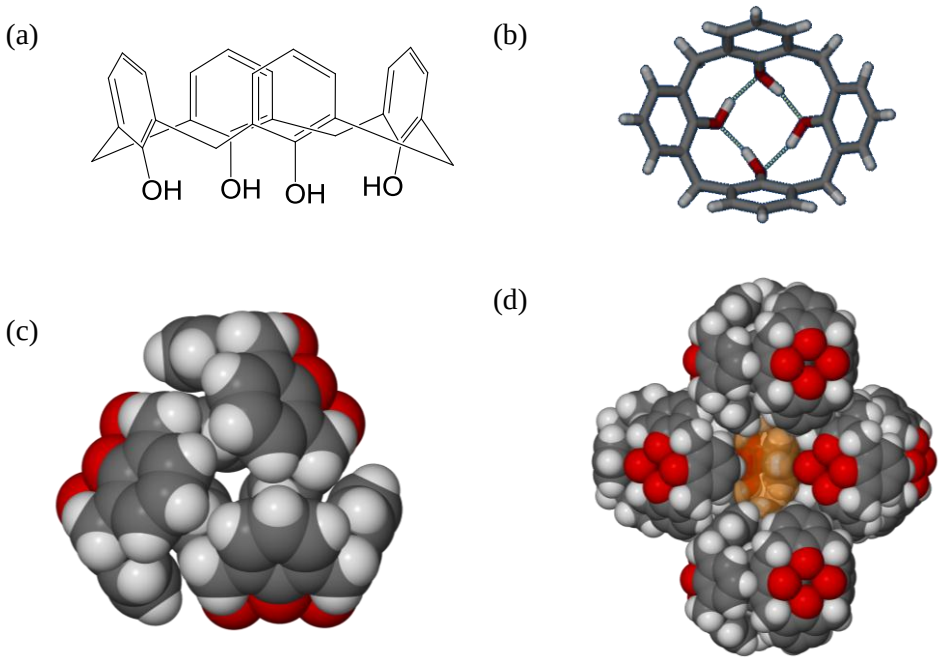

Figure 146. (a) Schematic of calix[4]arene. (b) The calix[4]ene molecule with the 4-membered hydrogen bond ring between the hydroxyl groups on the lower rim. (c) A trimer of calix[4]arene molecules that is almost spherical in shape and (d) the inefficient hcp arrangement of the trimers form interstitial voids; one void (shown as a semi-transparent orange surface) is surrounded by five trimers.

Crystals of **C4** were grown in the presence of highly volatile compounds such as freons and various halons in order to entrap the gases in stable crystals. This could not be done by sublimation but, the empty hcp lattice can fortunately also be obtained by precipitation from toluene. Crystals that entrap gases were therefore grown from a solution of each respective gas in toluene. Using this method, methane (1:2 H:G) and tetrafluoromethane were encapsulated and could only be released at temperatures 320 and 370 °C above their respective boiling points ($T_{onset\ of\ release}$ = 150 to 170 °C and 240 °C).[88] The guest molecule is entrapped within an assembly of organic molecules and is stabilised by dispersion/van der Waals interactions only.

Following the discovery of *p-tert*-butylcalix[4]arene's cooperative guest transport mechanism, its gas sorption capabilities were also studied.[89] This was not the case with **C4**, since it did not appear to absorb gases. As a continuation of this work, the likelihood of **C4** absorbing CO_2 was investigated further in this study. It was believed that all that may be required is a very high CO_2 pressure for sorption to occur and that perhaps the right conditions for CO_2 sorption had not yet been discovered. A study of carbon dioxide storage within the lattice voids of calix[4]arene was carried out using supercritical CO_2 (sCO_2).

6.1 GAS SORPTION EXPERIMENTS WITH CALIX[4]ARENE

Calix[4]arene was synthesised according to well-known literature procedures. The first synthesis of calix[*n*]arenes was reported in 1944 by Zinke *et al.*[90] and the methods were further developed by Cornforth and co-workers,[91] Buriks, Fauke, and Munch,[92] Gutsche and co-workers[93] and Patrick and Egan.[94] The guest-free material was prepared by subliming the as-synthesised product twice. Firstly, the permeability of sublimed calix[4]arene to CO_2 was tested. A sorption isotherm was measured at 0 °C on an IGA (Figure 147).

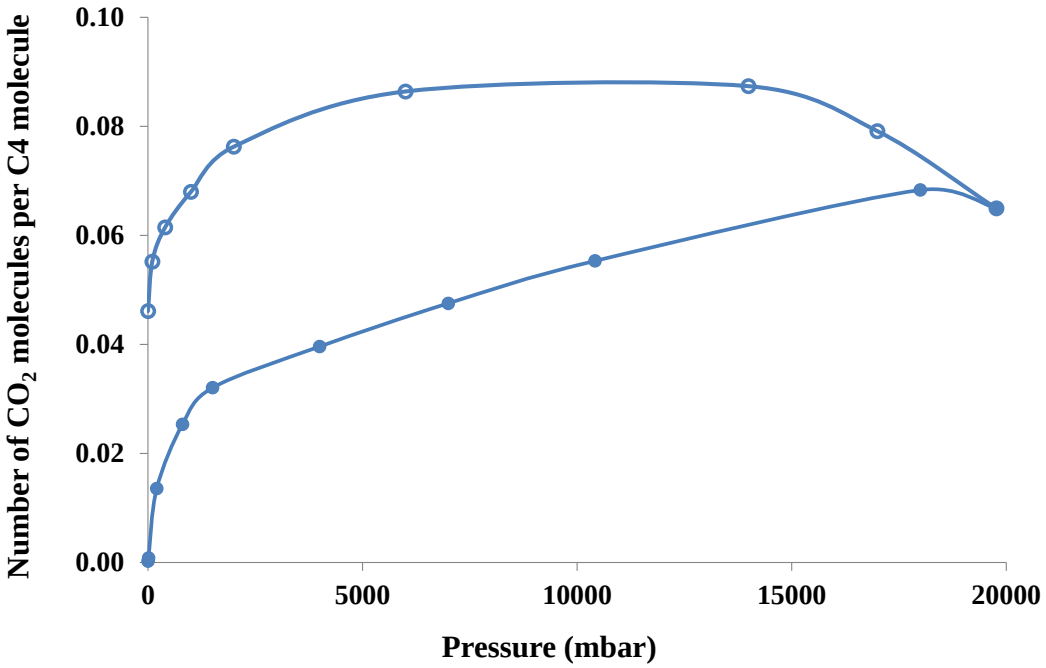

Figure 147. CO_2 sorption isotherm of **C4** measured at 0 °C.

The maximum H:G ratio that was reached during the sorption experiment was 0.08 CO_2 molecules per **C4** molecule, which represents 24% occupancy of the interstitial cavities. The low occupancy of CO_2 determined from the sorption isotherm demonstrates that **C4** does not absorb CO_2 readily. Since **C4** is relatively impermeable to CO_2 at 20 bar pressure, the prospect of permeability at a higher CO_2 pressure of 60 bar was also tested. A sample consisting of single crystals and powder was enclosed in a steel pressure vessel, which was pressurised to 60 bar CO_2 for 2 weeks. The diffraction quality of the single crystals was reduced significantly and only a unit cell could be determined. The original cell dimensions for **C4·apohost** (*a*, *b* = 14.344(2) Å, *c* =18.627(6) Å) had increased (*a*, *b* = 14.48(2) Å, *c* =19.04(6) Å). A PXRD pattern of the material showed that no apparent phase change had occurred under gas pressure (Figure 148).

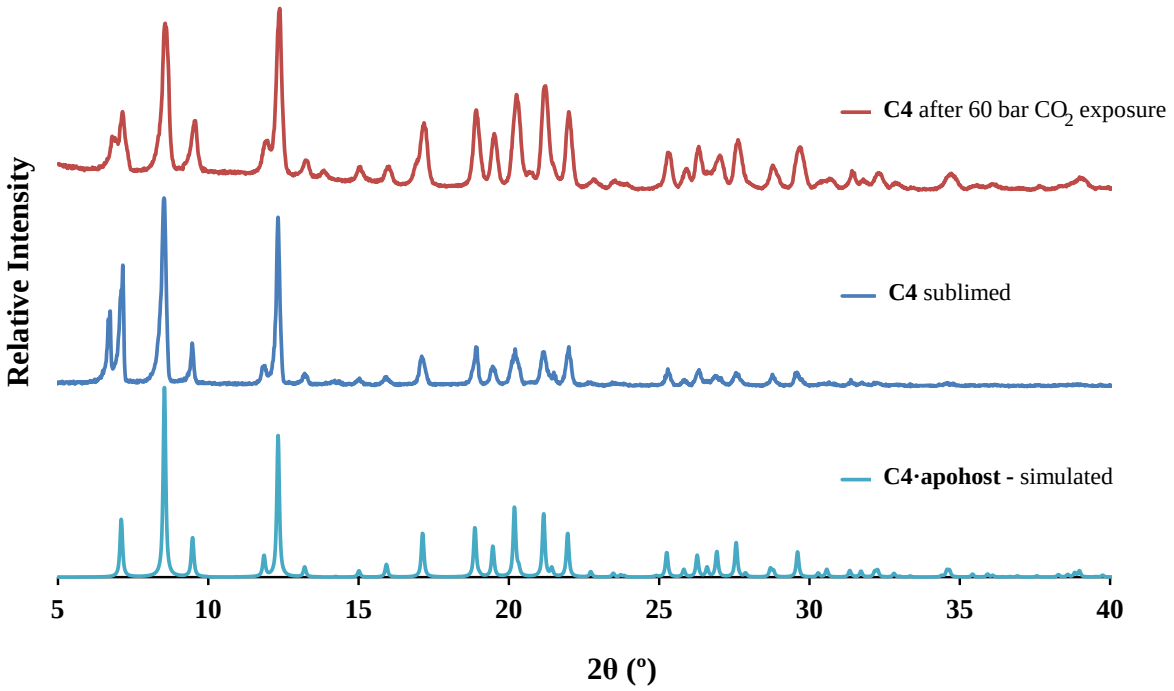

Figure 148. The experimental PXRD patterns of sublimed **C4** and **C4** after exposure to 60 bar CO_2 pressure for 2 weeks are compared to the simulated pattern of **C4·apohost**.

The expansion of the unit cell is not sufficient evidence for CO_2 inclusion and another technique was therefore necessary. An infrared spectrum (IR) using an attenuated total reflectance (ATR) accessory was recorded for the powdered sample that had been kept in the pressure vessel. The spectrum contained a strong vibrational band at 2332 cm^{-1}, which is not present in the spectrum of sublimed **C4** (Figure 149). The strong vibrational band is red-shifted from the centre of the P and R bands of pure gaseous CO_2 (2303 cm^{-1}) and does not have fine rotational structure as would be anticipated for a free gas.[56] This is not unequivocal proof of CO_2 inclusion since surface-adsorbed CO_2 will also exhibit a 10-20 cm^{-1} red-shifted vibrational band with no rotational fine structure.[56] However, 12 hours after the first IR spectrum was recorded, another spectrum was measured in which the CO_2 vibrational band at 2332 cm^{-1} had not diminished at all. After one week at ambient conditions the band diminished slightly but was still present (Figure 150). The extreme hysteresis of desorption implies that the CO_2 is stored in internal cavities and is not adsorbed to the surface.

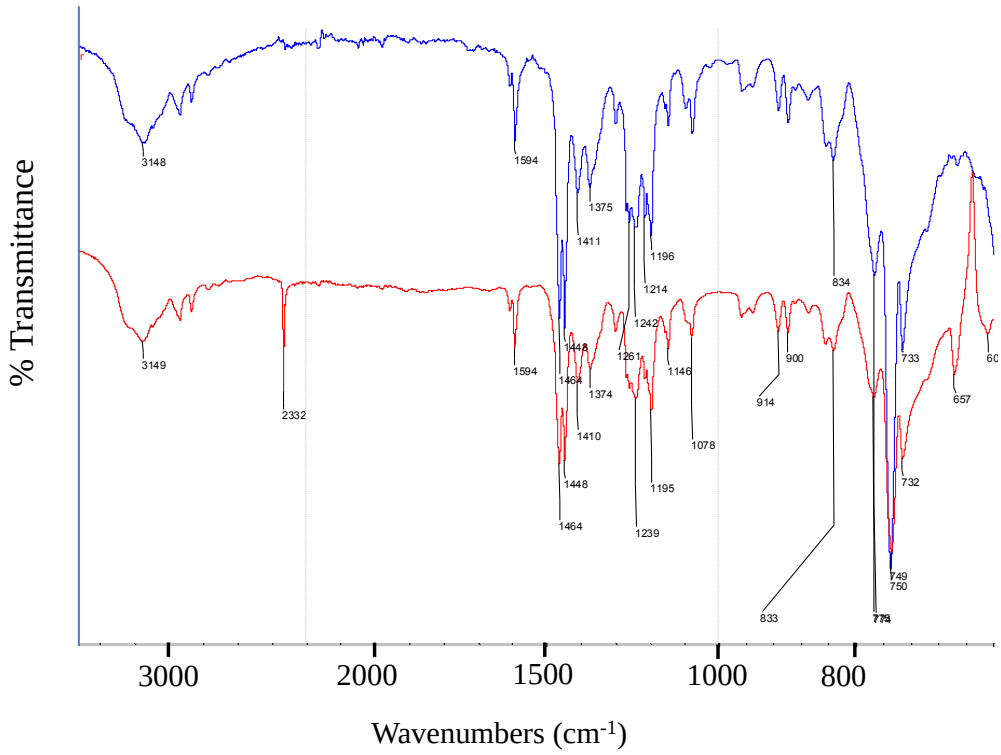

Figure 149. IR spectra of sublimed **C4** (blue) and **C4** that has been exposed to 60 bar CO_2 pressure for 2 weeks (red).

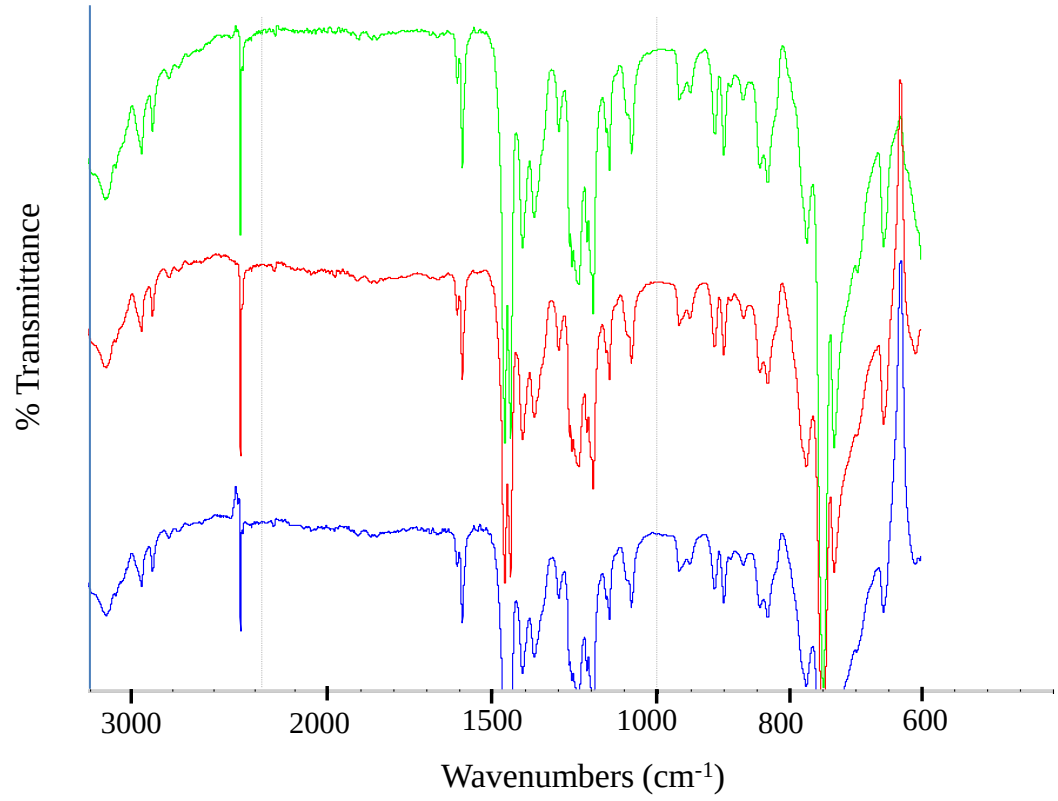

Figure 150. IR spectra of **C4** that has been exposed to 60 bar CO_2 for 2 weeks (green) and that measured for the same sample that has been left under ambient conditions for 12 hours (red) and one week (blue).

A TGA trace was measured for sublimed **C4** as well as the **C4** after 60 bar CO_2 exposure (Figure 151). The weight decreased by 1.86% from room temperature to 250 °C, which corresponds to *ca.* 0.2 CO_2 molecules per **C4** molecule. The mass loss represents a 60% occupancy of the interstitial voids (assuming a 3:1 H:G ratio (3.13 %) for complete occupancy). It is possible that the remaining CO_2 is retained up to the sublimation temperature of the host, or that even at 60 bar pressure, not all the interstitial voids are occupied by CO_2.

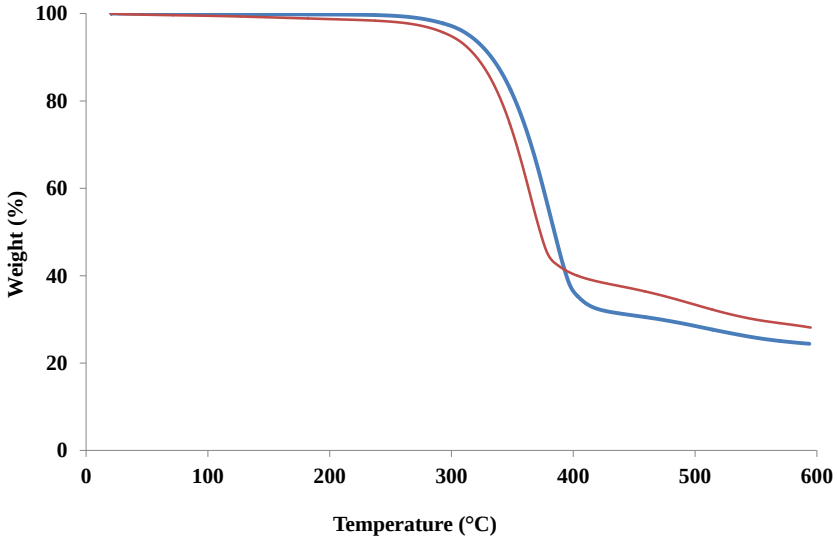

Figure 151. TGA trace of sublimed **C4** (blue) compared to **C4** that was exposed to 60 bar CO_2 for 2 weeks (red).

6.2 SUPERCRITICAL CO_2 EXPERIMENTS

6.2.1 Exchange of guest molecules for CO_2

Since the uptake of CO_2 by **C4** is incomplete, even at very high pressure and long exposure times, an exchange of the original guest molecules in a **C4** solvate for CO_2 was attempted. The 1:1 (H:G) acetone clathrate[95] of **C4** crystallises in the orthorhombic space group *Pnma* (*a* = 17.01 0(8) Å, *b* = 14.1 27(6) Å, *c* = 10.667(3) Å) but can also be partially desolvated to form a 3:1 clathrate[95] with the same packing arrangement and hexagonal symmetry as **C4·apohost** (3:1 acetone clathrate, $P6_3/m$, *a* = *b* = 14.543(5) Å *c* = 18.228(7) Å, γ = 120°). Using a *SAMDRI-PVT-3D* critical point dryer from *Tousimis*, a crushed sample of the 1:1 acetone clathrate crystals was submerged in liquid CO_2 and the temperature was increased until sCO_2 conditions were achieved. A phase change from the original orthorhombic phase of the 1:1 acetone clathrate to the hexagonal phase occurred, as confirmed by the PXRD patterns shown in Figure 152.

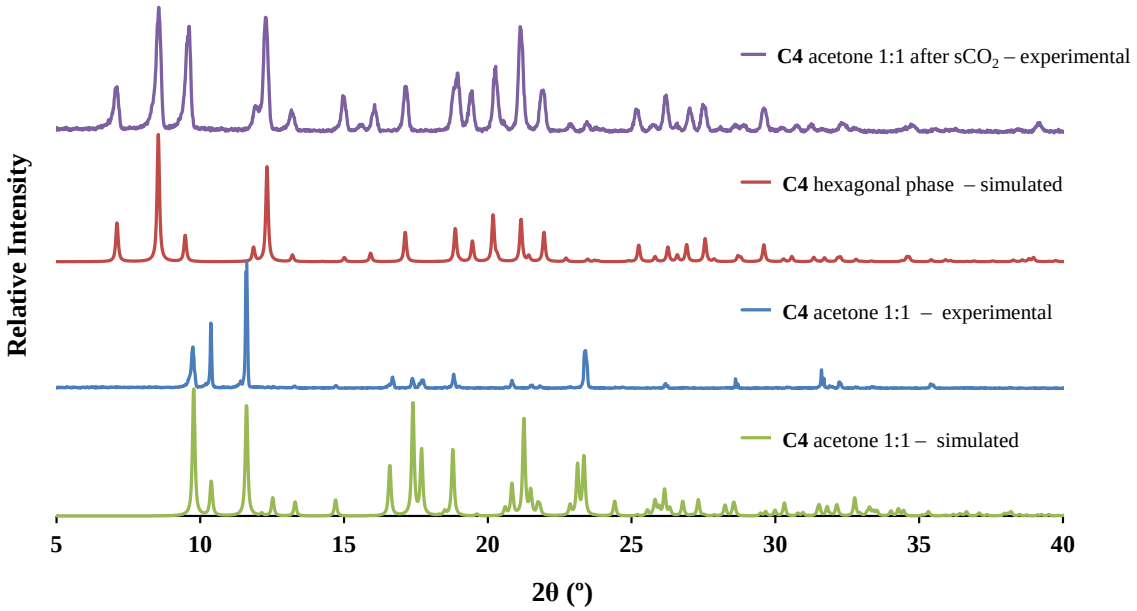

Figure 152. Simulated and experimental PXRD patterns of the 1:1 acetone clathrate of **C4** before and after sCO_2 exchange.

IR of the 1:1 acetone clathrate before and after sCO_2 exchange confirmed the presence of CO_2 in the sample (Figure 153). The absorption band at 2332 cm^{-1} is present after supercritical CO_2 exchange, while the absorption band from the C=O stretch of the acetone at 1703 cm^{-1} is almost completely absent and slightly red-shifted to 1716 cm^{-1}.

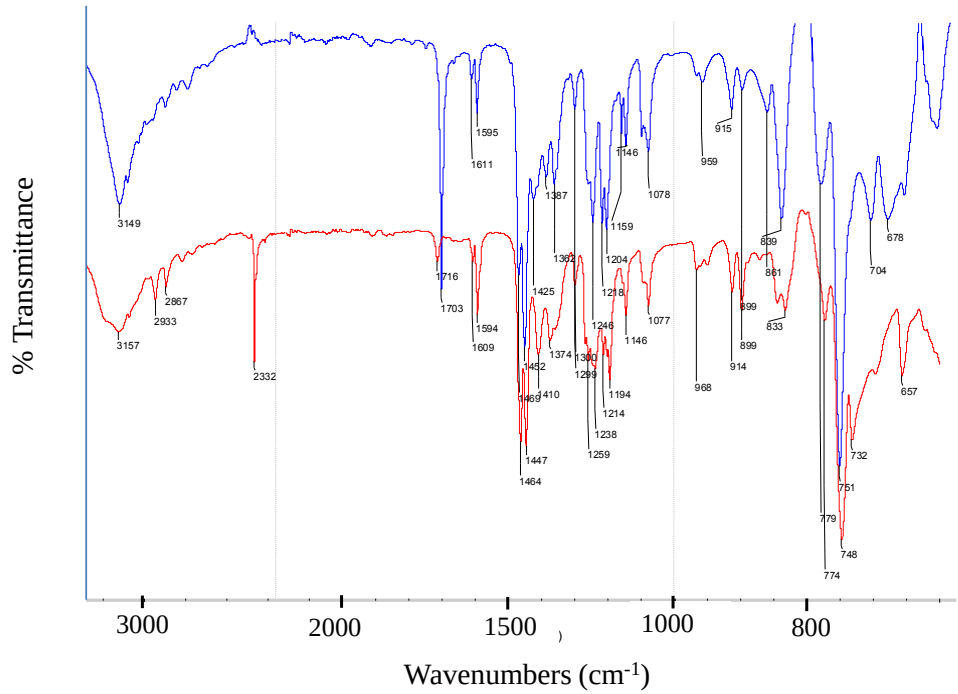

Figure 153. The IR spectrum of the 1:1 acetone clathrate of **C4** (blue) and the IR spectrum measured for the same sample after sCO_2 exchange (red).

Since the stoichiometry of the exchange cannot be determined from the IR spectrum, a H^1 NMR spectrum was recorded for the sample after sCO_2 exchange. The singlet that represents the acetone protons at 2.18 ppm in the H^1 NMR spectrum, shown in Figure 154, integrates to 0.45 protons, which is $1/13^{th}$ the amount (0.45/6 protons for one acetone molecule = 0.075 = $1/13^{th}$) that was present in the 1:1 clathrate. Thus only trace amounts of acetone are still present in the sample. This information, combined with the IR spectra, serves as a confirmation that the 1:1 acetone clathrate did not simply convert to the 3:1 acetone clathrate, but that CO_2 molecules have indeed replaced most of the acetone molecules in the sample.

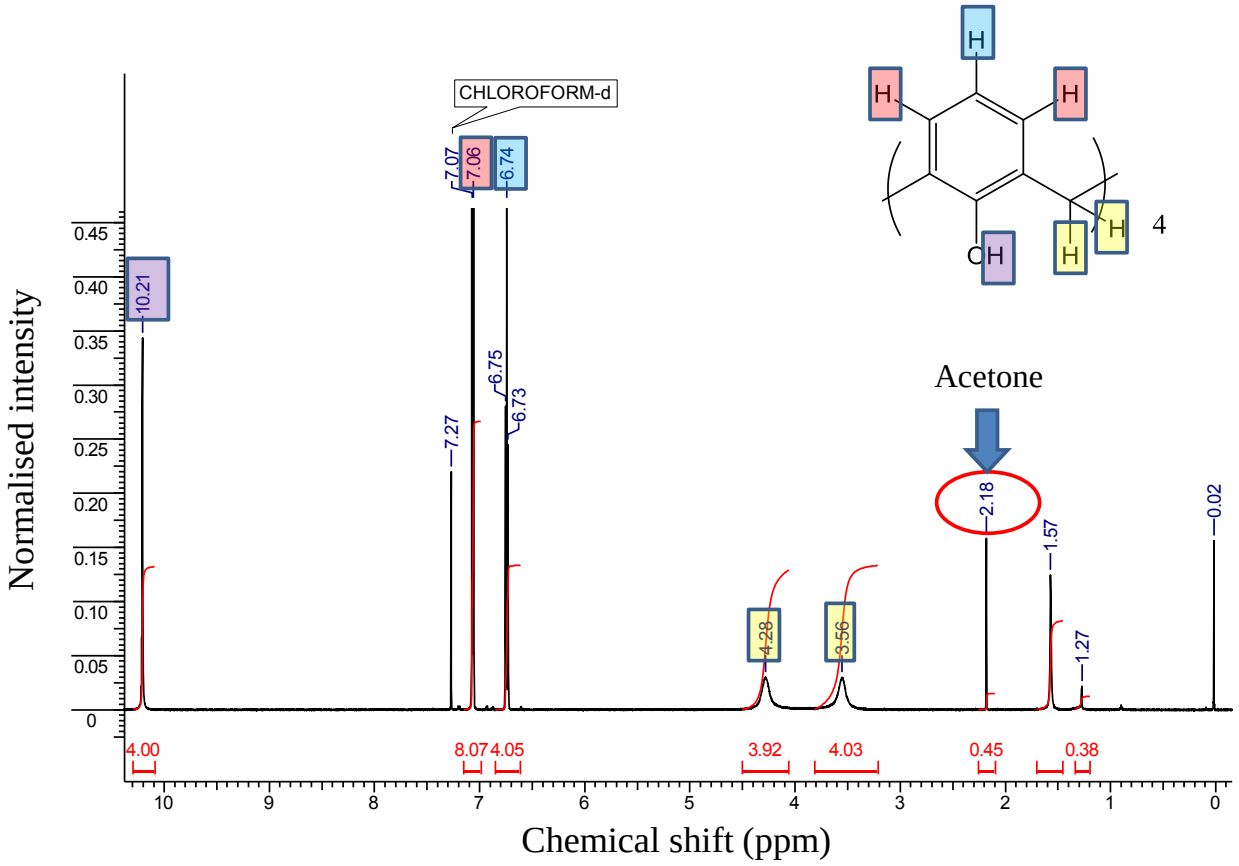

Figure 154. H^1 NMR spectrum of the 1:1 acetone clathrate of **C4** after sCO_2 exchange.

The TGA trace of the 1:1 acetone clathrate shows a stepwise loss of mass (6.47%) corresponding to a loss of 2/3 of the original amount of acetone in the clathrate (Figure 155). In sharp contrast, the TGA trace of the sample after sCO_2 exchange only shows a gradual decrease in the mass (4.16% up to 250 °C), which cannot be explicitly assigned to any particular guest. The absence of a stepwise loss might indicate that it is not acetone but CO_2 that is desorbed. In that case, the 4.16% mass loss corresponds to CO_2 desorption with a H:G ratio of 1:0.44. This represents a H:G ratio of 3:1.3 or 1.3 CO_2 molecules per interstitial cavity.

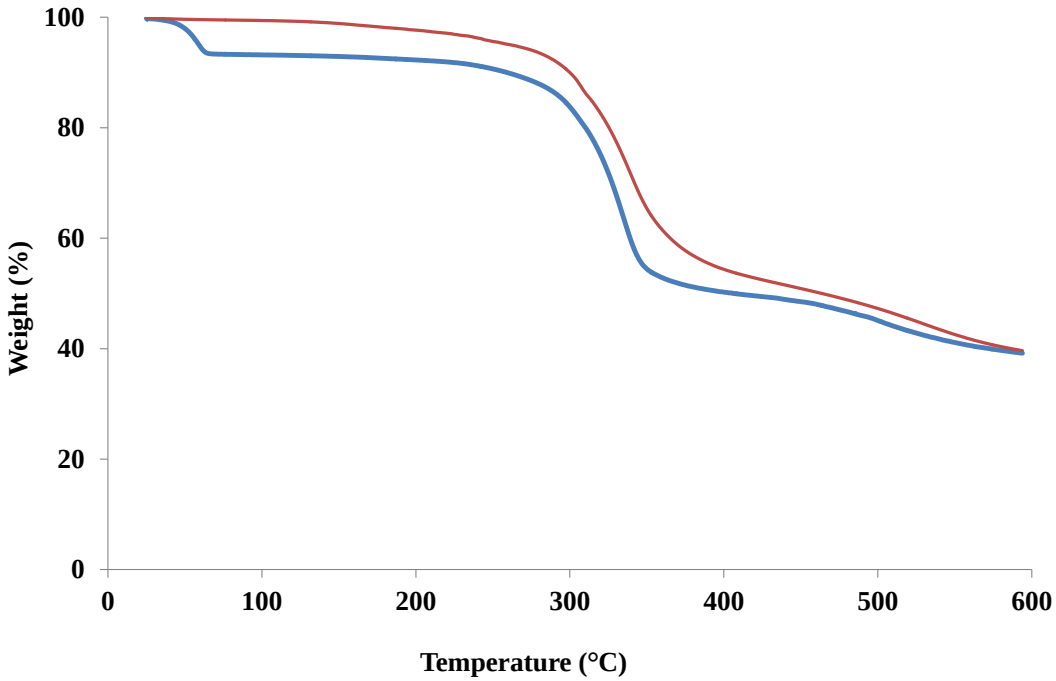

Figure 155. TGA trace of the 1:1 acetone clathrate of **C4** (blue) and the TGA trace after the 1:1 acetone clathrate of **C4** was exposed to sCO_2 (red).

During the sCO_2 exchange experiments a change in crystal morphology was observed. Some of the original block-shaped crystals were replaced by small hexagonal crystals. This indicated that the replacement of the acetone for the CO_2 is perhaps not an exchange process but that recrystallisation from supercritical CO_2 may have occurred. This observation led to further studies of the solubility of **C4·apohost** in sCO_2.

6.2.2 Recrystallisation of calix[4]arene from supercritical CO_2

Supercritical CO_2 (Tc = 31.1 °C, Pc = 73.8 bar) has the useful combination of gas-like diffusivity and liquid-like density, which can be tuned easily by changes in pressure. It is a good solvent for most non-polar and some polar low molecular weight substances and has been widely used as a solvent and anti-solvent during the synthesis, modification and purification of polymer materials and some pharmaceutical compounds.[96] The solubility of calix[4]arene and a number of *p-tert*-butylcalix[*n*]arenes in sCO_2 has been reported.[97] Graham *et al.* found that calix[4]arene is 30% more soluble in sCO_2 than *p-tert*-butylcalix[4]arene.

When a fine powder of **C4·apohost** that had been sublimed twice was subjected to supercritical CO_2 conditions for 4 hours, small hexagonal-shaped crystals formed. It therefore

appears that **C4** dissolves in sCO_2 and CO_2 molecules consequently become entrapped within the interstitial voids formed by the hcp arrangement of the **C4** trimers when the host recrystallises. A structure of the recrystallised **C4·sCO₂** was determined from SCD data, and one molecule of CO_2 per **C4** trimer could be modelled. The model is consistent with a 3:1 H:G ratio (Figure 156). In the model, the CO_2 molecule is situated on a special position (a mirror plane passes through the central carbon) with high thermal parameters (O atom, U_{iso} = 0.17, C atom U_{iso} = 0.87). A bond length restraint was used in order to restrain the C=O bond length of the CO_2 molecule to 1.120(2) Å. The high thermal parameters of the CO_2 molecule and the fact that a restraint was used to model it, is an indication that the molecule is disordered. Indeed, there is a large reported maximum (positive) residual density of 2.06 eA^{-3} in the void that could not be successfully modelled. The CO_2 molecule with a van der Waals volume of 35.3 $Å^3$ is probably disordered over several positions within the 142 $Å^3$ void, but the disorder cannot be modelled more accurately due to the hexagonal symmetry of structure. Placing the CO_2 molecule on a symmetry site enabled easy modelling (without disorder) of the molecule; however it is most likely not the true (nor the only) position of the molecule within the void.

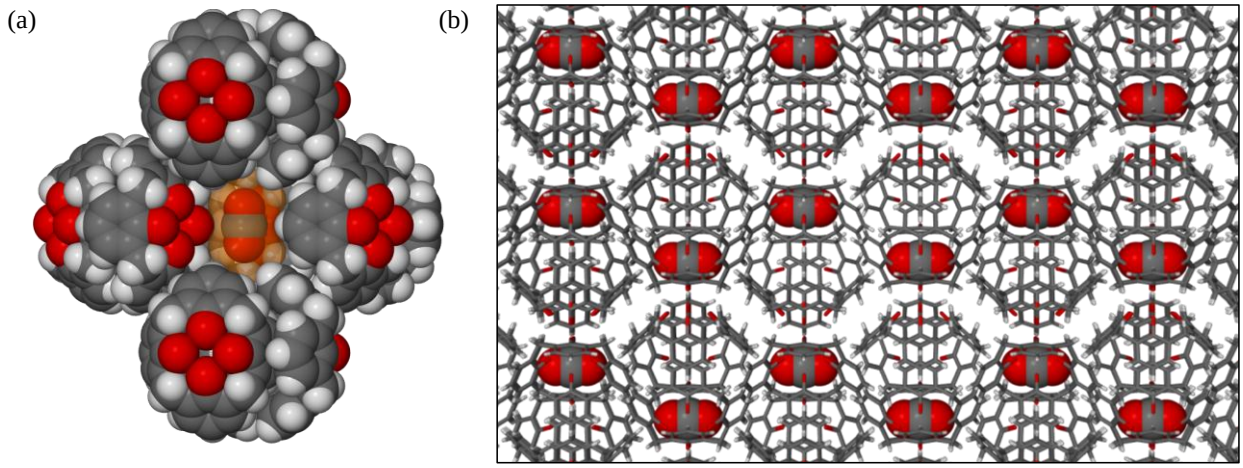

Figure 156. (a) A molecule of CO_2 entrapped in the interstitial space between five **C4** trimers. The solvent-accessible surface of 142 $Å^3$ calculated with MSROLL[39] (probe radius = 1.4 Å) is shown in orange. (b) The packing arrangement of **C4·sCO₂** viewed along [100]. The CO_2 molecules are shown in space-filled representation, and the host molecules are shown in capped-stick representation.

As a control experiment, the SCD structure of a crystal of **C4·apohost** that had been sublimed twice was determined using a SMART DUO diffractometer at room temperature. The interstitial voids of ~141 $Å^3$ appear to be almost devoid of electron density peaks. The electron count using SQUEEZE amounts to 9 electrons per 141 $Å^3$ void at 298 K. The residual electron density (9 electrons) may be due to the protons on the -OH functional groups of the **C4** molecule that were not modelled. The SQUEEZE electron count for **C4** that was recrystallised from sCO_2

is 43 electrons per 142 $Å^3$ void. The increase in the electron density by 34 electrons corresponds to an occupancy of ~1.5 CO_2 molecules per cavity. Therefore, the 3:1.3 H:G ratio of the TGA trace after sCO_2 exchange and the 3:1.5 H:G ratio from the SQUEEZE electron count of the SCD structure are in close agreement. The H:G ratio is slightly higher than the expected 3:1 ratio of most of the calix[4]arene solvates. However, since the position cannot be modelled from SCD data alone, a computational approach to finding the true occupancy (one or two molecules per cavity), interaction site and location of CO_2 molecule/s within the cavity was necessary.

6.3 DETERMINING THE OPTIMISED POSITION OF CO_2 WITHIN THE CAVITIES USING COMPUTATIONAL METHODS

In order to confirm the likely position(s) of CO_2 within the interstitial cavities in **C4**, quench dynamics (molecular mechanics) and CASTEP (density functional theory) calculations were carried out in Material Studio V6.0. The quench dynamics calculations were employed in order to quickly find the most stable positions for the CO_2, since it can be utilised to find all the energetic local minima of the system. A higher level of theory is necessary to more accurately find the lowest energy position (global minimum) and to ultimately determine the interaction energies involved in the inclusion of CO_2. Density functional theory with a functional that will account for dispersion forces was then used to accurately determine the interaction energies involved with the van der Waals confinement of CO_2 molecules within the **C4** cavities.

Since the SQUEEZE electron count from the SCD structure suggests that an average of 1.5 CO_2 molecules are included in the interstitial space, the likelihood that half the cavities contain two CO_2 molecules needs to be considered as well. Two molecules of CO_2 (35.33 $Å^3$) in a 142 $Å^3$cavity is equivalent to a packing coefficient of 0.49, which is comparable to the packing coefficients in **IMMOF-3** (0.47) and **MC1** (0.42).

Therefore two different models were studied:

(i) a model with one CO_2 molecule in the cavity, and

(ii) a model with two CO_2 molecules in the cavity.

The calculations that were performed on both models are discussed further below.

6.3.1 Quench dynamics calculations: finding numerous stable positions

Quench dynamics calculations were performed on the **C4·sCO2** crystal structure. A dynamics simulation makes use of classical equations of motion that are modified to take into account the effects of temperature and pressure. The result of a dynamics run is a trajectory file that contains the atomic configuration and atomic velocities at a sequence of time steps. In effect, a statistical population of structures of different energies/enthalpies is generated in a chosen time period. The energy of a particular structure can be compared to that of other structures in order to find the most stable structure.

From previous calculations performed on *p-tert*-butylcalix[4]arene,[98] it was determined that the polymer consistent forcefield (PCFF)[99], intended for application to polymers and organic materials, performs the best. The structure that was optimised with the PCFF forcefield yielded a model in which the atomic positions are most similar to those of the SCD structure. The **C4·sCO2** crystal structure was imported into the Materials Studio software suite. Hydrogen atoms were added to the hydroxyl groups and the positions of all of the hydrogen atoms were optimised via a CASTEP geometry optimisation (DFT, details to follow). The charges calculated during the CASTEP optimisation were used in the subsequent dynamics simulation. The positions of the host **C4** atoms were fixed (made non-mobile); however the position of the CO_2 molecule was allowed to vary. A dynamics simulation of ultrafine quality (convergence requirement: 2×10^{-5} kcal mol^{-1}) and an atom based summation method was run and the energy calculated (quenched) every 5000 steps of 1 fs with a total simulation time of 500 ps.

The results of the quench dynamics calculations performed on both models are discussed.

(i) Model with one CO_2 molecule per void

The energies of the quench dynamics simulation are shown in Figure 157. The two lowest energy populations that have been circled in Figure 157 represent the two alternative positions of the CO_2 molecule within the void. In the first position (*position a*), the location of the CO_2 molecule is identical to that of the SCD model. The CO_2 molecule is situated in the centre of the 142 $Å^3$ void, aligned with the apical trimers and it appears to be confined by van der Waals forces only. There are no noticeable close contacts with the "surface" of the cavity. The second lowest energy position is with the CO_2 molecule positioned with the same vertical alignment in the direction of the apical trimers, but slightly off-centre and shifted closer to the side of the cavity. At this position, the central carbon of the CO_2 molecule is in close contact with the hydroxyl oxygen

atom of one of the equatorial calix[4]arene molecules that line the cavity (C···O distance = 3.156 Å). This position (*position b*) has three-fold symmetry and the electron density of one CO_2 molecule will be shared between all three positions in a crystal structure. The two different positions are shown in blue (*position a*) and orange (*position b*) in Figure 158.

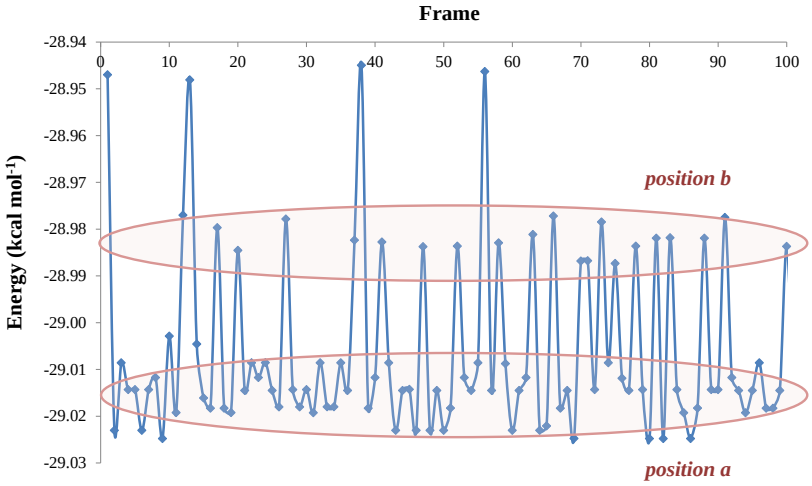

Figure 157. The quench dynamics energies calculated for the different CO_2 positions within the interstitial void. The two most prominent energy populations have been encircled.

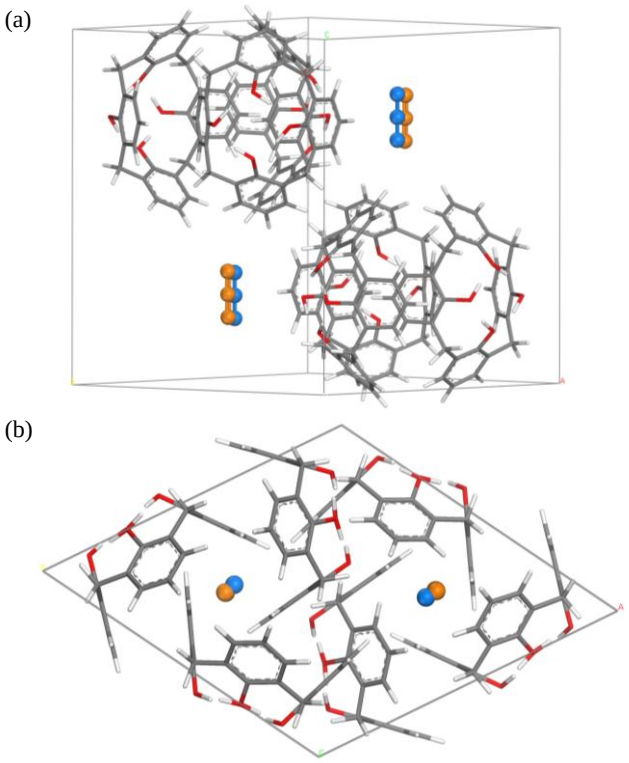

Figure 158. (a) The two lowest energy positions for the CO_2 molecule are shown relative to two trimers of **C4** in the unit cell. The blue CO_2 molecule is in the the centre of the interstitial void (*position a*), whilst the orange CO_2 molecule is in one of the three symmetry-related positions that is slightly shifted towards the side of the interstitial void (*position b*). (b) The two opposing CO_2 positions viewed along [001].

Figure 159 shows *position a* and *position b* relative to the Connolly surface of the interstitial void.

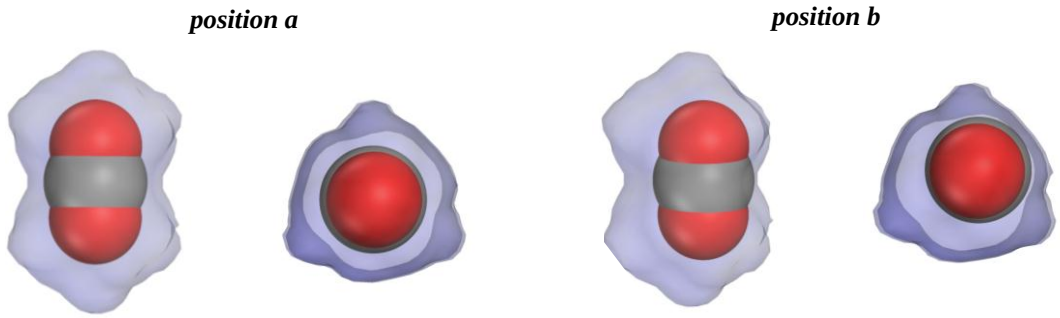

Figure 159. The CO_2 molecule is shown in space-filled representation (van der Waals volume) while the Connolly surface of the cavity with a probe radius of 1.4 Å is shown as a transparent purple surface. A view perpendicular to the longest length of the cavity is shown as well as a view from above, along the direction of the apical trimers and *c* axis.

Based on the quench dynamics calculations *position a* is more favourable than *position b*, however CASTEP geometry optimisations and single point energy calculations are necessary to confirm this premise and to determine accurate interaction energies.

(ii) Model with two CO_2 molecules per void

The energies of the quench dynamics simulation of model (ii) are shown in Figure 160. Contrary to model (i) it is slightly more difficult to isolate a population of structures of similar energy.

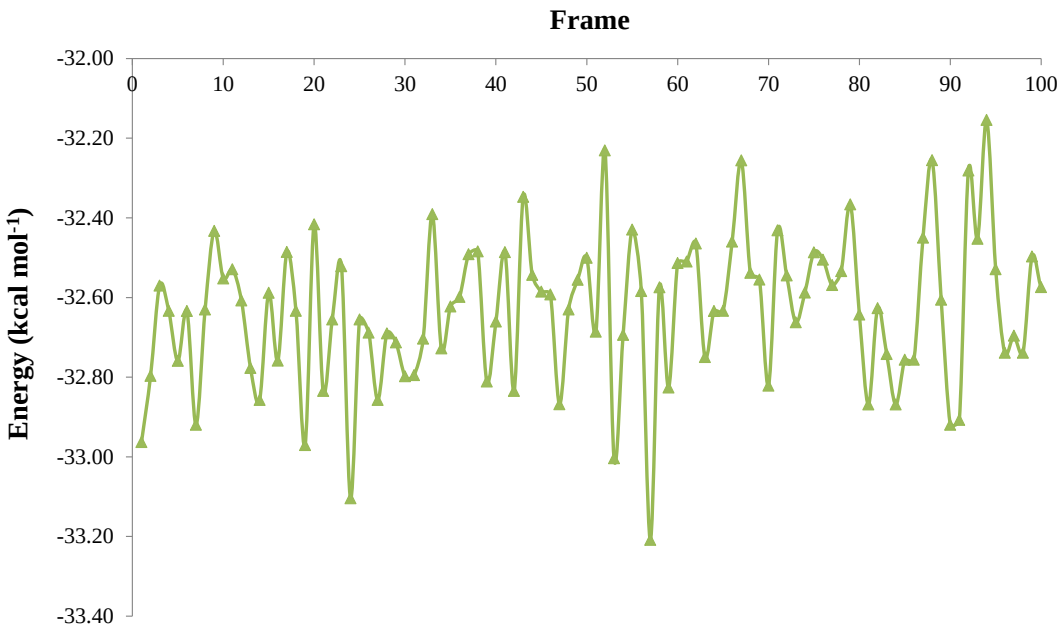

Figure 160. The quench dynamics energies calculated for model (ii) with two CO_2 molecules within the interstitial void. The dynamics simulation did not provide any clear statistical populations of energy values.

However, in the quenched structures there are two well-known CO_2-CO_2 dimer configurations that are apparent, either the T-shaped or slipped-parallel configurations (Figure 161).[100]

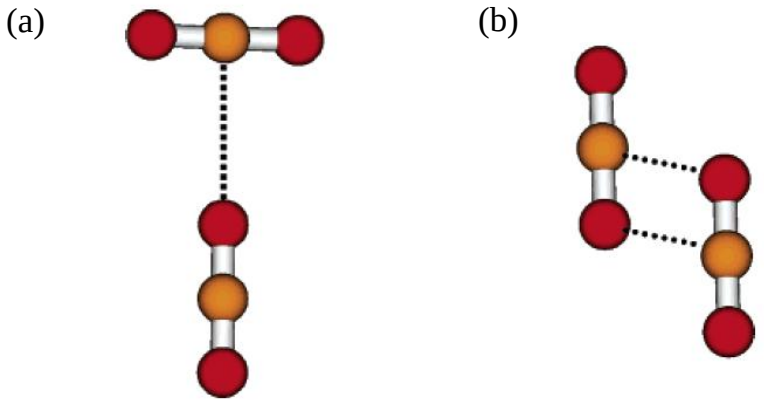

Figure 161. The (a) T-shaped and (b) slipped-parallel configurations of the CO_2 dimer.[100]

The geometry of the CO_2 dimers included in **C4** is not an ideal T-shape or slipped parallel configuration, conceivably due to steric constraints imposed by the cavity. Three distinguishable structures of different energy were derived from the dynamic simulation, i.e. structures with (a) the CO_2 molecules forming a slightly offset slipped-parallel configuration, (b) the T-shaped configuration or (c) with a combination of the slipped-parallel and T-shaped configurations (Figure 162).

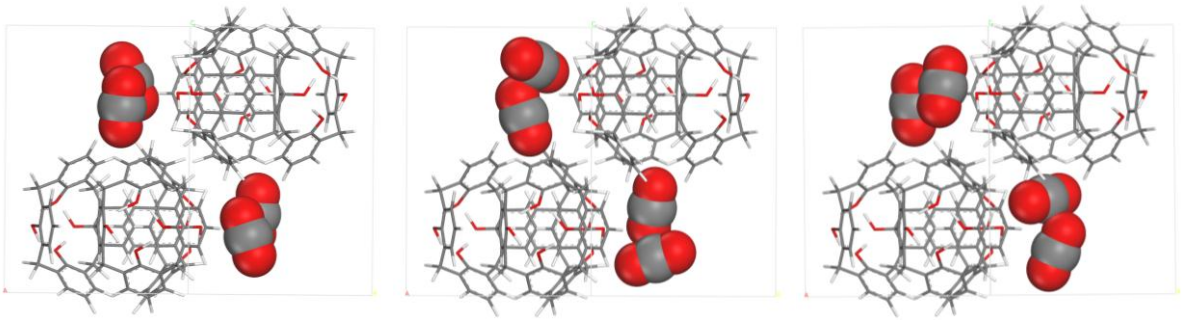

(a) slipped-parallel configuration (b) T-shaped configuration (c) combination of slipped-parallel and T-shaped configurations

Figure 162. The three different configurations of the two CO_2 molecules within the **C4** void.

The two CO_2 molecules are in van der Waals contact with each other and with the cavity wall as shown in Figure 163.

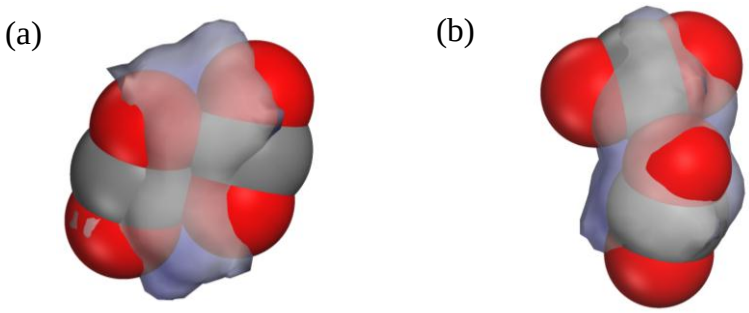

Figure 163. The optimised CO_2 dimer in (a) an approximate slipped-parallel configuration and (b) an approximate T-shaped configuration within the **C4** interstitial void. The Connolly surface of the interstitial void is shown as a semi-transparent purple surface (probe radius = 1.4 Å) and the CO_2 molecules are in space-filled representation (van der Waals volume).

Energy calculations with the CASTEP module were performed to accurately calculate the host-guest and guest-guest interaction energies and the results will determine whether the short host-guest and guest-guest contacts are indeed attractive or repulsive.

6.3.2 CASTEP calculations: Finding accurate positions and calculating interaction energies

Geometry optimisations were performed on the **C4·sCO₂** structure as a crystallographic system with all non-hydrogen atoms (except for the CO_2 atoms) and the unit cell parameters fixed, using the CASTEP[101] module of the Materials Studio software suit. The optimisations were performed using the GGA PBE[102] functional (BFGS algorithm[103]) with Grimme DFT-D dispersion correction[104] and optimisation and SCF convergences of 1×10^{-5} eV and 1×10^{-6} eV $atom^{-1}$, respectively. Calculations were performed on both models containing either one or two CO_2 molecules per void. To this end, geometry optimisations of (i) the empty host framework, (ii) the host including one CO_2 molecule in either *position a* or (iii) *position b*, the host including two CO_2 molecules per void in either (iv) the slipped-parallel configuration or the (v) T-shaped configuration were executed. Thereafter single point energies of the converged structures were calculated using the same functional and ultra-fine quality. Single point energy calculations were also performed on the guest molecules in the absence of the host to enable the calculation of the host-guest and guest-guest interaction energies. The total interaction energy can be calculated using equation (3):

total interaction energy = host-guest interaction energy + guest-guest interaction energy (3)

The total interaction energy is the lattice enthalpy of the host framework when it includes a guest molecule or guest molecules minus the lattice enthalpy of the empty host framework. It follows

that the host-guest interaction energy is then the total interaction energy minus the guest-guest interaction energy. The results of the single point energy calculations for model (i) with only one CO_2 molecule per interstitial void are summarised in Table 29.

Table 29. The results of the single point energy calculations of the model with one CO_2 molecule per void.

	Single point energy per unit cell (kcal mol^{-1})
host	-895131.5323
host with CO_2, *position a* (middle)	-942553.2937
host with CO_2, *position b* (to the side)	-942552.1476
only CO_2 *position a*	-47413.29826
only CO_2 *position b*	-47413.38612

The single point energy values were used to calculate the host-guest interaction energy as well as the Boltzmann distribution for each of the two positions (Table 30). The most stabilising position for the CO_2 molecule is in the centre of the void (*position a*) with a host-guest interaction energy of -8.46 kcal mol^{-1} at this position. In order to calculate the Boltzmann distribution it was taken into account that *position b* has three-fold symmetry and that the CO_2 molecule is in effect disordered over four different positions. The Boltzmann distribution suggests that at 298 K the CO_2 molecule will be located in the centre of the void with a probability of 72.8% and at one of the three symmetry-related positions towards the side of the void with a probability of 27.2%.

Table 30. The host-guest interaction energy and normalised Boltzmann distribution for the two positions.

Location of CO_2 molecule	**Host-guest interaction energy (kcal mol^{-1})**	**Boltzmann distribution**
position a 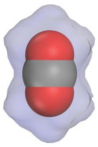	-8.46	72.8%
position b 	-7.23	27.2%

In contrast, the CASTEP geometry optimisations of model (ii) with two CO_2 molecules per void did not converge within the allowed number of iterations (100). The algorithm was subsequently changed to the damped molecular dynamics (MD) algorithm[105] and an SCF

smearing factor of 0.1 eV was used. This algorithm resulted in the geometry optimisations converging within 16-20 iterations.

In comparison to model (i) with one CO_2 per void, the single point energies for model (ii) with two CO_2 molecules per void yielded entirely different results. On condition that there are two molecules per void, each with a unique position relative to the host, the single point energy of the host with one CO_2 per void in each of the two positions needs to be computed in addition to the same type of calculations performed on model (i). Single point energies for one CO_2 in the crystal lattice in the absence of the host were also calculated. The single point energies of model (ii) are summarised in Table 31.

Table 31. The results of the single point energy calculations with two CO_2 molecules per void.

Calculation	Model	Single point energy per unit cell (kcal mol^{-1})
1	host	-895131.5323
2	host with 2 CO_2 per void, *slipped-parallel*	-986665.2348
3	host with 2 CO_2 per void, *T-shaped*	-986506.2691
4	host with 1 CO_2 per void, *slipped-parallel (a)*	-939364.7369
5	host with 1 CO_2 per void, *slipped-parallel (b)*	-939370.0962
6	host with 1 CO_2 per void, *T-shaped (a)*	-939772.3533
7	host with 1 CO_2 per void, *T-shaped (b)*	-939210.3511
8	guest: 2 CO_2 *per void, slipped-parallel*	-94649.3583
9	guest: 2 CO_2 *per void, T-shaped*	-94644.9816
11	guest: 1 CO_2 per void, *slipped-parallel (a)*	-47326.4867
12	guest: 1 CO_2 per void, *slipped-parallel (b)*	-47328.8672
13	guest: 1 CO_2 per void, *T-shaped (a)*	-47324.9003
14	guest: 1 CO_2 per void, *T-shaped (b)*	-47324.7776

In order to determine the total host-guest interaction energy for the different dimer configurations, the host-guest interaction energy with of each individual CO_2 molecule in its unique position (position (a) or (b)) was summed. The guest-guest interaction energies were calculated by subtracting the single point energies of the individual CO_2 molecules (in the absence of the host) from the single point energy of the CO_2 dimers (in the absence of the host). The results are shown in Table 32.

Table 32. Host-guest and guest-guest interaction energies calculated for two molecules of CO_2 in the **C4** void.

Dimer configuration	Host-guest interaction energy (kcal mol^{-1})	Guest-guest interaction energy (kcal mol^{-1})
slipped-parallel 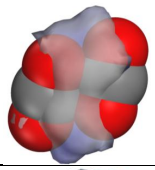	47.73	6.00
T-shaped 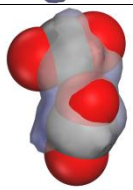	610.45	4.70

It can be concluded that the inclusion of two molecules within the **C4** interstitial void is highly unfavourable. The host-guest and guest-guest interactions are repulsive. The smallest total repulsive interaction energy exists when the molecules are in the slipped-parallel configuration. The T-shaped dimer is most unfavourable owing to the massive host-guest repulsion energy term, probably linked to the obvious protrusion of the CO_2 out of the Connolly surface of the cavity. If the unit cell parameters and host atoms were not fixed and the system was allowed to expand, it is possible that the inclusion of two CO_2 molecules might become more likely. However, since the unit cell parameters and atomic positions from the SCD structure were utilised and fixed in the calculations, it can be concluded that the SQUEEZE electron count that suggests a H:G ratio of 3:1.5 is inaccurate. High-angle reflections are necessary for an accurate SQUEEZE electron count, and the low scattering factor of the organic **C4** host (with Mo radiation) might impede the accuracy of the SQUEEZE results. The CASTEP calculations have indicated that it is most favourable if one CO_2 molecule is included per void (H:G ratio of 3:1), and the most stable position for the CO_2 is in the centre of the cavity with its oxygen atoms directed towards the apical trimers. The computationally determined position is almost identical to the experimental position determined from the SCD model. The high thermal parameters for the CO_2 molecule in the model are due to positional disorder of the CO_2. The Boltzmann distribution indicates that the CO_2 molecule is most likely located at *position a* (73% probability) but it can also be located at *position b* (28% probability).

6.3.3 Molecular electrostatic potential maps

The inclusion of CO_2 in the interstitial voids of **C4** appears to be due to van der Waals confinement only. However, in order to gain a better understanding of the electrostatic differences between *position a* and *b* of model (i), the electrostatic interactions with the void surface need to be considered. Molecular electrostatic potential (MEP) maps can be used as a means of characterising the electrostatic interactions between host and guest molecules. The molecular electrostatic potential $V(\mathbf{r})$ is a useful tool for the study of non-covalent interaction between molecules. MEP maps have been applied to characterise the electrostatic interactions involved in processes such as molecular recognition,[106] enzyme interactions[107] and molecular reactivity.[108] The electrostatic potential is calculated from the electron density and the atomic charges via the following equation (4)[109]:

$$V(r) = \sum_A \frac{Z_A}{|R_A - r|} - \int \frac{\rho(r')dr'}{|r' - r|} \quad (4)$$

V(r) is the interaction energy of the model with a unit point charge positioned at *r* in 3D space and is expressed in atomic units (au, Hartree). Z_A is the nuclear charge and R_A is the position of the nuclei. Using equation (4), a 3D contour map is generated to which a colouring scheme is applied to highlight the differences in electrostatic potential across a surface.[110]

The electrostatic potential of the **C4** host was calculated using the VAMP module of Materials Studio V6.0 as a single point energy calculation using the NDDO Hamiltonian type and the AM1* Hamiltonian. A SCF convergence of 5×10^{-7} kcal mol^{-1} was used and the grid size for the imported electrostatic potential is 0.1 Å. The atomic coordinates of the **C4** host was obtained from the **C4·sCO2** SCD structure. The single point energy calculation on the geometrically optimised (CASTEP) structure of the empty host (discussed in the previous section) was used for electron density data. The electron density data were used to construct the three dimensional 0.01 e^- Å^{-3} (0.0015 au, e^- bohr^{-3}) electron density contours of the host molecules. The electrostatic potential calculated for the host structure was then mapped onto the outermost electron density contour of the host molecules and a colour map of the electrostatics was generated and is shown in Figure 164.

The electron densities of the CO_2 molecules in *position a* and *position b* were also imported into the 3D VAMP electrostatic field. Consequently, the electrostatic potential of the cavity could be mapped onto the outer electron density contour of the CO_2 molecule (Figure 165).

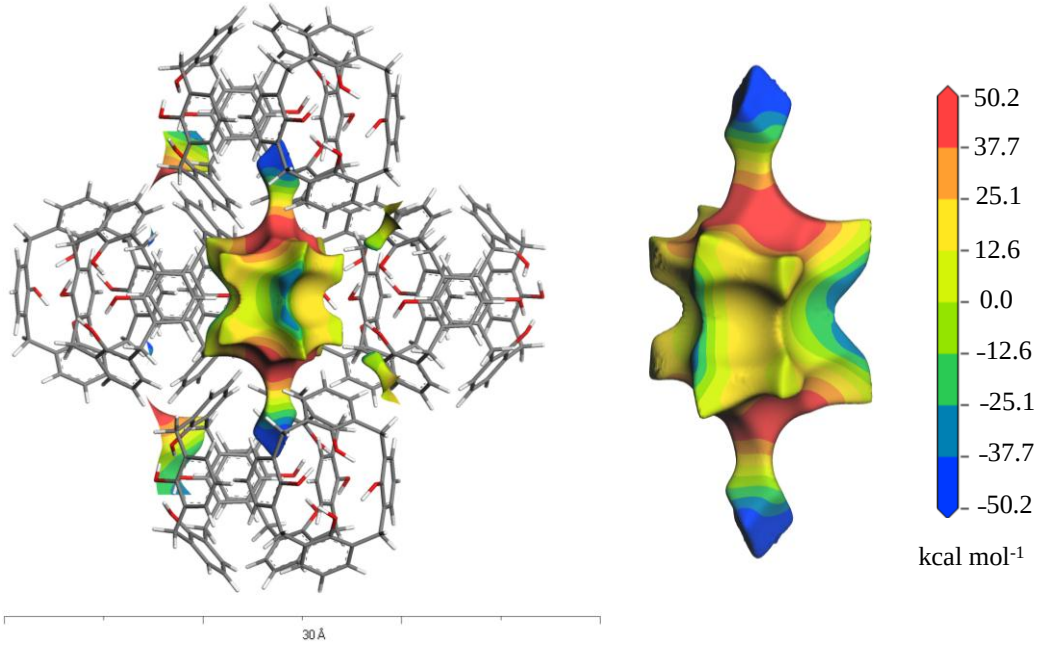

Figure 164. The molecular electrostatic potential mapped unto the outer electron density contour (0.0015 e^- $bohr^{-3}$) of the host framework.

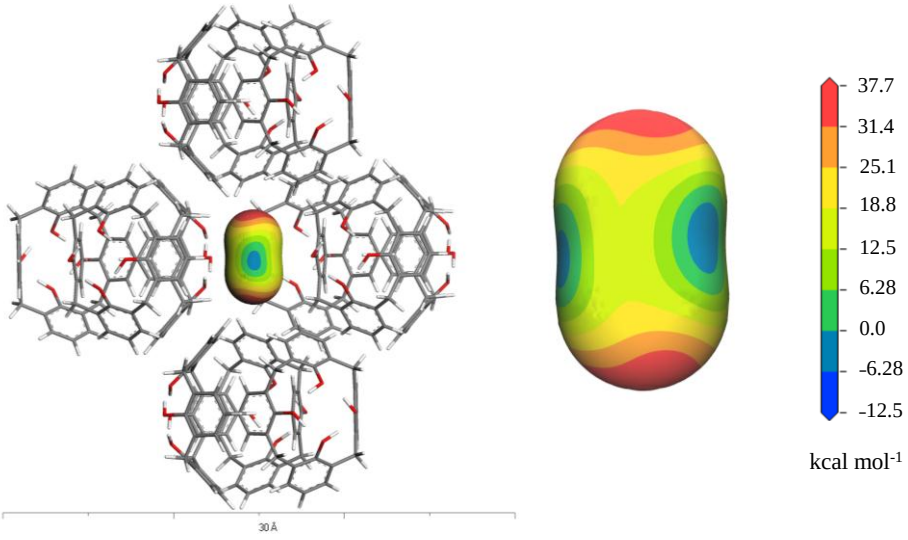

Figure 165. The molecular electrostatic potential mapped unto the outer electron density contour (0.0015 e^- $bohr^{-3}$) of the CO_2 molecule when it is located in the centre of the cavity (*position a*).

The oxygen atoms of the CO_2 molecule experience a positive electrostatic potential produced by the protons of the apical **C4** trimers (Figure 166a). The central carbon atom of the CO_2 molecule experiences a negative electrostatic potential at three sites that correlate to the position of the hydroxyl oxygen atoms of the equatorial **C4** trimers (Figure 166b). The positive electrostatic potential at either end of the cavity is more than three times the negative

electrostatic potential experienced in the equatorial plane, and is thus the dominant electrostatic interaction that stabilises the CO_2 in *position a*.

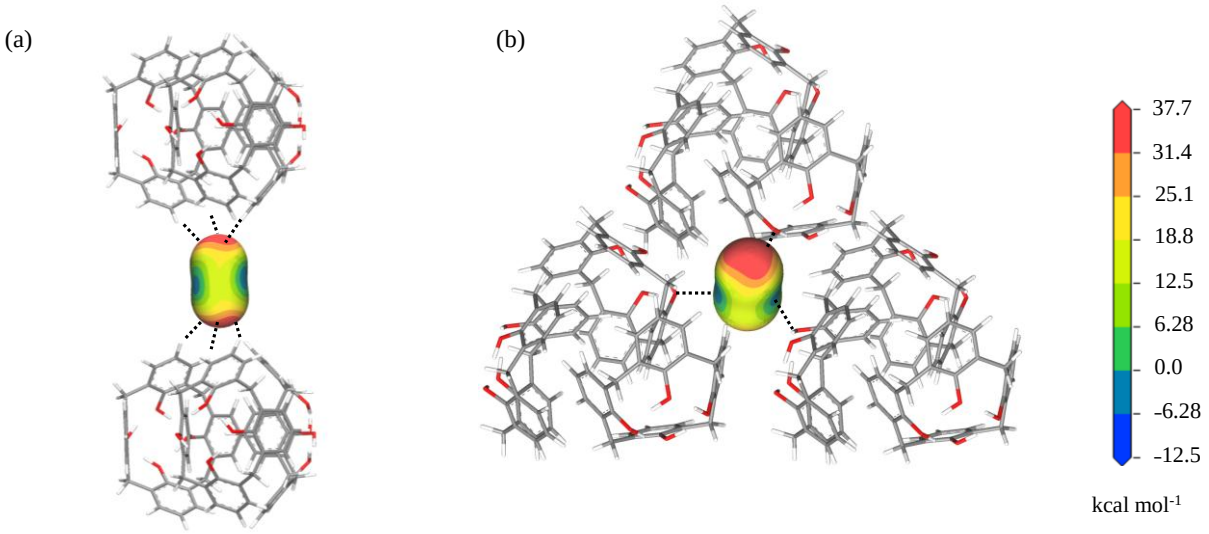

Figure 166. (a) The host protons are responsible for the positive electrostatic potential that the oxygen atoms of the CO_2 molecule experience. (b) The host hydroxyl groups create three symmetry-related negative electrostatic potential points around the central carbon of the CO_2 molecule. The scale bar shows that the positive electrostatic potential is three times as large as the negative electrostatic potential.

When the CO_2 molecule is located towards the side of the cavity (*position b*) it forms a stronger electrostatic interaction with one of the hydroxyl oxygen atoms, as evidenced by the enlargement of the most negative electrostatic potential contour on one side of the CO_2 molecule shown in Figure 167. This results in the central carbon atom not experiencing a negative electrostatic potential from the other two hydroxyl groups that surround the molecule. Simultaneously, there is a small decrease in the amount of positive electrostatic potential it experiences at the apical positions.

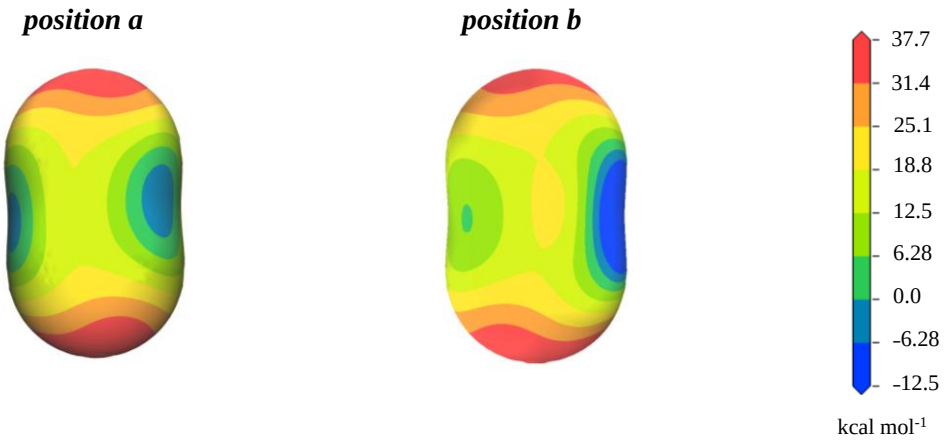

Figure 167. The electrostatic potential of the host cavity mapped onto the outer electron density contour of the CO_2 molecule when it is in the centre of the cavity (*position a*) compared to when it is towards the side of the cavity (*position b*).

The interatomic separations between the central carbon atom of the CO_2 molecule and the hydroxyl oxygen atoms in the equatorial plane are shown in Figure 168.

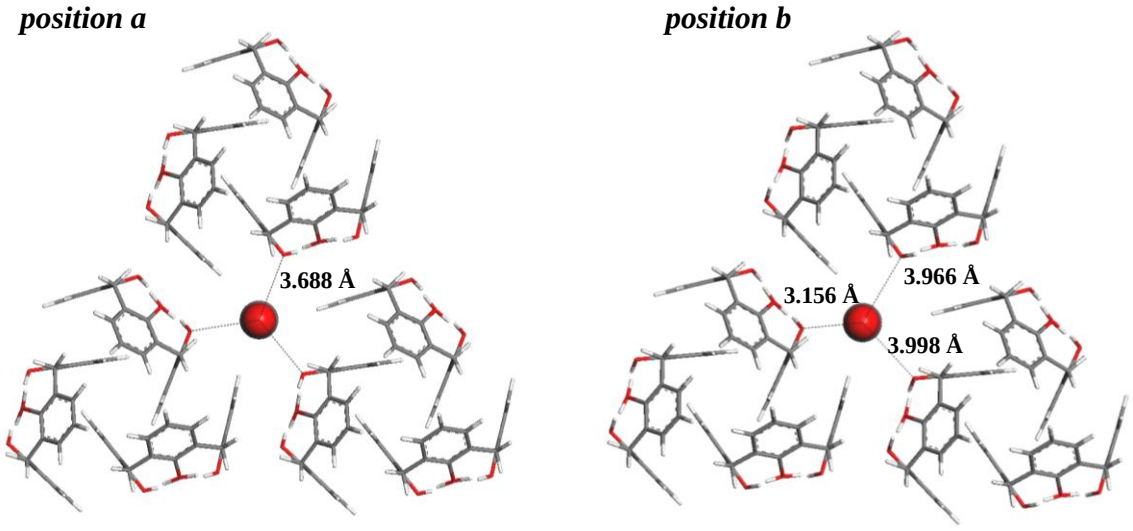

Figure 168. The C···O distances between the central carbon atom of the CO_2 molecule and the hydroxyl oxygen atoms of the calix[4]arene molecules.

The C···O distance in the SCD model (**C4·sCO2**) of 3.680(4) Å is in very close agreement with the distance measured for the geometrically optimised structure obtained with CASTEP, with the CO_2 molecule in the most favourable position, i.e. *position a*. The SCD model is therefore supported and the high thermal parameters for the CO_2 molecule are an indication of positional disorder over *position a* and *position b*.

6.4 SUMMARY AND CONCLUSIONS

This chapter aimed to show, in principle, that even non-porous materials can be used for gas storage purposes. Calix[4]arene's ability to entrap volatile guests has been previously studied; however the present study provides the first evidence for an inclusion complex with CO_2. Unlike *p-tert*-butylcalix[4]arene, **C4** is poorly permeable to CO_2. However, **C4** can be dissolved in supercritical CO_2 and CO_2 molecules become included within the interstitial voids. By measuring IR spectra at weekly intervals it was determined that the CO_2 molecules are retained for ~4 weeks under ambient conditions. Based on the SQUEEZE electron count of a crystal grown from sCO_2, there are 33 additional electrons in the interstitial void as compared to a sublimed crystal. The electron count is consistent with a 3:1.5 H:G ratio. A computational study involving models with either one or two CO_2 molecules in the cavity was carried out using the FORCITE, CASTEP and VAMP modules of Materials Studio V6.0. Molecular mechanics

calculations were used to determine the most probable position of the CO_2 molecule/s given that the high symmetry of the SCD structure prevents unrestrained modelling of the CO_2 molecule/s. The CASTEP geometry optimisations and single point energy calculations were performed in order to determine the interaction energies involved the inclusion of CO_2. It was found that a cavity with one CO_2 molecule is much more stable than a cavity with two CO_2 molecules. The H:G ratio (3:1.5) derived from the SQUEEZE results was inaccurate; however, the SQUEEZE manual states that inaccurate results are obtained when (i) the resolution of the data is inadequate (below $\theta = 25°$ for Mo radiation), (ii) the known part of the structure is not completed with hydrogen atoms and/or (iii) if the disordered electron density is not well outside the van der Waals surface of the known structure. Specifically conditions (i) and (ii) were not adequately fulfilled in the **C4** structures that were discussed.

The optimisations carried out with CASTEP showed that the most stable position of the CO_2 molecule is in the centre of the cavity, with its oxygen atoms directed towards the protons of the apical trimers. A stabilisation energy of -8.46 kcal mol^{-1} and Boltzmann distribution of 72.8% was calculated for this position in comparison to the -7.23 kcal mol^{-1} and 27.2% distribution for the position in which the CO_2 molecule is located closer to the side of the cavity. A MEP map of the cavity revealed that the most stabilising electrostatic interactions for the inclusion of CO_2, are the interactions between the guest oxygen atoms and the host protons of the apical **C4** trimers.

The computational study was successful in validating the position of the CO_2 molecule within the **C4** interstitial void that had been determined experimentally by SCD methods. This method of validation can be applied to other SCD structures of host-guest compounds with positional or symmetry-related disorder of the guest. It may prove to be especially useful for data collected under gas pressure, which often yield models in which the gas molecules are disordered over several positions within a large channel or discrete void.

6.5 EXPERIMENTAL SECTION

6.5.1 Crystallographic tables

	C4·apohost	**C4·sCO2**
Empirical formula	$C_{14}H_{10}O_2$	$C_{14.17}H_{10}O_{2.33}$
Formula weight	210.22	217.55
Temperature/K	295(2)	298(2)
Wavelength/Å	0.71073	0.71073
Crystal system	hexagonal	hexagonal
Space group	$P6_3/m$	$P6_3/m$
a /Å	14.355(12)	14.5068(10)
b /Å	14.355(12)	14.5068(10)
c /Å	18.651(15)	18.3346(13)
α /°	90.00	90.00
β /°	90.00	90.00
γ /°	120.00	120.00
Volume/Å^3	3329(5)	3341.5(4)
Z	12	12
Calculated density/g cm^{-3}	1.258	1.297
Absorption coefficient (mm^{-1})	0.084	0.088
F_{000}	1320	1364
Reflections collected	20256	19092
Independent reflections	2331 [R_{int} = 0.0676]	1977 [R_{int} = 0.0690]
Data/restraints/parameters	2331 / 0 / 155	1977 / 1 / 159
Goodness-of-fit on F^2	1.154	1.436
Final R indices [I>2σ(I)]	R1 = 0.1181, wR2 = 0.2565	R1 = 0.1093, wR2 = 0.3517
R indices (all data)	R1 = 0.1322, wR2 = 0.2620	R1 = 0.1351, wR2 = 0.3779

CHAPTER 7

CONCLUSIONS AND FUTURE STUDIES

Supramolecular chemistry encompasses a wide variety of chemical principles and techniques that may be used to elucidate and explain structure-related properties in crystalline materials. Many topics that fall within the supramolecular chemistry and materials science realm such as crystal engineering, self-assembly, inclusion compounds, intermolecular interactions, incommensurate and commensurate structures, induced fit, polymorphism, thermal expansion and, most importantly, porosity were encountered during this study. Using the structural information obtained from single crystal X-ray crystallography under different conditions, the dynamics of various solid-state phenomena were successfully studied. In situ X-ray diffraction studies of gas inclusion compounds are, to date, quite rare and there are not many known gas inclusion structures reported in the literature. For instance, a CSD search for CO_2 yielded 72 unique structures, of which only 36 structures contain CO_2 as a free unit (i.e. not complexed to a metal). Of these, 23 involve metal-organic hosts (mostly involved in catalysis, such as Rh-complexes), 8 are organic and 5 are inorganic/zeolitic hosts. An environmental gas cell designed and built by Barbour *et al.* was used to collect SCD data under controlled atmospheres.[111] It was shown that X-ray crystallography, when combined with other characterisation techniques such as thermal analysis, sorption experiments, HPDSC, NMR and IR, can provide a substantial amount of information about the sorption properties of supramolecular assemblies.

The work presented as part of this dissertation was mainly focused on the synthesis and studies of novel microporous materials with gas sorption and/or solvent exchange properties. Molecules tend to pack closely in the solid-state and, in most cases, porosity therefore needs to be created by design. Although structure prediction is not universally possible at this time, certain crystal engineering strategies that involve previous knowledge mined from databases such as the CSD have been successfully employed to create porosity. The strategies used to create porosity in this dissertation include the self-assembly of novel 2D and 3D metal-organic frameworks (MOFs) from organic ligands and transition metal salts, the self-assembly of a novel doughnut-shaped metallocycle and the crystallisation of calix-shaped calix[4]arene molecules that cannot pack efficiently in the solid state. These and other porous crystals can, in principle, find application in many processes such as molecular separation, gas storage and catalysis.

Traditionally, only zeolites were used for these applications; however metal-organic hybrid materials have recently emerged as a more diverse class of materials that can offer additional functionality.

During the course of this study it was demonstrated that porosity can take on many forms. This dissertation juxtaposed the different gas and vapour sorption properties of rigid scaffolds versus transformable and flexible frameworks. It was found that a rigid 3D MOF is physically and chemically more stable (single crystals are more robust) than 2D MOFs or 0D discrete metallocycles. At the same time, guest transport and inclusion in permanently porous materials with channels were compared to materials with discrete voids. While the 3D MOF with 6 Å × 6 Å channels described in Chapter 4 has the advantage of unhindered guest transport and is able to sorb a wide variety of gases and vapours, it was shown in Chapter 3 that the 2D MOFs with discrete cavities display selective uptake of CO_2 (relative to N_2 and CH_4) as well as gate-opening sorption properties involving a transformation from a "closed" to an "open" phase. In general, the significant amount of hysteresis in the desorption behaviour of transiently porous (**IMMOF-2, IGMC**) and non-porous (**C4**) materials make them more advantageous for storage applications than permanently porous materials.

At certain points in the study it was determined that the SCD model obtained from X-ray diffraction data was inadequate or unable to answer a specific research question on its own. This is due to the fact that the unit cell gives an average "picture" of the entire macroscopic single crystal. In these cases, computational methods were used to validate the experimental results. Computational studies were employed to explain the disorder of the phenylene spacer of **IMMOF-3**, the exclusion of vinyl chloride from the **IMMOF-3** channels and to determine the most stable positions of a CO_2 molecule within the interstitial voids of calix[4]arene.

The main findings of each chapter can be summarised in order to demonstrate how the macroscopic properties of three different types of materials can be adequately explained and studied by structural analysis of SCD data collected under different experimental conditions.

Chapter 3 encompasses a study of novel MOFs synthesised from seven rigid organic linkers (**L1**-**L7**) with coordinating imidazolyl and carboxylic acid groups and transition metal salts. **L1** to **L5** yielded MOFs that did not undergo single-crystal to single-crystal transformations; hence **L6** and **L7** were designed. They were synthesised using a novel method that involves a microwave reactor, which significantly reduced the reaction time of the nucleophilic substitution reaction of benzimidazole or napthaimidazole with 4-fluorobenzonitrile from 2-3 days to 30

minutes. A complete description of the procedures and complete characterisation of the precursors and products is provided in the experimental sections of Chapters 3 and 4. The evolution in the design of the organic ligands was based on the observation that increasing the π-electrons available for π-π interactions leads to more porous and robust frameworks. The 2D MOFs from **L6** have dynamic properties such as guest-responsive fitting, which was outlined in Chapter 3. The transformability of **IMMOF-1** and **IMMOF-2** is based on the sliding motion of adjacent layers, facilitated by weak π-π interactions between the benzimidazolyl groups of the ligand. In other words, the association of the 2D layers by weak interactions allowed for the mutual displacement of the layers under suitable conditions. In this manner, **IMMOF-2** was capable of transforming from a "closed" phase with very small voids that could be occupied by 4.1 wt% CO_2 to an "open" phase with 8.2 wt% CO_2 uptake at a very specific pressure of 32 bar. Moreover, this transformation, which creates additional space within the structure, occurs selectively with CO_2 at room temperature, relative to N_2 or CH_4. In the high pressure phase, desorption of half of the CO_2 molecules only occurs once the pressure is reduced to below 10 bar. In the low pressure phase, the remaining CO_2 is situated in small discrete voids of 60 $Å^3$ where it forms numerous stabilising close contacts with the host framework, which is probably the reason for the significant amount of hysteresis in the desorption. Desorption occurs over 3 days in a large single crystal or several hours in a powder of **IMMOF-2**. Consequently, **IMMOF-2** could be utilised for controlled-release applications or highly selective interim storage of CO_2.[112] There are only a few materials in the literature that have shown this gate-opening behaviour.[49,113] Moreover, it is extremely rare that a dynamic MOF retains its single crystallinity when it interconverts between an "open" and "closed" or dense structure. The mechanisms of gate-opening sorption and extreme hysteresis are not yet well understood, and structures of gas-loaded single crystals such as those of **IMMOF-2** yield an invaluable amount of information about these processes. Furthermore, this is only the second known example where constant pressure-gradient HPDSC measurements were combined with SCD structures under gas pressure to study a gate-opening sorption phenomenon. The first constant pressure-gradient HPDSC measurements were carried out in our group on MOF-508[44,114] ($[Zn_2(\mathbf{BDC})_2(\mathbf{BPY})]$, **BDC** = 1,4-benzene dicarboxylic acid, **BPY** = 4,4'-bipyridine), a compound known from the literature. However in this dissertation the HPDSC and SCD experiments were carried out on a novel MOF, the result being a more complete structural understanding of its sorption properties.

Chapter 4 explores the permanent porosity of a novel 3D MOF. In contrast to **IMMOF-2**, the 3D Zn(II)-MOF incorporating **L7**, (**IMMOF-3**), is an extremely robust framework. The

framework interactions play a different role in the 3D MOF to those in the 2D layered structures. **IMMOF-3** is stabilised by interactions between the framework constituents along all three dimensions. The hydrogen bonds between hydroxyl groups and the carboxyl oxygen atoms along the $[Zn\text{-}OH\text{-}]_n$ chain, as well as the π-π interactions between the aromatic naphtha(2,3-*d*)imidazolyl moieties of **IMMOF-3,** stabilise the framework, making it extremely robust. As a result, the framework can withstand high temperatures, guest removal and guest-exchange processes (i.e. the porosity and single-crystal quality of the crystals are maintained).

IMMOF-3 is capable of undergoing numerous single-crystal to single-crystal transformations, a useful attribute since it enables the direct study of host-guest and guest-guest interactions. SCD data suggest that the framework is selective for guests that can form hydrogen bonds with the basic oxygen atom of the carboxyl group of the ligand (e.g. water, methanol, ethanol, *n*-propanol and *iso*-propanol).

The structural response of the framework to guests of varying size, shape and polarity was also investigated, such that the channel volume expands when hydrogen-bonded guests, such as a series of alcohols of increasing size, are included. Expansion of the channel is also observed upon the inclusion of other large molecules such as iodine. Preliminary computational studies reveal that the framework is in a destabilised state when it includes a larger guest and, consequently, that host-guest interactions must provide significant stabilisation of this high-energy state.

The SCD data collections that were carried out with crystals of **IMMOF-3** placed under gas pressures generally yielded gas inclusion complexes with low site-occupancy factors for the guest molecules. The high mobility of the gases at the experimental temperatures used generally results in dynamic disorder of the guest molecules. Strong interactions are required to fix the positions of the molecules within the channel. For instance, the halogen-bonding interactions of methyl bromide, vinyl bromide and vinyl fluoride with the carboxyl oxygen atom of the framework serve to fix their positions. The highest occupancy per channel section determined from the SQUEEZE electron count was achieved with acetylene. The small size of the acetylene molecule, in combination with the hydrogen-bond interaction of the acetylenic hydrogen atom with the basic oxygen of the carboxyl group, explains the high occupancy and the enhanced affinity of the framework for this gas. The sorption capacity of the framework was studied further by measuring sorption isotherms with various gases. Based on the sorption isotherms, it

was found that the hydrophilic channels have a higher capacity for CO_2 in comparison to hydrocarbons (CH_4, C_2H_4, C_2H_6) and N_2.

Interestingly, the gas inclusion complexes of **IMMOF-3** also showed temperature dependence for the host-guest and guest-guest interaction distances. When CO_2 is included, a decrease in the temperature reduces the guest-guest interaction distances whilst the host-guest distances are increased. In contrast, the methyl bromide molecules are closer to the framework at lower temperatures owing to a reduced host-guest interaction distance (halogen bond to carboxyl oxygen atom) while there are no discernible guest-guest interactions. The results demonstrate that temperature-dependent studies of host-guest complexes might yield experimental evidence of whether the host-guest or guest-guest interactions are dominant in the stabilisation of the guest molecules within a void.

The response of the empty host framework to temperature was also investigated. **IMMOF-3** displays anisotropic thermal expansion, with anomalously large PTE along the *c* axis and NTE along the *a* and *b* axes. The thermal response, which involves substantial changes in the coordination environment around the Zn(II) metal centre, is further evidence of its flexibility. The anisotropic thermal expansion was enhanced by the presence of methanol, ethanol and *n*-propanol within the channels, with an incremental increase in the magnitudes of the linear expansion coefficients for both the PTE and the NTE, depending on the guest size. *Iso*-propanol inhibited the extent of thermal expansion, as the framework is already in an expanded/destabilised state. To our knowledge, this is the first study of the fine-tuning of thermal expansion coefficients by means of including a series of guest molecules within a host framework.[115]

Chapter 5 describes the gas sorption and guest inclusion properties of a novel metallocycle (**MC1**). The preparation of the metallocycle was not straightforward owing to the crystallisation of concomitant polymorphs if the stoichiometric ratio of the metal:ligand was varied even slightly. It was established that the metallocycle is the kinetic product of the crystallisation, while the concomitant 1D polymeric phase is a thermodynamic product. Moreover, the **MC1** phase converts to an unknown phase upon direct heating to 150 °C, or if left to stand in the open for several months and thus this transiently porous material is not very stable/robust. Nonetheless, the apohost of the **MC1** phase can be generated as a single crystal by stepwise heating. Once the apohost was prepared, gas sorption isotherms with CO_2, N_2 and C_2H_4 were measured. **MC1** includes CO_2 with a larger H:G ratio than either N_2 or C_2H_4 and there is hysteresis apparent in all

three sorption isotherms. SCD with gas-loaded single crystals provided structural information about the host-guest interactions that may be causing the hysteresis, as well as about the deformation of the host itself upon gas inclusion.

Chapter 6 described the first evidence for a CO_2 inclusion complex with a well-known organic host material, calix[4]arene (**C4**). This non-porous material is able to entrap CO_2 after recrystallisation from supercritical CO_2. IR, H^1NMR and X-ray diffraction techniques were used as experimental evidence for the inclusion of CO_2, while the most likely position of the CO_2 within the interstitial voids was validated by DFT and molecular mechanics computations.

In conclusion, the quote by Leopold Ruzicka that suggests that crystals are the *cemetery of chemistry*[19] is proving to be completely wrong. The dynamic changes induced in the various host-guest compounds by varying the physical and the chemical conditions demonstrate that solid materials are capable of extremely interesting chemistry.

SUGGESTED FUTURE STUDIES

Future studies may include:

(i) Selectivity experiments with **IMMOF-3** that involve exposure of the crystals to a mixture of solvents or gases, where after the uptake is determined by analysing the remaining solvent or gas to determine its composition using suitable methods of analysis ("head-space analysis" by gas chromatography). The experimental selectivity studies can be supplemented with a computational study aimed at calculating interaction energies of various guest molecules with the host framework.

(ii) The plot of the unit cell axes of **IMMOF-3** at different temperatures has a peculiar deviation from linearity around the temperature range 200 to 250 K. The non-linear expansion at these temperatures was present for both the apohost and solvent inclusion complexes, and this phenomenon needs further investigation. Whether the vibrational motion of the phenylene ring of the organic ligand plays a role in the NTE along the *a* and *b* axes also needs to be confirmed using other analytical techniques. Solid-state NMR studies may be beneficial for studying dynamic motion of the framework at elevated temperatures. NMR spectroscopy may be used to determine whether an order-disorder transition is taking place close to the temperature at which the deviation from linear thermal expansion was observed.

(iii) Finally, a more extensive and versatile collection of MOFs with different topologies can be synthesised with organic ligands **L1**-**L7** and the many metal nitrate salts that are available. Specifically, **L7** should be reacted with other metal nitrate salts in the hope of producing more 3D functional materials. There are a vast number of supramolecular assemblies that can be formed as hybrid systems, such as MOFs. Consequently, the possibilities for producing functional framework materials are endless and it is the in-depth exploration of the structure-related properties that results in the most fascinating science.

REFERENCES

1. J. M. Lehn, *Acc. Chem. Res.* **1978**, *11*, 49-57.
2. J. M. Lehn, *Pure Appl. Chem.* **1978**, *50*, 871-892.
3. J. L. Atwood, J. W. Steed, *Encyclopedia of Supramolecular Chemistry*. 2004; Vol. 2.
4. G. R. Desiraju, *Crystal Engineering, the Design of Organic Solids*. Elsevier: Amsterdam, 1989.
5. G. R. Desiraju, *Angew. Chem Int. Ed. Engl.* **1995**, *34*, 2311-2327.
6. G. M. J. Schmidt, *Pure Appl. Chem.* **1971**, *27*, 647-678.
7. J. E. Davies, F. H. Allen, J. J. Galloy, O. Johnson , O. Kennard, C. F. Macrae, E. M. Mitchell, G. F. Mitchell, J. M. Smith, D. G. Watson *J. Chem. Inf. Comput. Sci.* **1991**, *31*, 187-204.
8. G. R. Desiraju, *The crystal as a supramolecular entity*. John Wiley & Sons Ltd.: England, 1996.
9. E. Fischer, *Ber. Dtsch. Chem. Ges.* **1894**, *27*, 2985-2993.
10. (a) B. H. Davis, S. Kenneth, W. Sing, *Handbook of Porous Solids*. Wiley: Weinheim, 2002; Vol. 2; (b) J. Lipkowski, Werner Clathrates. In *Comprehensive Supramolecular Chemistry*, J. L. Atwood, J. E. D. Davies, D. D. MacNicol, F. Vögtle, Eds. Pergamon: Oxford, 1996; Vol. 6, pp 691-714; (c) T. Jacobs, Self-assembly of new porous materials, PhD dissertation, Stellenbosch University, Stellenbosch, 2009.
11. E. P. Kyba, R. C. Helgeson, K. Madan, G. W. Gokel, T. L. Tarnowski, S. S. Moore, D. J. Cram, *J. Am. Chem. Soc.* **1977**, *99* (8), 2564-2571.
12. L. R. Nassimbeni, *Acc. Chem. Res.* **2003**, *36* (8), 631-637.
13. N. Ko, H. Furukawa, Y. B. Go, N. Aratani, S. B. Choi, E. Choi, A. O. Yazaydin, R. Q. Snurr, M. O'Keeffe, J. Kim, O. M. Yaghi, *Science* **2010**, *329*, 424-428.
14. S. Brunauer, P. H. Emmet, E. Teller, *J. Am. Chem. Soc.* **1938**, *60*, 309-319.
15. A. I. Cooper, J. R. Holst, *Adv. Mater.* **2010**, *22*, 5212-5216.
16. J. L. C. Rowsell, O. M. Yaghi, *Angew. Chem. Int. Ed.* **2005**, *44*, 4670-4679.
17. (a) P. A. Wright, *Microporous Framework solids*. Royal Society of Chemistry: UK, 2008; (b) D. P. Broom, *Hydrogen Storage Materials: The Characterisation of Their Storage Properties.* Springer-Verlag: London, 2011.
18. S. M. Neville, S. R. Batten, D. R. Turner *Coordination polymers: Design, Analysis & Application*. Royal Society of Chemistry: UK, 2009.

19. L. J. Barbour, *Aust. J. Chem.* **2006**, *59*, 595-596.
20. (a) D. J. Cram, E. Maverick, *Comprehensive Supramolecular Chemistry*. 1 ed.; Pergamon: Oxford, 1996; Vol. 1; (b) B. Dietrich, *Comprehensive Supramolecular Chemistry*. 1 ed.; Pergamon: Oxford, 1996; Vol. 1.
21. Z. Minghua, Y. Zheng, *Sci. China. Chem.* **2010**, *54*, 1371-1394.
22. (a) J. L. Atwood, L. J. Barbour, A. Jerga, *Science* **2002**, *296* (5577), 2367-2369; (b) L. J. Barbour, *Chem. Commun.* **2006**, *11*, 1163-1168; (c) L. J. Barbour, J. L. Atwood, A. Jerga, *Chem. Commun.* **2002**, 2952-2953; (d) L. J. Barbour, J. L. Atwood, G. O. Lloyd, P. K. Thallapally, *Chem. Commun.* **2004**, 922-923.
23. (a) G. O. Lloyd, L. Dobrzanska, H. G. Raubenheimer, L. J. Barbour, *J. Am. Chem. Soc.* **2005**, *127*, 13134-13135; (b) G. O. Lloyd, L. Dobrzanska, H. G. Raubenheimer, L. J. Barbour, *J. Am. Chem. Soc.* **2006**, *128*, 698-699; (c) G. O. Lloyd, L. Dobrzanska, C. Esterhuysen, L. J. Barbour, *Angew. Chem Int. Ed.* **2006**, *45*, 5856-5859; (d) G. O. Lloyd, L. Dobrzanska, L. J. Barbour, *New. J. Chem.* **2007**, *31*, 669-676; (e) J. A. Gertenbach, T. Jacobs, D. Das, L. J. Barbour, *Aust. J. Chem.* **2010**, *63*, 573-577; (f) T. Jacobs, G. O. Lloyd, J. A. Gertenbach, K. K. Muller-Nedebock, C. Esterhuysen, L. J. Barbour, Angew. Chem., Int. Ed., **2012**, *51*, 4913–4916 (g) T. Jacobs, L. J. Barbour, *CrystEngComm*, **2013**, *15*, 1512-1514.
24. L. Schlapbach, A. Zuttel, *Nature* **2001**, *414* (6861), 353-358.
25. L. J. Barbour, *Chem. Commun.* **2006**, *11*, 1163-1168.
26. (a) L. J. Barbour, J. L. Atwood, A. Jerga, B. L. Schottel, *Science* **2002**, *298*, 1000-1002; (b) J. W. Steed, *Science* **2002**, *298*, 976-977.
27. (a) H. Kayser, *Wied. Ann. Phys.* **1881**, *12*, 526; (b) H. Kayser, *Wied. Ann. Phys.* **1881**, *14*, 450; (c) A. Fick, *Phil. Mag.* **1855**, *10*, 30; (d) M. Suzuki, *Adsorption Engineering, Chemical Engineering Monographs 25, Kondansha Ltd and Elsevier Publishers B.V.*, 1990.
28. F. Rouquerol, J. Rouquerol, K. Sing, *Adsorption by Powders and Porous Solids, Academic Press, San Diego*, 1999.
29. K. S. W. Sing, D. H. Everett, R. A. W. Haul, L. Moscou, R. A. Pierotti, J. Rouquerol, T. Siemieniewska, P*ure Appl. Chem.* **1985**, *57*, 603-619.
30. S. Lowell, J. E. Shields, M. A. Thomas, M. Thommes, *Characterization of Porous Solids and Powders: Surface Area, Pore Size and Density*, Kluwer Academic Publishers, Dordrecht, The Netherlands, 2004.

31. J. Rouquerol, D. Avnir, C. W. Fairbridge, D. H. Everett, J. H. Haynes, N. Pernicone, J. D. F. Ramsay, K. S. W. Sing, K. K. Unger, *Pure Appl. Chem.* **1994**, *66*, 1739-1758.

32. (a) *SADABS*, Version 2.05; Bruker AXS Inc.: Madison, WI, 2002; (b) R. H. Blessing, *Acta Crystallogr., Sect. A: Found. Crystallogr.* **1995**, *51*, 33-38.

33. G. M. Sheldrick, *Acta Crystallogr., Sect. A: Found. Crystallogr.* **2008**, *64*, 112-122.

34. L. J. Barbour, *Journal of Supramolecular Chemistry* **2001**, *1*, 189-191.

35. M. A. White, Thermal Analysis and Calorimetry Methods. In *Comprehensive Supramolecular Chemistry*, J. E. Davies; J. A. Ripmeester, Eds. Pergamon: Oxford, 1996; Vol. 8, pp 179-197.

36. *PLATON, A Multipurpose Crystallographic Tool*, Utrecth University: Utrecht, The Netherlands, 2008.

37. (a) A. L. Spek, P. van der Sluis, *Acta Crystallogr., Sect. A: Found. Crystallogr.* **1990**, *46*, 194-201; (b) A. L. Spek, *J. Appl. Cryst.* **2003**, *36*, 7-13.

38. *POV-RAY*^{TM} *for Windows*, Version 3.6; Persistence of Vision Raytracer Pty. Ltd.: 2004.

39. (a) M. L. Connolly, *Science* **1983**, *221*, 709-713; (b) M. L. Connolly, *J. Mol. Graphics* **1993**, *11*, 139-143.

40. B. Lee, F. M. Richards, *J.Mol. Biol.* **1971**, *55*, 379-400.

41. D. K. Ross, M. J. Benham, *Z. Phys. Chem.* **1989**, *163*, 25-32.

42. (a) C. R. Reid, I. P. O'Koye, K. M. Thomas, *Langmuir* **1998**, *14*, 2415-2425; (b) A. W. Harding, N. J. Foley, P. R. Norman, D. C. Francis, K. M. Thomas, *Langmuir* **1998**, *14*, 3858-3864; (c) I. P. O'Koye, M. Benham, K. M. Thomas, *Langmuir* **1997**, *13*, 4054-4059; (d) N. J. Foley, K. M. Thomas, P. L. Forshaw, D. Stanton and P. R. Norman, *Langmuir* **1997**, *13*, 2083-2089; (e) A. J. Fletcher, K. M. Thomas, *Langmuir* **1999**, *15*, 6908-6914; (f) A. J. Fletcher, K. M. Thomas, *Langmuir* **2000**, *16*, 6253-6266.

43. L. J. Barbour, K. Achleitner, J. R. Greene, *Thermochim. Acta* **1992**, *205*, 171-177.

44. E. Batisai, *Synthesis and Sorption Studies of Porous Metal-Organic Hosts*, PhD dissertation, Stellenbosch University, Stellenbosch, 2012.

45. (a) O. M. Yaghi, M. O'Keeffe, N. W. Ockwig, H. K. Chae, M. Eddaouddi, J. Kim, *Nature* **2003**, *423*, 705-714; (b) N. W. Ockwig, O. Delgado-Friedrichs, M. O'Keeffe, O. M. Yaghi,

Acc. Chem. Res. **2005**, *38*, 176-182; (c) A. K. Cheetham, C. N. R. Rao, R. K. Feller, *Chem. Commun.* **2006**, *46*, 4780-4795.

46. (a) B. F. Hoskins, R. Robson, *J. Am. Chem. Soc.* **1989**, *111*, 5962-5964; (b) B. F. Hoskins, R. Robson, *J. Am. Chem. Soc.* **1990**, *112*, 1546-1554.

47. M. Eddaoudi, J. Kim, N. Rosi, D. Vodak, J. Wachter, M. O'Keefe, O. M. Yaghi, *Science* **2002**, *295*, 469-472.

48. H. Li, M. Eddaoudi, M. O'Keeffe, O. M. Yaghi, *Nature* **1999**, *402*, 276-279.

49. S. Horike, S. Shimomura, S. Kitagawa, *Nat. Chem.* **2009**, *1*, 695-704.

50. R. Kitaura, K. Seki, G. Akimyama, S. Kitagawa, *Angew. Chem Int. Ed.* **2003**, *42*, 428-430.

51. H. Choi, M. Dincă, , J. R. Long, *J. Am. Chem. Soc.* **2008**, *130*, 7848-7850.

52. R. Matsuda, R. Kitaura, S. Kitagawa, Y. Kubota, T. Kobayashi, S. Horike, M. Takata, *J. Am. Chem. Soc.* **2004**, *126*, 14063-14070.

53. S. G. Telfer, T. Sato, R. Kuroda, J. Lefebvre, D. B. Leznoff, *Inorg. Chem.* **2004**, *43*, 421-429.

54. A. Aijaz, P. Lama, E. C. Sanudo, R. Mishra, P. K. Bharadwaj, *New. J. Chem.* **2010**, *34*, 2502-2514.

55. A. P. Nelson, O. K. Farha, K. L. Mulfort, J. T.Hupp, *J. Am. Chem. Soc.* **2009**, *131*, 458-460.

56. B. F. Graham, J. M. Harrowfield, R. D. Tengrave, *J Incl Phenom Marcocycl Chem* **2002**, *43*, 179-182.

57. (a) L. C. Fetterly, *Non-Stoichiometric Compounds*, Academic Press, New York, **1964**; (b) M. D. Hollingsworth, K. D. M. Harris, *Comprehensive Supramolecular Chemistry, Vol. vol. 6*, Pergamon Press, **1996**; (c) K. D. M. Harris, *J. Mol. Struct.* **1996**, *374*, 241; (d) K. D. M. Harris, *Supramol. Chem.* **2007**, *19*, 47-53; (e) K. D. M. Harris, *Chem. Soc. Rev.* **1997**, *26*, 279-289; (f) A. E. Smith, *Acta Crystallogr.* **1952**, *5*, 224-235; (g) K. D. M. Harris, J. M. Thomas, *J. Chem. Soc., Faraday Trans.* **1990**, *86*, 1095-1101; (h) K. D. M. Harris, *J. Solid State Chem.* **1993**, *106*, 83-98; (i) F. Guillaume, *J. Chim. Phys. (Paris)* **1999**, *96*, 1295; (j) M. D. Hollingsworth, *Science* **2002**, *295*, 2410-2413.

58. (a) A. J. O. Rennie, K. D. M. Harris, *Proc. R. Soc. London, Ser. A* **1990**, *430*, 615-640; (b) B. A. Palmer, B. M. Kariuki, V. K. Muppidi, C. E. Hughes, K. D. M. Harris, *Chem. Commun.* **2011**, *47*, 3760-3762.

59. H. Flack, A. Gavezzotti. In *http://www.iucr.org/iucr-top/comm/cteach/pamphlets/21/21.html*, IUCr, Ed. Commission on Crystallographic Teaching, Chester, **2005**, Vol. 21.

60. J. R. Li, R. J. Kuppler, H. C. Zhou, *Chem. Soc. Rev.* **2009**, *38*, 1477-1504.

61. T. Borjigin, F. Sun, J. Zhang, K. Cai, H. Ren, G. Zhu, *Chem. Commun.* **2012**, *48*, 7613-7615.

62. P. H. Svensson, L. Kloo, *Chemical Reviews* **2003**, *103*, 1649-1684.

63. (a) Z. Wang, B. Zhang, H. Fujiwara, H. Kobayashi, M. Kurmoo, *Chem. Commun.* **2004**, 416-417; (b) C. Ouvrard, J. L. Questel, M. Berthelot, C. Laurence, *Acta Cryst.* **2003**, *B59*, 512-526.

64. A. Forni, P. Metrangolo, T. Pilati, G. Resnati, *Crystal Growth & Design* **2004**, *4*, 291-295.

65. C. Serre, C. Mellot-Draznieks, S. Surblé, N. Audebrand, Y. Filinchuk, G. Férey, *Science* **2007**, *315*, 1828-1831.

66. L. D. DeVries, P. M. Barron, E. P. Hurley, C. Hu, W. Choe *J. Am. Chem. Soc.* **2011**, *133*, 14848-14851.

67. (a) R.M. Hazen C. T. Prewitt, *Am. Mineral* **1977**, *62*, 309-315; (b) I.D. Brown, A. Dabkowski, A. McClearly *Acta Cryst. Sect. B* **1997**, *53*, 750-761.

68. (a) A. L. Goodwin, M. Calleja, M. J. Conterio, M. T. Dove, J. S. O. Evans, D. A. Keen, L. Peters, M. G. Tucker *Science* **2008**, *319*, 794-797; (b) A. L. Goodwin, B. J. Kennedy, C. J. Kepert *J. Am. Chem. Soc.* **2009**, 6334-6335; (c) M. L. Katz, J. L. Korcok , D. L. Lenznott, *J. Am. Chem. Soc.* **2009**, *131*, 4866-4871; (d) A. E. Phillips, G. J. Halder, K. W. Chapman, A. L. Goodwin, C. J. Kepert *J. Am. Chem. Soc.* **2010**, *132*, 10-11.

69. (a) J. S. O. Evans, *J. Chem. Soc., Dalton Trans.* **1999**, *1999*, 3317-3326; (b) P. Lightfoot, D. A. Woodcock, M. J. Maple, L. A. Villaescusa, P. A. Wright *J. Mater. Chem.* **2001**, *11*, 212-216.

70. D. Das, T. Jacobs, L. J. Barbour *Nature Materials* **2010**, *9*, 36-39.

71. G. H. Greyling, Negative Thermal Expansion of Organic Compounds, MSc thesis, Stellenbosch University, Stellenbosch, 2011.

72. Y. Wu, A. Kobayashi, G. J. Halder, V. K. Peterson, K. W. Chapman, N. Lock, P. D. Southon, C. J. Kepert *Angew. Chem.Int. Ed.* **2008**, *47*, 8929-8932.

73. (a) A. L. Goodwin, C.J. Kepert, *Phys. Rev. B* **2005**, *71*, 140301-140304; (b) A. L. Goodwin, K. W. Chapman, C. J. Kepert, *J. Am. Chem. Soc.* **2005**, *127*, 17980-17981.

74. (a) V. Korthuis, N. Khosrovani, A. W. Sleight, N. Roberts, R. Dupree, W. W. Warren *Chem. Mater.* **1995**, *7*, 412-417; (b) T. A. Mary, J. S. O. Evans, T. Vogt, A. W. Sleight *Science* **1996**, *272*, 90-92; (c) J. S. O. Evans, Z. Hu, J. D. Jorgensen, D. N. Argyriou, S. Short, A. W. Sleight, *Science* **1997**, *275*, 61-65; (d) C. Lind, A. P. Wilkinson, Z. B. Hu, S. Short, J. D. Jorgensen *Chem. Mater.* **1998**, *10*, 2335-2337; (e) J. S. O. Evans, W. I. F. David, A. W. Sleight *Acta Crystallogr. Sect. B* **1999**, *55*, 333-340.

75. A. K. A. Pryde, K. D. Hammonds, M. T. Dove, V. Heine, J. D. Gale, M. C. Warren *J. Phys. Condens. Matter* **1996**, *8*, 10973-10982.

76. J. Rouquerol, D. Avnir, C. W. Fairbridge, D.H. Everett, J. H. Hayes, N. Pernicone, J. D. F. Ramsay, K. S. W. Sing, K. K. Unger, *Pure Appl. Chem.* **1994**, *66*, 1739-1758.

77. Y. Wei, K. Chen, P. Liao, B. Zhu, R. Lin, H. Zhou, B. Wang, W. Xue, J. Zhang, X. Chen, *Chem. Sci.* **2013**, *4*, 1539-1546.

78. C. Yang, X. Wang, M. A. Omary *Angew. Chem.* **2009**, *48*, 2500-2505.

79. A. E. Phillips, A. L. Goodwin, G. J. Halder, P. D. Southon, C. J. Kepert, *Angew. Chem Int. Ed.* **2008**, *47*, 1596-1599.

80. (a) T. Jacobs, Self-assembly of new porous materials, PhD dissertation, Stellenbosch University, Stellenbosch, 2009; (b) A. Kleyn, Guest-induced flexibility in crystals, PhD dissertation, Stellenbosch University, Stellenbosch, 2012; (c) L. Loots, The Structural Analysis of Imidazole-Functionalised Metallocycles, PhD dissertation, Stellenbosch University, Stellenbosch, 2012; (d) S.V. Potts, Inclusion Studies of Metal-Organic Hosts, PhD dissertation, Stellenbosch University, Stellenbosch, 2011 ; (e) M. du Plessis, Structural Characterisation of Coordination Compounds Incorporating Imidazole-Based Ligands, MSc thesis, Stellenbosch University, Stellenbosch, 2012.

81. Y. Gao, B. Twamley, J. M. Shreeve, *Inorg. Chem.* **2006**, *45*, 1150-1155.

82. (a) L. Dobrzańska, G. O. Lloyd, L. J. Barbour, *New J. Chem.* **2007**, *31*, 669-676, (b) L. Dobrzańska, G. O. Lloyd, C. Esterhuysen, L. J. Barbour, *Angew. Chem. Int. Ed.* **2006**, *45*, 5856-5859.

83. (a) D. Braga, F. Grepioni and L. Maini, *Chem. Commun.* **2010**, *46*, 6232-6242; (b) B. Moulton and M. J. Zaworotko, *Chem. Rev.* **2001**, *101*, 1629-1658; (c) J. L. Atwood, J. W. Steed, *Encyclopedia of Supramolecular Chemistry*, Marcel Dekker, Inc., 2004.

84. Material StudioV4.3, *Accelrys*.

85. J. L. Atwood, L. J. Barbour, A. Jerga and B. L. Schottel, *Science* **2002**, *298*, 1000-1002.

86. G. D. Andreetti, R. Ungaro, A. Pochini, *J. Chem. Soc. Chem. Commun*. **1979**, 1005-1007.

87. S. J. Dalgarno, P. K. Thallapally, L. J. Barbour and J. L. Atwood, *Chem. Soc. Rev.* **2007**, *36*, 236-245.

88. J. L. Atwood, L. J. Barbour and A. Jerga, *Science* **2002**, *296*, 2367-2369.

89. (a) J. L. Atwood, L. J. Barbour and A. Jerga, *Angew. Chem. Int. Ed.* **2004**, *43*, 2948-2950; (b) J. L. Atwood, L. J. Barbour, P. K. Thallapally and T. B. Wirsig, *Chem. Commun*. **2005**, 51.

90. Zinke, A.; Ziegler, *E. Ber. Drsch. Chem. Ges.* **1944**, *77B*, 264-272.

91. J. W. Cornforth, H. P. D'Arcy, G. A. Nicholls, R. J. W. Rees, J. A. Stock, *Brit. J. Pharmacol. Chemother.* **1955**, *10*, 73-88.

92. R. S. Buriks, A. R. Fauke, J. H. Munch, *US. Patent* 4259464; filed 1976, issued 1981

93. C. D. Gutsche, T. C. Kung, M. L. Hsu, "Abstracts of Papers", 1lth Midwest Regional Meeting of the American Chemical Society, Carbondale, IL, 1975, no. 517*; American Chemical Society:* Washington, D.C., 1975.

94. (a) T. B. Patrick, P. A. Egan, *J. Org. Chem.* **1977**, *42*, 382; (b) C. D. Gutsche, J. A. Levine, *J. Am. Chem. Soc.* **1982**, *104*, 2652-2653.

95. R. Ungaro, A. Pochini, G. D. Andreetti, V. Sangermano, *J. Chem. Soc., Perkin Trans. 2* **1984**, 1979-1985.

96. M. F. Kemmere, T. Meyer, *Supercritical carbon dioxide*, Wiley-VCH Verlag GmbH & Co. KGaA, Weinheim, 2006; (b) O.R. Davies, A. L. Lewis, M. J. Whitaker, H. Y. Tai, K. M. Shakesheff, S. M. Howdle, *Advanced Drug Delivery Reviews* **2008**, *60*, 373–387.

97. B. F. Graham, A. F. Lagalante, T. J. Bruno, J. M. Harrowfield, R. D. Trengove, *Fluid Phase Equilibria* **1998**, *150–151*, 829-838.

98. C. G. Marais, Thermodynamics and kinetics of sorption, MSc thesis, Stellenbosch University, Stellenbosch, 2008.

99. (a) H. Sun, *Macromolecules* **1995**, *28*, 701-712; (b) H. Sun, *J. Comp. Chem* **1994**, *15*, 752-768; (c) H. Sun, S. J. Mumby, J. R. Maple, A. T. Hagler, *J. Am. Chem. Soc.* **1994**, *116*, 2978-2987; (d) H. Sun, S. J. Mumby, J. R. Maple, A. T. Hagler, *J. Phys. Chem.* **1995**, *99*, 5873-5882.

100. P. Raveendran, Y. Ikushima, S. L. Wallen, *Acc. Chem. Res.* **2005**, *38*, 478-485.

101. S. J. Clark, M. D. Segall, C. J. Pickard, P. J. Hasnip, M. J. Probert, K. Refson, M. C. Payne, *Zeitschrift fuer Kristallagraphie* **2005**, *220 (5-6)*, 567-570.

102. (a) J. P. Perdew, K. Burke, M. Ernzerhof, *Phys. Rev. Lett.* **1996**, ***77***, 3865-3868; (b) J. P. Perdew *et al.*, *Phys. Rev. Lett.* **2008**, *100*, 136406.

103. B. G. Pfrommer, M. Cote, S. G. Louie, M. L. Cohen, *J. Comput. Phys.* **1997**, *131*, 133-140.

104. S. Grimme, *J. Comput. Chem.* **2006**, *27*, 1787-1799.

105. M. I. J. Probert, *J. Comput. Phys.* **2003**, *191*, 130-146.

106. (a) E. P. Bishop, R. Rohs, S. C. J. Parker, S. M. West, P. Liu, R. S. Mann, B. Honig, T. D. Tullius, *ACS Chemical Biology* **2011**, *6* (12), 1314-1320; (b) A. Chang, B. A. Hackett, C. C. Winter, U. J. Buchholz, R. E. Dutch, *J. Virol.* **2012**, *86* (18), 9843-9853; (c) F. S. Dukhovich, M. B. Darkhovskii, *J. Mol. Recognit.* **2003**, *16* (4), 191-202; (d) P. Sjoberg, J. S. Murray, T. Brinck, P. Evans, P. Politzer, *J. Mol. Graph.* **1990**, *8* (2), 81-85.

107. (a) M. Negri, M. Recanatini, R. W. Hartmann, *J. Comput.-Aided Mol. Des.* **2011**, *25* (9), 795-811; (b) J. E. Mendieta-Wejebe, M. C. Rosales-Hernandez, H. Rios, J. Trujillo-Ferrara, G. Lopez-Perez, F. Tamay-Cach, R. Ramos-Morales, J. Correa-Basurto, *J Mol Model* **2008**, *14* (6), 537-545.

108. (a) K. Kadas, S. Kugler, G. NaraySzabo, *J. Phys. Chem.* **1996**, *100* (20), 8462-8467; (b) I. Alkorta, J. J. Perez, H. O. Villar, *J. Mol. Graph.* **1994**, *12* (1), 3-13.

109. P. Politzer, J. S. Murray, *Theor. Chem. Acc.* **2002**, *108* (3), 134-142.

110. (a) J. S. Murray, P. Politzer, *Computational Molecular Science* **2011**, *1* (2), 153-163; (b) G. Naray-Szabo, G. G. Ferenczy, *Chem. Rev.* **1995**, *95* (4), 829-847.

111. J. Jacobs, G. O. Lloyd, J. A. Gertenbach, K. K. Müller-Nedebock, C. Esterhuysen, L. J. Barbour, *Angew. Chem. Int. Ed.* **2012**, *124*, 4997-5000.

112. K. W. Chapman, D. F. Sava, G. J. Halder, P. J. Chupas, T. M. Nenoff, *J. Am. Chem. Soc.* **2011**, *133(46)*, 18583-18585.

113. (a) S. Kitagawa, M. Kondo, *Bull. Chem. Soc. Jpn.* **1998**, *71*, 1739–1753; (b) D. Tanaka, K. Nakagawa, M. Higuchi, S. Horike, Y. Kubota, T. C. Kobayashi, M. Takata, S. Kitagawa, *Angew. Chem. Int. Ed.* **2008**, *120*, 3978-3982; (c) J. A. R. Navarro, E. Barea, A. Rodriguez-Dieguez, J. M. Salas, C. O. Ania, J. B. Parra, N. Masciocchi, S. Galli, A. Sironi, *J. Am. Chem. Soc.* **2008**, *130*, 3978–3984; (d) S. Galli, N. Masciocchi, G. Tagliabue, A. Sironi, J. A. R. Navarro, J. M. Salas, L. Mendez-Linan, M. Domingo, M. Perez-Mendoza, E. Barea, *Chem. Eur. J.* **2008**, *14*, 9890–9901; (e) S. Aguado, G. Bergeret, M. P. Titus, V. Moizan, C. Nieto-Dragni, N. Bat, D. Farrusseng, *New J. Chem*. **2011**, *35*, 546-550; (f) D. Fairen-Jimenez, S. A. Moggach, M. R. Wharmby, P. A. Wright, S. Parsons, T. Düren, *J. Am. Chem. Soc.* **2011**, *133 (23)*, 8900-8902.

114. B. Chen, C. Liang, J. Yang, D. S. Contreras, Y. L. Clancy, E. B. Lobkovsky, O. M. Yaghi, S. Dai, *Angew. Chem. Int. Ed.* **2006**, *118*, 1418-1421.

115. I. Grobler, V. J. Smith, P. M. Bhatt, S. A. Herbert, L. J. Barbour, *J. Am. Chem. Soc.* **2013**, *135*, 6411-6414.

Appendix A

Supplementary CD

The supplementary CD contains:

(i) CIF and RES files of all relevant structures.

(ii) Publication in *J. Am. Chem. Soc.*

(iii) Conference posters.

NMR spectra

A1. Synthesis of **L6**

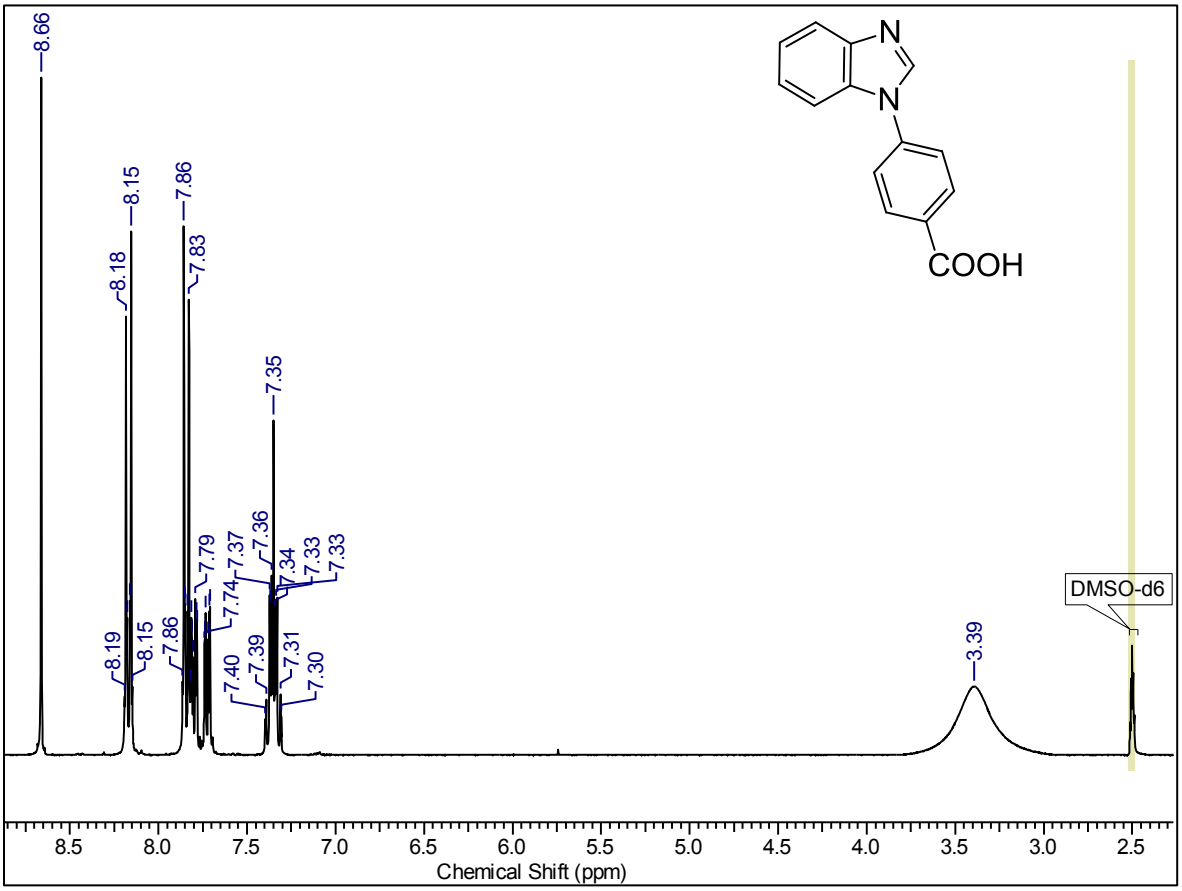

Spectrum 1. H^1 NMR spectrum of **L6**

A2. Synthesis of **L7**

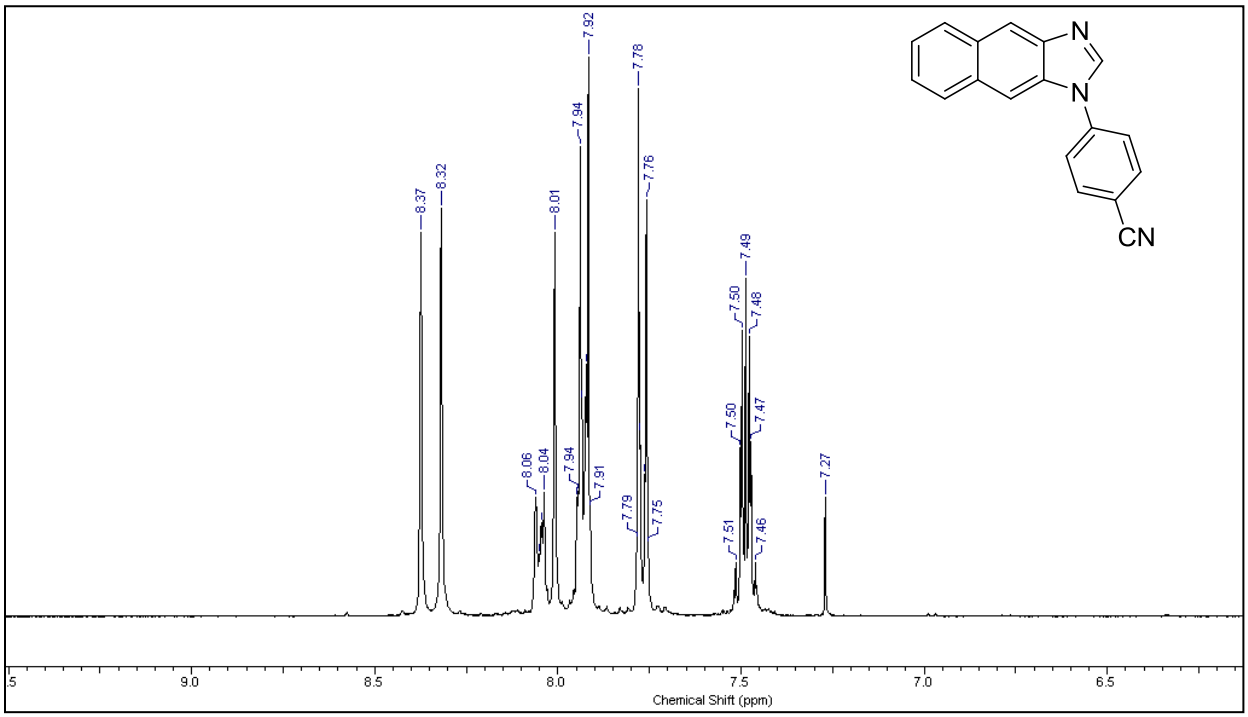

Spectrum 2. H^1NMR spectrum of the cyanide precursor of **L7.**

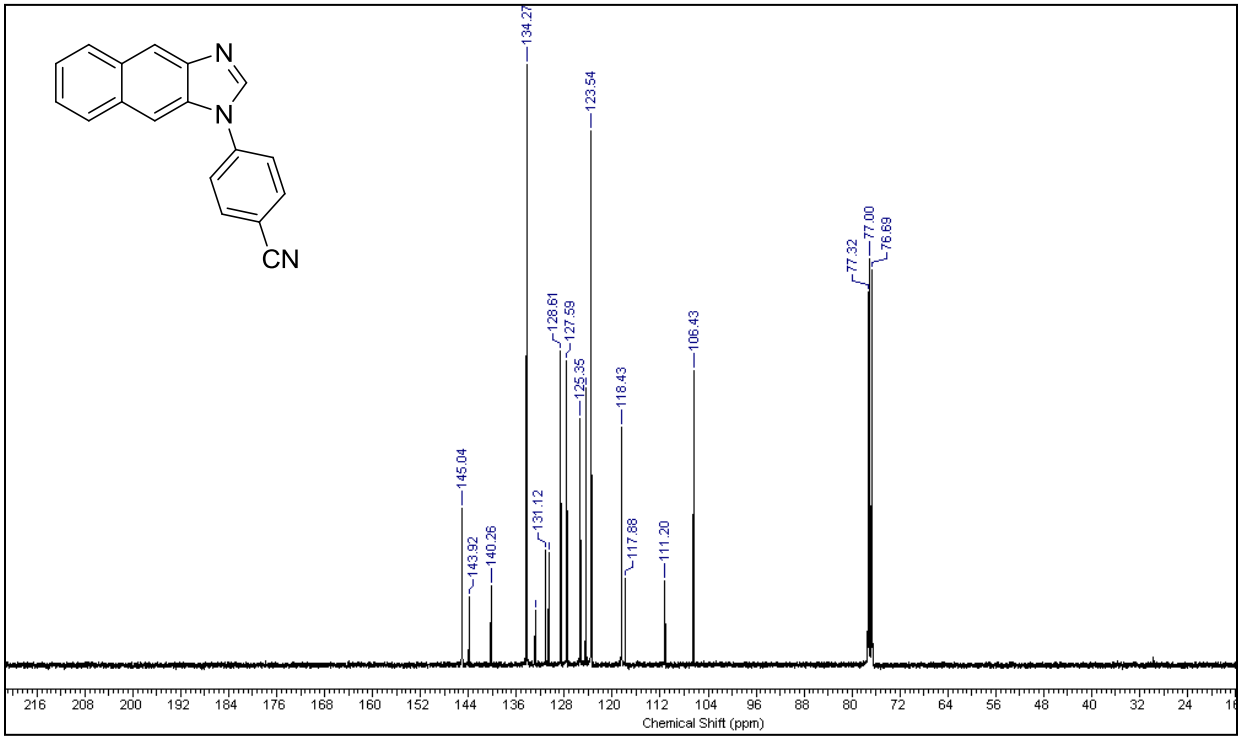

Spectrum 3. C^{13}NMR spectrum of the cyanide precursor of **L7.**

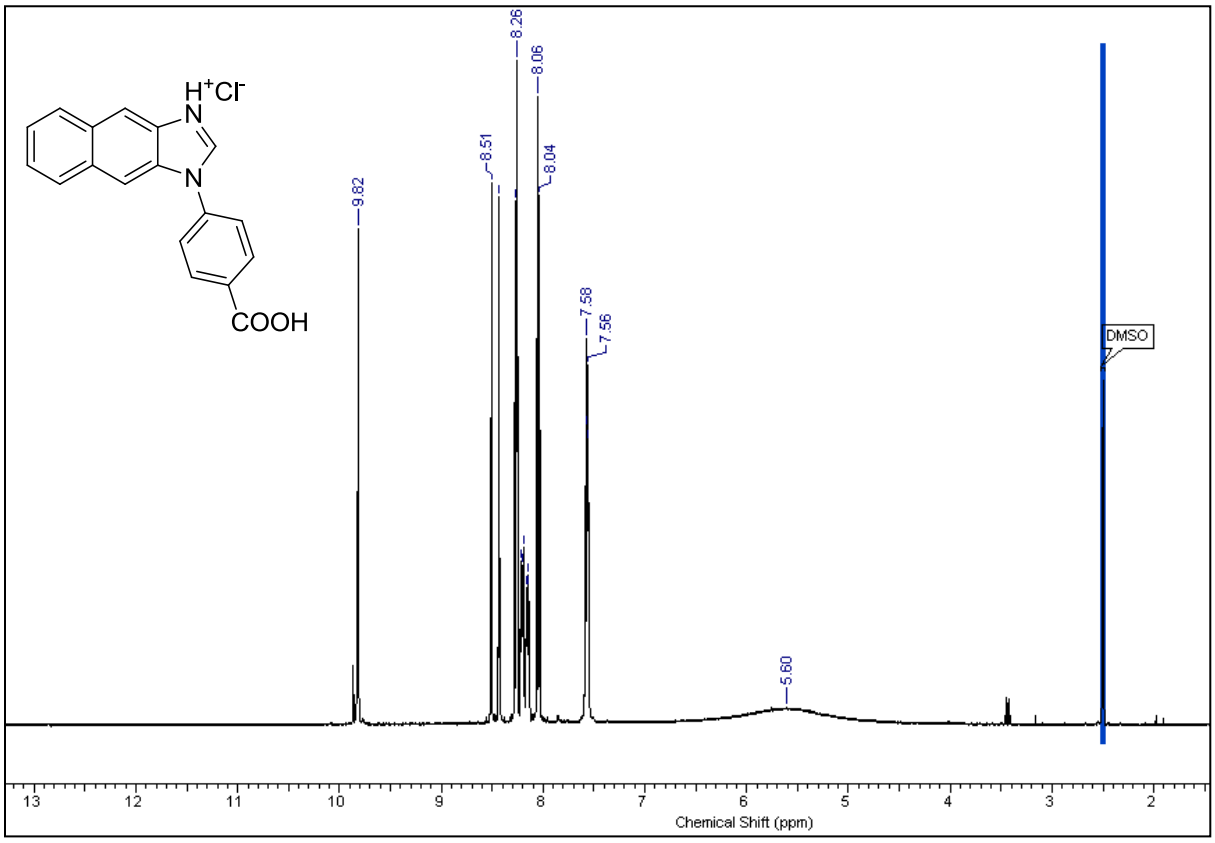

Spectrum 4. H^1NMR spectrum of the salt of **L7** formed in the presence of hydrochloric acid**.**

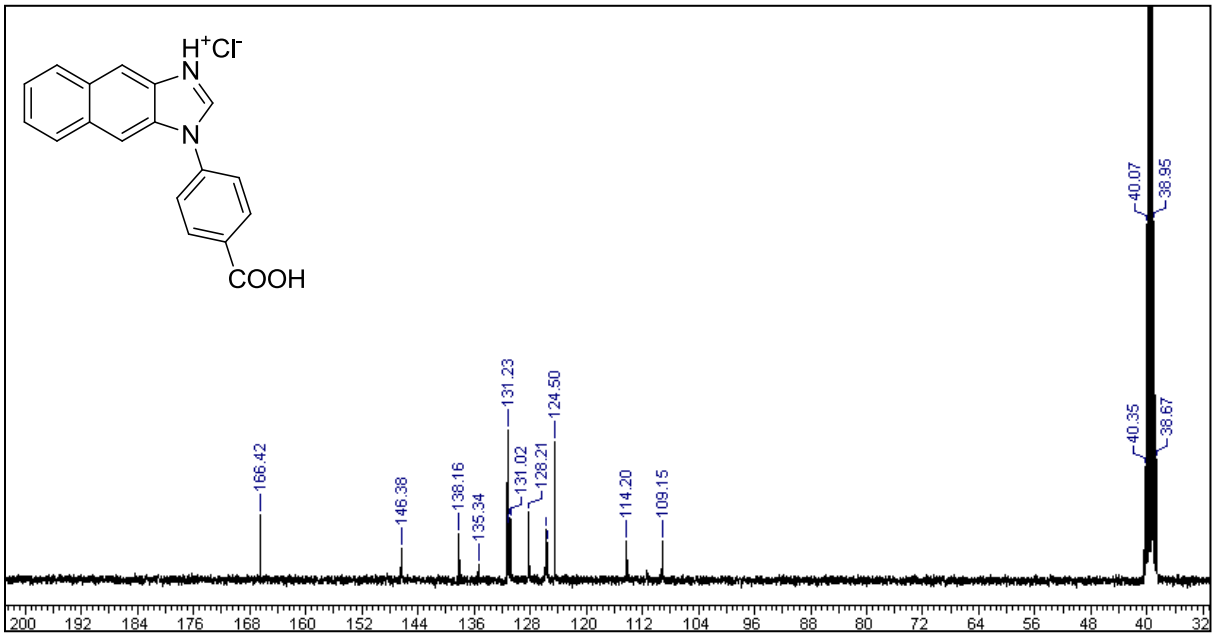

Spectrum 5. C^{13}NMR spectrum of the salt of **L7** formed in the presence of hydrochloric acid**.**

Appendix B

Table B1. Unit cell determinations at variable temperatures for the as-synthesised framework, **IMMOF-3$_{MeOH}$.**

	Unit cell parameters						
***T* (K)**	***a, b* (Å)**	**St. dev.***	***c* (Å)**	**St. dev. ***	**Cell volume (Å^3)**	**St. dev. ***	**Crystal mosaicity**
100	26.774	0.009	5.0312	0.0019	3607	4	0.62
115	26.749	0.008	5.035	0.0019	3603	4	0.62
130	26.758	0.010	5.046	0.002	3613	5	0.62
145	26.757	0.010	5.054	0.002	3618	5	0.62
160	26.739	0.010	5.064	0.002	3621	5	0.61
175	26.733	0.010	5.076	0.002	3628	5	0.62
190	26.752	0.011	5.091	0.002	3643	5	0.62
205	26.747	0.010	5.105	0.002	3652	5	0.62
220	26.706	0.015	5.114	0.003	3647	7	0.62
235	26.726	0.013	5.133	0.003	3666	7	0.62
250	26.663	0.013	5.140	0.003	3654	6	0.62
265	26.656	0.013	5.159	0.003	3666	7	0.63
280	26.643	0.012	5.182	0.002	3678	7	0.63
295	26.559	0.014	5.194	0.003	3663	7	0.63
310	26.543	0.016	5.214	0.003	3674	8	0.62
325	26.488	0.016	5.245	0.003	3680	8	0.62
340	26.476	0.017	5.281	0.004	3702	8	0.62
355	26.444	0.017	5.310	0.003	3714	9	0.63
370	26.43	0.02	5.305	0.004	3705	10	0.66

*Standard deviation calculated from unit cell refinement using the Apex II Data software suite.

Table B2. Unit cell determinations at variable temperatures for **IMMOF-3$_{EtOH}$.**

	Unit cell parameters						
***T* (K)**	***a, b* (Å)**	**St. dev.***	***c* (Å)**	**St. dev. ***	**Cell volume (Å^3)**	**St. dev. ***	**Crystal mosaicity**
100	26.69	0.02	5.109	0.004	3639	5	0.62
115	26.70	0.02	5.122	0.005	3650	5	0.62
130	26.69	0.02	5.130	0.005	3654	5	0.62
145	26.66	0.02	5.136	0.004	3651	5	0.62
160	26.63	0.02	5.142	0.004	3646	4	0.63
175	26.665	0.019	5.161	0.004	3669	5	0.62
190	26.64	0.03	5.168	0.006	3668	6	0.62
205	26.66	0.03	5.184	0.006	3684	7	0.61
220	26.67	0.02	5.200	0.004	3698	6	0.62
235	26.65	0.03	5.209	0.005	3699	6	0.61
250	26.55	0.05	5.205	0.011	3670	8	0.61
265	26.58	0.03	5.225	0.006	3690	7	0.63
280	26.65	0.02	5.248	0.005	3726	7	0.62
295	26.601	0.016	5.252	0.003	3717	4	0.64
310	26.56	0.03	5.258	0.007	3710	8	0.62
325	26.54	0.03	5.264	0.007	3709	9	0.63
340	26.63	0.04	5.299	0.009	3759	9	0.63
355	26.53	0.02	5.294	0.004	3725	6	0.62
370	26.54	0.02	5.307	0.006	3738	6	0.63

*Standard deviation calculated from unit cell refinement using the Apex II software suite.

Table B3. Unit cell determinations at variable temperatures for **IMMOF-3$_{n\text{-PrOH}}$.**

	Unit cell parameters						
***T* (K)**	***a, b* (Å)**	**St. dev.***	***c* (Å)**	**St. dev. ***	**Cell volume (Å^3)**	**St. dev. ***	**Crystal mosaicity**
100	26.812	0.013	5.156	0.003	3707	6	0.62
115	26.773	0.016	5.160	0.004	3699	7	0.62
130	26.765	0.014	5.166	0.003	3701	6	0.63
145	26.752	0.015	5.174	0.003	3703	7	0.63
160	26.717	0.016	5.178	0.003	3696	7	0.62
175	26.698	0.015	5.184	0.003	3695	7	0.63
190	26.700	0.015	5.196	0.003	3704	6	0.61
205	26.724	0.016	5.220	0.003	3728	7	0.61
220	26.704	0.018	5.232	0.004	3731	7	0.62
235	26.686	0.018	5.249	0.004	3738	8	0.62
250	26.651	0.014	5.260	0.003	3736	7	0.62
265	26.642	0.016	5.272	0.003	3742	8	0.61
280	26.648	0.017	5.288	0.003	3755	8	0.62
295	26.614	0.016	5.295	0.003	3751	8	0.62
310	26.604	0.020	5.309	0.004	3757	10	0.63
325	26.59	0.02	5.311	0.004	3755	10	0.64
340	26.511	0.013	5.298	0.003	3734	7	0.64
355	26.489	0.011	5.289	0.003	3711	7	0.65
370	26.50	0.02	5.291	0.004	3717	10	0.64

*Standard deviation calculated from unit cell refinement using the Apex II software suite.

Table B4. Unit cell determinations at variable temperatures for **IMMOF-3$_{iso\text{-PrOH}}$.**

	Unit cell parameters						
***T* (K)**	***a, b* (Å)**	**St. dev.***	***c* (Å)**	**St. dev. ***	**Cell volume (Å^3)**	**St. dev. ***	**Crystal mosaicity**
100	26.192	0.014	5.392	0.003	3699	6	0.76
115	26.203	0.017	5.400	0.003	3707	8	0.76
130	26.194	0.014	5.403	0.003	3708	7	0.77
145	26.202	0.015	5.412	0.003	3716	7	0.78
160	26.202	0.019	5.413	0.004	3717	7	0.78
175	26.235	0.016	5.423	0.003	3733	7	0.78
190	26.17	0.02	5.414	0.004	3708	9	0.78
205	26.18	0.02	5.422	0.004	3715	8	0.77
220	26.201	0.019	5.431	0.004	3728	7	0.77
235	26.230	0.018	5.442	0.004	3744	8	0.77
250	26.223	0.016	5.450	0.003	3748	9	0.78
265	26.27	0.03	5.463	0.005	3769	11	0.80
280	26.26	0.02	5.465	0.005	3767	9	0.78
295	26.31	0.03	5.472	0.005	3787	10	0.78
310	26.35	0.03	5.456	0.006	3787	10	0.79
325	26.45	0.06	5.400	0.012	3778	13	0.81
340	26.67	0.04	5.384	0.007	3805	10	0.79
355	26.64	0.03	5.292	0.006	3755	11	0.79
370	26.64	0.04	5.296	0.007	3760	12	0.79

*Standard deviation calculated from unit cell refinement using the Apex II software suite.